

# **INFLUENCES OF MICROBIAL AND MINERAL PARTICLES ON OCEANIC OPTICS**

## **FINAL REPORT**

**Curtis D. Mobley**  
Sequoia Scientific, Inc.  
9725 S.E. 36<sup>th</sup> Street, Suite 308  
Mercer Island, WA 98040

and

**Dariusz Stramski**  
Marine Physical Laboratory  
Scripps Institution of Oceanography  
University of California, San Diego  
San Diego, CA 92093-0238

Office of Naval Research  
Contract No. N00014-97-C-0024

March, 1999

SEQUOIA

**DISTRIBUTION STATEMENT A**  
Approved for Public Release  
Distribution Unlimited

19990423 071

# **INFLUENCES OF MICROBIAL AND MINERAL PARTICLES ON OCEANIC OPTICS**

## **FINAL REPORT**

On Work Performed by

**Curtis D. Mobley**  
Sequoia Scientific, Inc.  
9725 S.E. 36<sup>th</sup> Street, Suite 308  
Mercer Island, WA 98040

and

**Dariusz Stramski**  
Marine Physical Laboratory  
Scripps Institution of Oceanography  
University of California, San Diego  
San Diego, CA 92093-0238

Prepared for

Dr. Joan Cleveland  
Environmental Optics Program  
Code 322OP  
Office of Naval Research  
800 North Quincy Street  
Arlington, VA 22217-5000

March, 1999

 S E Q U O I A

**REPORT DOCUMENTATION PAGE**Form Approved  
OMB No. 074-0188

Public reporting burden for this collection of information is estimated to average 1 hour per response, including the time for reviewing instructions, searching existing data sources, gathering and maintaining the data needed, and completing and reviewing this collection of information. Send comments regarding this burden estimate or any other aspect of this collection of information, including suggestions for reducing this burden to Washington Headquarters Services, Directorate for Information Operations and Reports, 1215 Jefferson Davis Highway, Suite 1204, Arlington, VA 22202-4302, and to the Office of Management and Budget, Paperwork Reduction Project (0704-0188), Washington, DC 20503

<b>1. AGENCY USE ONLY (Leave blank)</b>		<b>2. REPORT DATE</b> March 1999	<b>3. REPORT TYPE AND DATES COVERED</b> Final Report	
<b>4. TITLE AND SUBTITLE</b> Influences of Microbial and Mineral Particles on Oceanic Optics			<b>5. FUNDING NUMBERS</b> N00014-97-C-0024	
<b>6. AUTHOR(S)</b> Curtis D. Mobley and Dariusz Stramski				
<b>7. PERFORMING ORGANIZATION NAME(S) AND ADDRESS(ES)</b> Sequoia Scientific, Inc. 9725 S.E. 36 <sup>th</sup> Street, Suite 308 Mercer Island, WA 98040			<b>8. PERFORMING ORGANIZATION REPORT NUMBER</b> Project 24 Final Report	
<b>9. SPONSORING / MONITORING AGENCY NAME(S) AND ADDRESS(ES)</b> Environmental Optics Program, Code 322OP Office of Naval Research 800 North Quincy Street Arlington, VA 22217-5000 Attn: Dr. Joan Cleveland			<b>10. SPONSORING / MONITORING AGENCY REPORT NUMBER</b>	
<b>11. SUPPLEMENTARY NOTES</b>				
<b>12a. DISTRIBUTION / AVAILABILITY STATEMENT</b>			<b>12b. DISTRIBUTION CODE</b>	
<b>13. ABSTRACT (Maximum 200 Words)</b> The effects of microbial and mineral particles, and of dissolved substances, on marine light fields were investigated using a database of single-particle optical properties as input to the Hydrolight radiative transfer numerical model. This database now includes 24 microbial species as well as generic mineral particles, organic detritus, and microbubbles. Significant results include: (1) It is possible to define generic prochlorophytes and Synechococcus species, but this cannot be done for nanoplankton. (2) The detailed species composition of small nanoplankton is not crucial, so long as the various-sized particles obey a Junge size distribution overall, with the same total concentration of these particles. (3) The natural variability in the parameters used in simple bio-optical models for dissolved substances and detritus can have effects on the remote-sensing reflectance that are as large as a factor-of-two change in the chlorophyll concentration. (4) Organic detritus can have a large effect on remotely sensed signals and therefore deserves more research attention. An improved methodology for estimating the remote-sensing reflectance from above-water measurements is presented.				
<b>14. SUBJECT TERMS</b> Hydrolight, optical oceanography, ocean color, remote sensing, microbes			<b>15. NUMBER OF PAGES</b> 144	
			<b>16. PRICE CODE</b>	
<b>17. SECURITY CLASSIFICATION OF REPORT</b> UNCLASSIFIED	<b>18. SECURITY CLASSIFICATION OF THIS PAGE</b> UNCLASSIFIED	<b>19. SECURITY CLASSIFICATION OF ABSTRACT</b> UNCLASSIFIED	<b>20. LIMITATION OF ABSTRACT</b> Unlimited	

## TABLE OF CONTENTS

1. Research Objectives .....	1
2. Approach .....	2
3. Work Completed .....	2
4. Results .....	4
5. Scientific Impact .....	5
6. Recommendations for Future Research .....	6
7. References .....	6
Appendix A. Reprint of <i>Effects of microbial particles on oceanic optics: A database of single-particle optical properties,</i> by D. S. Stramski and C. D. Mobley (1997) .....	A.1
Appendix B. Reprint of <i>Effects of microbial particles on oceanic optics: Radiative transfer modeling and example simulations,</i> by C. D. Mobley and D. S. Stramski (1997) .....	B.1
Appendix C. Reprint of <i>A database of single-particle optical properties,</i> by D. S. Stramski, A. Bricaud, and A. Morel (1998) .....	C.1
Appendix D. Draft of <i>Origins of variability in remote-sensing reflectances,</i> by C. D. Mobley and D. S. Stramski .....	D.1
Appendix E. Reprint of <i>Estimation of the remote-sensing reflectance from above-water measurements,</i> by C. D. Mobley (1999) .....	E.1



# INFLUENCES OF MICROBIAL AND MINERAL PARTICLES ON OCEANIC OPTICS

## 1. Research Objectives

This work addressed the long-term goal of understanding in detail how various types of microbial and mineral particles and dissolved substances determine the inherent and apparent optical properties (IOPs and AOPs) of oceanic waters.

It is well known that the optical properties of oceanic waters are highly variable. For so-called Case 1 waters, a number of bio-optical models have been developed to predict the optical properties as functions of the Chlorophyll concentration. Although these models often give good predictions of average values on a global basis, they can be in error by an order of magnitude when applied at a particular location and time, even in Case 1 waters. Our guiding hypothesis was that

**The “inherent” or “natural” variability in optical properties is not random, and the variability can be explained by the detailed composition of the water body.**

In order to test this hypothesis, we sought to answer questions such as the following:

- How does variability in the detailed composition of oceanic water determine the variability in the IOPs (such as absorption and scattering coefficients) and AOPs (such as spectral reflectance and diffuse attenuation functions)?
- What information about the nature of suspended particles can we hope to extract from in-situ or remotely sensed data?
- Is it possible to quantitatively classify the *optical* properties of water using the Case 1/Case 2 scheme? (The Case 1/Case 2 classification is based on water composition; the optical distinction between Case 1 and Case 2 is unclear.)

Answering such questions is fundamental to the development of bio-geo-optical models for Case II waters, for which the presently available bio-optical models are known to fail, even when computing average values.

## 2. Approach

The key to testing our hypothesis is having control over the detailed composition of a water body, so that we can see how a change in composition changes the optical properties. Such control is not possible in nature, or even in the laboratory because of scale considerations. (For example, a laboratory tank cannot reproduce horizontally homogeneous waters and boundary conditions, nor can it reproduce the optical environment of a large body

of water.) We therefore must resort to numerical modeling, which can give us complete control over all variables.

We first developed a database of the single-particle optical properties (absorption and scattering cross sections, and scattering phase functions) of different types of microbes (ranging in size from viruses to nanoplankton) and other particles (air bubbles, detritus, and generic mineral particles). This database was used as input to radiative transfer numerical models to study the effects of different types of particles on oceanic light fields. This approach gave us complete control in determining the constituents of a simulated water body and in examining the optical influences of different types of particles. The database development was carried out by Stramski, and the modeling was performed by Mobley; both investigators participated equally in the analysis of the results.

The single-particle optical properties were obtained from a combination of laboratory experiments and Mie scattering calculations (Stramski and Mobley, 1997; Stramski, *et al.* 1998). The single-particle properties were combined with particle concentrations and standard models for dissolved substances to determine the bulk IOPs of a water body. These bulk IOPs are then used as input to the Hydrolight 4.0 radiative transfer model (Mobley, 1998; see also <http://www.sequoiasci.com/hydrolight.html>). Hydrolight computes the full spectral radiance distribution within the water (including water-leaving radiances and all quantities derived from the radiance, such as irradiances and diffuse attenuation functions). Changes in various light-field quantities (e.g., water-leaving radiances or diffuse attenuation functions) were monitored as the input to the model was systematically varied.

### **3. Work Completed**

Many major accomplishments were achieved during the course of this research. Some of the highlights are as follows:

- By the end of the first year of this work, the database of single-particle microbial optical properties contained five microbial species: marine viruses, heterotrophic bacteria, cyanobacteria, small diatoms, and chlorophytes. This initial database is described in Stramski and Mobley (1997; a copy of this paper is attached as Appendix A).
- Formats for archiving the single-particle data were developed. These formats were designed to be convenient for inputting the data into Hydrolight and other radiative transfer models.
- The Hydrolight software was modified to accept any number of components on the database archive format. This allowed runs with over 30 components to be made routinely towards the end of the study. When running this special version of Hydrolight, it is necessary only to provide Hydrolight with a list of component names and concentrations; the database is then automatically accessed and the water IOPs are constructed as the corresponding sum of component IOPs.

- The initial five-component database was used to develop and verify the usefulness of our approach to dissecting and understanding the contributions of individual components to IOPs and light-field quantities. This work is described in Mobley and Stramski (1997a; a copy of this paper is attached as Appendix B).
- The database of single-particle optical properties was expanded from its initial five microbes to 24 microbes plus several non-microbial components. The non-microbial components include air bubbles, generic mineral particles (polydisperse particles with a high index of refraction), organic detrital particles (polydisperse particles with a low index of refraction), and dissolved substances (CDOM). The database requires over 50 Mbytes of computer storage. This expanded database is described in Stramski, *et al.* (1998; a copy of this paper is attached as Appendix C).
- Using this larger database, we completed several hundred Hydrolight simulations using various combinations and concentrations of particulate and dissolved components. Component concentrations used in these simulations ranged from low values characteristic of open ocean waters to high values characteristic of productive coastal waters. Bloom conditions and Case 2 waters were simulated. We studied the effects of water composition on both in-water optical properties (such as the scalar irradiance and diffuse attenuation), on the remote-sensing reflectance, and on the point spread function. A draft paper describing a few of these simulations is attached as Appendix D.
- Errors in the estimation of the remote-sensing reflectance owing to inaccurate removal of surface-reflected sky radiance were investigated. This work was necessary in order to separate variability in remote-sensing reflectances owing to measurement methodologies from variability owing to water composition. This work is described in Mobley (1999; a copy of this paper is attached as Appendix E).
- Collaboration on several related papers was performed. Although this work was not a core part of the database and modeling studies, it contributed to the overall goals of the research: understanding the effects of various particle components on oceanic light fields and determining what information can and cannot be extracted from in-water and remotely sensed optical data. Papers that have already resulted from these collaborations include the following:

Flatau *et al.* (submitted): Evaluation of the possible effects of bubble clouds in seawater on remote-sensing reflectance.

Lee *et al.* (1998): Development of semi-analytic models suitable for inversion of hyperspectral remote-sensing data in shallow waters.

Lee *et al.* (in press): Development of models for retrieval of IOP and bottom depth from hyperspectral remote sensing data in shallow waters.

Ohlmann *et al.* (in press). Studies of pigmented particle concentrations on ocean radiant heating.

Stephany *et al.* (1998): Studies of the retrieval of bioluminescence information from in situ irradiance measurements.

Tyrrell *et al.* (1999): Studies of coccolithophore blooms on ocean light fields.

#### 4. Results

The results of this work are described in the cited publications. Some of the major findings are as follows:

- **It is not necessary to include each microbial component in order to realistically simulate the optical properties of a water body.** For example, it is sufficient to use an “average” or “generic” prochlorophyte and an average *Synechococcus* in simulations. This is not surprising because, for example, different prochlorophyte strains have similar optical cross sections and particle sizes.
- **It is *not* possible to define an “average small nanoplankton.”** This is because the various species of small nanoplankton can have significantly size distributions, and hence optical properties. In other words, it is not possible to average the single-particle optical properties of nanoplankton in the 4-8  $\mu\text{m}$  size range, for example, and then use the resulting average in numerical simulations.
- **The detailed species composition of the small nanoplankton is not crucial, so long as the various-sized particles obey a Junge size distribution overall, with the same total concentration of these particles.** That is to say, for nanoplankton in the 4-8  $\mu\text{m}$  size range, for example, the individual species are less important than the total concentration and size distribution of the nanoplankton.
- **The simple bio-optical models commonly and naively used for the IOPs of dissolved substances and detritus can have large effects on the remote-sensing reflectance  $R_{rs}$ .** These models have various parameters whose values are commonly assumed to have “typical” values. However, these parameters can vary widely in magnitude. For example, absorption by detritus is often modeled by an equation of the form

$$a_{\text{det}}(z, \lambda) = a_{\text{det}}(z, \lambda_0) \exp[-\gamma(\lambda - \lambda_0)] .$$

The wavelength reference point  $\lambda_0$  is usually taken to be 400 or 440 nm. Values of the exponent slope parameter  $\gamma$  as reported in the literature range from 0.006 to 0.014, with an average value of about 0.011. Our simulations showed that the natural variability in

$\gamma$  gives a variability in  $R_{rs}$  that can be as large as the variability induced by a factor-of-two change in the total microbial concentration. The surprisingly large variability in  $R_{rs}$  owing to the variability of the  $\gamma$  parameter highlights the importance of properly modeling all components of a water body, not just the microbial components, even in Case 1 waters.

- **Preliminary simulations with the database and a Monte Carlo numerical model (Mobley, 1996) showed that our database and radiative transfer models are ideal for understanding in detail how the water composition, including the particle size distribution, determines the Point Spread Function (PSF).** Although the literature contains measurements of the PSF in various waters, very little work has been done on understanding variability in the PSF. Note in particular that there are no bio-optical models for the PSF, because the PSF depends on particle size distributions, as well as on particle concentrations.

## 5. Scientific Impact

This work already has had, and will continue to have, significant impact on how we pursue an understanding of ocean optics properties and variability. In particular, note that

- The database developed by Stramski and co-workers is unique and far superior to any other such database in the world. Parts of the database have already been made available to several academic researchers, and such requests are likely to increase now that the database is greatly expanded and becoming known in the scientific community. (Note, however, that the database is not in the public domain. All requests for access to the database should be referred to D. Stramski.)
- Our methodology has been firmly established as a rigorous way to dissect and understand the effects of individual particulate or dissolved components on IOPs and AOPs.
- This work is an important step towards achieving scale closure—the reconciliation of single-particle (small scale) optical properties with the large-scale optical character of the ocean.
- Achieving a detailed understanding of the roles played by various types of particles and other components on oceanic radiative transfer is a prerequisite to advancing bio-optical models beyond their present, over-simplified, one-parameter (the chlorophyll concentration) description of very complicated and variable situations.
- The modeling methodology developed in the course of this work is finding wide application in other research projects.

- This work leads to a quantitative understanding of what information about oceanic particulates and dissolved substances we can and cannot expect to extract from remotely sensed signals, which are the basis for "ocean color" assessments of the ocean's upper layer.

## 6. Recommendations for Future Research

Our simulations suggest the following topics as the highest priority for further research with new funding:

- **Existing "gaps" in the database need to be filled.** In particular, larger bloom-forming microbes characteristic of coastal waters need to be added to the database.
- **Organic detritus deserves more research attention.** Detritus can be highly scattering and may have a significant effect on remotely sensed signals because of its high backscattering.
- **The database-PSF modeling should be pursued because of the importance of the PSF in underwater visibility and imaging.** Indeed, we now have the tools to develop models of the PSF given the particle composition of a water body as input. Such models would greatly advance our understanding of the PSF and would provide direct input into performance models of Navy underwater imaging systems.

## 7. References

- Flatau, P. J., M. K. Flatau, J. R. V. Zaneveld, and C. Mobley. Remote sensing of bubble clouds in seawater. *Quart. J. Royal Metro. Soc.*, submitted.
- Lee, Z. P., K. L. Carder, C. D. Mobley, R. G. Steward, and J. S. Patch, 1998. Hyperspectral remote sensing for shallow waters: 1. A semi-analytical model. *Applied Optics*, 37(27), 6329-6338.
- Lee, Z. P., K. L. Carder, C. D. Mobley, R. G. Steward, and J. S. Patch, 1999. Hyperspectral remote sensing for shallow waters: 2. Deriving bottom depths and water properties by optimization. *Applied Optics*, in press.
- Mobley, C. D., 1996. Monte Carlo simulation of a point light source in an infinite medium. Tech. Report, Project 7311, SRI International, Menlo Park, CA, 39 pp.
- Mobley, C. D., 1998. HYDROLIGHT 4.0 users' guide. Sequoia Scientific, Inc., Mercer Island, WA, 106 pages.

- Mobley, C. D., 1999. Estimation of the remote-sensing reflectance from above-water measurements. *Appl. Optics*, submitted. (A copy of this paper is attached as Appendix B.)
- Mobley, C. D. and D. Stramski, 1997a. Effects of microbial particles on oceanic optics: Methodology for radiative transfer modeling and example simulations. *Limnol. Oceanogr.*, 42(3), 550-560. (A copy of this paper is attached as Appendix A.)
- Mobley, C. D. and D. Stramski, 1997b. Origins of variability in remote-sensing reflectances. Technical report NRL16-97T-05-2, Sequoia Scientific, Inc., 91 pages.
- Mobley, C. D. and D. Stramski, 1999. Origins of variability in remote-sensing reflectances, journal article in preparation. (A draft of this paper is attached as Appendix C.)
- Mobley, C.D. and D. Stramski, 1998. Origins of variability in oceanic light fields. Paper presented at *Ocean Optics XIV*, Nov 10-13, Kona, HI.
- Ohlmann, J. C., D. A. Siegel, and C. D. Mobley. Ocean radiant heating: 1. Optical influences. *J. Phys. Ocean.*, in press.
- Stephany, S., F. M. Ramos, H. F. de Campos Velho, and C. D. Mobley, 1998. A methodology for internal light source estimation. *Comp. Model. Simul. Engin.*, 3(3), 161-165.
- Stramski, D., A. Bricaud, and A. Morel, 1998. A database of single-particle optical properties. Paper presented at *Ocean Optics XIV*, Nov 10-13, Kona, HI. (A copy of this paper is attached as Appendix C.)
- Stramski, D. and C. D. Mobley, 1997. Effects of microbial particles on oceanic optics: A database of single-particle optical properties. *Limnol. Oceanogr.*, 42(3), 138-549.
- Tyrrell, T., P. M. Holligan, and C. D. Mobley, 1999. Optical impacts of oceanic coccolithophore blooms. *J. Geophys. Res.*, 104 (C2), 3223-3241.

## APPENDIX A

Reprint of

*Effects of microbial particles on oceanic optics:  
A database of single-particle optical properties*

by

Dariusz Stramski and  
Curtis D. Mobley

Published in

*Limnology and Oceanography*  
Vol. 42, No. 3, pages 538-549 (1997)



## Effects of microbial particles on oceanic optics: A database of single-particle optical properties

Dariusz Stramski

Marine Physical Laboratory, Scripps Institution of Oceanography, University of California at San Diego, La Jolla, California 92093-0701

Curtis D. Mobley

Sequoia Scientific, 9725 S.E. 36th Street, Suite 308, Mercer Island, Washington 98040

### Abstract

We describe a database of the single-particle optical properties of marine microbial particles. This database includes representatives from five classes of particles: viruses (VIR), heterotrophic bacteria (BAC), cyanobacteria (CYA), small nanoplanktonic diatoms (DIA), and nanoplanktonic chlorophytes (CHLO). The optical properties of VIR, whose mean size is  $0.07\ \mu\text{m}$ , were determined from Mie scattering calculations using reasonable approximations about the size distribution and refractive index of viral particles. The database for BAC, CYA, DIA, and CHLO was created from laboratory measurements of microbial cultures and modeling of particle optics. BAC are represented by a mixed natural population of bacterial species ( $\sim 0.55\ \mu\text{m}$  in size), CYA by *Synechococcus* (clone WH 8103,  $\sim 1\ \mu\text{m}$ ), DIA by *Thalassiosira pseudonana* ( $\sim 4\ \mu\text{m}$ ), and CHLO by *Dunaliella tertiolecta* ( $\sim 7.5\ \mu\text{m}$ ). The database includes the single-particle optical properties that are useful in radiative transfer modeling: the absorption and scattering cross sections and scattering phase functions. Additionally, the database includes the attenuation cross sections, optical efficiency factors, single-scattering albedos, and backscattering properties. For phytoplankton species, chlorophyll- and carbon-specific optical coefficients are also available. The optical quantities are generally determined at 1-nm intervals in the spectral region from 350 to 750 nm. The scattering phase function is determined at 5-nm intervals in wavelength and  $1^\circ$  intervals in scattering angle. The size distribution and refractive index of the particles are also included. This database, when combined with radiative transfer modeling, provides a powerful approach to advancing our understanding of oceanic optics.

Achieving a detailed understanding of the roles played by various types of particles in oceanic radiative transfer is a prerequisite to advancing our knowledge of the marine optical environment and applying optical techniques to the study of the ocean. It is the fundamental processes of absorption and scattering of light by many individual particles and soluble materials present in seawater that determine the magnitudes and variability of the bulk optical properties and light field characteristics in the ocean. To achieve a comprehensive understanding of the marine optical environment and to construct reliable predictive and inverse optical models, we must first understand how each of these various water components absorbs and scatters light, and hence affects underwater radiative transfer.

It is well known that there is great variability in the inherent optical properties (IOPs) of seawater in the world's oceans. This variability induces a correspondingly large variability in oceanic apparent optical properties (AOPs), even after accounting for variability in the AOPs associated with the incident lighting and sea state. The optical properties of

seawater are determined in large part by the suspended particulates, and the optical variability can be traced primarily to the biological components of the water, at least in case 1 waters where phytoplankton and co-varying materials are the dominant components (Morel and Prieur 1977). Most efforts to date have been focused on developing bio-optical relationships for such waters using a parameterization of seawater composition in terms of chlorophyll concentration alone. It has been well documented that changes in the chlorophyll *a* concentration (*Chl*) are accompanied by more or less systematic variations in the IOPs and AOPs, such as the spectral absorption coefficient  $a(\lambda)$ , the scattering coefficient  $b(\lambda)$ , the diffuse attenuation coefficient for downwelling irradiance  $K_d(\lambda)$ , and ocean reflectance  $R(\lambda)$  (e.g. Smith and Baker 1978; Gordon and Morel 1983; Morel 1988). The correlations between chlorophyll concentration and optical properties have formed the basis of statistically derived bio-optical models that predict IOPs and AOPs given *Chl*, or vice versa (e.g. Morel 1988).

Although such chlorophyll-based bio-optical models may often satisfactorily predict *average* values as obtained from water samples taken at many locations and times, these models say nothing about the variability observed in different water samples, each of which has the same chlorophyll concentration. We here refer to this variability as random, which is used in a sense that the measured optical properties differ in a seemingly random manner from the mean values predicted by chlorophyll-based bio-optical models. As a result of this variability, any particular measured IOP or AOP can

### Acknowledgments

The development of the database was supported by the ONR Environmental Optics Program grants N00014-88-J-1216, N00014-93-1-0134, and N00014-95-1-0491 as well as NASA grant NAGW-3574. Use of the database in radiative transfer modeling is being supported by the ONR Environmental Optics Program contract N00014-94-C-0114.

We thank A. Morel for comments on the manuscript.

frequently differ by a factor of two or more from the value predicted by the bio-optical model. For example, data presented in Gordon and Morel (1983) show a three-fold variation in the scattering coefficient  $b(550)$  at any given chlorophyll concentration in case 1 waters. These random variations are much larger in case 2 waters, which include most coastal areas of the world's oceans where components other than phytoplankton and their derivatives are optically significant (e.g. resuspended sediments, terrigenous particles, or dissolved organic matter). The data of Gordon and Morel show that  $b(550)$  may vary by one order of magnitude or more for a given *Chl* if case 2 waters are considered.

A major motivation for the present work is provided by the hypothesis that the seemingly random variability in the chlorophyll-based bio-optical models can be explained in terms of the detailed composition of seawater. We think that much of this variability is due to the wide range of microbial particles (chlorophyll-bearing or not) and nonliving particles present in seawater. We thus expect that an improved understanding of the marine optical environment can be gained if we progress beyond the overly simplified parameterization of marine particulates in terms of chlorophyll concentration alone.

The most rigorous approach to understanding the complicated marine optical environment begins with determining the optical properties of each of the various optically significant components of seawater. A definitive approach clearly should consider the optical properties of every species of aquatic components present in a water body, as well as the possible intraspecies variability in these properties. Such an approach is clearly unattainable because of the wide variety of particulate and dissolved species in natural water bodies. An alternative approach is to select a number of species or components that realistically represent the mix of suspended and dissolved matter that affects the marine optical environment. We are taking such an approach in the present work, which combines the single-particle optical database of various microbial particles with radiative transfer modeling. In contrast to correlational, chlorophyll-based bio-optical models derived from statistical analysis of (usually incomplete) field data, our approach leads to the development of a comprehensive mechanistic model of the marine optical environment.

To utilize such a mechanistic approach requires knowledge of the optical cross sections of various kinds of aquatic components including microbial particles. These optical cross sections represent the amount of absorption and scattering that may be attributed to a unit concentration of a given component. In this work we specifically use the absorption and scattering cross sections that are attributed to a single particle representative of a given microbial species. These single-particle cross sections provide linkages between the bulk IOPs of a water body and the number concentrations of its particulate components. Importantly, if the optical cross sections and concentrations are known for a given species of particulate assemblage, it is possible to determine the contribution of this species to the bulk optical properties of the water body and hence to determine its effect on radiative transfer in that water body.

Recent progress in two research areas has made it possible

to undertake this study. First, there has been a considerable effort to study the optical properties of different types of microbial particles, from the smallest bacteria to various nanoplankton species (e.g. Morel et al. 1993; Stramski et al. 1995 and references therein). Second, a numerical radiative transfer model (Hydrolight 3.0) has been developed that is both accurate and computationally efficient enough to permit extensive studies of oceanic light fields as particle types, concentrations, and optical properties are systematically varied (Mobley 1994). This paper represents the first part of our work, wherein we describe the database of single-particle optical properties of several kinds of microbial particles covering the size range from  $\sim 0.05 \mu\text{m}$  (viruses) to  $\sim 10 \mu\text{m}$  (nanoplanktonic chlorophytes). This database is a result of several recent studies that combined laboratory experiments and Mie scattering calculations, and includes spectral cross sections for absorption and scattering as well as scattering phase functions. Our companion paper (Mobley and Stramski 1997) is the second part wherein we describe the use of our database in radiative transfer modeling.

## Methods

The present database of the single-particle optical properties includes representatives from four classes of microbial marine particles: heterotrophic bacteria (BAC), cyanobacteria (CYA), small nanoplanktonic diatoms (DIA), and nanoplanktonic chlorophytes (CHLO). The fifth category of particles included in the database is viruses (VIR), which will also be referred to as microbial particles.

The database for BAC, CYA, DIA, and CHLO was created by a combination of laboratory experiments and modeling of particle optics, which we describe first. As depicted in Fig. 1, the approach used in generating this database consists of three major tasks: culturing of microorganisms, measurements, and calculations. The general design of the experiments, conditions under which the cultures were grown, and sampling strategy differed among these four microbial classes. The methodology of the measurements and calculations, however, was virtually the same regardless of the microorganism studied. We first summarize the most relevant information about the specific experiments with BAC, CYA, DIA, and CHLO. The detailed description of these experiments and methodology used can be found elsewhere (Stramski and Kiefer 1990; Stramski and Reynolds 1993; Stramski et al. 1993, 1995).

The data for BAC represent a mixed natural population of bacterial cells (typically  $\sim 0.5 \mu\text{m}$  in size) rather than a single species. The bacteria were obtained from surface waters off Southern California and grown in unenriched particle-free seawater. The batch cultures were kept in the dark at  $\sim 20^\circ\text{C}$ . All measurements and analyses were made 7–10 days after inoculation during the stationary phase of growth. The final cell properties included in the optical database are averages based on three separate experiments performed in a similar manner.

Each of the three remaining microbial classes (CYA, DIA, and CHLO) is represented by a single species of photosynthetic microorganisms. The cyanobacteria are represented by

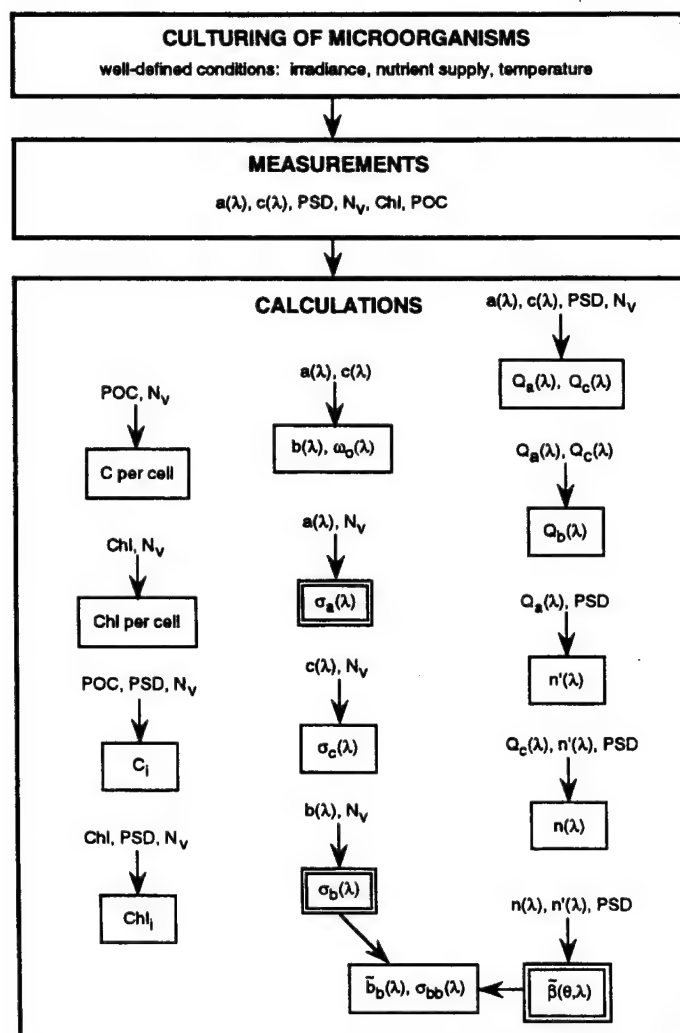


Fig. 1. Schematic representation of the approach for creating the optical database of microbial particles. The three highlighted quantities,  $\sigma_a(\lambda)$ ,  $\sigma_b(\lambda)$ , and  $\bar{\beta}(\theta, \lambda)$ , are used as input to our radiative transfer modeling as described by Mobley and Stramski (1997).

an oceanic species belonging to the genus *Synechococcus* (clone WH 8103, which is  $\sim 1 \mu\text{m}$  in size), diatoms by the neritic species *Thalassiosira pseudonana* ( $\sim 4 \mu\text{m}$ ), and chlorophytes by *Dunaliella tertiolecta* ( $\sim 7.5 \mu\text{m}$ ). These microbes were grown in monospecific cultures under defined conditions of irradiance, temperature, and nutrient supply. Specifically, CYA were grown at a temperature of  $\sim 22.5^\circ\text{C}$  in a nutrient-replete medium under a day/night cycle in natural irradiance. The culture vessel was placed in the laboratory near an east-facing window. The duration of light and dark periods was nearly the same (i.e. 12 h). Because of cloudy skies, the integrated daily dosage of photosynthetically active scalar irradiance  $E_0(\text{PAR})$  was low ( $1.7 \text{ mol quanta m}^{-2}$ ). The final database of the optical properties of CYA represents averages based on seven measurements made over a single day/night cycle. These measurements were taken at intervals of 2–4 h.

Similarly, DIA were grown in a nutrient-replete culture

exposed to a day/night cycle in natural irradiance with light period lasting  $\sim 12 \text{ h}$ . The temperature of the medium was  $\sim 23^\circ\text{C}$ . The maximum instantaneous irradiance  $E_0(\text{PAR})$  incident upon the culture varied approximately from 500 to  $600 \mu\text{mol quanta m}^{-2} \text{ s}^{-1}$  and the daily dosage of  $E_0(\text{PAR})$  varied from 3.8 to  $6.8 \text{ mol quanta m}^{-2}$  among different days of the experiment. The final optical database for this species has been generated by averaging 25 measurements that were made during three successive day/night cycles.

The experiments with CHLO were conducted under nutrient-replete conditions at a temperature of  $20^\circ\text{C}$ . Light of constant intensity was provided on a 14:10 L/D cycle by halogen-vapor lamps. For all measurements and analyses the cells were harvested at the light–dark transition. Two experiments were made with high levels of irradiance (the cells were grown under fluctuating light caused by surface-wave focusing and under constant light). In both high-light experiments the daily dosage of  $E_0(\text{PAR})$  was very similar,  $\sim 41 \text{ mol quanta m}^{-2}$ . The third experiment was made under low irradiance (constant with time during the light period). The daily dosage of  $E_0(\text{PAR})$  in this experiment was  $2.3 \text{ mol quanta m}^{-2}$ . For the purpose of generating the present database, the results representing the cells adapted to high and low levels of irradiance were averaged.

The second major task of the approach depicted in Fig. 1 involves measurements. The spectra of the beam attenuation coefficient,  $c(\lambda)$ , and absorption coefficient,  $a(\lambda)$ , of microbial suspensions were measured with a double-beam spectrophotometer in appropriate geometric configurations. These measurements were done in the spectral region from 350 to 750 nm with a 1-nm resolution (with the exception of the experiments with CHLO, where the range 400–750 nm was examined). The concentrations of cells,  $N_v$ , were determined by using microscopic techniques for counting microorganisms. The particle size distributions (PSD) of BAC and CHLO cells were determined by microscopy. The nonsphericity of the cells was taken into account in this size analysis. The size distribution of CYA and DIA was obtained with an electronic particle sizer (Coulter) that provides a measure of particle size in terms of the volume-equivalent spherical diameter. Finally, the major biochemical characteristics of the cultures, which include the concentrations of Chl *a* and particulate organic carbon (POC), were measured by spectrophotometry of pigment extracts in acetone and dry combustion technique, respectively. The chlorophyll determinations were made for CYA, DIA, and CHLO and carbon determinations were made for CYA and DIA.

As a final task, the data obtained from measurements were used to compute the single-particle optical and biochemical properties that comprise our final database. The major portion of Fig. 1 gives an overview of the entire computational process. The left-hand column in Fig. 1 refers to the biochemical characteristics of the cells. The cellular contents of Chl *a* (Chl per cell) and POC (C per cell) were calculated as the ratios of the concentrations of these components in suspension to cell concentration. The intracellular concentrations of Chl *a* ( $Chl_i$ ) and carbon ( $C_i$ ) were determined as the ratios of the cellular contents to the average cell volumes. The study of relationships between these biochemical char-

acteristics and optical properties of the cells is beyond the scope of this paper, but we use the information about the chlorophyll content per cell in some radiative transfer simulations, as described by Mobley and Stramski (1997).

The calculations of the optical properties symbolized in the middle column in Fig. 1 are straightforward and do not involve any assumptions. First, for each of the four microbial categories the spectrum of the scattering coefficient  $b(\lambda)$  is obtained as the difference between  $c(\lambda)$  and  $a(\lambda)$ , and the single-scattering albedo  $\omega_0(\lambda)$  is computed as the ratio  $b(\lambda):c(\lambda)$ . Then, the spectrum of the absorption cross section  $\sigma_a(\lambda)$  is calculated as  $a(\lambda):N_v$ . The spectra of the attenuation cross section  $\sigma_c(\lambda)$  and scattering cross section  $\sigma_b(\lambda)$  are calculated in a similar manner. Note that these calculations yield the single-particle properties,  $\sigma_a(\lambda)$  and  $\sigma_b(\lambda)$ , which are necessary to carry out our radiative transfer modeling.

Another required optical property for this modeling is the scattering phase function,  $\beta(\theta, \lambda)$ , of each microbial particle. Because routine measurements of the scattering phase function with high spectral resolution is presently impossible to accomplish, we calculated this function by combining the measurements of  $a(\lambda)$ ,  $c(\lambda)$ , PSD, and  $N_v$  with theoretical models of light scattering and absorption by particles. These calculations are symbolized in the right-hand column in Fig. 1. First, the efficiency factors for absorption,  $Q_a(\lambda)$ , and attenuation,  $Q_c(\lambda)$ , are calculated, and from these quantities the scattering efficiency  $Q_b(\lambda)$  is obtained as the difference between  $Q_c(\lambda)$  and  $Q_a(\lambda)$  (see Bricaud and Morel 1986). These efficiencies are hereafter referred to as experimental estimates. In the next step, the spectra of the imaginary part  $n'(\lambda)$  and the real part  $n(\lambda)$  of the refractive index of microbial particles are derived. This derivation combines optical models of light absorption and scattering by particles and the experimental estimates of the efficiency factors,  $Q_a(\lambda)$  and  $Q_c(\lambda)$  (see below). Finally, by using PSD,  $n'(\lambda)$ , and  $n(\lambda)$  as input, the scattering phase function  $\beta(\theta, \lambda)$  is calculated from Mie theory for homogeneous spheres by means of an algorithm given by Bohren and Huffman (1983). These calculations are made at 5-nm intervals in the wavelength  $\lambda$  and 1° intervals in the scattering angle  $\theta$ . Because the backscattering properties of particles are of special interest in the remote sensing of ocean color, we have also determined the backscattering ratio  $\bar{b}_b(\lambda)$  from  $\beta(\theta, \lambda)$  (Morel and Bricaud 1986) and then the backscattering cross section,  $\sigma_{bb}(\lambda) = \bar{b}_b(\lambda)\sigma_b(\lambda)$ , as indicated in Fig. 1.

The determination of the index of refraction of particles relative to the aqueous medium,  $m(\lambda) = n(\lambda) - in'(\lambda)$ , deserves special attention. The spectra of the imaginary part of the refractive index,  $n'(\lambda)$ , are derived with an inverse method developed by Bricaud and Morel (1986). This method uses the formula that describes the absorption efficiency of homogeneous spheres as a function of the absorption thickness parameter  $\rho' = 4\alpha n'$  (Duysens 1956; van de Hulst 1957). The parameter  $\rho'$  combines  $n'$  with the size parameter  $\alpha = \pi D n_w/\lambda$ , where  $D$  is the particle diameter and  $n_w$  is the refractive index of the medium (water in our study). The input to the calculations is the measured PSD, which accounts for the polydispersion of microbial cultures. The theoretical estimates of absorption efficiency  $Q_a$  at any given wavelength  $\lambda$  are varied iteratively as a function of the sole

variable  $n'$  until the calculated  $Q_a$  matches its experimental counterpart. These calculations are performed for each wavelength separately, thus yielding the  $n'(\lambda)$  spectrum. This method provides a unique solution because  $Q_a$  is a monotonic function of  $n'$  for any given  $\lambda$  and PSD.

The real part of the refractive index,  $n(\lambda)$ , of the examined microorganisms was also derived through an inverse method. This method involves an iterative search that is based on the concept described by Stramski et al. (1988), with the exception that we now use the Mie scattering theory rather than the anomalous diffraction approximation. The assumption of homogeneous spheres is still invoked in this derivation of  $n(\lambda)$ . For each wavelength  $\lambda$  the Mie calculations of the attenuation efficiency  $Q_c$  are performed iteratively by varying the refractive index  $n$  within the plausible range for microorganisms, generally from 1.01 to 1.10. The input to these calculations includes the measured PSD and the derived  $n'(\lambda)$ . Given that PSD and  $n'(\lambda)$  are fixed, the variation in the real part of the refractive index  $n$  is the only factor that induces the changes in the theoretical estimates of  $Q_c$ . This iteration continues until the calculated efficiency  $Q_c$  converges on its experimental counterpart, which yields the solution for  $n$  at the examined wavelength  $\lambda$ .

This method for deriving  $n(\lambda)$  involves some complexity and limitations, which can be discussed within the framework of the Mie scattering theory. According to this theory, the attenuation efficiency  $Q_c$  of a nonabsorbing particle displays characteristic variations as a function of the phase-shift parameter  $\rho = 2\alpha(n - 1)$ . With increasing values of the phase-shift,  $Q_c$  initially increases and reaches the first major maximum for  $\rho$  of about 4. Beyond this maximum,  $Q_c$  exhibits a series of oscillations with diminishing amplitude. These oscillations occur around  $Q_c = 2$ , which is the limiting magnitude of the attenuation efficiency for large  $\rho$  values. If absorption is added, the oscillations as well as the magnitude of  $Q_c$  at its first maximum decrease with increasing  $n'$ . Furthermore, if one considers the attenuation efficiency representing a relatively narrow particle size distribution (like a culture of single microbial species), the effect of such polydispersion is to reduce the maximum magnitude of  $Q_c$ , shift the position of this maximum toward smaller values of  $\rho$ , and damp the  $Q_c$  oscillations that otherwise occur beyond the first maximum (Morel and Bricaud 1986).

All these features of the theoretical function  $Q_c(\rho)$  have important implications for the utility of our inverse method for deriving  $n(\lambda)$ . It is essential to this method that the experimental estimates of  $Q_c(\lambda)$  are determined over a broad spectral range. We have determined  $Q_c(\lambda)$  from the beam attenuation measurements covering the range from near ultraviolet to near infrared. Such information enables us to approximately identify the portion of the theoretical curve  $Q_c(\rho)$  that corresponds to the experimental spectrum  $Q_c(\lambda)$ . This identification is critical when solving for  $n(\lambda)$  because for fixed  $\lambda$ ,  $n'(\lambda)$ , and PSD,  $Q_c$  is not a monotonic function of  $n$ , and therefore multiple solutions may be found. In addition to the constraint that  $n$  for viable microbial cells suspended in water is known to be  $<1.10$ , the information about the entire spectral pattern of  $Q_c(\lambda)$  thus plays a crucial role in determining the correct solution for  $n(\lambda)$  at individual wavelengths. Regardless of the issue of multiple solutions,



no satisfactory convergence between the experimental and theoretical estimates of  $Q_c$  was reached in some spectral regions for DIA and CHLO. The values of  $n$  for the spectral regions with no satisfactory convergence were thus obtained by interpolation or extrapolation.

The described method for deriving  $n(\lambda)$  is best suited for microbial particles less than a few micrometers in size. The problems arise with increasing particle size, and in fact this method is not applicable to particles that are so large that  $Q_c$  is nearly constant and no longer sensitive to changes in  $n$ . The behavior of the function  $Q_c(\rho)$  suggests that the method is probably limited to microorganisms that are smaller than  $\sim 10 \mu\text{m}$ . Additionally, the method is appropriate only for monodisperse particles or polydisperse assemblages having narrow size distributions, such as the microbial cultures in our experiments.

The derived values of the index of refraction [and hence the scattering phase function  $\bar{\beta}(\theta, \lambda)$  as well] are potentially subject to greater uncertainties than other optical characteristics in our database, such as  $\sigma_s(\lambda)$ ,  $\sigma_b(\lambda)$  and  $\sigma_c(\lambda)$ , which are determined from measurements in a direct way. These uncertainties exist partly because the optical models for deriving  $n'$  and  $n$  are based on idealized assumptions about particles (sphericity and homogeneity), which actual microbial particles may not satisfy, and partly because data from measurements used as input to these calculations may be subject to experimental error. These factors, for example, have likely led to the abovementioned lack of convergence in our calculations for DIA and CHLO, although the effect of polydispersion could have also been part of this problem.

To a first approximation, the derived values of  $n'(\lambda)$  and  $n(\lambda)$  represent the bulk refractive index of the examined cells. Strictly speaking, our estimates of the refractive index can be regarded as the values that provide the best match between the experimental and theoretical efficiency factors,  $Q_s$  and  $Q_c$ , within the framework of the theories used for homogeneous and spherical particles. Note also that while the refractive index is critical for understanding the magnitude and variability of the single-particle optical properties, it is of no direct importance for the use of our optical database in the radiative transfer modeling. For the sole purpose of such modeling, determination of the refractive index would not be necessary if the capability to directly measure the volume-scattering function were available.

In contrast to the above-described four classes of microbial particles, no measurements of viruses (VIR) were made and all optical properties of these particles were determined using Mie scattering calculations for homogeneous spheres assuming that there is no absorption. These determinations are discussed in greater detail elsewhere (Stramski and Kiefer 1991). Briefly, the Mie calculations were made by using reasonable approximations about the size distribution and the real part of the refractive index of viral particles. The assumed size distribution represents isometric heads of tailed viruses and is based on published data that describe nearly 180 species of viruses that infect various bacteria. This size distribution is consistent with rather scarce data on marine viruses. The real part of the refractive index is assumed to be 1.05 within the examined spectral region. This estimate was derived from the average composition of viral heads that

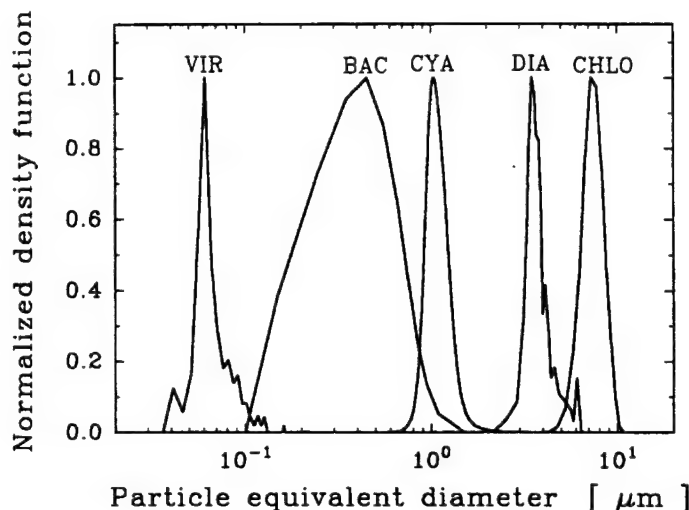


Fig. 2. Density functions of size distributions of microbial particles: VIR, viruses; BAC, heterotrophic bacteria; CYA, cyanobacteria *Synechococcus* (strain WH 8103); DIA, diatoms *Thalassiosira pseudonana*; CHLO, chlorophytes *Dunaliella tertiolecta*. For comparison, the size distributions were normalized to unity at the maximum.

are filled with DNA (25% of the particle volume) and water (75%) and enclosed by a thin rigid protein shell.

## Results and discussion

**Size distribution and refractive index**—The size distribution and refractive index are major determinants of the optical properties of particles. Fig. 2 shows the size distributions of the examined microbial particles. These size distributions are characterized by positive skewness with the mean diameter being greater than the modal diameter by 5–20%, depending on the type of microbial particles. The difference in the mean diameter  $D$  of the microbial population between the largest (CHLO) and smallest (VIR) particles in the present database is two orders of magnitude. The mean diameter  $D$  (calculated from the mean projected area; see Stramski and Reynolds 1993) of CHLO is  $\sim 7.6 \mu\text{m}$  and that of VIR is  $0.072 \mu\text{m}$ . The approximate values of  $D$  for BAC, CYA, and DIA are 0.55, 1.14, and  $4.01 \mu\text{m}$ . Accordingly, the mean projected area  $G$  of the particles changes by four orders of magnitude among the microbial classes, from about  $4 \times 10^{-3} \mu\text{m}^2$  for VIR to  $45 \mu\text{m}^2$  for CHLO. The range of the mean particle volume  $V$  covers six orders of magnitude, from  $2 \times 10^{-4} \mu\text{m}^3$  for VIR to  $230 \mu\text{m}^3$  for CHLO.

The spectra of the refractive index are presented in Fig. 3. The values of the imaginary part  $n''(\lambda)$  for the photosynthetic microorganisms (CYA, DIA, and CHLO) are much higher than for the heterotrophic microbes, BAC (Fig. 3A; note that viruses are not shown because they are assumed to be nonabsorbing). This difference is obviously a result of absorption by pigments (chlorophylls, carotenoids, phycobilins) that are present within the photosynthetic cells. The CYA, DIA, and CHLO have  $n'(\lambda)$  of the order of  $10^{-3}$  except for  $\lambda > 700 \text{ nm}$ , where absorption is very weak. Our measurements indicated that absorption vanishes at wavelengths

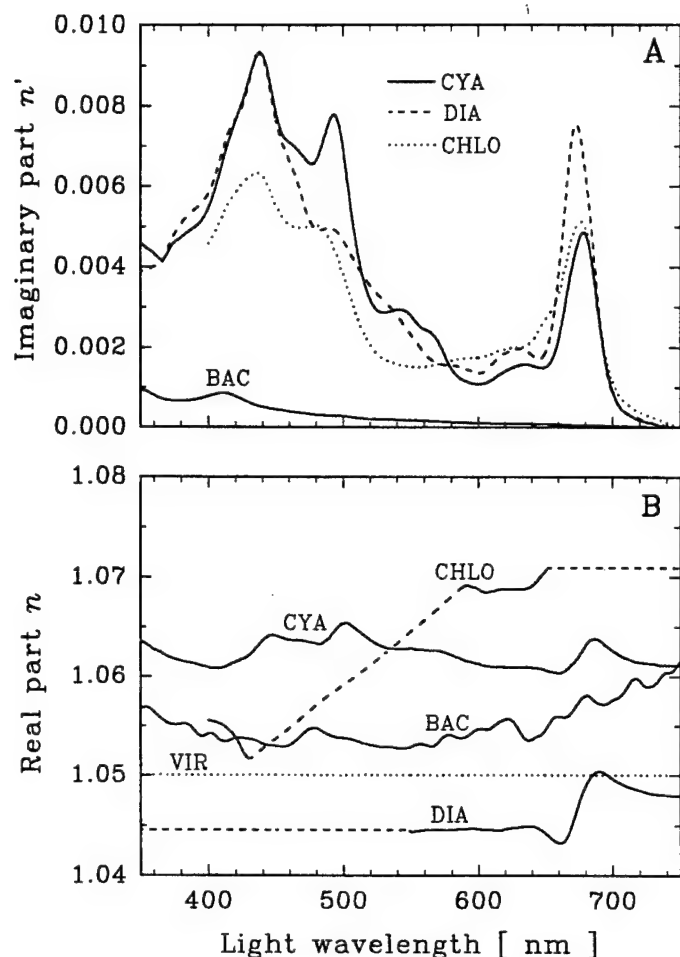


Fig. 3. Spectra of the refractive index of microbial particles relative to seawater. A. Imaginary part of the refractive index. B. Real part of the refractive index (dashed lines are used for DIA and CHLO in the spectral regions where extrapolation or interpolation was used). Symbols identifying microbial particles as in Fig. 2.

near 750 nm, and accordingly the  $n'$  values were assumed to be zero at this longwave end of the examined spectrum. This observation is consistent with numerous studies of phytoplankton absorption described in the past. The most pronounced features in the presented spectra  $n'(\lambda)$  for CYA, DIA, and CHLO are the blue ( $\sim 440$  nm) and red ( $\sim 675$  nm) maxima associated with absorption by Chl *a*. The CYA spectrum also displays a distinct maximum near 490 nm owing to the absorption by phycourobilin. In the red peak, the absorption by pigments other than Chl *a* is usually negligible. As a consequence, the magnitude of  $n'$  in this red spectral band strongly correlates with the intracellular concentration of Chl *a* (Stramski and Reynolds 1993; Stramski et al. 1995). In contrast to the photosynthetic microorganisms, BAC exhibit a rather featureless trend of decreasing  $n'$  with increasing  $\lambda$ . The only remarkable absorption feature occurs near 410 nm and is caused by respiratory cytochromes. The imaginary index  $n'(\lambda)$  of BAC in the blue and green is of the order of  $10^{-4}$  and less at wavelengths longer than 600 nm.

The magnitude of the real part of the refractive index  $n(\lambda)$  reflects the composition of microbial particles, primarily the

relative volumetric contents of water and solid constituents (e.g. Aas 1981). This fact has two important implications. First, the bulk refractive index of a living cell can be taken as a measure of the total organic solids present (Barer and Joseph 1954). Similarly, the value of  $n$  can also provide a measure of the intracellular carbon concentration, because carbon is one of relatively few major elements that make up cellular materials (Stramski and Morel 1990; Stramski and Reynolds 1993; Stramski et al. 1995). In general, living microbial cells have high water content. Therefore, the cells are rather weakly refringent when suspended in water, with the  $n$  values limited to the approximate range from 1.01 to 1.08 (Morel and Bricaud 1986). Our determinations fall within this range; the values of  $n$  are as low as 1.035 for DIA and as high as 1.07 for CHLO (Fig. 3, lower panel). The wavelength dependence of  $n$  within the examined spectral region is typically small. This dependence is clearly seen in the spectral curves for BAC and CYA where the values of  $n$  were derived at all wavelengths. This weak spectral dependence supports the assumed constancy of  $n(\lambda)$  for VIR and the extrapolations for DIA ( $\lambda < 550$  nm) and CHLO ( $\lambda > 700$  nm). For CHLO the values of  $n$  in the blue-green portion of the spectrum were obtained by interpolation between the two relatively narrow bands (near 400 and 600 nm) where solutions were found. For this species,  $n$  determined from our method near 400 nm is significantly lower than that near 600 nm.

**Optical efficiency factors and cross sections**—The differences in size and refractive index among the microbial particles are responsible for large differences in their single-particle optical properties. We begin our survey of the optical properties with Fig. 4, which shows the efficiency factors for absorption,  $Q_a(\lambda)$ , and scattering,  $Q_b(\lambda)$ . The maximum values of  $Q_a$  within the visible spectrum vary approximately from 0.016 for BAC (cytochrome peak near 410 nm) to 0.24 for CYA, 0.6 for DIA, and 0.68 for CHLO (the blue band of Chl *a* in the vicinity of 440 nm). The very low efficiency  $Q_a$  for heterotrophic bacteria is explained by very low values of the absorption parameter  $\rho'$  (0.019 at 410 nm and less at longer wavelengths), which in turn results from both the small size of bacterial cells and their low  $n'(\lambda)$ . Because both cell size and  $n'(\lambda)$  of CYA, DIA, and CHLO are larger, the values of  $\rho'$ , and hence  $Q_a$ , are significantly higher. In the blue band of Chl *a*,  $\rho'$  is 0.4, 1.4, and 1.8 for CYA, DIA, and CHLO. The interspecies changes in  $\rho'$  and the associated differences in  $Q_a$  for these three photosynthetic microbial classes are primarily caused by significant increases in cell size. The size parameter  $\alpha$  at 440 nm increases from 10.9 for CYA to 72.6 for CHLO. The differences in  $n'(\lambda)$  are small, so they have comparatively little effect on the observed differences in  $Q_a$ .

The scattering efficiency  $Q_b(\lambda)$  exhibits a significant increase with increasing size of microbial particles (Fig. 4B). Viruses have very low  $Q_b(\lambda)$ , which decreases from  $2 \times 10^{-3}$  in the near ultraviolet to  $2 \times 10^{-4}$  in the red portion of the spectrum. The small size of these particles yields very low values of the phase shift parameter  $\rho$ , of the order of  $10^{-2}$ . The  $Q_b(\lambda)$  values for BAC and CYA are 2–3 orders of magnitude greater. Between 400 and 700 nm,  $Q_b$  for BAC

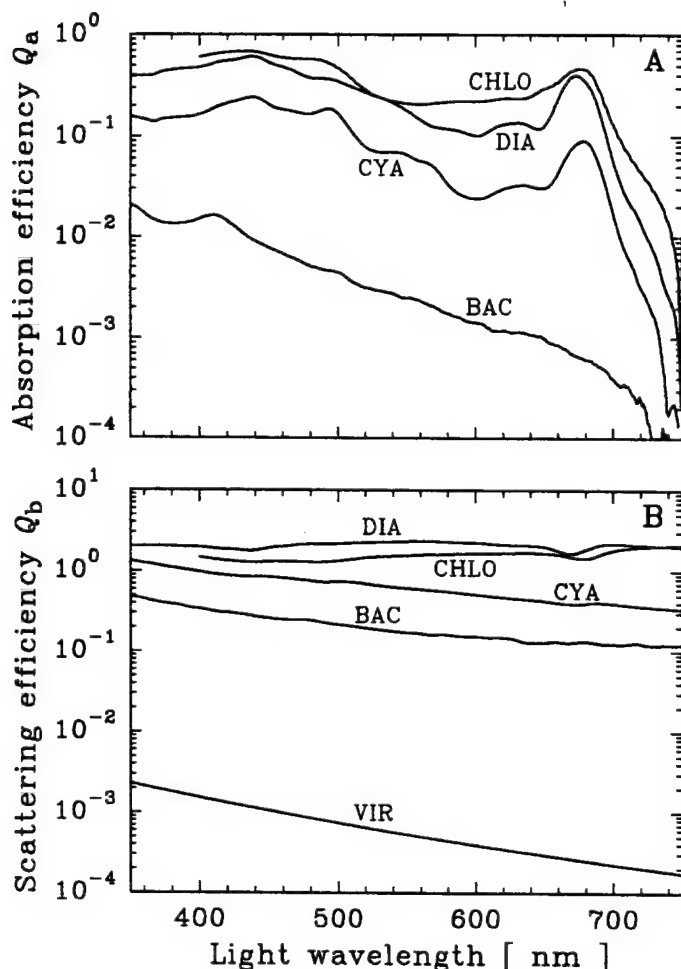


Fig. 4. Spectra of the optical efficiency factors of microbial particles. A. Absorption efficiency. B. Scattering efficiency. Symbols identifying microbial particles as in Fig. 2.

changes from 0.34 to 0.12 and for CYA from 0.97 to 0.40. The  $p$  values for these microorganisms are much higher than those for VIR. For BAC,  $p$  at 400 nm is 0.6 and for CYA is nearly 1.5. Given the range of  $p$  values, VIR, BAC, and CYA all display a decrease in  $Q_b$  with increasing  $\lambda$ , which corresponds to the first ascending slope of theoretical curve  $Q_b(p)$  (a comparison of the spectral shapes of scattering is discussed in greater detail below). DIA have the highest scattering efficiency among the examined species, even though CHLO are larger in size. The reason for this phenomenon is that  $p$  for DIA ranges from 2.15 to 4.3 across the spectrum, and the major maximum of  $Q_b$  must occur just within this range as the Mie scattering theory predicts. As shown,  $Q_b(\lambda)$  for DIA is generally close to 2, and a maximum value of 2.35 occurs near 560 nm. For CHLO, the phase shift parameter  $p$  increases further and is never  $< 6$  (for  $\lambda < 750$  nm), so  $Q_b(\lambda)$  is lower; for example,  $Q_b(400) = 1.46$  and  $Q_b(700) = 1.81$ . In the spectral region 430–490 nm,  $Q_b$  for this species is reduced to values as low as 1.27.

Figures 5 and 6 illustrate the absorption  $\sigma_a(\lambda)$  and scattering cross sections  $\sigma_s(\lambda)$ , respectively. Each of these figures includes two panels: panel A serves to compare the

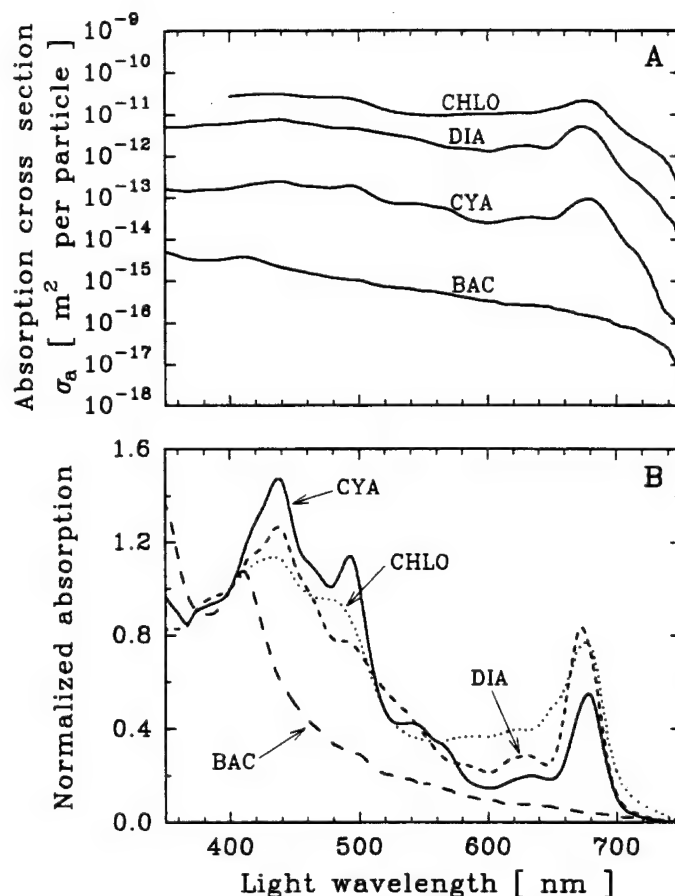


Fig. 5. Spectra of the absorption cross section of microbial particles. A. Comparison of magnitude. B. Comparison of spectral shape (for this comparison the spectra are normalized to unity at 400 nm). Symbols identifying microbial particles as in Fig. 2.

magnitudes and panel B the spectral shapes. The comparison of shapes is facilitated by normalizing the spectral curves to unity at 400 nm. The absorption cross section  $\sigma_a(\lambda)$  of BAC is of the order of  $10^{-15} \text{ m}^2 \text{ cell}^{-1}$  in the blue and  $10^{-16} \text{ m}^2 \text{ cell}^{-1}$  at longer visible wavelengths. The values of  $\sigma_a(\lambda)$  for photosynthetic microorganisms are much higher;  $\sigma_a(\lambda)$  for CHLO is 4–5 orders of magnitude greater than BAC. DIA have  $\sigma_a(\lambda)$  of the order of  $10^{-12}$  and CYA  $10^{-13}$ – $10^{-14} \text{ m}^2 \text{ cell}^{-1}$ .

The understanding of these interspecies variations is achieved easily if we recall that the absorption cross section is the product of the absorption efficiency factor and the geometric projected area of the particle,  $\sigma_a(\lambda) = Q_a(\lambda)G$ . For example, in the blue (at 425 nm)  $\sigma_a$  is  $\sim 10^4$  higher for CHLO if compared to BAC, because  $Q_a$  and  $G$  of CHLO are roughly 50-fold and 200-fold greater, respectively. Note that because  $Q_a$  increases with particle diameter (in addition to  $n'$ ), some contribution to the 50-fold increase in  $Q_a$  in this example is made by the increased cell size of CHLO. Although we here compare nonpigmented heterotrophic cells (low  $n'$ ) with highly pigmented photosynthetic cells (high  $n'$ ), it is seen that the effect of cell size alone, both directly through  $G$  and indirectly through  $Q_a$ , is extremely important to the observed interspecies range of the absorption cross

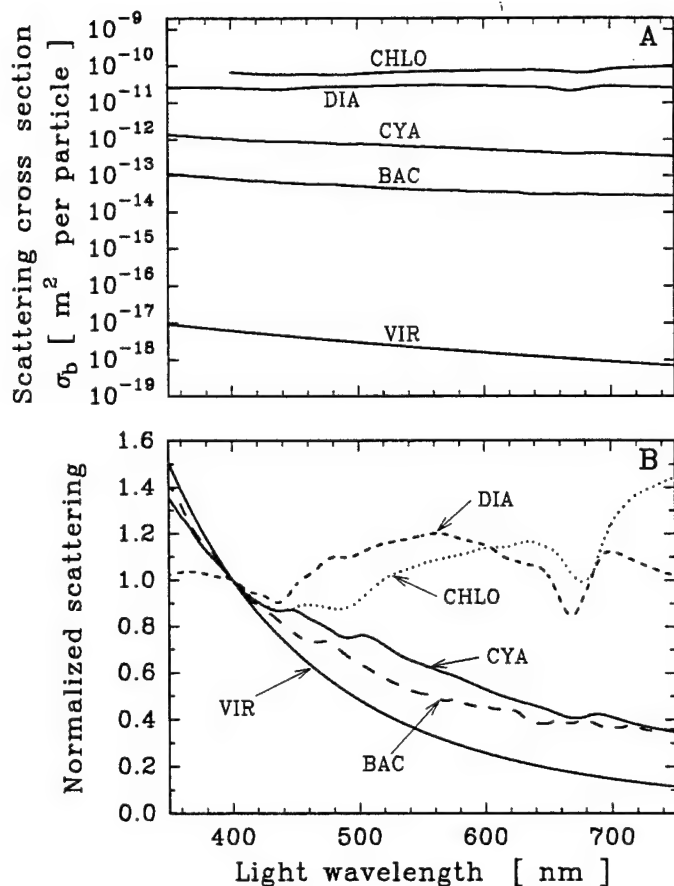


Fig. 6. Spectra of the scattering cross section of microbial particles. A. Comparison of magnitude. B. Comparison of spectral shape (for this comparison the spectra are normalized to unity at 400 nm). Symbols identifying microbial particles as in Fig. 2.

section. The spectral shapes of  $\sigma_s(\lambda)$  shown in Fig. 5B are identical to those of  $Q_s(\lambda)$  and are very similar to those of the imaginary part of the refractive index  $n'(\lambda)$ . Again, the curves for CYA, DIA, and CHLO display characteristic features associated with pigments present in photosynthetic cells, and the BAC curve shows the cytochrome band at 410 nm.

The range of the scattering cross sections  $\sigma_b(\lambda)$  in the present database covers 7–8 orders of magnitude, from  $10^{-18}$   $\text{m}^2 \text{ cell}^{-1}$  for VIR to  $10^{-11}$  for CHLO (Fig. 6A). The values of  $\sigma_b(\lambda)$  for BAC are much lower than for larger photosynthetic species, but this difference is smaller if compared to what has been observed for  $\sigma_s(\lambda)$ . There are  $\sim 3$  orders of magnitude difference in  $\sigma_b(\lambda)$  between BAC and CHLO. Again, the interpretation of these variations is provided by the relationship  $\sigma_b(\lambda) = Q_b(\lambda)G$ , which is analogous to the case of absorption. Because BAC are much more efficient in scattering than in absorbing light, their scattering cross sections, if compared to larger microbes, are reduced to lesser extent than their absorption cross sections. Note also that  $\sigma_b(\lambda)$  for DIA are 2.5–3 times lower than for CHLO, although the  $Q_b(\lambda)$  values for diatoms are higher. This is because the larger size of CHLO more than compensates for

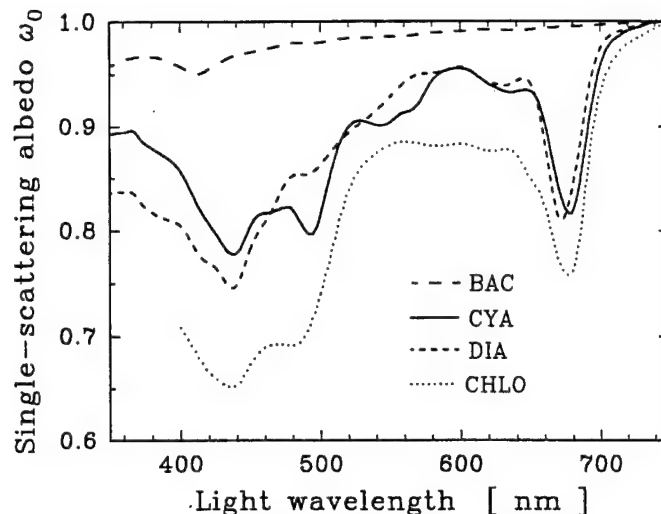


Fig. 7. Spectra of the single-scattering albedo of microbial particles. Symbols identifying microbial particles as in Fig. 2.

their lower  $Q_b(\lambda)$ ; the projected area  $G$  of CHLO is 3.5-fold greater than for DIA.

The shape of scattering spectra also varies considerably among the microbial species (Fig. 6B). The spectral shape of scattering for a given species is determined by the range of values for the phase shift parameter  $p$  associated with the examined spectral region. The observed changes of scattering with wavelength for VIR, BAC, and CYA can be reasonably well described as  $\lambda^\alpha$ , where the best-fit values for  $\alpha$  are  $-3.42$ ,  $-1.82$ , and  $-1.71$ , respectively. Such spectral behavior is characteristic of particles having sizes that are small or comparable to the wavelength of light. Note that the exponent for VIR is fairly close to  $-4$ , which describes molecular scattering. Larger species (DIA and CHLO) show comparatively little overall spectral trend, on which well-pronounced features associated with the effect of absorption are superimposed in the blue and red bands of Chl *a*.

Figure 7 shows the single-scattering albedo  $\omega_0(\lambda)$ . These data support the fact that the attenuation of the beam incident on the microbial particles is due primarily to scattering. This is the case even within the absorption bands of Chl *a* in photosynthetic microorganisms where the values of  $\omega_0(\lambda)$  remain relatively high, 0.65–0.8. For weakly absorbing heterotrophic bacteria, scattering accounts for  $>90\%$  of the beam attenuation. Recall that according to our assumption,  $\omega_0(\lambda)$  for VIR is 1.

**Scattering phase function**—The scattering phase functions  $\tilde{\beta}(\theta)$  for a selected wavelength of 550 nm are compared in Fig. 8. As seen, the shape of  $\tilde{\beta}(\theta)$  changes dramatically among the microbial particles, which primarily reflects the differences in particle size. The  $\tilde{\beta}(\theta)$  function for smallest particles, VIR, is fairly close to the symmetric pattern of molecular scattering, and displays relatively little variation with the scattering angle. At  $\theta = 100^\circ$  the scattering function has a minimum, which is 35% of  $\tilde{\beta}(0^\circ)$ . For the remaining microbial particles, including BAC whose mean diameter is virtually identical to the light wavelength of 550 nm, the  $\tilde{\beta}(\theta)$  function is strongly peaked in the forward direction.



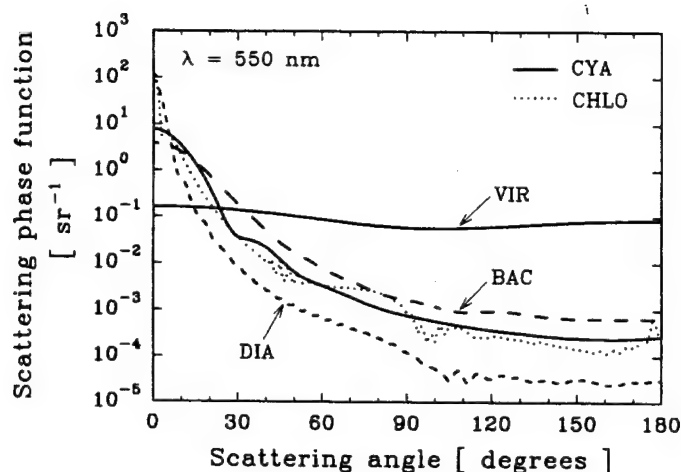


Fig. 8. Scattering phase functions of microbial particles for light wavelength 550 nm. Symbols identifying microbial particles as in Fig. 2.

Within the first  $10^\circ$  of the forward scattering lobe,  $\beta(\theta)$  decreases by 34.3, 55.7, 99.2, and 98.7% for BAC, CYA, DIA, and CHLO. The fraction of light scattered into backward directions by these microorganisms is extremely small as compared to forward scattering. For example,  $\beta(180^\circ)$  is a very small fraction of  $\beta(0^\circ)$ , varying from  $1.8 \times 10^{-4}$  for BAC to as low as  $3.8 \times 10^{-7}$  for DIA.

Similar interspecies variations in  $\beta(\theta)$  occur at other wavelengths. It is, however, important to emphasize that  $\beta(\theta)$  may also exhibit significant variations with wavelength  $\lambda$  for a given microbial species. Figure 9 provides a comparison of  $\beta(\theta)$  at three wavelengths (400, 550, and 700 nm) for two selected microbial classes, BAC and DIA. The curves for BAC show that there is a significant spectral variation in  $\beta(\theta)$  over the entire range of scattering angles with the exception of  $\theta$  in the vicinity of  $15^\circ$  (Fig. 9A). In contrast to small scattering angles ( $<15^\circ$ ),  $\beta(\theta)$  at larger angles is significantly higher at longer wavelengths than at shorter wavelengths. For example,  $\beta(45^\circ, 700 \text{ nm}) = 3.8 \beta(45^\circ, 400 \text{ nm})$  and  $\beta(180^\circ, 700 \text{ nm}) = 3.1 \beta(180^\circ, 400 \text{ nm})$ . Somewhat larger cells, namely CYA, are characterized by similar spectral variations of  $\beta(\theta)$  (not shown here). VIR, like BAC, show a narrow range of scattering angles where spectral variations of  $\beta(\theta)$  are small (not shown here). This range of angles for VIR is in the vicinity of  $75^\circ$ , which represents a significant shift from the  $15^\circ$  value for BAC. Additionally, the spectral variations in  $\beta(\theta)$  for VIR are not as large as for BAC; for example,  $\beta(180^\circ, 700 \text{ nm}) = 1.5 \beta(180^\circ, 400 \text{ nm})$ . For DIA,  $\beta(\theta)$  is only weakly dependent on  $\lambda$  in forward directions, but significant spectral variations may occur at large scattering angles (Fig. 9B). For example, at  $\theta = 90^\circ$  the magnitude of the scattering phase function is 3-fold higher at 700 nm than at 400 nm. A similar pattern of wavelength dependence of the scattering function was also observed for the largest cells in the database, CHLO.

**Backscattering properties**—A requirement for interpreting measured or modeled remotely sensed reflectance is that we know the backscattering properties of particles. The back-

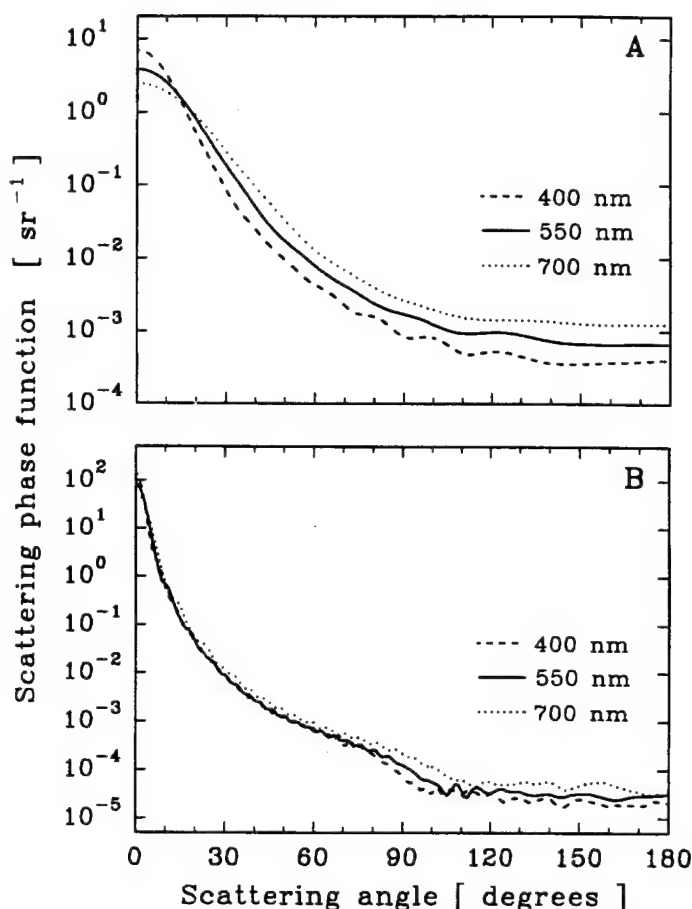


Fig. 9. Comparison of scattering phase functions at three light wavelengths, 400, 550, and 700 nm. A. BAC (heterotrophic bacteria). B. DIA (a diatom *Thalassiosira pseudonana*).

scattering ratio (sometimes referred to as the backscattering probability or the backscattering fraction),  $b_b(\lambda)$ , is shown in Fig. 10. This ratio describes the scattering that occurs into the backward directions (from  $90^\circ$  to  $180^\circ$ ) as a fraction of total scattering. As expected, because of their very small size, VIR have the highest  $b_b(\lambda)$ , ranging from 0.3 at 350 nm to 0.45 at 750 nm. These values are thus fairly close to 0.5, which corresponds to molecular scatterers. The backscattering ratio is strongly reduced for larger microbial species. For BAC,  $b_b(\lambda)$  is of the order of  $10^{-3}$ , reaching 0.01 at the long wavelength end of the spectrum. CYA have the  $b_b(\lambda)$  values that are more than 2-fold lower than those for BAC. The lowest backscattering ratio in this database is associated with DIA, whose  $b_b(\lambda)$  is  $<5 \times 10^{-4}$ .

The backscattering ratio exhibits an increasing trend with increasing wavelength of light (Fig. 10B). The wavelength dependence of  $b_b$  for VIR, BAC, and CYA can be described as  $\lambda^\kappa$ , where the best-fit value for  $\kappa$  is 0.49, 1.91, and 1.77. These increases in  $b_b$  with increasing  $\lambda$  can be understood noting that a given particle becomes smaller relative to the wavelength of light as  $\lambda$  increases and by recalling that smaller particles are more effective backscatterers. Although the overall spectral trend is also present in the curves rep-

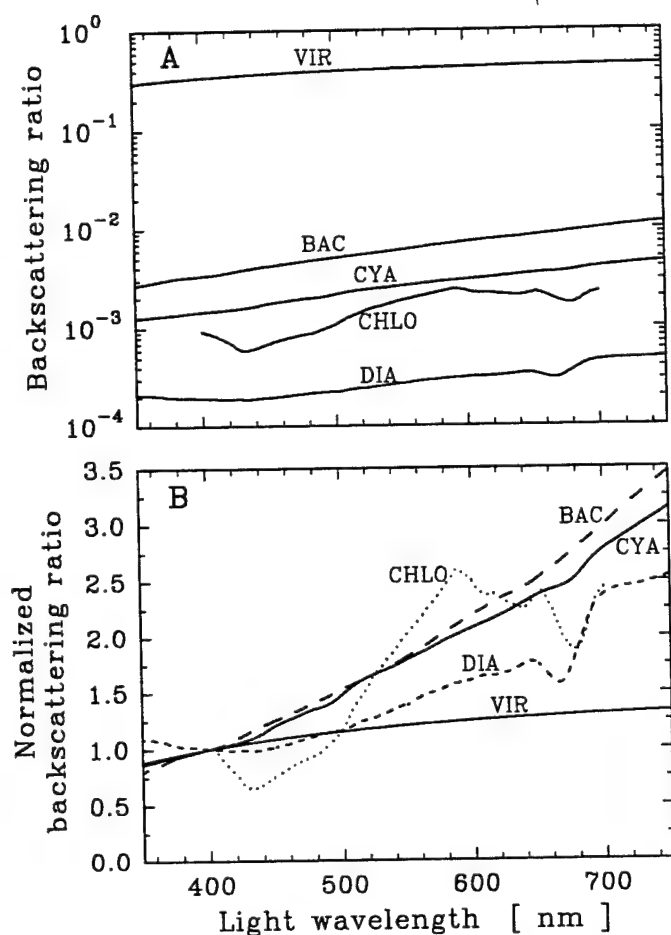


Fig. 10. Spectra of backscattering ratio of microbial particles. A. Comparison of magnitude. B. Comparison of spectral shape (for this comparison the spectra are normalized to unity at 400 nm). Symbols identifying microbial particles as in Fig. 2.

resenting DIA and CHLO, there are strong effects of absorption on the spectra of  $\bar{b}_b(\lambda)$  for these species.

Figure 11 illustrates the backscattering cross section  $\sigma_{bb}(\lambda)$ , which is related to the backscattering ratio and the scattering cross section through their product,  $\sigma_{bb}(\lambda) = \bar{b}_b(\lambda)\sigma_b(\lambda)$ . Accordingly, the curves for  $\sigma_{bb}(\lambda)$  can be interpreted using the curves for  $\sigma_b(\lambda)$  and  $\bar{b}_b(\lambda)$  discussed above. Note that the interspecies variation in  $\sigma_{bb}(\lambda)$  has been significantly reduced as compared to  $\sigma_b(\lambda)$ . If we compare the extreme curves, the values of  $\sigma_{bb}(\lambda)$  for CHLO are 4–5 orders of magnitude higher than those for VIR, as opposed to 7–8 orders of magnitude for  $\sigma_b(\lambda)$ . This difference is obviously a consequence of high backscattering ratio of very small particles. Several interesting features are also seen in the spectral behavior of  $\sigma_{bb}(\lambda)$  (Fig. 11B). The spectra  $\sigma_{bb}(\lambda)$  are nearly independent of wavelength for BAC and CYA. This result is explained by the fact that the exponents  $\alpha$  and  $\kappa$  in the functions  $\sigma_b(\lambda) \sim \lambda^\alpha$  and  $\bar{b}_b(\lambda) \sim \lambda^\kappa$  are very similar numbers with opposite sign. For VIR, the increase in  $\bar{b}_b(\lambda)$  with  $\lambda$  occurs at a much slower rate than the decrease of  $\sigma_b(\lambda)$ , hence  $\sigma_{bb}(\lambda)$  decreases as  $\lambda^{-2.93}$ . The spectral shapes of  $\sigma_{bb}(\lambda)$  for DIA and CHLO are similar to those for back-

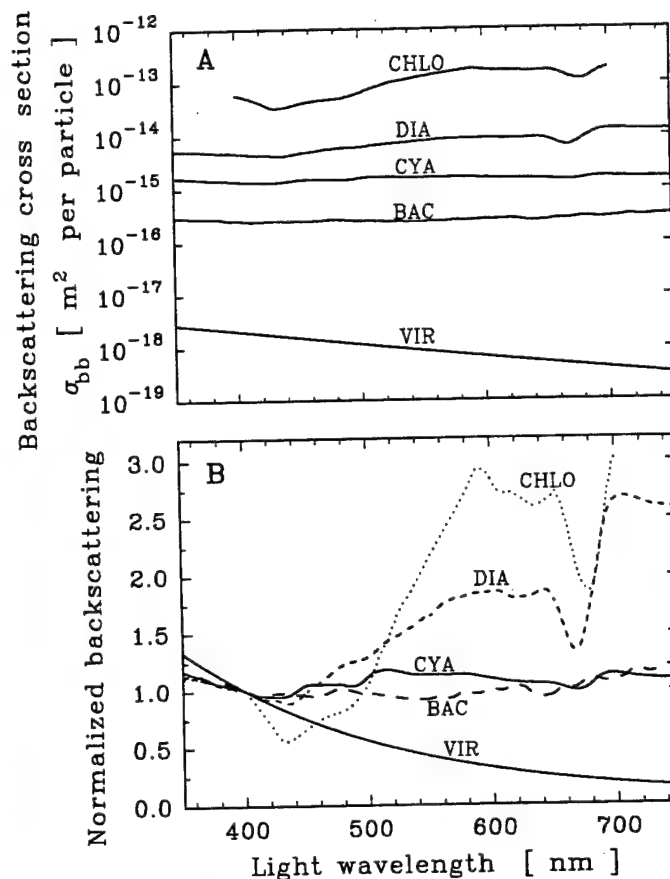


Fig. 11. Spectra of backscattering cross section of microbial particles. A. Comparison of magnitude. B. Comparison of spectral shape (for this comparison the spectra are normalized to unity at 400 nm). Symbols identifying microbial particles as in Fig. 2.

scattering ratios, although the features associated with absorption are now reinforced, because they are present in both  $\bar{b}_b(\lambda)$  and  $\sigma_b(\lambda)$ .

**Chlorophyll-specific and carbon-specific optical coefficients**—Our database also includes the spectra of the chlorophyll-specific absorption, scattering, and attenuation coefficients for CYA, DIA, and CHLO. We do not here discuss these coefficients because they are not used in our radiative transfer simulations. Note, however, that these coefficients are easily determined as the ratio of the optical cross sections on a per particle basis (discussed and shown above) to the cellular contents of Chl *a*. These cellular contents are  $4.63 \times 10^{-12}$  mg Chl *a* per cell for CYA,  $3.09 \times 10^{-10}$  for DIA, and  $1.71 \times 10^{-9}$  for CHLO. Similarly, the spectra of carbon-specific optical coefficients were determined for CYA and DIA (not shown here), and the cellular carbon contents are  $2.04 \times 10^{-10}$  mg C per cell for CYA and  $6.68 \times 10^{-9}$  for DIA.

**Intraspecies optical variability**—Up to this point in our discussion, we have presented the database of the optical properties that represent certain averages for each microbial species. Note, however, that the optical properties of any

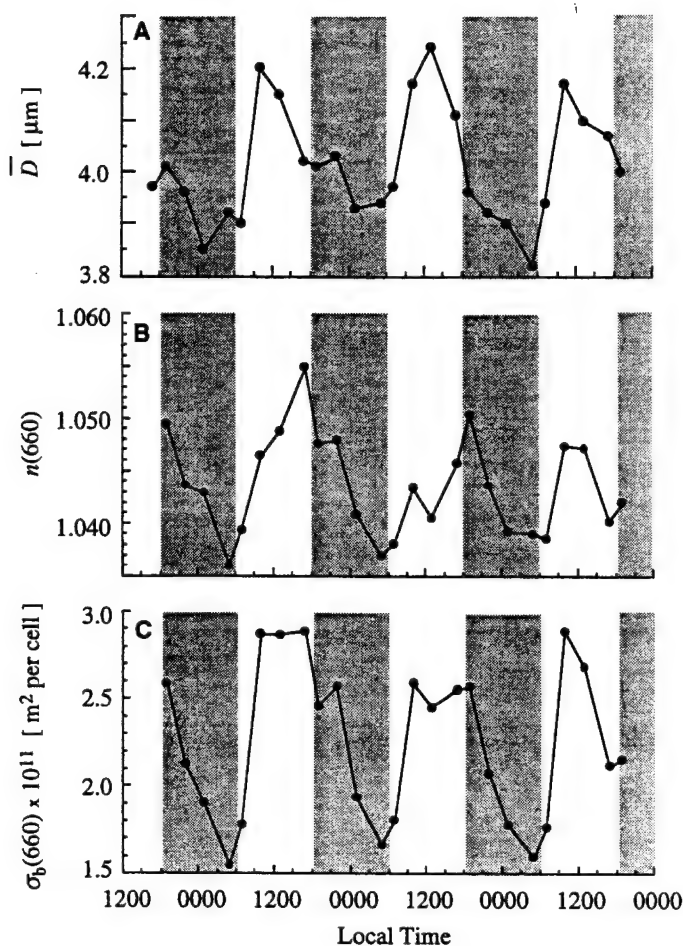


Fig. 12. Diel variations in the selected properties of a marine diatom *Thalassiosira pseudonana*. A. Mean cell diameter. B. Real part of the refractive index at 660 nm relative to seawater medium. C. Scattering cross section at 660 nm.

microbial species may vary considerably in response to changes in the ambient conditions for growth. Such variations occur because living microorganisms are capable of altering their cell size, shape, biochemical composition, and, hence, refractive index, which are all important determinants of the cellular absorption and scattering properties. Some recent studies were specifically designed to provide a comprehensive characterization of the changes in the optical properties of phytoplankton in response to varying magnitude and spectral composition of growth irradiance (Stramski and Morel 1990), limitation of growth by nitrogen availability (Reynolds et al. 1997), and over a day-night cycle (Stramski and Reynolds 1993; Stramski et al. 1995).

A detailed consideration of such intraspecies optical variability is beyond the scope of the present paper, so we choose to show only one example, namely diel variations in certain properties of the diatom *Thalassiosira pseudonana* (Fig. 12). The data illustrated in this figure are adapted from the study by Stramski and Reynolds (1993). As seen, both cell size and refractive index exhibited a distinct diel pattern. The cells were smallest throughout the second half of the dark period, with a mean diameter  $\bar{D}$  as small as 3.80  $\mu\text{m}$ .

Cell size increased rapidly after sunrise, reaching a maximum in late morning or midday, with  $\bar{D}$  being then as high as 4.25  $\mu\text{m}$ . The real part of the refractive index,  $n$ , also varied significantly over a diel cycle, with a well-defined minimum at the end of the dark period and a gradual increase throughout the daylight hours, so that a maximum occurred near sunset (with the exception of the third day, when  $n$  peaked earlier in midday). At  $\lambda = 660$  nm, the values of  $n$  ranged from 1.036 to 1.055, indicating that the refractive index increment ( $n - 1$ ) increased by >50% during the illuminated portion of the day. These variations in cell size and refractive index resulted in large variations of cellular scattering cross section  $\sigma_b$ , as illustrated for  $\lambda = 660$  nm in the bottom panel of Fig. 12. There was a deep minimum in  $\sigma_b$  just before sunrise and a sharp increase in the morning. The magnitude of these oscillations was highest on day 1 of the experiment when the daily maximum to minimum ratio in  $\sigma_b$  was 1.86. The scattering cross section of this species can thus vary nearly 2-fold over a diel cycle. The main point of relevance to the present work is that this result illustrates how much variability is unaccounted for in the developed database of the average properties. Note that in this particular case, the average values of spectral  $\sigma_b(\lambda)$ , which are included in our database of DIA, were obtained by averaging the curves just like those of Fig. 12C. Such averaging was performed at each wavelength.

## Conclusions

This work represents a first step toward creating a comprehensive database of the optical properties of marine particles. Achieving this goal is a complex and laborious task. The major complication arises from the great variety of particulate species in seawater and from both inter- and intra-species variability in their properties. It is obvious that a successful approach to creating such database cannot include every species, but instead a manageable number of particulate components must be chosen. It seems that these components can be best defined by two simple criteria. First, the sum of particulate components should account for the total bulk optical properties in a water body as accurately as possible. Second, each of the particulate components should play a specific, well-defined role in the functioning of the marine ecosystem. The latter criterion is important in the pursuit of the linkage of optical information with biological and ecosystem models. We envision that any particulate component in the ultimate database will generally include multispecies assemblages of similarly sized particles that have similar functions in the marine environment. As an example, heterotrophic bacteria, including many different species of similarly sized living microorganisms that are all heterotrophs, can be considered as one such distinct component. Of course, similarly sized photoautotrophic microorganisms or nonliving particles (minerals or biogenic detritus) can form separate components as well. Some planktonic species or taxa with unique optical properties (e.g. coccolithophores) will likely require consideration as separate components.

The database presented here includes five microbial components, some multispecies and some monospecific. To rep-

resent natural populations of marine particles more realistically, this database must be expanded. Specifically, detritus and mineral particles need to be added. More microbial species, both photoautotrophs and heterotrophs, from various size ranges have to be included. These additions will allow the creation of several multispecies categories of microorganisms in these size ranges, rather than using single species categories as in the present database (DIA, CHLO). The use of information from several laboratory experiments with various microorganisms made in the past (Bricaud et al. 1988; Morel and Ahn 1990, 1991; Ahn et al. 1992; Morel et al. 1993) will help to expand our database. As an example, data on Prochlorophytes, the smallest photosynthetic microorganisms that often dominate the assemblage of photoautotrophs in the oligotrophic tropical ocean and must therefore be considered as separate component in the database, are already available (Morel et al. 1993). Also note that including the intraspecies variability seems to represent the greatest challenge in expanding this optical database.

Although the present database is not complete, it provides a comprehensive characterization of the examined microbial components. Both information about the magnitude and spectral behavior of various optical properties at the level of single particles and data about particle size and refractive index are provided, which is critical in understanding the optical properties. The major significance and applicability of the database stems from the fact that all basic information on single-particle optical properties required to carry out radiative transfer modeling (with the exception of polarization properties) is included. In our companion paper (Mobley and Stramski 1997) we show how powerful a combination of such a database and radiative transfer modeling is in the study of oceanic optics.

## References

- AAS, E. 1981. The refractive index of phytoplankton. Univ. Oslo, Inst. Rep. Ser. 46.
- AHN, Y.-H., A. BRICAUD, AND A. MOREL. 1992. Light backscattering efficiency and related properties of some phytoplankters. *Deep-Sea Res.* **39**: 1835–1855.
- BARER, R., AND S. JOSEPH. 1954. Refractometry of living cells. Part I. Basic principles. *Q. J. Microsc. Sci.* **95**: 399–423.
- BOHREN, C. F., AND D. R. HUFFMAN. 1983. Absorption and scattering of light by small particles. Wiley.
- BRICAUD, A., A.-L. BEDHOMME, AND A. MOREL. 1988. Optical properties of diverse phytoplanktonic species: Experimental results and theoretical interpretation. *J. Plankton Res.* **10**: 851–873.
- , AND A. MOREL. 1986. Light attenuation and scattering by phytoplanktonic cells: A theoretical modeling. *Appl. Opt.* **25**: 571–580.
- DUYSSENS, L. M. 1956. The flattening of the absorption spectra of suspensions as compared to that of solutions. *Biochim. Biophys. Acta* **19**: 1–12.
- GORDON, H. R., AND A. MOREL. 1983. Remote assessment of ocean color for interpretation of satellite visible imagery—A review. Lecture notes on coastal and estuarine studies. Springer.
- MOBLEY, C. D. 1994. Light and water. Radiative transfer in natural waters. Academic.
- , AND D. STRAMSKI. 1997. Effects of microbial particles on oceanic optics: Methodology for radiative transfer modeling and example simulations. *Limnol. Oceanogr.* **42**: 550–560.
- MOREL, A. 1988. Optical modeling of the upper ocean in relation to its biogenous matter content (case I waters). *J. Geophys. Res.* **93**: 10,749–10,768.
- , AND Y.-H. AHN. 1990. Optical efficiency factors of free living marine bacteria: Influence of bacterioplankton upon the optical properties and particulate organic carbon in oceanic waters. *J. Mar. Res.* **48**: 145–175.
- , AND ———. 1991. Optics of heterotrophic nanoflagellates and ciliates. A tentative assessment of their scattering role in oceanic waters compared to those of bacterial and algal cells. *J. Mar. Res.* **49**: 177–202.
- , F. PARTENSKY, D. VAULOT, AND H. CLAUSTRE. 1993. *Prochlorococcus* and *Synechococcus*: A comparative study of their optical properties in relation to their size and pigmentation. *J. Mar. Res.* **51**: 617–649.
- , AND A. BRICAUD. 1981. Theoretical results concerning light absorption in a discrete medium, and application to specific absorption by phytoplankton. *Deep-Sea Res.* **28**: 1375–1393.
- , AND A. BRICAUD. 1986. Inherent optical properties of algal cells including picoplankton: Theoretical and experimental results, p. 521–555. *In* Photosynthetic picoplankton. Can. Bull. Fish. Aquat. Sci. 214.
- , AND L. PRIEUR. 1977. Analysis of variations in ocean color. *Limnol. Oceanogr.* **22**: 709–722.
- REYNOLDS, R. A., D. STRAMSKI, AND D. A. KIEFER. 1997. The effect of nitrogen-limitation on the absorption and scattering properties of the marine diatom *Thalassiosira pseudonana*. *Limnol. Oceanogr.* **42**: In press.
- SMITH, R. C., AND K. S. BAKER. 1978. Optical classification of natural waters. *Limnol. Oceanogr.* **23**: 260–267.
- STRAMSKI D., AND D. A. KIEFER. 1990. Optical properties of marine bacteria, p. 250–268. *In* Ocean Optics X. SPIE 1302.
- , AND ———. 1991. Light scattering by microorganisms in the open ocean. *Prog. Oceanogr.* **28**: 343–383.
- STRAMSKI D., AND A. MOREL. 1990. Optical properties of photosynthetic picoplankton in different physiological states as affected by growth irradiance. *Deep-Sea Res.* **37**: 245–266.
- , ———, AND A. BRICAUD. 1988. Modeling the light attenuation and scattering by spherical phytoplanktonic cells: A retrieval of the bulk refractive index. *Appl. Opt.* **27**: 3954–3956.
- , AND R. A. REYNOLDS. 1993. Diel variations in the optical properties of a marine diatom. *Limnol. Oceanogr.* **38**: 1347–1364.
- , G. ROSENBERG, AND L. LEGENDRE. 1993. Photosynthetic and optical properties of the marine chlorophyte *Dunaliella tertiolecta* grown under fluctuating light caused by surface wave focusing. *Mar. Biol.* **115**: 363–372.
- , A. SHALAPYONOK, AND R. A. REYNOLDS. 1995. Optical characterization of the oceanic unicellular cyanobacterium *Synechococcus* grown under a day-night cycle in natural irradiance. *J. Geophys. Res.* **100**: 13,295–13,307.
- VAN DE HULST, H. C. 1957. Light scattering by small particles. Wiley.

Submitted: 23 February 1996

Accepted: 20 August 1996

Amended: 29 January 1997

## **APPENDIX B**

Reprint of

*Effects of microbial particles on oceanic optics:  
Methodology for radiative transfer modeling and  
example simulations*

by

Curtis D. Mobley and  
Dariusz Stramski

Published in

*Limnology and Oceanography*  
Vol. 42, No. 3, pages 550-560 (1997)



## Effects of microbial particles on oceanic optics: Methodology for radiative transfer modeling and example simulations

Curtis D. Mobley

Sequoia Scientific, 9725 S.E. 36th St, Suite 308, Mercer Island, Washington 98040

Dariusz Stramski

Marine Physical Laboratory, Scripps Institution of Oceanography, University of California at San Diego, La Jolla, California 92093-0701

### Abstract

Radiative transfer numerical modeling provides a powerful means of separating and understanding the effects of various types of microbial particles on oceanic light fields. We illustrate the methodology for achieving this separation and provide various idealized examples. We begin with a database of the single-particle optical properties of marine microbial particles and then construct the total absorption and scattering properties of natural waters for given concentrations of the various particle types. When used as input to the Hydrolight radiative transfer numerical model, these absorption and scattering properties generate underwater light fields. Because this modeling process rests upon the optical properties of the individual microbial components, rather than just on the total absorption and scattering properties of a water body, it is possible to analyze the effects of the various particulate components on quantities such as diffuse attenuation coefficients and remote-sensing reflectances. We find that different microbial compositions in two water bodies can give considerably different optical properties, even though the chlorophyll concentration is the same in each of the water bodies. Our simulations show how variability in chlorophyll concentrations obtained from remotely sensed ocean color signals can be explained by the detailed composition of the water body. This approach suggests that it may be possible to distinguish between blooms of small picophytoplankton and larger nanophytoplankton by using remotely sensed signals.

Stramski and Mobley (1997, hereafter referred to as SM) described a database of single-particle optical properties for five types of microbial particles. These particle types were marine viruses (VIR), heterotrophic bacteria (BAC), cyanobacteria (CYA), small nanophytoplanktonic diatoms (DIA), and nanophytoplanktonic chlorophytes (CHLO). In the present paper, the particular microbes found in the database are viewed as representatives of broader classes of particles. For example, the particular species of DIA in the database (*Thalassiosira pseudonana*) has cells with diameters of  $\sim 4 \mu\text{m}$ , and the particular species of CHLO (*Dunaliella tertiolecta*) has cells  $\sim 8 \mu\text{m}$  in size. We thus take DIA as representative of small nanophytoplankton of size  $4 \mu\text{m}$ , and we take CHLO as representative of nanophytoplankton of size  $8 \mu\text{m}$ . The particular species involved are not important for the purposes of this paper. Moreover, it is sufficient for our present purposes to consider only five types of microbial particles, even though realistic simulations of actual water bodies might require more microbial types (such as prochlorophytes, larger bloom-forming species, or coccolithophores). We do include detritus (DET) and colored dissolved organic matter (CDOM) in some of our examples.

The database includes, among other things, the single-particle absorption and scattering cross sections,  $\sigma_a(\lambda)$  and  $\sigma_s(\lambda)$ , respectively, and the scattering phase functions  $\beta(\theta,$

$\lambda)$  for each microbial type. Here  $\lambda$  is the wavelength and  $\theta$  is the scattering angle. These cross sections and phase functions allow us to determine the individual contributions of the various microbial particles to the bulk inherent optical properties (IOPs) of a water body, given the concentrations of the various particle types. It is the bulk IOPs—in particular the total absorption coefficient  $a$ , the total scattering coefficient  $b$ , and the total scattering phase function  $\bar{\beta}$ —that determine how light interacts with the water body.

We first describe how the bulk IOPs are constructed from the single-particle quantities found in the database and from additional information about water components such as detritus and CDOM. As an example, we discuss in some detail the IOPs obtained when the microbial components are present at concentrations typical of productive coastal waters (although our general methods are equally applicable for any concentrations). The bulk IOPs are the input required by any radiative transfer model that is used to simulate underwater spectral radiance distributions. In our simulations, we use the Hydrolight radiative transfer numerical model (Mobley 1994), which we briefly describe.

Finally, we discuss several radiative transfer simulations chosen to illustrate the power of our approach for understanding the effects of microbial particles and other substances on oceanic light fields. The first of these simulations shows the effects of the different microbial types on in-water scalar irradiances and diffuse attenuation functions and on remote-sensing reflectances. We then illustrate how water bodies with the same chlorophyll concentrations but with different microbial compositions can have different remote-sensing reflectances; such water bodies would be regarded

### Acknowledgments

This work was supported by the Environmental Optics Program of the Office of Naval Research under ONR contract N00014-94C-0114.

We thank A. Morel for his comments on the paper.

as identical by a bio-optical model that attempts to parameterize quantities of interest in terms of the chlorophyll concentration alone. We end with an example showing how our approach can be used to develop or evaluate algorithms for the interpretation of remotely sensed ocean color data. These radiative transfer simulations are intended only to illustrate our approach for understanding the underlying relationships between the composition of a water body and its optical properties. Such simulations do not yield general conclusions. General conclusions can be obtained only from more extensive simulations involving a larger number of microbial particle types and a wider range of environmental conditions than can be presented in this initial paper.

### Bulk inherent optical properties

The total IOPs of a water body are the sums of the IOPs attributable to the each of the various constituents of the water body. Thus, the total absorption coefficient is the sum of the absorption coefficients of the water itself, of each microbial component, and of any other component present in the water, such as mineral particles, detritus, or dissolved substances. Corresponding sums give the total scattering coefficient and the total volume scattering function in terms of the constituent contributions.

In the simulations discussed below, we consider hypothetical water bodies composed of eight constituents: the water itself, the five microbial types contained in the database (VIR, BAC, CYA, DIA, and CHLO), DET, and CDOM. The total absorption coefficient  $a(z, \lambda)$ , which has units of inverse meters and in general depends on both depth  $z$  and wavelength  $\lambda$ , can then be written as

$$\begin{aligned} a(z, \lambda) &= \sum_{j=1}^8 a_j(z, \lambda) \\ &= a_w(\lambda) + \sum_{i=1}^5 C_i(z) [\sigma_a(\lambda)]_i + a_{\text{DET}}(z, \lambda) \\ &\quad + a_{\text{CDOM}}(z, \lambda). \end{aligned} \quad (1)$$

The absorption coefficient for water,  $a_w(\lambda)$ , is taken from Smith and Baker (1981).  $C_i(z)$  is the concentration in particles per cubic meter of the  $i$ th microbial component (the concentration in general depends on depth). The single-particle absorption cross section of the  $i$ th microbial type is denoted by  $[\sigma_a(\lambda)]_i$  and has units of meters squared per particle. The absorption cross sections  $[\sigma_a(\lambda)]_i$  are taken from the database (e.g. see fig. 5A of SM). The absorption by DET is modeled with an empirical formula from Roesler et al. (1989),

$$a_{\text{DET}}(z, \lambda) = a_{\text{DET}}(z, 400) \exp[-0.011(\lambda - 400)],$$

which represents an average detrital absorption as determined from various waters. This model requires an independent determination of the detrital absorption as a function of depth at some reference wavelength, which we take to be 400 nm. The absorption by CDOM is modeled by a similar formula (Bricaud et al., 1981):

$$a_{\text{CDOM}}(z, \lambda) = a_{\text{CDOM}}(z, 400) \exp[-0.014(\lambda - 400)].$$

Once again, this model represents an average and requires an independent determination of  $a_{\text{CDOM}}(z, 400)$ . In the simulations described below, we vary  $a_{\text{DET}}(z, 400)$  from 20 to 60% of the total microbial absorption at 400 nm, and we allow  $a_{\text{CDOM}}(z, 400)$  to vary from 20 to 40% of the total microbial absorption at 400 nm. These ranges are chosen only to illustrate how DET and CDOM are included in simulations. The exact values chosen for  $a_{\text{DET}}(z, 400)$  and  $a_{\text{CDOM}}(z, 400)$  are not crucial for our examples.

The total scattering coefficient  $b(z, \lambda)$ , with units of inverse meters, is determined from

$$\begin{aligned} b(z, \lambda) &= \sum_{j=1}^7 b_j(z, \lambda) \\ &= b_w(\lambda) + \sum_{i=1}^5 C_i(z) [\sigma_b(\lambda)]_i + b_{\text{DET}}(z, \lambda). \end{aligned} \quad (2)$$

CDOM is assumed to be nonscattering. Thus,  $b_{\text{CDOM}} = 0$  and is not shown in the equation. As for absorption, the pure-water scattering coefficient  $b_w(\lambda)$  is taken from Smith and Baker (1981). The single-particle scattering cross sections for the five microbial components,  $[\sigma_b(\lambda)]_i$ , are taken from the database (see fig. 6A in SM). For the simulations described below, the scattering coefficient for detritus is allowed to vary from 20 to 60% of the total microbial scattering at 400 nm. Its magnitude is taken to be independent of wavelength, although a  $\lambda^{-1}$  dependence would also be realistic. Once again, the exact form used for  $b_{\text{DET}}(z, \lambda)$  is not crucial for our examples.

The total volume-scattering function  $\beta(z, \theta, \lambda)$ , with units of  $\text{m}^{-1} \text{sr}^{-1}$ , is likewise a sum of the volume-scattering functions of the various components. Each of the component volume-scattering functions can be written as the product of the corresponding scattering coefficient and scattering phase function. Because the phase functions are determined by the particle types, it is reasonable to take the component phase functions to be independent of depth. The depth dependence of the total phase function is then determined by the depth dependencies of the component scattering coefficients. The total phase function is then computed as a weighted sum of the component phase functions:

$$\begin{aligned} \tilde{\beta}(z, \theta, \lambda) &= \sum_{j=1}^7 \frac{b_j(z, \lambda)}{b(z, \lambda)} \tilde{\beta}_j(\theta, \lambda) \\ &= \frac{b_w(\lambda)}{b(z, \lambda)} \tilde{\beta}_w(\theta) + \sum_{i=1}^5 \frac{b_i(z, \lambda)}{b(z, \lambda)} \tilde{\beta}_i(\theta, \lambda) \\ &\quad + \frac{b_{\text{DET}}(z, \lambda)}{b(z, \lambda)} \tilde{\beta}_{\text{DET}}(\theta). \end{aligned} \quad (3)$$

The phase function for molecular scattering by water is

$$\tilde{\beta}_w(\theta) = 0.06225(1 + 0.835 \cos^2 \theta).$$

The phase functions for the microbial components are taken from the database (selected examples of these phase functions were seen in figs. 8 and 9 of SM). Because detrital particles are generally polydisperse, we take the detrital phase function to be an average particle phase function computed from volume-scattering functions measured in situ by

Table 1. Parameter values used in simulations. The microbe concentrations range from "low open ocean" to "high coastal" values. The absorption and scattering values for detritus and colored dissolved organic matter cover a corresponding range of values. For the three chlorophyll-bearing microbes (cyanobacteria, small diatoms, and chlorophytes),  $Chl^*$  is the chlorophyll content in mg Chl per cell.

Viruses	$3 \times 10^9 - 1 \times 10^{14}$ particles $m^{-3}$
Heterotrophic bacteria	$1 \times 10^{11} - 2 \times 10^{12}$
Cyanobacteria	$1 \times 10^9 - 1 \times 10^{11}$ ( $Chl^* = 4.63 \times 10^{-12}$ )
Small diatoms	$3 \times 10^8 - 1 \times 10^{10}$ ( $Chl^* = 3.09 \times 10^{-10}$ )
Chlorophytes	$1 \times 10^7 - 4 \times 10^8$ ( $Chl^* = 1.71 \times 10^{-9}$ )
Detritus (DET)	$a_{DET}(400) = 0.2 - 0.6$ of $a_{MICROBE}(400)$ $b_{DET} = 0.2 - 0.6$ of $b_{MICROBE}(400)$
Yellow matter (CDOM)	$a_{CDOM}(400) = 0.2 - 0.4$ of $a_{MICROBE}(400)$ $b_{CDOM} = 0$

Petzold (1972) in various waters. The determination of this average particle phase function is described by Mobley et al. (1993). This phase function is plotted in Fig. 4 below.

In order to evaluate Eq. 1 and 2, we must specify the concentrations  $C_i$  of the various microbial components. In our studies of ocean waters we are using the range of concentrations shown in Table 1. The lowest concentrations correspond to values that can be found in oligotrophic open-ocean waters, which we call low open-ocean values of  $C_i$ . If each of the chlorophyll-bearing microbes (CYA, DIA, and CHLO) is present at the lowest concentration seen in Table 1, the corresponding chlorophyll concentration is  $Chl \sim 0.1$   $mg\ m^{-3}$ . The highest concentrations found in Table 1 are representative of values found in productive coastal waters; we call these high coastal concentrations. The corresponding chlorophyll concentration is  $Chl \sim 4.2$   $mg\ m^{-3}$ . The ranges of microbial concentrations in Table 1 were chosen based on data available in the literature. For example, concentrations of viruses in the marine environment were reported by Proctor and Fuhrman (1990) and Maranger and Bird (1995); the concentrations of nanophytoplankton, heterotrophic bacteria, and cyanobacteria were based on Takahashi and Bienfang (1983), Davis et al. (1985), Cho and Azam (1990), Li et al. (1992), and Li (1995).

Figure 1 shows the absorption coefficients for the individual microbial components when present at the high coastal concentrations seen in Table 1. The figure also shows the corresponding total microbial absorption coefficient (the sum of the five microbial absorption coefficients) and the total absorption coefficient given by the bio-optical model of Morel (1991):

$$a(\lambda) = [a_w(\lambda) + 0.06a_{Chl}^*(\lambda)Chl^{0.65}] \times [1 + 0.2\exp\{-0.014(\lambda - 440)\}]. \quad (4)$$

In Eq. 4,  $a_{Chl}^*(\lambda)$  is the chlorophyll-specific absorption coefficient (units of  $m^2$  per mg Chl), which is tabulated by Morel (1991). The top curve in Fig. 1 is Eq. 4 evaluated for a value of  $Chl = 4.2$   $mg\ Chl\ m^{-3}$ , which, as already noted, corresponds to the high coastal concentration of the chlorophyll-bearing microbes.

The figure shows that when these five components are present at the high coastal concentrations, the small nano-

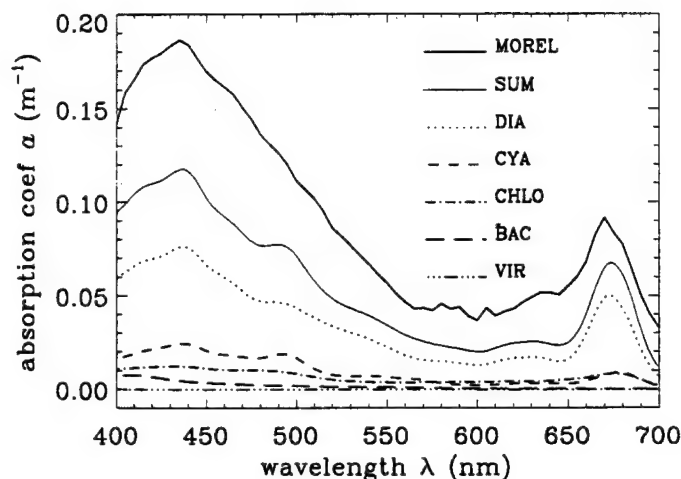


Fig. 1. The bottom five lines give the absorption coefficients for individual microbial components when present at the high coastal concentrations shown in Table 1; the components are identified by the line pattern. The light solid line is the sum of the five microbial curves. The heavy solid (top) line is the total absorption coefficient predicted by the Morel model of Eq. 4 with a chlorophyll concentration of  $Chl = 4.2$   $mg\ m^{-3}$ .

phytoplanktonic species (here represented by DIA) is the major microbial contributor to the total absorption. The cyanobacteria, which are 10 times more numerous than the diatoms, contribute only about half as much to the absorption because the per-cell absorption cross sections are much less for CYA than for DIA (see fig. 5A of SM). The larger nanophytoplankton (here represented by CHLO) contribute even less. Although CHLO has a much higher absorption cross section than does DIA, the cell concentration of CHLO is less than that of DIA by a factor of 25. The heterotrophic bacteria contribute still less; furthermore, by hypothesis, the viruses are nonabsorbing. The total microbial absorption at these concentrations is about two-thirds of the total absorption predicted by Eq. 4. This difference occurs because the Morel model is derived from samples of ocean waters that contain additional absorbing phytoplanktonic components as well as detritus and dissolved substances, which are not included in our sum-of-microbes values. Note that in Eq. 4, 20% of the total absorption at 440 nm is assumed to come from CDOM, which in that model covaries with the chlorophyll concentration. The remaining difference in the Morel and sum-of-microbes curves is easily accounted for by detritus, which is implicitly contained in the Morel model, and by additional microbial components not included in our sum. It is, in fact, remarkable that two-thirds of the absorption can be accounted for by including only four absorbing components (one of which, BAC, is weakly absorbing) in the microbe sum. We comment in passing that the difference between the sum-of-microbes and Morel absorptions is greater at lower chlorophyll concentrations (that is, at lower microbial concentrations). This is consistent with the general rule that detritus contributes proportionately more to the total absorption in oligotrophic waters than in productive waters.

We emphasize that our discussion of Fig. 1 is valid only for the particular microbe types and concentrations used in



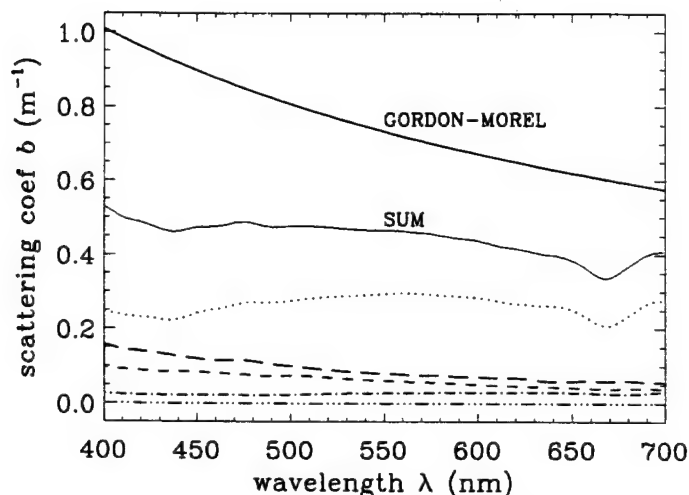


Fig. 2. As for Fig. 1, except that the curves now give the scattering coefficients. The top curve is the total scattering coefficient predicted by the Gordon-Morel model of Eq. 5 with  $Chl = 4.2 \text{ mg m}^{-3}$ .

evaluating Eq. 1. In particular, this example does not imply that small diatoms always dominate absorption in coastal waters. Indeed, had our database contained 4- $\mu\text{m}$  chlorophytes and 8- $\mu\text{m}$  diatoms, we might have found that the chlorophytes dominated the absorption. The relevant point is that a knowledge of single-particle optical properties allows us to understand precisely how different types of particles with different optical properties and concentrations each contributes to the total absorption. In this example, we saw how moderately sized particles with moderate absorption cross sections had a greater influence than did more numerous smaller particles or more absorbing larger particles. Later examples will show how this detailed understanding of the absorption (and scattering) properties of a water body, when combined with radiative transfer modeling, can yield a correspondingly detailed understanding of the light field of a water body. This caveat about the generality of the conclusions also applies to each of those examples.

Figure 2 shows the individual and total microbial scattering coefficients for the high coastal concentrations. Once again, for these concentrations, small nanophytoplankton (DIA in our database) are the major microbial contributor to the scattering coefficient, although now the heterotrophic bacteria are the second most important. The larger nanophytoplankton (CHLO), which are the most efficient scatterers on a per-cell basis (see fig. 6A of SM), now contribute very little to the total scattering because of their relatively small numbers. The top curve in Fig. 2 shows the scattering coefficient predicted by the bio-optical model of Gordon and Morel (1983):

$$b(\lambda) = \left(\frac{550}{\lambda}\right)^{0.30} Chl^{0.62}. \quad (5)$$

The difference between the sum-of-microbes and the Gordon-Morel values is accounted for by the fact that Eq. 5 was derived from oceanic water samples containing detritus and other microorganisms not included in our five-component

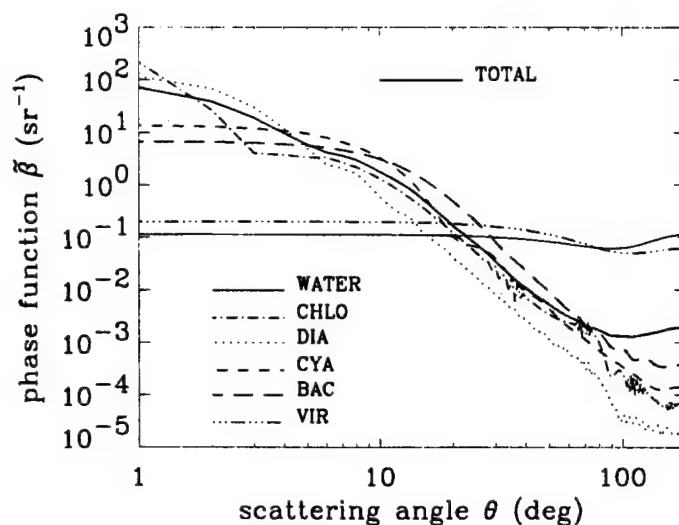


Fig. 3. Phase functions at 400 nm for microbes and water. The heavy solid line is the total phase function computed by Eq. 3 when each microbe is present at the high coastal concentration. The light solid line is the phase function for pure water; the patterned lines are for individual microbes.

sum. Although the scattering properties of detritus have not been rigorously studied, polydisperse detrital particles are likely to be efficient scatterers, thus contributing significantly to the total scattering (Stramski and Kiefer 1991).

Figure 3 shows the microbe phase functions at 400 nm. The virus phase function is similar to that of pure water, although forward scattering is noticeably stronger than back-scattering for VIR. As the particle size increases, the phase functions typically become more strongly scattering at small scattering angles and less scattering at large angles. The total phase function shown in the figure was computed from Eq. 3 for the high coastal concentrations. This total microbe phase function is replotted in Fig. 4, where it is compared with the average particle phase function derived from Pet-

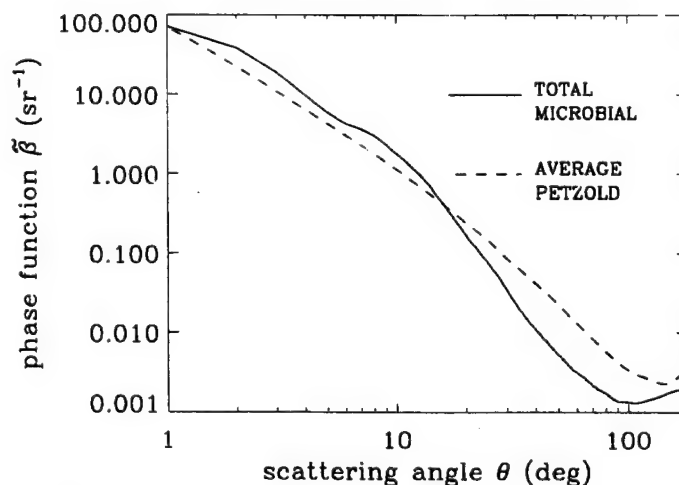


Fig. 4. Comparison of the total phase function of Fig. 3 with the average particle phase function derived from Petzold's measurements.

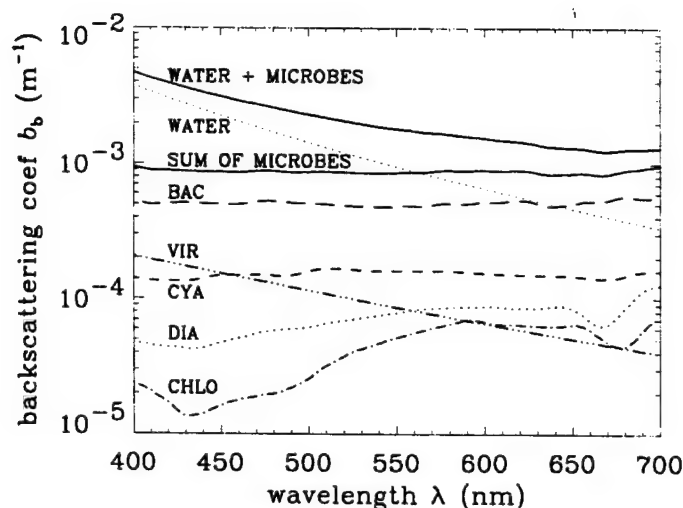


Fig. 5. Backscattering coefficients for microbes when present at high coastal concentrations. The top three curves show the total microbial contribution to the backscatter, the contribution by water, and the total (water plus microbes) backscatter coefficient. The remaining lines are for individual microbes, as labeled.

zold's (1972) measurements, as mentioned previously. The average Petzold phase function of Fig. 4 is based on measurements of several ocean waters, which likely included mineral as well as detrital and microbial particles. This average phase function is the one used for  $\beta_{\text{DET}}(\theta)$ , as previously mentioned.

Figure 5 shows the backscattering coefficient  $b_b(\lambda)$ . This information is implicitly contained in  $b(\lambda)$  and  $\beta(\theta, \lambda)$ , but it is worth consideration because of its importance for the interpretation of remotely sensed ocean color data. We see that even for the relatively high microbe concentrations considered here, the water itself is the dominant backscatterer at the blue end of the spectrum. The heterotrophic bacteria are the single most important microbe in the determination of the backscatter coefficient; they were much less important in the determination of the total scattering coefficient (Fig. 2). The nanophytoplankton (DIA and CHLO) are rather unimportant in the determination of  $b_b(\lambda)$ , although DIA dominated the total scattering  $b(\lambda)$ . The origins of these results are seen in the backscattering ratios of fig. 10A of SM. The smaller particles contribute relatively more of their scattering to backward directions, and the spread in the backscattering cross sections is not as great as for the total scattering cross sections (figs. 11A and 6A of SM), so that the relative contributions of the various microbe types can be different for  $b$  and for  $b_b$ . Viruses, which have by far the highest backscattering ratio, do contribute somewhat to backscattering at blue wavelengths, but even there the contribution by VIR is small compared to that of BAC and water, because of the very small backscattering cross section of VIR.

Remember that the curves seen in Figs. 1–5 hold only for the particular microbe concentrations used in their construction. At other concentrations, the curves will be different. In a given natural water body, with its particular concentrations for the various kinds of microbes, both the magnitudes and the relative contributions of the different microbial types can

be different from that seen above. These figures are intended only to show the reasonableness of our IOP models. In particular, we have seen that we can obtain reasonable values for the total absorption and scattering properties even if only a few broad classes of microbes (rather than innumerable individual species) are considered.

The total absorption and scattering coefficients and the total scattering phase function give us all of the information about the water body that is needed to solve the radiative transfer equation. We next discuss a numerical model for effecting this solution.

### The Hydrolight radiative transfer model

Hydrolight is a radiative transfer numerical model that computes spectral radiance distributions within and leaving natural water bodies. In brief, the model solves the time-independent, depth-dependent radiative transfer equation (RTE) by using accurate and computationally efficient techniques based on invariant imbedding theory. Input to the model consists of information about the absorbing and scattering properties of the water body, about the sky radiance incident onto the water surface, about the wave state of the wind-blown sea surface, and about the bottom of the water column. The water-inherent optical properties can vary arbitrarily with wavelength and depth; that is, Hydrolight is not a layered model, in which depth profiles of IOPs are approximated by a number of homogeneous layers. The model includes internal sources such as bioluminescence (not used in this study), as well as inelastic-scattering effects owing to Raman scattering by the water itself and to fluorescence by chlorophyll and by dissolved organic matter. Standard output from the model includes the spectral radiance as a function of depth, direction, and wavelength within the water body, as well as the water-leaving radiance in all upward directions. Derived quantities such as irradiances, reflectances, and diffuse attenuation functions are computed from their definitions by using the radiance distribution obtained from the solution of the RTE.

To compute the spectral radiance, Hydrolight solves the integro-differential radiative transfer equation subject to boundary conditions at the sea surface and at the bottom of the water column of interest. Because of their mathematical complexity, these equations must be solved numerically for any realistic situation. To solve the RTE, Hydrolight requires the following specific information:

*Inherent optical properties of the water body*—The IOPs must be specified as functions of depth and wavelength. In this study, the IOPs are provided via the absorption and scattering coefficients and the scattering phase function, but any equivalent set of information (such as the beam attenuation coefficient, the albedo of single scattering, and the phase function) can be used. We have seen in the previous section how the IOPs are determined for the present simulations (although actual measured values can be used as input to the model, if such data are available).

*State of the wind-blown sea surface*—Hydrolight models the sea surface using the Cox-Munk capillary wave slope

statistics, which adequately describe the optical reflection and transmission properties of the sea surface for moderate wind speeds and for solar angles and lines of sight away from the horizon. In this case, only the wind speed needs to be specified.

**Sky spectral radiance distribution**—The sky radiance can have any wavelength or directional dependence (describing the background sky, clouds, and the sun). In the present simulations, the sky radiance distribution incident onto the sea surface is obtained from semi-empirical models that are built into Hydrolight. These sky models are based on the work of Gregg and Carder (1990) and Harrison and Coombes (1988).

**Nature of the bottom boundary**—In the present simulations we consider only infinitely deep water, in which case only the IOPs of the water column need to be given. Hydrolight then uses the IOPs to compute the needed bi-directional radiance reflectance of the water body below the maximum depth at which the radiance is to be computed. For opaque bottoms at finite depths, the required bottom reflectance can be given in terms of the irradiance reflectance of the bottom.

Hydrolight uses mathematically sophisticated invariant imbedding techniques to solve the RTE. The details of this solution method are given in Mobley (1994). For many applications, invariant imbedding is computationally extremely fast compared to other solution methods. Computation time is almost independent of the depth variability of the IOPs, and computation time depends only linearly on the depth to which the radiance is desired. All quantities are computed with equal accuracy, and there is no statistical noise in the results. Hydrolight has been compared with Monte Carlo and discrete ordinates models by Mobley et al. (1993).

### Example simulations

The combination of Hydrolight and our database of microbial optical properties gives us a powerful tool for the detailed study of the effects of microbial particles on oceanic optical properties. We next present several simulations, which are primarily intended to illustrate the power of our modeling and analysis methodology. Additionally, we obtain some interesting insights into how microbial particles influence oceanic light fields. In so doing, we also learn something about one of the origins of the natural variability in chlorophyll concentrations as retrieved from remote-sensing reflectance measurements.

For simplicity, a common set of environmental conditions was imposed for all of the simulations discussed below. In particular, the sky was modeled as being cloudless. Various atmospheric parameters (such as relative humidity, aerosol type, and ozone concentration) used by the semi-empirical sky radiance model were set to values typical of the North Atlantic in summer. The sun was placed at a zenith angle of  $30^\circ$ . The wind speed was  $5 \text{ m s}^{-1}$ . The water was taken to be homogeneous and infinitely deep. Thus, the concentrations seen in Eq. 1 and 2 were independent of depth, as were the values of the absorption and scattering coefficients for DET and CDOM. Constant-depth IOPs are unrepresentative

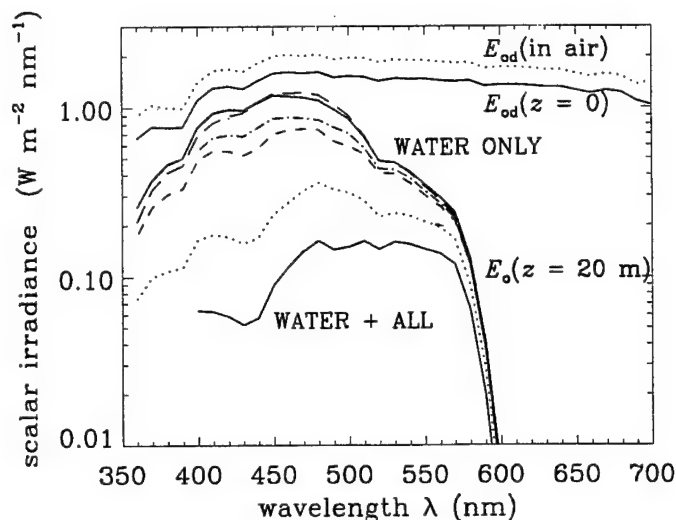


Fig. 6. Scalar irradiances for simulations of pure water, water plus a single microbial type at its high coastal concentration, and water plus all microbes together at their high coastal concentrations. Unlabeled lines are water plus a single microbial type, coded as in Fig. 1.

of most natural waters, but we used depth-independent IOPs for the present simulations in order to highlight the effects of different microbial types on the light fields. Depth-dependent effects must of course be included in any exhaustive study.

**Scalar irradiance**—Our first example illustrates how our approach can isolate the effects of different microbial types on the scalar irradiance  $E_o(z, \lambda)$ . We performed a series of simulations for which the IOPs were built up first from water alone, then from water plus a single microbial component at its high coastal concentration, and finally from water plus all microbial components together at their high coastal concentrations. Fig. 6 shows selected results from these simulations. The upper dotted line gives the downwelling scalar irradiance owing to the sky radiance incident onto the sea surface; this curve is computed solely from the sky radiance distribution. The upper solid curve gives the downwelling scalar irradiance just beneath the sea surface, when the water body consists only of pure water. This curve represents both the downwelling sky light that is transmitted through the sea surface and that part of the upwelling light just below the surface that is reflected downward by the surface. This curve therefore can be obtained only after the RTE is solved. Upwelling scalar irradiances just below the surface are  $<10\%$  of the downwelling scalar irradiances at blue wavelengths and are much less at red wavelengths. The fraction of the upwelling scalar irradiance that is reflected downward by the surface is smaller still. Thus, these two curves give a good idea of how much incident scalar irradiance is lost in passing through the wind-blown air–water surface.

The remaining curves in Fig. 6 are of more interest; they show the total scalar irradiance at a depth of  $z = 20 \text{ m}$ . The two  $E_o(20, \lambda)$  curves for water alone and for water plus VIR are indistinguishable in the figure. This shows that viruses, even at the high concentration of  $10^{14}$  particles per cubic

Table 2. Quantities used in the discussion of Fig. 6. All quantities have appropriate units: inverse meters for  $a$  and  $b$ ,  $\text{W m}^{-2} \text{nm}^{-1}$  for irradiances, etc. Irradiances and radiances are the values at  $z = 20 \text{ m}$ .

	Quantity	Pure Water	Pure water + BAC	Change
410 nm	$a$	0.0162	0.0238	+47%
	$b$	0.0068	0.1527	$\times 21$
	$\omega_0$	0.2957	0.8652	$\times 2.9$
	$E_d$	0.6939	0.5346	-23%
	$E_u$	0.0440	0.0363	-18%
	$L_p$	0.0190	0.0230	+21%
	$E_0$	0.9301	0.8161	-12%
	$R_{rs}$	0.0102	0.0083	-19%
	$R_{tr}$	0.0050	0.0059	+18%
480 nm	$a$	0.0176	0.0199	+13%
	$b$	0.0034	0.1166	$\times 34$
	$\omega_0$	0.1619	0.8539	$\times 5.3$
	$E_d$	0.9119	0.8085	-11%
	$E_u$	0.0285	0.0442	+151%
	$L_p$	0.0120	0.0301	$\times 2.5$
	$E_0$	1.1097	1.1931	+8%
	$R_{rs}$	0.0050	0.0059	+18%
	$R_{tr}$	0.0050	0.0059	+18%

meter, have no significant effect on the scalar irradiance even in this idealized situation. Their relative effect in a real ocean containing many other types of particles would be even less. The curves for water plus CHLO, water plus CYA, and water plus DIA show progressively smaller irradiances. The diatoms clearly have the greatest effect on  $E_0(20, \lambda)$  of any single microbial type. The bottom curve shows  $E_0(20, \lambda)$  as computed for water plus all microbes together at the high coastal concentrations. (This curve begins at 400 nm because CHLO data are available only for wavelengths between 400 and 700 nm.) This curve does not include any effects due to DET or CDOM. The sharp dropoff of the irradiances at wavelengths  $> 570 \text{ nm}$  is due to the high absorption by water at those wavelengths.

A slight exception to the general trends just discussed is seen in the curve for water plus BAC. We see that at wavelengths between 450 and 510 nm,  $E_0(20, \lambda)$  is actually slightly greater for water plus BAC than it is for water alone. This may seem counterintuitive on the grounds that heterotrophic bacteria are absorbing particles (albeit weakly absorbing), and thus their presence should decrease the amount of light reaching any depth. How, then, could the presence of these particles increase  $E_0(20, \lambda)$ ? The resolution of this paradox is obtained from a close examination of the digital output from these two simulations.

Table 2 shows several quantities needed to understand the effects of BAC on the underwater light field. Data are presented for two wavelengths: 410 nm, where the presence of BAC decreases  $E_0(20, \lambda)$  by 12%, and 480 nm, where the presence of BAC increases  $E_0(20, \lambda)$  by 8%. Comparing corresponding quantities for these two wavelengths, we see that the absorption coefficient  $a$  increases at both wavelengths when BAC are added to the water, as expected, but that the percentage increase over the pure water  $a$  value is much less at 480 nm (13%) than at 410 nm (47%). On the other hand, adding BAC to the water increases the scattering coefficient

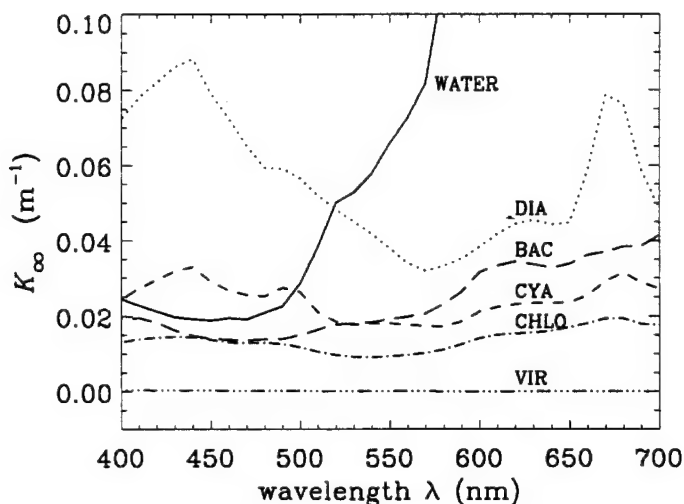


Fig. 7. Component asymptotic diffuse attenuation functions for pure water and for each of the five microbial types, when each microbe is present at its high coastal concentration.

$b$  by a factor of 34 at 480 nm, but only by a factor of 21 at 410 nm. The albedos of single scattering,  $\omega_0$ , are thus almost equal at the two wavelengths for the water-plus-BAC system, which is highly scattering. However, pure water is much more of an absorbing medium at 480 nm than it is at 410 nm. One consequence of this transition from a predominately absorbing to a predominately scattering medium is seen in the downwelling and upwelling plane irradiances. At 410 nm both  $E_d$  and  $E_u$  decrease, but at 480 nm  $E_d$  decreases and  $E_u$  increases. Another consequence is that the horizontal radiance perpendicular to the plane of the sun's incident rays, denoted by  $L_p$  in the table, increases by only 21% at 410 nm but by a factor of 2.5 at 480 nm.

We can now deduce what is causing the increase in  $E_0$  at 480 nm. At 480 nm the huge increase in scattering due to the BAC is redirecting much of the downwelling radiance into roughly horizontal or upward directions. (Recall from Figs. 3 and 5 that BAC are efficient scatterers at large scattering angles.) This horizontal and upwelling radiance causes the increases in  $E_u$  and  $E_0$  (recall that radiance of a given magnitude in any direction contributes equally to  $E_0$ , whereas  $E_u$  has a cosine weighting factor that prevents nearly horizontal radiances from contributing greatly to  $E_0$ ). This redirection of the radiance by scattering is so strong that it outweighs the losses due to absorption in the computation of  $E_u$  and  $E_0$ . However, at 410 nm the redirection by scattering is less pronounced, so that the absorption effects dominate and both  $E_u$  and  $E_0$  decrease with the addition of BAC. We note another consequence of the relative changes in absorption and scattering at these two wavelengths: the remote-sensing reflectance,  $R_{rs}$ , decreases at 410 nm and increases at 480 nm.

Such a detailed discussion of these effects is admittedly of only academic interest, because a body of pure water or pure water plus heterotrophic bacteria never occurs in nature. However, we want to show that our database and modeling methodology allow us to dissect and thoroughly understand any feature of the light field that attracts our attention. In



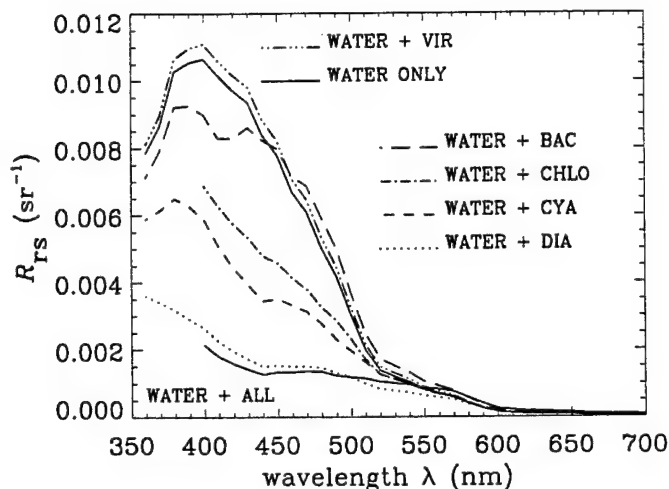


Fig. 8. Remote sensing reflectances corresponding to the simulations of Fig. 6.

particular, understanding the effects of microbial particles on oceanic light fields requires the ability to understand the complex effects of absorption and scattering on radiative transfer within the water body. This ability will prove valuable in studies of more realistic situations.

**Diffuse attenuation**—Another example can be derived from the simulations just discussed. Hydrolight derives various diffuse attenuation functions ( $K_d$ ,  $K_u$ , and so on) as functions of depth and wavelength by integration of the computed radiance distribution. The asymptotic diffuse attenuation function  $K_x(\lambda)$  is also computed directly from the inherent optical properties. To avoid the complications of surface boundary effects, we discuss here only the asymptotic  $K$  function. By using the simulations of pure water alone and pure water plus a single microbial component, which have already been discussed in connection with Fig. 6, we define the component asymptotic diffuse attenuation function for the  $i$ th microbial component by

$$K_x(i) = K_x(\text{water} + \text{component } i) - K_x(\text{water alone}).$$

This equation is applied at each wavelength. Fig. 7 shows the  $K_x(i)$  obtained when the microbial components are present at their respective high coastal concentrations.

The  $K_x(i)$  curves of Fig. 7 can be understood if we recall that the asymptotic  $K$  function is related to the absorption coefficient  $a$  and the asymptotic average cosine of the radiance distribution,  $\bar{\mu}_\infty$ , by  $K_\infty = a/\bar{\mu}_\infty$ . To the extent that  $K_x$  is an absorption-like parameter (as is often stated), the curves for  $K_x(i)$  should correlate with those for  $a(i)$  seen in Fig. 1. Although these correlations are apparent, they are by no means perfect. Note, for example, that the  $K_x(\text{BAC})$  curve increases noticeably with wavelength, whereas the BAC absorption curve seen in Fig. 1 decreases with wavelength. This difference in behaviors is due to the  $\bar{\mu}_\infty$  factor, which is largely determined by scattering (Berwald et al. 1995). In essence, high scattering in combination with a significant probability of scattering at large scattering angles effectively redirects the radiance distribution (from its initial

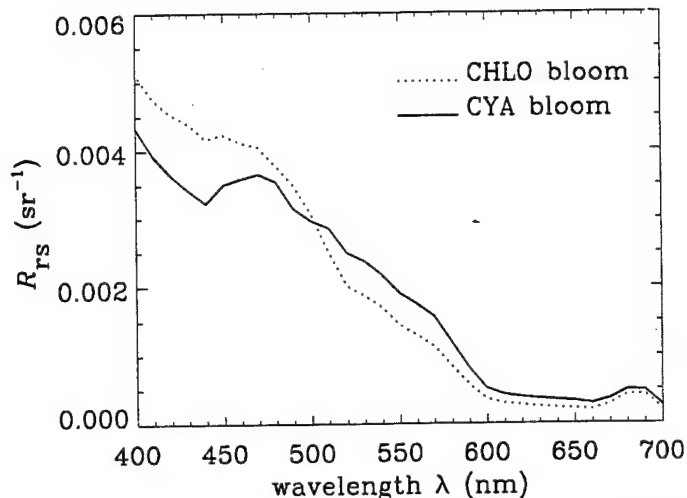


Fig. 9. Remote sensing reflectances corresponding to idealized cyanobacteria (CYA) and nanophytoplankton (CHLO) blooms. In both cases the chlorophyll concentration is  $\text{Chl} = 1 \text{ mg m}^{-3}$ .

downward direction) and thereby reduces the average cosine. A sufficient decrease in  $\bar{\mu}_\infty$  can cause an increase in  $K_\infty$ , even though  $a$  is also decreasing. This is precisely the situation here. The BAC are very highly scattering relative to their absorption, especially at red wavelengths (recall fig. 7 from SM), and their phase functions are very broad (Fig. 3, or fig. 9A from SM). Thus, we again see how the combination of our database and radiative transfer modeling allow us to obtain a detailed understanding of the effect of a particular microbial component on the underwater light field.

**Remote-sensing reflectance**—Figure 8 shows  $R_{rs}$  for the same series of simulations discussed in Fig. 6. We now see that adding viruses to pure water increases  $R_{rs}$  slightly at all wavelengths. This makes sense because we are modeling VIR as being nonabsorbing but scattering particles. The strong backscattering ratio for VIR (see fig. 10A of SM) means that viral particles are likely to scatter downwelling radiance into upward directions (as does the water itself), and  $R_{rs}$  consequently increases. (Recall that, to a first approximation,  $R_{rs}$  is proportional to  $b_b/a$ .) The increase in  $R_{rs}$  is small because the magnitude of scattering by VIR is small, even at high concentrations. We have already commented on the effects of BAC on  $R_{rs}$  at 410 and 480 nm; the full curve is seen here. The curve for water plus DIA is very close to the curve for water plus all microbes together. Thus, phytoplankton cells of roughly  $4 \mu\text{m}$  in size have by far the dominant influence on the remote-sensing reflectance at these concentrations.

The above examples have all been based on one set of microbial concentrations, namely the high coastal concentrations shown in Table 1. Our modeling and analysis methodology is equally applicable for any set of concentrations. Of course, the particular conclusions drawn from a simulation will vary with concentrations and external environmental conditions, just as do light fields in natural water bodies. In the following examples, we vary the microbial concentrations and also include DET and CDOM in the simulations.

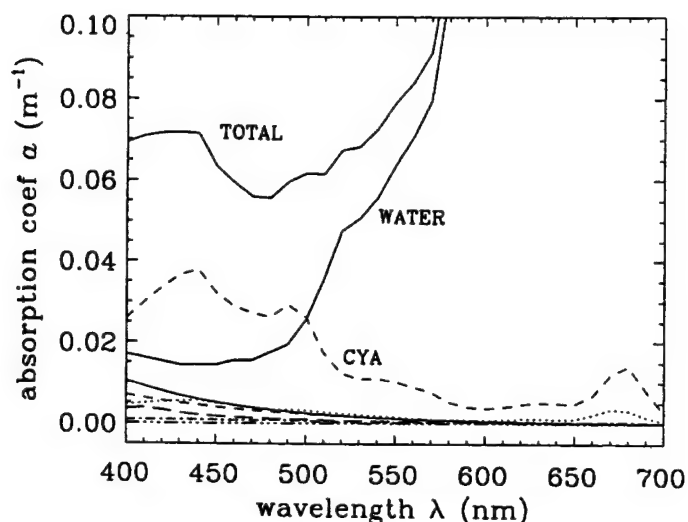


Fig. 10. Component and total absorption coefficients corresponding to the cyanobacteria bloom of Fig. 9.

One of the important uses of the remote-sensing reflectance (in essence, a normalized water-leaving radiance) is the retrieval of chlorophyll concentrations from remotely sensed spectral radiances via semi-empirical algorithms (Gordon and Morel 1983; Gordon et al. 1988). However, it is well known that there is considerable variability in the retrieved values of chlorophyll when compared to sea truth measurements, even when the algorithms are applied to case 1 waters for which they were developed. We think that this natural, seemingly random variability can be understood through a detailed examination of the optical effects of the different components of the water body.

We next present two simulations that illustrate how variability in the microbial composition of a water body can give different remote-sensing reflectances, even though the water bodies have the same chlorophyll concentrations. To do this, we used moderate concentrations of all microbial types except for one, which was given a high concentration corresponding to a bloom. These simulations also included DET and CDOM, as well as fluorescence by chlorophyll and CDOM. In particular, the concentrations of VIR, BAC, CYA, DIA, and CHLO were given base values of  $10^{13}$ ,  $10^{12}$ ,  $10^{10}$ ,  $7.4 \times 10^8$ , and  $3 \times 10^7$  particles per cubic meter, respectively. To simulate a cyanobacteria bloom, we increased the CYA concentration from  $10^{10}$  to  $1.56 \times 10^{11}$ ; all other concentrations were kept at their base values. The resulting chlorophyll concentration was then  $1.0 \text{ mg m}^{-3}$ , as can be seen from Table 1. To simulate a chlorophyte bloom, we increased the concentration of CHLO from  $3 \times 10^7$  to  $4.25 \times 10^8$ ; all other concentrations were kept at their base values. The resulting chlorophyll concentration was still  $1.0 \text{ mg m}^{-3}$ . In both simulations, the absorption by DET at 400 nm,  $a_{\text{DET}}(400)$  as seen in Eq. 1, was set to 20% of the absorption by the microbes at 400 nm, and  $b_{\text{DET}}(400)$  was set to 30% of the scattering by microbes at 400 nm. Finally,  $a_{\text{CDOM}}(400)$  was set to 40% of the absorption by microbes at 400 nm. These particular percentage contributions by DET and CDOM were arbitrarily chosen so that DET and CDOM would be signif-

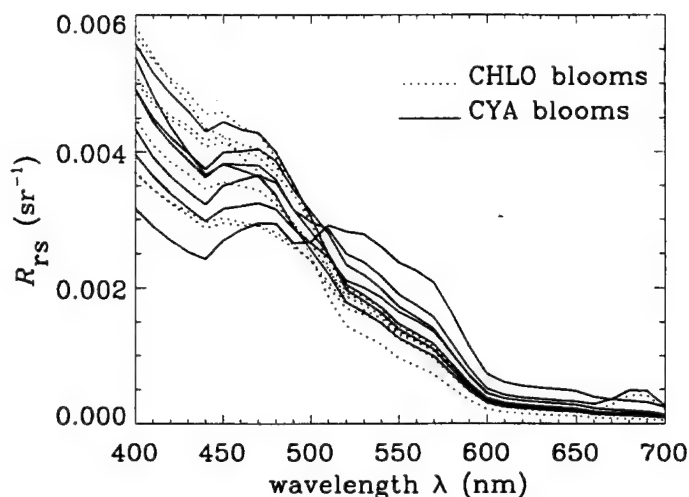


Fig. 11. Remote sensing reflectances corresponding to cyanobacteria (CYA) and chlorophyte (CHLO) blooms for which the non-bloom components vary over a range of values. The chlorophyll concentrations range from  $0.5$  to  $1.7 \text{ mg m}^{-3}$ .

icantly present in the hypothetical water bodies being simulated; the exact values chosen for these quantities are unimportant in these examples.

Figure 9 shows  $R_{rs}$  for the two simulations just defined. The two  $R_{rs}$  curves are clearly different, although they should be the same if regarded from the viewpoint of bio-optical models that attempt to parameterize such quantities in terms of the chlorophyll concentration alone. Chlorophyll retrieval algorithms usually use a ratio of water-leaving radiances at two wavelengths to obtain a chlorophyll value from a statistically derived relationship between the ratio and the chlorophyll concentration. For example, an algorithm commonly used with Coastal Zone Color Scanner (CZCS) data uses the ratio of the water-leaving radiances in bands centered at 443 and 550 nm. The ratio of  $R_{rs}(440)/R_{rs}(550)$  for the simulations of Fig. 9 is 1.7 for the CYA bloom and 2.9 for the CHLO bloom. These different ratios, if used in a CZCS-type algorithm, would yield different chlorophyll concentrations. We thus see in this simple example how variability in the microbial composition of a water body can give rise to variability in chlorophyll concentrations derived from remotely sensed signals.

Also note that in these simulations,  $R_{rs}$  for the CHLO bloom generally decreases with increasing wavelength, whereas  $R_{rs}$  for the CYA bloom reaches a minimum at 440 nm and then rises to a relative maximum at 470 nm, after which it decreases again. (The bumps in the two curves near 680 nm arise from chlorophyll fluorescence.) The origin of the local maximum at 470 nm in the CYA curve can be immediately understood when the contributions of all of the components to the absorption are considered. Fig. 10 shows the contributions of water, CYA, the other microbes, DET, and CDOM to the total absorption coefficient. We see that the total absorption is determined primarily by CYA and by the water itself. To a first approximation,  $R_{rs}$  is inversely proportional to the absorption coefficient. Thus, the bump in  $R_{rs}$  is now seen to be due to the dip in the total absorption

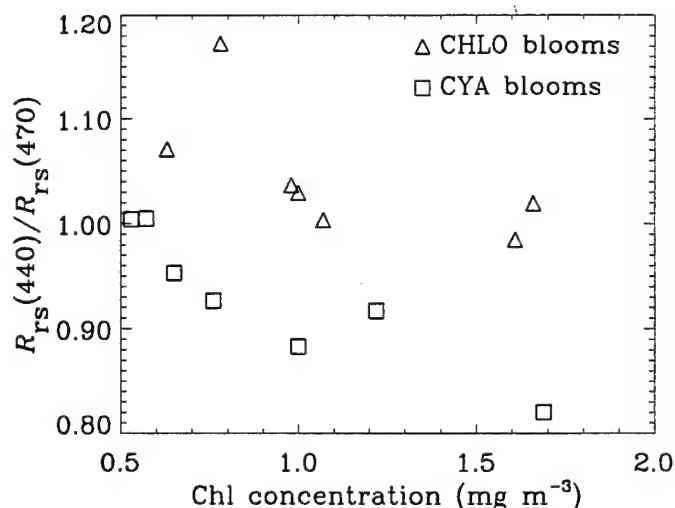


Fig. 12. Remote sensing reflectance ratios computed for 440 and 470 nm, as a function of chlorophyll concentration, for the simulations of Fig. 11.

coefficient, which arises from the high CYA absorption near 440 nm and the increase in water absorption beyond 500 nm.

The presence of the bump in the CYA-bloom  $R_{rs}$  curve near 470 nm and the absence of such a bump in the CHLO-bloom curve suggests that it might be possible to distinguish between CYA and CHLO blooms from  $R_{rs}$  signals (if the cyanobacteria are rich in phycocourolin pigment). Thus, we consider the ratio  $R_{rs}(440)/R_{rs}(470)$  as a potential means of distinguishing these two situations. Fig. 9 indicates that this ratio might be less than one for CYA bloom and greater than one for CHLO blooms. To test this simple hypothesis, we performed a sequence of simulations in which either the CYA or CHLO concentrations were held at the bloom values given above, while the concentrations of the nonbloom microbial components and of DET and CDOM were varied over a broad range of values. (The DET and CDOM  $a$  and  $b$  coefficients at 440 nm were varied over the ranges shown in Table 1.) The corresponding chlorophyll concentrations ranged from 0.5 to 1.7  $\text{mg m}^{-3}$ . Fig. 11 shows the  $R_{rs}$  curves generated in these simulations. The curves represent more realistic conditions with various degrees of noise than do the idealized blooms shown in Fig. 9.

Figure 12 shows the  $R_{rs}(440)/R_{rs}(470)$  values as a function of the chlorophyll concentration. As anticipated, the two groups of points for CYA blooms and CHLO blooms separate reasonably well in such a plot, even though the non-bloom components vary considerably in their contributions to the IOPs. Moreover, we note that for a given value of chlorophyll, there is no unique value of the  $R_{rs}(440)/R_{rs}(470)$  ratio. Once again we see how water composition can lead to difficulties in the retrieval of chlorophyll from a simple ratio algorithm.

The examples discussed above were based on idealized situations chosen to highlight the capabilities of our approach to separate and understand the effects of different types of microbial particles on various measures of oceanic light fields. Studies leading, for example, to improved algorithms for the interpretation of ocean color signals must

be based on much more realistic simulations. In particular, depth dependence of component concentrations must be included, and a wide range of external conditions such as solar angle and sensor viewing direction must be considered. Intraspecies variability in the optical properties of microorganisms (such as the diel variability illustrated in fig. 12 of SM) must be included in simulations, because such variability is an additional source of noise in the interpretation of field data. All of these effects can be studied with the existing database and Hydrolight model.

However, to make our simulations more realistic, we must expand the database of single-particle optical properties. As pointed out by Stramski and Mobley (1997), additional microbial categories need to be included in order to adequately represent all optically significant microbial types. Mineral particles characteristic of terrestrial runoff and resuspended sediments must be added to the database, especially if we are to address the optics of case 2 waters. Such additions to the database are under way.

## References

- BERWALD, J., D. STRAMSKI, C. D. MOBLEY, AND D. KIEFER. 1995. Influences of absorption and scattering on vertical changes in the average cosine of the underwater light field. *Limnol. Oceanogr.* **40**: 1347–1357.
- BRICAUD, A., A. MOREL, AND L. PRIEUR. 1981. Absorption by dissolved organic matter of the sea (yellow substance) in the UV and visible domains. *Limnol. Oceanogr.* **26**: 43–53.
- CHO, B. C., AND F. AZAM. 1990. Biogeochemical significance of bacterial biomass in the ocean's euphotic zone. *Mar. Ecol. Prog. Ser.* **63**: 253–259.
- DAVIS, P. G., D. A. CARON, P. W. JOHNSON, AND J. M. SIEBURTH. 1985. Phototrophic and apochlorotic components of picoplankton and nanoplankton in the North Atlantic: Geographic, vertical, seasonal and diel distributions. *Mar. Ecol. Prog. Ser.* **21**: 15–26.
- GORDON, H. R., AND OTHERS. 1988. A semianalytic model of ocean color. *J. Geophys. Res.* **93**: 10,909–10,924.
- , AND A. MOREL. 1983. Remote assessment of ocean color for interpretation of satellite visible imagery—a review. Lecture notes on coastal and estuarine studies. Springer.
- GREGG, W. W., AND K. L. CARDER. 1990. A simple spectral solar irradiance model for cloudless maritime atmospheres. *Limnol. Oceanogr.* **35**: 1657–1675.
- HARRISON, A. W., AND C. A. COOMES. 1988. An opaque cloud cover model of sky short wavelength radiance. *Solar Energy* **41**: 387–392.
- LI, W. K. W. 1995. Composition of ultraphytoplankton in the central North Atlantic. *Mar. Ecol. Prog. Ser.* **122**: 1–8.
- , P. M. DICKIE, B. D. IRWIN, AND A. M. WOOD. 1992. Biomass of bacteria, cyanobacteria, prochlorophytes and photosynthetic eukaryotes in the Sargasso Sea. *Deep-Sea Res.* **39**: 501–519.
- MARANGER, R., AND D. F. BIRD. 1995. Viral abundance in aquatic systems: A comparison between marine and fresh waters. *Mar. Ecol. Prog. Ser.* **121**: 217–226.
- MOBLEY, C. D. 1994. Light and water: Radiative transfer in natural waters. Academic.
- , AND OTHERS. 1993. Comparison of numerical models for computing underwater light fields. *Appl. Opt.* **32**: 7484–7504.
- MOREL, A. 1991. Light and marine photosynthesis: A spectral model with geochemical and climatological implications. *Prog. Oceanogr.* **26**: 263–306.
- PETZOLD, T. J. 1972. Volume scattering functions for selected ocean waters. *Scripps Inst. Oceanogr. Ref.* 72–78.

- PROCTOR, L. M., AND J. A. FUHRMAN. 1990. Viral mortality of marine bacteria and cyanobacteria. *Nature* **343**: 60–62.
- ROESLER, C. S., M. J. PERRY, AND K. L. CARDER. 1989. Modeling in situ phytoplankton absorption from total absorption spectra in productive inland marine waters. *Limnol. Oceanogr.* **34**: 1510–1523.
- SMITH, R. C., AND K. BAKER. 1981. Optical properties of the clearest natural waters. *Appl. Opt.* **20**: 177–184.
- STRAMSKI, D., AND D. KIEFER. 1991. Light scattering by microorganisms in the open ocean. *Prog. Oceanogr.* **28**: 343–383.
- , AND C. D. MOBLEY. 1997. Effects of microbial particles on oceanic optics: A database of single-particle optical properties. *Limnol. Oceanogr.* **42**: 538–549.
- TAKAHASHI, M., AND P. K. BIENFANG. 1983. Size structure of phytoplankton biomass and photosynthesis in subtropical Hawaiian waters. *Mar. Biol.* **76**: 203–211.

*Submitted: 23 February 1996*

*Accepted: 20 August 1996*

*Amended: 29 January 1997*



## APPENDIX C

Reprint of

*A database of single-particle optical properties*

by

Dariusz Stramski,  
Annick Bricaud, and  
Andre Morel

Paper presented at

*Ocean Optics XIV*  
Kona, Hawaii  
November, 1998

(Journal Article in Preparation)

# **A DATABASE OF SINGLE-PARTICLE OPTICAL PROPERTIES**

Dariusz Stramski  
Marine Physical Laboratory  
Scripps Institution of Oceanography  
La Jolla, CA 92093-0238, U.S.A.

Annick Bricaud and Andre Morel  
Laboratoire de Physique et Chimie Marines, CNRS and  
Universite Pierre et Marie Curie  
BP 8, 06238 Villefranche-sur-Mer, France.

Paper presented at *Ocean Optics XIV*  
Kona, HI, November 1998

## ABSTRACT

We describe a database of the single-particle optical properties for various types of planktonic microorganisms. The current database includes 18 microbial components covering a size range from submicrometer viruses and heterotrophic bacteria to microplanktonic species of about 30  $\mu\text{m}$  in cell diameter. Each component of the database is characterized in terms of the spectral scattering phase functions and single-particle cross sections for absorption, scattering, attenuation and backscattering. These optical properties are determined at 1-nm intervals between 350 and 750 nm. Chlorophyll content per cell for each phytoplankton species in the database is also determined. In addition to microorganisms, the current database includes biogenic detritus (non-living particles with low refractive index), mineral particles (non-living particles with high refractive index), and gas bubbles. The development of our database promises a powerful means to study the effects of various individual components on the optics of natural water bodies as a function of varying composition of water.

## INTRODUCTION

Relationships between the optical properties and seawater components typically involve a parameterization of seawater composition in terms of chlorophyll concentration alone<sup>1</sup>. This overly simplified parameterization does not account for much of the optical variability observed in natural waters. As a result, any particular measured inherent optical property (IOP) or apparent optical property (AOP) can frequently differ by a factor of 2 – 5 or even more from the value predicted by a chlorophyll-based model. An improved understanding of aquatic optical environments can be gained if we progress beyond the chlorophyll parameterization and consider the effects of the detailed composition of water on the IOPs and AOPs. Among these effects, the detailed species composition of planktonic community is of particular importance. The most rigorous approach begins with determining the optical properties of the various optically significant components of water, including various planktonic microorganisms (both chlorophyll-containing species and species with no chlorophyll), non-living biogenic detritus, and mineral particles. We here describe the development of a database of the single-particle optical properties of the various types of marine particles, which is an extension of a preliminary version of the database presented in Stramski and Mobley<sup>2</sup>.

## CONCEPTUAL AND METHODOLOGICAL BACKGROUND

Our database is uniquely designed as a source of "comprehensive" information for scientific analysis, specifically for modeling and data interpretation in the areas of ocean optics and remote sensing of ocean color. "Comprehensive" refers to the wide range of optical properties provided by the database, its wide spectral coverage with hyperspectral resolution, and its wide coverage in terms of the various optically significant types of marine particles. The wide range of optical properties included in the database ensures its applicability to nearly all questions of modern ocean optics, perhaps with the sole exception of polarization properties of light. The database includes the spectral scattering phase functions and the spectral absorption, scattering, backscattering, and attenuation cross-sections for various types of marine particles. All these quantities are determined between 350 and 750 nm at 1-nm intervals. The data represent single-particle properties; that is, the properties are expressed on a per particle basis. This information allows one to calculate all fundamental bulk optical properties (the volume scattering function, the absorption, scattering, backscattering and beam attenuation coefficients) associated with any given numerical concentration of any given particle type in water. For chlorophyll-bearing planktonic species in the database, the amount of chlorophyll per particle is known. Thus, any analysis involving the database will include information that can be related to traditional bio-optical approaches based on chlorophyll parametrization of seawater composition. In addition, the database includes information about particle size and refractive index, two major physical characteristics that control the optical behavior of particles. This information is essential for understanding of the optical properties of a given type of particles, and the effects these particles may have on the bulk optical properties of a given water body.

The current database includes 18 planktonic (or microbial) components, each representing a particular class or species of planktonic microorganisms. This microbial database draws upon eight recent studies<sup>3-10</sup> that involved laboratory measurements of bacterial and phytoplankton cultures and theoretical modeling of particle optics. The general design of the experiments, conditions under which the cultures were grown, and sampling strategy differed among the studies. Details pertaining to the experiments can be found in those eight publications, and details pertaining to the determination of final quantities in the microbial database are described in Stramski and Mobley<sup>2</sup>. Viruses are the only component for which data are based on modeling alone (Mie scattering calculations for realistic approximations to the size distribution and refractive index)<sup>7</sup>.

The selection of studies for generating the microbial database was based on the following criterion; the suite of measurements performed on planktonic cultures must have included, as a minimum requirement, the spectral beam attenuation and absorption coefficients, particle size distribution, particle concentration and chlorophyll *a*

concentration (for chlorophyll-bearing species). The optical measurements in the selected studies were made from 350 nm or 400 nm to 750 nm at 1-nm or 2.5-nm intervals. Because all final optical quantities in the database are determined at 1-nm intervals from 350 to 750 nm, appropriate interpolation and/or extrapolation was applied to original optical data, if necessary. We note that although many publications exist that address some specific optical aspect of marine microorganisms (for example, absorption spectra in conjunction with studies of photosynthesis, or scattering properties at some selected wavelengths and angles measured with flow cytometers), only these eight selected studies<sup>3-10</sup> provide a comprehensive optical characterization of marine microorganisms that satisfy requirements for generating our database.

The selected studies employed a state-of-the-art approach for a comprehensive characterization of the optical properties of marine microorganisms. This approach involves the culturing of planktonic species under well-defined, controlled growth conditions, followed by as many relevant optical and ancillary measurements as practically possible at the present time. Most importantly, these measurements include the detailed spectra of the beam attenuation and absorption coefficients along with particle concentration and size distribution. As a result, the single-particle cross sections for absorption, scattering and beam attenuation in the database are subject to uncertainties associated solely with measurements (no assumptions or approximations based on the theory of particle optics are used for determining these optical cross sections). These uncertainties are quantifiable and generally very small. On the other hand, direct measurements of the volume scattering function (over the entire angular range from 0 to 180°) with hyperspectral resolution are presently impossible, and most likely will not be possible for many years to come. The scattering functions in our database are thus determined from calculations based on the theory of light scattering and absorption by particles (primarily Mie scattering calculations for homogeneous spheres). These calculations are driven by data from measurements, and consist of an inverse model for determining the spectral values of the complex refractive index of particles, followed by forward Mie calculations of the spectral scattering phase functions for the known refractive index and particle size distribution. We must accept a certain unknown degree of uncertainty in the estimated phase functions because of assumptions and approximations that are naturally associated with the use of Mie theory for calculating the optical behavior of actual planktonic cells. It is, however, important to emphasize that the eight selected studies<sup>3-10</sup> provide exceptionally rich experimental information about the investigated microorganisms, which maximizes reliability of such estimation of the scattering phase functions, and we believe that this is the most reasonable approach at the present time. Of course, had the hyperspectral measurements of the full scattering phase function been available, no such computational procedure would have been necessary and the phase function could have been determined directly from measurements just like the

optical cross sections for absorption and beam attenuation (and the total scattering which is simply the difference between beam attenuation and absorption).

The general approach for generating the microbial database involved measurements of the bulk optical properties of cell suspensions. Typically, thousands of cells were contained within the volume of the culture illuminated for the measurements of the beam attenuation and absorption coefficients. Consequently, an important feature of the microbial database is that the single-particle properties of any given species represent an "average" cell (or particle) derived from the investigated population of cells. This "average" single particle is characterized by the optical properties which, after multiplication by the number concentration of particles, reproduce exactly the bulk absorption and scattering properties of the actual population of particles. This feature of the database is essential to potential applications in ocean optics and ocean color remote sensing. We can conclude that the approach based on the bulk measurements of planktonic cultures is most suitable to the process of generating the single-particle optical property database and its wide-ranging applications.

Although one could envisage an alternative approach based on the optical measurements of individual planktonic cells (or individual particles in general) using techniques such as flow cytometry or microspectrophotometry, this would be impractical or unrealizable. The present single-particle analyses are typically more tedious than bulk optical measurements. More importantly, except for some particular scientific questions where the optical variability among individual cells within a given single-species population is of interest, the single-particle analyzers would provide a great deal of redundant information. Specifically, it would be unrealistic to attempt to develop understanding of aquatic optical environments based on the properties of each and every particle suspended in a water body. It is obvious that a successful, practical approach must be based upon a manageable number of particulate components (including planktonic species or groups) that realistically represent the mix of optically significant suspended materials. In this regard, the characterization of a given microbial species (or particle type) in terms of the single-particle optical properties representing an "average" particle of a given population is most appropriate. As described above, this concept underlies the methodology of the database development. Had we used the single-particle measurements instead of bulk measurements, we would have had to (numerically) average the cell-to-cell optical variability for any given microbial culture to accomplish the desired objective, that is to derive the average single-particle properties that reproduce the bulk properties for any given particle concentration.

It is important to emphasize that our database is not designed to represent every possible detail of the variability in the optical properties of planktonic microorganisms. We can define three general types of variability in these properties. First, the average single-particle properties may (and usually do) differ greatly among various species, even



if grown under identical conditions. These variations will be referred to as interspecies variability. Second, the average single-particle properties for any species may vary in response to changing conditions for growth, for example irradiance, nutrient availability, or temperature. These variations will be referred to as intraspecies variability. Finally, the optical properties for any given species grown under specified conditions may differ among individual cells. One can naturally expect that this type of cell-to-cell variations will occur over a much smaller range of values compared to the interspecies or intraspecies variability. As already mentioned, the detailed characterization of the cell-to-cell variability would have little, if any, value in pursuing most problems in ocean optics and it is beyond the scope of our database.

The current development of the database is focused on generating the optical characterization of interspecies variability. The single-particle optical properties vary over many orders of magnitude among optically significant species that range from very small, submicrometer viruses and bacteria to microplanktonic cells being tens of micrometers in size. This is why it is most important to focus on this type of characterization. We note, however, that it would be very useful to include intraspecies variability in the future versions of the database. This would account, for example, for the fact that low-light adapted and high-light adapted phytoplankton cells of any given species may have different optical properties. Similarly, cells may change their optical properties in response to the availability of nutrients or temperature. Including the intraspecies variability in the database would be a great challenge because the optical properties of various planktonic species would have to be examined over a broad range of growth conditions. Demand for very intense labor and overall complexity of this task will likely be a serious obstacle for pursuing this type of database development in the foreseeable future. We note that a few species in the current database were examined under varying growth conditions (for example, *T. pseudonana* was studied under diel cycle of irradiance<sup>8</sup>) and the final quantities in the database were obtained by averaging the observed variability. Most species in the database were, however, examined under predetermined single set of growth conditions. Therefore, we must realize that our objective at the present phase of database development is to generate data that characterize interspecies optical variability with adequate approximation, and that these data do not necessarily represent exact "average" properties of each species over a broad range of growth conditions.

In addition to planktonic microorganisms, our database includes three other components; biogenic detritus, mineral particles, and gas bubbles. The estimates of optical cross sections and phase functions for these three components were obtained from Mie scattering calculations based on approximations to the size distributions and refractive index of these components. The biogenic detritus was modeled as an assemblage of particles with wavelength-independent real part of refractive index of 1.04

(relative to water), diameters ranging from 0.05 to 500  $\mu\text{m}$ , and the Junge-type size distribution with a slope of  $-4$ . The spectrum of the imaginary part of refractive index was derived from microspectrophotometric data on individual detrital particles<sup>11</sup> using an inverse computational scheme. The mineral particles have the same characteristics except that the refractive index is 1.18. Finally, we assumed that gas bubbles obey the Junge-type distribution within the diameter range from 20 to 500  $\mu\text{m}$ , and that their refractive index is 0.75 (with no absorption).

## EXAMPLES OF DATA

Table 1 shows the various types of planktonic components included in the database. Values characterizing size and complex index of refraction of particles are also given. Heterotrophic bacteria represent a multispecies assemblage of these microbes, and three other components, generic Prochlorophyte (PROC), generic *Synechococcus* (SYNE), and generic phycocyanin-rich picophytoplankton (SYMA), result from averaging different strains or species. The optical variability among the strains/species belonging to any of these three components was small enough to justify this averaging process. The remaining nano- and microplankton components in the current database are represented by single species. We envision, however, that as the database expands, the components will generally include multispecies assemblages of similarly sized particle types, possibly with similar functions in the marine environment. An example of such component in the present database is heterotrophic bacteria, which represent many different species of similarly sized microorganisms that are all heterotrophs.

Spectra of absorption, total scattering and backscattering cross-sections, as well as backscattering ratio for 18 microbial components in the database are shown in Figures 1-4. The magnitude and spectral shapes of all these optical properties vary dramatically among the components. Examples of both interspecies variability and spectral variability in the scattering phase functions of microbial particles are shown in Figures 5 and 6. Figure 7 shows absorption, scattering and backscattering cross-sections for two generic components representing low-index and high-index non-living particles, that is biogenic detritus and minerals. Scattering and backscattering properties of the generic population of gas bubbles are illustrated in Fig. 8. Finally, examples of phase functions for detritus, minerals, and gas bubbles are compared with the Petzold particle phase function in Fig. 9.

The current database represents significant achievement in the process of creating a comprehensive database of the optical properties of marine particles. In order to further improve our capabilities for realistic descriptions of the various natural assemblages of marine particles, more work in this area is certainly needed. For example, the characterization of detrital and mineral particles as well as planktonic species, especially in the microplankton size range, needs improvement. The development of the single-

particle optical property database promises significant advances in the science of ocean optics. Such a database provides a foundation for a new generation of optical models that will describe the bulk inherent optical properties of natural waters as a function of the detailed composition of seawater, or more specifically, as a function of concentrations of various types of particles. In another presentation at this conference, Mobley and Stramski<sup>12</sup> show how powerful a combination of the database and radiative transfer modeling is in the study of ocean optics and ocean color remote sensing. This presentation is but the start; we shall continue to reap the benefits from this type of application with the passage of time and further improvements in the database. We emphasize, however, that in order to take a full advantage of the database development, an increased effort towards detailed characterization of the types and concentrations of particles in natural water bodies will be needed.

#### ACKNOWLEDGMENTS

This research was supported by ONR Environmental Optics Program (DS), NASA Biogeochemistry Program (DS), Centre National de la Recherche Scientifique (DS and AB) and Universite Pierre et Marie Curie (AM).

## REFERENCES

1. Morel, A. 1988. Optical modeling of the upper ocean in relation to its biogenous matter content (case I waters), J. Geophys. Res. 93: 10749-10768.
2. Stramski, D., and C. D. Mobley. 1997. Effects of microbial particles on oceanic optics: A database of single-particle optical properties, Limnol. Oceanogr., 42, 538-549.
3. Ahn, Y.-H., A. Bricaud, and A. Morel. 1992. Light backscattering efficiency and related properties of some phytoplankters. Deep-Sea Res. 39: 1835-1855.
4. Bricaud, A., A.-L. Bedhomme, and A. Morel. 1988. Optical properties of diverse phytoplanktonic species: experimental results and theoretical interpretation. J. Plankton Res. 10: 851-873.
5. Morel, A., Y.-H. Ahn, F. Partensky, D. Vaultot, and H. Claustre. 1993. Prochlorococcus and Synechococcus: A comparative study of their optical properties in relation to their size and pigmentation. J. Mar. Res. 51: 617-649.
6. Stramski D., and D. A. Kiefer. 1990. Optical properties of marine bacteria, p. 250-268. In Ocean Optics X, SPIE Proceedings, 1302.
7. Stramski D., and D. A. Kiefer. 1991. Light scattering by microorganisms in the open ocean. Prog. Oceanogr. 28: 343-383.
8. Stramski D., and R.A. Reynolds. 1993. Diel variations in the optical properties of a marine diatom. Limnol. Oceanogr. 38: 1347-1364.
9. Stramski, D., G. Rosenberg, , and L. Legendre. 1993. Photosynthetic and optical properties of the marine chlorophyte *Dunaliella tertiolecta* grown under fluctuating light caused by surface wave focusing. Marine Biology, 115, 363-372.
10. Stramski D., A. Shalapyonok, and R. A. Reynolds. 1995. Optical characterization of the oceanic unicellular cyanobacterium *Synechococcus* grown under a day-night cycle in natural irradiance. J. Geophys. Res. 100: 13295-13307.
11. Iturriaga R., and D. A. Siegel. 1989. Microspectrophotometric characterization of phytoplankton and detrital absorption properties in the Sargasso Sea. Limnol. Oceanogr. 34: 1706-1726.
12. Mobley C. D., and D. Stramski. 1998. Origins of variability in oceanic light fields. Ocean Optics XIV, SPIE Conference, Kailua-Kona, Hawaii.

Table 1. Microbial components in the database and source of raw data. Values for the average equivalent spherical diameter (D), the real part of refractive index at 550 nm (n), and imaginary part of refractive index at 440 and 675 nm (n') are also given for each component.

i	Label	Microbial species	D [μm]	n 550 nm	n' · 10 <sup>3</sup> 440 nm	n' · 10 <sup>3</sup> 675 nm	Source of raw data
1	VIRU	Viruses	0.07	1.050	0	0	Stramski and Kiefer, 1991
2	HBAC	Heterotrophic bacteria	0.55	1.055	0.509	0.057	Stramski and Kiefer, 1990
3	PROC	generic Prochlorophyte; the average of: PMED - Prochlorococcus strain MED	0.66	1.051	18.51	10.30	
4	SYNE	generic Synechococcus; the average of: PNAS - average of Prochlorococcus strains NATL and SARG SM41 - Synechococcus strain MAX41 (Cyanophyceae) SM01 - Synechococcus strain MAX01 (Cyanophyceae) SROS - Synechococcus strain ROS04 (Cyanophyceae) SDC2 - Synechococcus strain DC2 (Cyanophyceae) SI03 - Synechococcus strain WH8103 (Cyanophyceae)	0.59	1.055	23.25	13.77	Morel et al., 1993
			0.70	1.046	13.78	6.687	Morel et al., 1993
			1.05	1.051	5.587	2.930	
			0.92	1.047	5.415	2.905	Morel et al., 1993
			0.94	1.049	4.505	2.547	Morel et al., 1993
			1.08	1.049	4.516	2.154	Morel et al., 1993
			1.14	1.050	4.249	2.375	Morel et al., 1993
			1.14	1.062	9.251	4.668	Stramski et al., 1995
5	SYMA	generic phycocyanin-rich picophytoplankton; the average of: SCYS - Synechocystis (Cyanophyceae) MAR1 - Anacystis marina (Cyanophyceae)	1.41	1.055	6.495	2.757	
			1.39	1.050	4.530	1.910	Ahn et al., 1992
			1.43	1.060	8.460	3.603	Ahn et al., 1992
6	PING	Pavlova pinguis (Haptophyceae)	3.97	1.046	4.177	2.709	Bricaud et al., 1988
7	PSEU	Thalassiosira pseudonana (Bacillariophyceae)	3.99	1.045	9.231	7.397	Stramski and Reynolds, 1993
8	LUTH	Pavlova lutheri (Haptophyceae)	4.26	1.045	5.767	2.403	Bricaud et al., 1988
9	GALB	Isochrysis galbana (Haptophyceae)	4.45	1.056	7.673	5.101	Ahn et al., 1992
10	HUXL	Emiliana huxleyi (Haptophyceae)	4.93	1.050	5.012	2.950	Ahn et al., 1992
11	CRUE	Porphyridium cruentum (Rhodophyceae)	5.22	1.051	3.351	2.443	Bricaud et al., 1988
12	FRAG	Chroomonas fragarioides (Cryptophyceae)	5.57	1.039	4.275	2.904	Ahn et al., 1993
13	PARV	Prymnesium parvum (Haptophyceae)	6.41	1.045	2.158	1.329	Bricaud et al., 1988
14	BIOC	Dunaliella bioculata (Chlorophyceae)	6.71	1.038	10.49	7.839	Ahn et al., 1993
15	TERT	Dunaliella tertiolecta (Chlorophyceae)	7.59	1.063	6.260	5.076	Stramski et al., 1993
16	CURV	Chaetoceros curvisetum (Bacillariophyceae)	7.73	1.024	2.877	1.480	Bricaud et al., 1988
17	ELON	Hymenomonas elongata (Haptophyceae)	11.77	1.046	13.87	7.591	Ahn et al., 1992
18	MICA	Prorocentrum micans (Dinophyceae)	27.64	1.045	2.466	1.710	Ahn et al., 1992

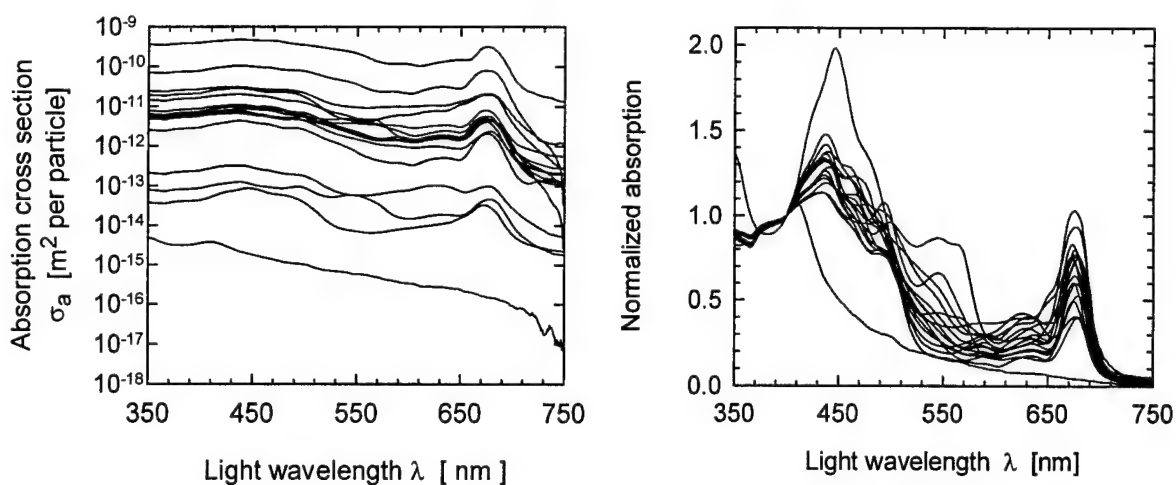


Fig. 1. Absorption cross sections ( $\sigma_a$ ) of the 18 microbial components in the database (left-hand panel). In the right-hand panel each absorption curve is normalized at 400 nm to facilitate comparison of the spectral shapes.

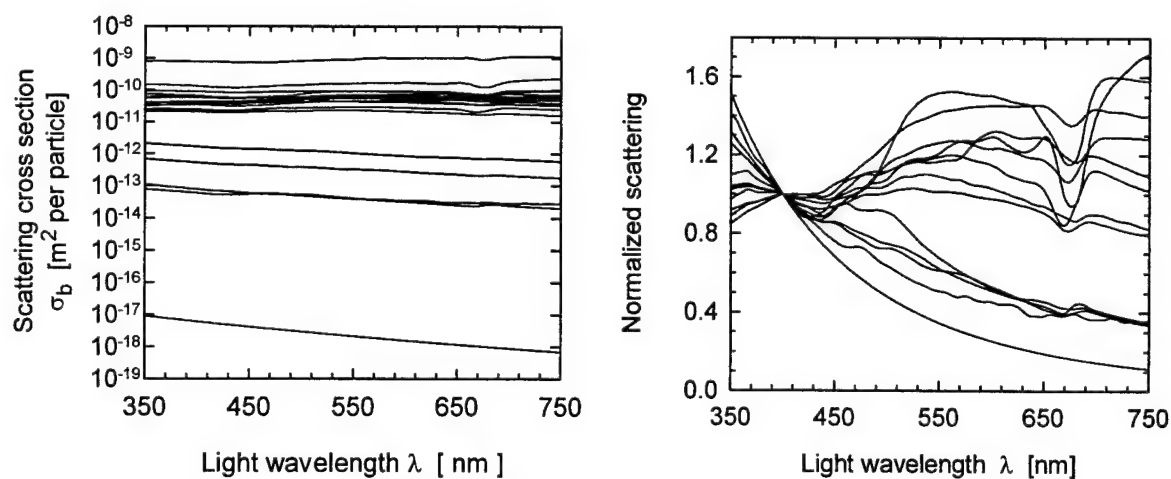


Fig. 2. Scattering cross sections ( $\sigma_b$ ) of the 18 microbial components in the database. (left-hand panel). In the right-hand panel each scattering curve is normalized at 400 nm to facilitate comparison of the spectral shapes.



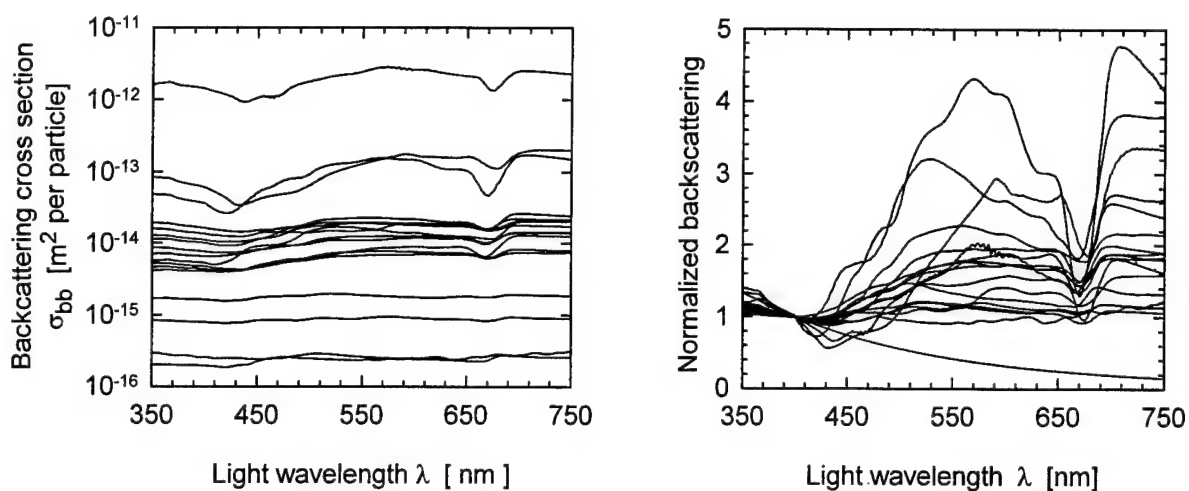


Fig. 3. Backscattering cross sections ( $\sigma_{bb}$ ) of the 18 microbial components in the database (left-hand panel). In the right-hand panel each backscattering curve is normalized at 400 nm to facilitate comparison of the spectral shapes.

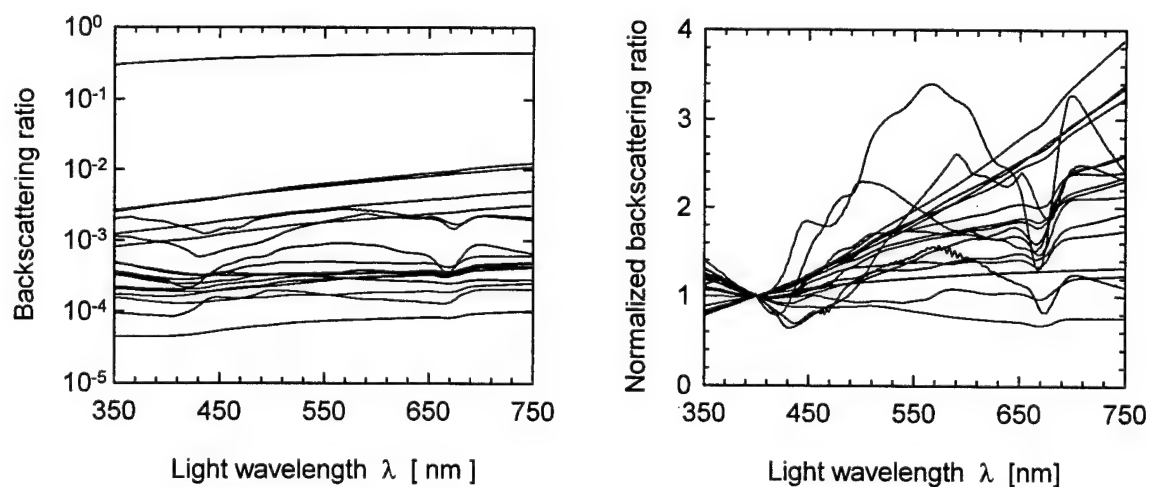


Fig. 4. Backscattering ratio (i.e., ratio of backscattering to total scattering) of the 18 microbial components in the database (left-hand panel). In the right-hand panel each curve is normalized at 400 nm to facilitate comparison of the spectral shapes.

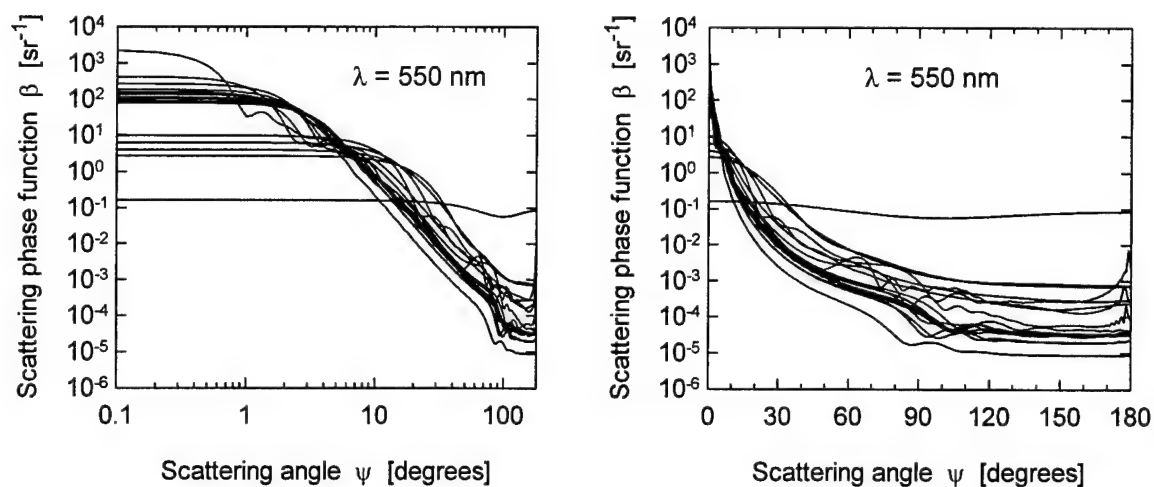


Fig. 5. Scattering phase functions ( $\beta$ ) at 550 nm of the 18 microbial components in the database. The left-hand panel is a log-log plot to facilitate comparison of forward angle scattering. The right-hand panel is a semi-log plot to facilitate comparison of large-angle scattering including backscattering.

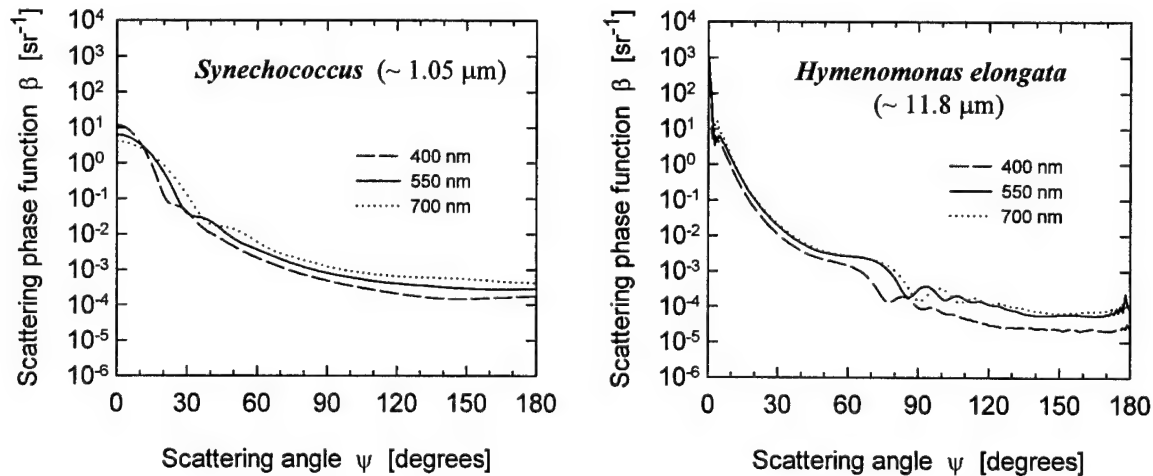


Fig. 6. Scattering phase functions ( $\beta$ ) at three different wavelengths, 400, 550, and 750 nm, for two microbial species selected from the database: *Synechococcus* (left-hand panel), and *Hymenomonas elongata* (right-hand panel). The average cell size for these species is indicated.

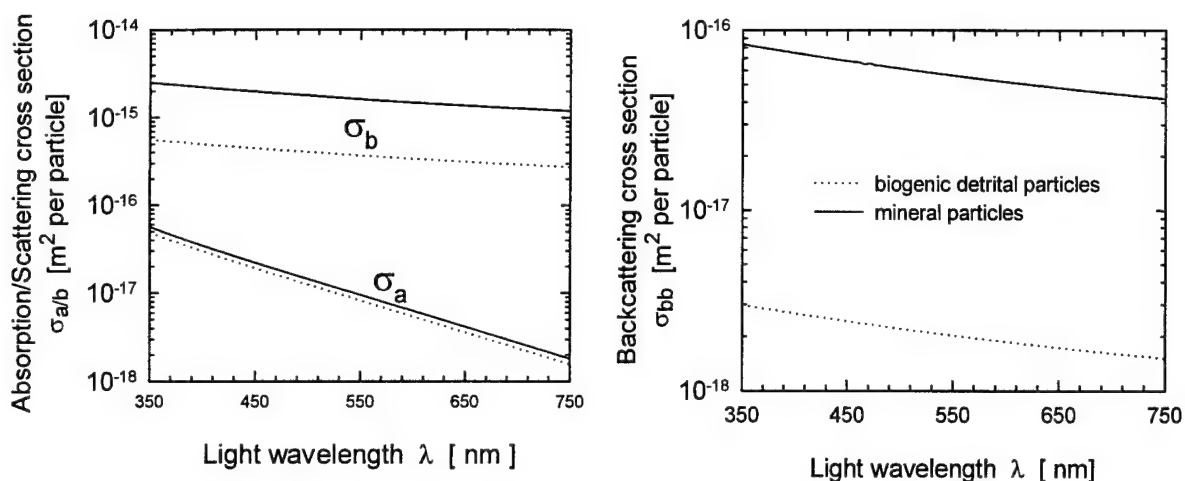


Fig. 7. Left-hand panel: Absorption ( $\sigma_a$ ) and scattering ( $\sigma_b$ ) cross sections for generic assemblages of biogenic detrital particles (dotted lines) and mineral particles (solid lines). Right-hand panel: Backscattering cross sections of biogenic detritus and mineral particles.

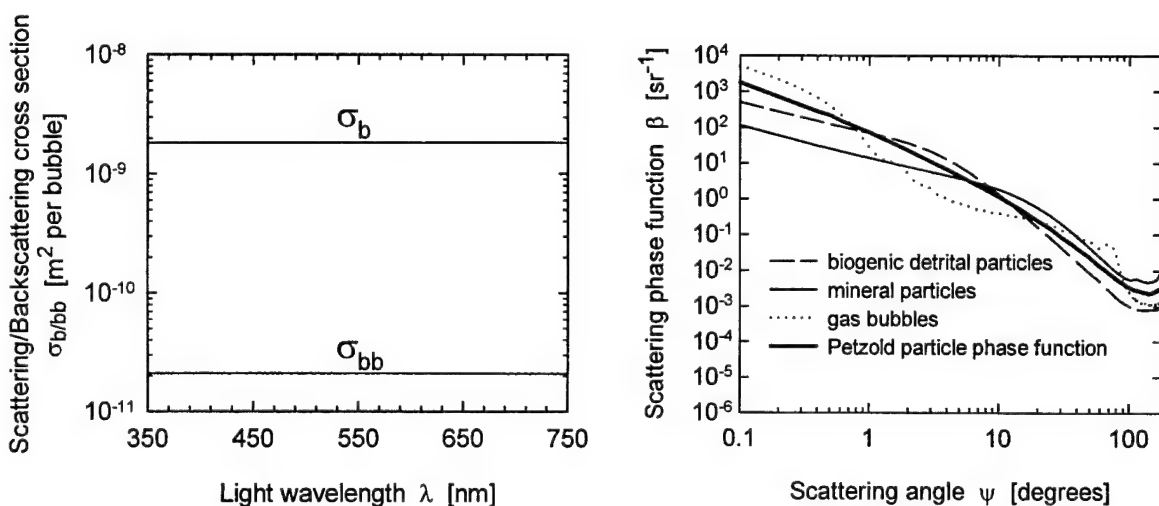


Fig. 8. Scattering ( $\sigma_b$ ) and backscattering ( $\sigma_{bb}$ ) cross sections for generic assemblage of gas bubbles.

Fig. 9. Comparison of scattering phase functions (at 550 nm) of detrital particles, mineral particles, and gas bubbles with the Petzold particle phase function.

**APPENDIX D**

Draft of

*Origins of variability in remote-sensing reflectances*

by

Curtis D. Mobley and  
Dariusz Stramski

(Journal article in preparation)

# **Origins of Variability in Remote-Sensing Reflectances**

**Curtis D. Mobley**  
Sequoia Scientific, Inc.  
Mercer Island, WA 98040

**Dariusz Stramski**  
Marine Physical Laboratory  
Scripps Institution of Oceanography  
La Jolla, CA 92093-0238

(First draft of a journal article  
showing preliminary results)

## ABSTRACT

The remote-sensing reflectance  $R_{rs}$  is the ratio of the water-leaving radiance to the downwelling irradiance just above the sea surface. This paper examines the variability in predicted values of  $R_{rs}$  that is associated with various parameters of the underlying models for the inherent optical properties (IOPs) of a water body. In particular, the Hydrolight radiative transfer numerical model is used in conjunction with a database of microbial optical properties to quantify the effects on  $R_{rs}$  of assuming various reasonable values for the quantum efficiencies of chlorophyll and CDOM (colored dissolved organic matter) fluorescence, and of assuming various models for the absorption and scattering spectra of microbial particles, CDOM, and detritus. The numerical simulations show that the ranges of IOP parameter values reported in the literature can lead to variations in predicted  $R_{rs}$  values of tens of percent about the values obtained when using average values for the various IOP parameters. In some cases, the changes induced in  $R_{rs}$  by variability in the IOP model parameters can be as great as the change induced in  $R_{rs}$  by a factor-of-two change in the chlorophyll concentration of a water body. These uncertainties in  $R_{rs}$  place limits on the extent to which it is possible to retrieve information from  $R_{rs}$ . For given concentrations of microbes, CDOM, and detritus, the wavelength dependence of  $R_{rs}$  is most sensitive to the assumed parameters of the CDOM and detritus absorption and scattering models;  $R_{rs}$  is less sensitive to the CDOM fluorescence model. The detailed microbial species composition within broad categories such as prochlorophytes, *Synechococcus*, and small nanoplankton has relatively little effect on  $R_{rs}$ , so long as the total particle concentration within a category is constant. Idealized simulations of single-species blooms indicate that it may be possible to identify blooms of heterotrophic bacteria or prochlorophytes from their characteristic  $R_{rs}$  signatures. However, the development of reliable algorithms for extracting such information from  $R_{rs}$  will require additional study.



## 1. Introduction: Parameters influencing variability in $R_{rs}$

This paper discusses errors arising when making predictions of the remote-sensing reflectance given the absorption and scattering properties of a water body. The effects of various parameters commonly used in bio-optical models of absorption and scattering are quantified through numerical simulation.

The remote-sensing reflectance  $R_{rs}$  is defined as

$$R_{rs}(\theta, \phi, \lambda) \doteq \frac{L_w(\theta, \phi, \lambda)}{E_d(\lambda)} . \quad (1)$$

Here  $\theta$  and  $\phi$  specify the polar and azimuthal directions in some convenient coordinate system, and  $\lambda$  is the wavelength.  $L_w(\theta, \phi, \lambda)$  is the water-leaving radiance in direction  $(\theta, \phi)$ , that is, the radiance heading upward above the sea surface which originated from underwater light that was transmitted upward through the sea surface into direction  $(\theta, \phi)$ .  $E_d(\lambda)$  is the downwelling plane irradiance incident onto the sea surface. The measurements implicit in Eq. (1) are generally made within a few meters of the sea surface and at wavelengths from the near ultraviolet to the near infrared, e.g., from 350 to 800 nm.

It is well known that, to first order, the remote-sensing reflectance depends on the absorption coefficient  $a$  and the backscatter coefficient  $b_b$  according to

$$R_{rs} \sim \frac{b_b}{a + b_b} . \quad (2)$$

Because  $a$  and  $b_b$  are highly variable in natural waters, so is  $R_{rs}$ . However, the high correlation between  $R_{rs}$  and  $b_b/(a + b_b)$  allows us to extract information about  $b_b/(a + b_b)$  from measurements of  $R_{rs}$ . More importantly, if additional assumptions are made, it is often possible to extract even more information from  $R_{rs}$ . In particular, if one presumes to know how  $b_b$  and  $a$  depend on individual water constituents such as chlorophyll-bearing particles, CDOM, detritus, and mineral particles, then it may be possible to extract information about  $a$  and  $b_b$  individually, or about quantities such as the chlorophyll concentration. This extraction is a type of inverse problem that rests upon the assumed models for the inherent optical properties (IOPs) of the various constituents. Examples of such inversions can be seen in Lee *et al.* (1994, 1996).

The constituent IOP models generally depend on one or more parameters, which can be simple numbers (such as the chlorophyll fluorescence quantum efficiency) or complicated functions (such as the quantum efficiency function for CDOM fluorescence). These parameters are usually given typical values when modeling the absorption and scattering properties of a

particular water component. However, many of these parameters can vary considerably and in ways that are poorly understood. It is therefore convenient to view these parameters as a source of uncertainty, or error, in predicted values of the IOPs, and hence in predicted values of  $R_{rs}$ .

Parameters commonly used in constituent IOP models are as follows:

**The CDOM absorption parameter  $\alpha$ .** An example of a constituent IOP model is the commonly used relationship between the absorption by CDOM at one wavelength and the absorption at all other wavelengths (Bricaud et al., 1981):

$$a_{\text{CDOM}}(\lambda) = a_{\text{CDOM}}(\lambda_0) \exp[-\alpha(\lambda - \lambda_0)]. \quad (3)$$

Here  $\lambda_0$  is a reference wavelength, which is usually taken to be 400 or 440 nm. The CDOM absorption exponent parameter  $\alpha$  typically has a value around 0.014, when  $\lambda$  is in nanometers. However, Roesler *et al.* (1989) reports values for  $\alpha$  ranging from 0.011 to 0.019, and Højerslev (1998) reports values between 0.007 and 0.030. Equation (3) shows, for example, that if  $\lambda_0 = 400$  nm, then the 0.007 to 0.030 range in  $\alpha$  gives CDOM absorption values at  $\lambda = 440$  nm that are from ~30% more to 50% less than the values predicted using  $\alpha = 0.014$ . Predictions of CDOM absorption at 550 nm differ by a factor of ~30 for the possible range of  $\alpha$  values. Assuming a particular value for  $\alpha$  will therefore lead to a particular conclusion about the absorption properties of a water body. If a particular value of  $\alpha$  is assumed when predicting  $R_{rs}$  for a given water body, there will be some uncertainty as to the true value of  $R_{rs}$  for that water body. Conversely, if a measured  $R_{rs}$  is used to deduce the absorption, there will be a corresponding uncertainty in the true value of the absorption.

Note, however, that the variability in CDOM absorption does not translate simply into a proportionate variability in the total absorption or in the remote sensing reflectance. The reason is that the absorption by CDOM is only one component of the total absorption, and because  $R_{rs}$  depends in complicated ways on the absorption and on other quantities (such as the scattering phase function). Thus the uncertainty induced in  $R_{rs}$  by the variability in  $\alpha$  depends also on the contributions of the other constituents to the total absorption. Note also that the value of  $\alpha$  affects not just the total absorption itself, but also CDOM fluorescence calculations, because the energy available for fluorescence comes from that absorbed by CDOM at each wavelength.

**The detritus absorption parameter  $\gamma$  and scattering parameter  $n$ .** Absorption by detritus is usually modeled by an equation of the same form as Eq. (3), but with a different exponent parameter  $\gamma$  in place of  $\alpha$  (Roesler *et al.*, 1989). Values of  $\gamma$  are found to range from 0.006 to

0.014, with 0.011 being average. Unlike CDOM, which has negligible scattering, detritus scatters light strongly, although very few studies of scattering by detritus have actually been made. Scattering by detritus is therefore usually modeled by a simple power law:

$$b_{\text{det}}(\lambda) = b_{\text{det}}(400) \left( \frac{400}{\lambda} \right)^n \quad (4)$$

The value of the parameter  $n$  is commonly taken to be 0 or 1.

**The CDOM spectral fluorescence quantum efficiency function  $\eta^{\text{CDOM}}(\lambda' \rightarrow \lambda)$ .** This quantity determines how much of the light absorbed by CDOM at wavelength  $\lambda'$  is fluoresced to wavelength  $\lambda$ . The  $\eta^{\text{CDOM}}(\lambda' \rightarrow \lambda)$  functions can vary considerably in both shape and magnitude. Figure 1 shows three examples of  $\eta^{\text{CDOM}}(\lambda' \rightarrow \lambda)$  as measured by Hawes (1992) in three different waters. Note that there is almost an order of magnitude difference in the maximum values of these functions.

**The chlorophyll fluorescence quantum efficiency  $\Phi^{\text{chl}}$ .** Although the “shape” of the  $\eta^{\text{chl}}(\lambda' \rightarrow \lambda)$  function for chlorophyll fluorescence varies little from one water body to the next (see, for example, Mobley 1994, section 5.15), the “magnitude” of the function as expressed by the chlorophyll fluorescence quantum efficiency

$$\Phi^{\text{chl}}(\lambda') = \int_{\lambda'}^{700} \eta^{\text{chl}}(\lambda' \rightarrow \lambda) d\lambda$$

can vary from less than 0.01 to 0.10, depending on the species composition and current physiological state of the chlorophyll-bearing phytoplankton (Kiefer *et al.*, 1989; Kiefer and Reynolds, 1992). The typical range of  $\Phi^{\text{chl}}$  in oceanic waters is 0.01 to 0.05, with an average value of around 0.02. Note that  $\Phi^{\text{chl}}$  determines what fraction of the radiant energy absorbed by chlorophyll-bearing microbes is re-emitted at wavelengths near 685 nm.

**The chlorophyll specific absorption coefficient  $a^*(\lambda)$ .** The function  $a^*(\lambda)$  converts a given chlorophyll concentration into the absorption due to chlorophyll-bearing microbes. Figure 2 shows chlorophyll-specific absorption coefficients  $a^*(\lambda)$  as measured by Sathyendranath *et al.* (1987) for eight different species of phytoplankton. Note that although the general shapes of the curves are similar, there is a factor-of-two range in the magnitudes of the particular  $a^*(\lambda)$  values for the different species. If these individual curves were used to predict the phytoplankton absorption, there would be a corresponding range in the magnitude of the spectral absorption

attributed to phytoplankton for a given chlorophyll concentration.

The inherent variability in parameters such as  $\alpha$ ,  $\gamma$ ,  $n$ ,  $\Phi^{\text{chl}}$ ,  $\eta^{\text{CDOM}}$ , and  $a^*$  leads to inherent variability in the light fields within and leaving water bodies. This is true even when the commonly used descriptors of water bodies, such as the chlorophyll concentration or the CDOM absorption at 400 nm, are the same. The magnitude of the variability in the light field depends in complicated and indirect ways on the variability in these quantities. Moreover, the variability will be different for different light-field quantities, such as water-leaving radiance or in-water irradiance. For example, the variability in  $\Phi^{\text{chl}}$  or  $\eta^{\text{CDOM}}$  may be quite unimportant as regards the computation of scalar irradiance within the water, because fluoresced light is a very small part of the total ambient irradiance (which is largely determined by elastically scattered downwelling sunlight). On the other hand, changes in  $\Phi^{\text{chl}}$  or  $\eta^{\text{CDOM}}$  may significantly affect  $R_{\text{rs}}$ , because in some waters the isotropically fluoresced light may be comparable in magnitude to elastically backscattered sunlight.

Understanding the influences of these parameters on the remote-sensing reflectance  $R_{\text{rs}}$  is clearly fundamental to predicting and interpreting remotely sensed signals. The later sections of this paper consider the effects of each of these quantities in turn.

## 2. A Database of Microbial Optical Properties

In order to use the Hydrolight radiative transfer model to study the effects of various parameters on  $R_{\text{rs}}$ , it is first necessary to model the IOPs of the water body. Now we wish to take a closer look at how the detailed composition of a water body can affect  $R_{\text{rs}}$ . We therefore take the foundation of our IOP models to be a database of the optical properties of a variety of microbial particles. A preliminary version of this database was described in Stramski and Mobley (1997), and the currently available database is described in Stramski *et al.* (1998). The current database contains the absorption and scattering cross sections and the scattering phase functions for 24 microbial species, which are shown in Table 1. Previous simulations (Mobley and Stramski, in preparation) have shown that not all microbial components need to be included in order to realistically simulate the IOPs of a water body. In particular, it is possible to average the optical properties of the two prochlorophyte species (PMED and PNAS in Table 1) to obtain a "generic" prochlorophyte (called PROC in Table 1). This averaging can be performed because the absorption and scattering properties of the two prochlorophyte species are very similar. The same can be done with the five *Synechococcus* species, and with SCYS and MARI. It is *not*, however, possible to simply average the small nanoplankton species (species PING to CURV in Table 1) without adversely affecting the realism of the IOP model. This is not surprising, because the nanoplankton species have different size distributions and considerably different

optical cross sections. In any case, the effective number of microbial components used in the present study is then 18, as numbered in Table 1. These microbial components are augmented by the IOPs of the water itself as given by Smith and Baker (1981), and by models for the absorption and scattering by CDOM and detritus as given by Eqs. (3) and (4). We then have a 21-component model of the bulk IOPs, in which the concentration of each of the components (except for water itself) can be varied as desired.

For simplicity in the simulations below, we take the concentrations of the various constituents to be independent of depth. The model for the total absorption is then given by

$$\begin{aligned}
 a(\lambda) &= \sum_{j=1}^{21} a_j(\lambda) \\
 &= a_w(\lambda) + \sum_{i=1}^{18} C_i [\sigma_a(\lambda)]_i + a_{\text{CDOM}}(\lambda) + a_{\text{det}}(\lambda).
 \end{aligned} \tag{5}$$

Here  $C_i$  is the concentration of the  $i^{\text{th}}$  microbial component (in particles per cubic meter), and  $[\sigma_a(\lambda)]_i$  is the absorption cross section (in meters squared per particle) of the  $i^{\text{th}}$  microbial component. An equation of the same form as Eq. (5) gives the total scattering coefficient  $b(\lambda)$  as a function of the component concentrations and scattering cross sections. The total scattering phase function is given by (Mobley, 1994, Eq. 3.13)

$$\tilde{\beta}(\psi, \lambda) = \sum_{j=1}^{21} \frac{b_j(\lambda)}{b(\lambda)} \tilde{\beta}_j(\psi, \lambda).$$

Here  $\tilde{\beta}_j(\psi, \lambda)$  is the scattering phase function of the  $j^{\text{th}}$  component;  $\psi$  is the scattering angle. The cross sections and phase functions for the 18 microbial components are found in the database.

Figure 3 shows for reference the absorption cross sections  $[\sigma_a(\lambda)]_i$  of the 18 microbial components; for ease of display each component is normalized to its value at 400 nm. The absolute values of the absorption cross sections span almost 8 orders of magnitude among the various microbial species. Figure 4 shows the normalized scattering cross sections  $[\sigma_b(\lambda)]_i$ , which span 9 orders of magnitude in their absolute values. The absorption and scattering cross sections from 400 to 700 nm are based on laboratory measurements made on single-species microbial cultures, as described in Stramski and Mobley (1997, and references therein). The cross sections from 350 to 400 nm were obtained by objectively extrapolating the curves using simple models derived from typical microbial absorption and scattering cross sections measured in the region from 350 to 400 nm. The values below 400 nm allow us to begin the Hydrolight simulations at 350 nm, which is necessary in order to include inelastic scattering effects in the region of greatest interest, which is from 400 to 700 nm.

Figure 5 shows an example scattering phase function  $\tilde{\beta}_i(\psi, \lambda)$ , namely the one for *Thalassiosira pseudonana* (species  $i = 7$ , PSEU, in Table 1). The database contains the phase functions for all microbes of Table 1 at 0.1 degree intervals from  $\psi = 0$  to 5 degrees, and at 1 degree intervals from  $\psi = 5$  to 180 degrees. The phase functions are given at wavelength intervals of 1 nm between 400 and 750 nm. The well behaved nature of the phase functions with wavelength makes it reasonable to use the phase function at 400 nm for wavelengths from 350 to 400 nm.

There are admittedly gaps in the database, in particular between  $\sim 1.5$  and  $4 \mu\text{m}$  and at sizes greater than  $8 \mu\text{m}$  (see also Fig. 6 below). We will therefore concentrate our attention below to the regions where microbial particles are well represented in the database, namely from  $0.5$  to  $1.5 \mu\text{m}$ , and from  $4$  to  $8 \mu\text{m}$ . We can nevertheless hope that the available larger nanoplankton (ELON and MICA) are representative of other species in those size ranges, so as to add a bit more realism to our simulations. But regardless of its incompleteness as regards the larger nanoplankton, this database is the most extensive ever assembled and allows for considerable realism in simulations of the remote-sensing reflectance.

### 3. A Base Model for Simulating $R_{rs}$

We next define a “base” model for use in studying the effects of different parameters on the remote-sensing reflectance. The base set of microbial concentrations seen in Table 1 was defined subject to the constraint that the overall size distribution of the microbial components obey a power law (a Junge distribution) with an exponent of  $-4$ . In other words, if  $n(x)dx$  is the number of particles per unit volume in the size interval from  $x$  to  $x+dx$ , then  $n(x) \sim x^{-4}$ . Such a size distribution is typical of oceanic particles in the size range from a few tenths of a micrometer to a few hundred micrometers (see, for example, Mobley 1994, Fig. 3.2). Figure 6 shows the particle size distributions of the 18 individual species for the microbial particles at the base concentrations (light solid lines). The sum of these distributions at each size is shown as a heavy solid line. The concentrations of the individual species were chosen so that this sum obeys the  $-4$  power law (dashed line) in the size regions where the database contains particles. For example, the individual small nanoplankton species (microbes PING through CURV in Table 1), which have mean sizes from  $4$  to  $8 \mu\text{m}$ , have various concentrations; but the sum of their individual distributions obeys the  $-4$  law between  $4$  and  $8 \mu\text{m}$ . The total small nanoplankton concentration is  $10^9 \text{ m}^{-3}$ . The only exception to forcing the particles to follow a  $-4$  power law is marine viruses (VIRU). The concentration of VIRU was allowed to be an order of magnitude less than what would be expected from the  $-4$  law, in order to keep the concentration of VIRU within the range observed in natural waters. The chlorophyll concentration resulting from all



microbes at the base concentration is  $0.718 \text{ mg Chl m}^{-3}$ .

The total absorption at 400 nm due to the microbes at the base concentration is  $a_{\text{mic}}(400) = 0.018 \text{ m}^{-1}$ ; the microbe scattering coefficient is  $b_{\text{mic}}(400) = 0.096 \text{ m}^{-1}$ . In order to complete the base IOP model, the absorption by CDOM and detritus at 400 nm are taken to be comparable to that of the microbes, namely  $a_{\text{CDOM}}(400) = 0.02 \text{ m}^{-1}$  and  $a_{\text{det}}(400) = 0.02 \text{ m}^{-1}$ . The CDOM and detritus absorption coefficients at other wavelengths are given by Eq. (3), with the respective exponent parameters  $\alpha = 0.014$  and  $\gamma = 0.011$ . CDOM is assumed to be non-scattering. The scattering coefficient for detritus is taken to be  $b_{\text{det}}(400) = 0.02 \text{ m}^{-1}$ , which is about 20% of the scattering due to the various microbes. The detritus scattering coefficient at other wavelengths is given by Eq. (4) with the parameter value  $n = 1$ . Because detrital particles cover a wide range of sizes, the phase function for detritus is assumed to be the “typical particle” phase function tabulated in Mobley (1994, Table 3.10, column 6).

Figure 7 shows the total absorption  $a(\lambda)$  and the contributions by water, microbes, CDOM, and detritus to the total for the base concentrations of microbes and for CDOM and detritus as just specified. For wavelengths greater than  $\sim 550 \text{ nm}$ , the absorption is determined primarily by the water itself. Overall, the simulated sea water is least absorbing at blue-green wavelengths. This water corresponds closely to Jerlov Type II water. Figure 8 repeats the absorption curves of Fig. 7 with an ordinate that makes it easier to see the contributions of the various components. The shape of the total absorption curve for the microbes is quite representative of phytoplankton absorption curves as measured on bulk samples of sea water.

Figure 9 shows the total scattering coefficient  $b(\lambda)$  and the contributions by water, microbes, and detritus to the total for the base concentrations of microbes and detritus. Unlike the situation just seen for absorption, the scattering coefficient at all wavelengths is determined primarily by the microbes. The water itself is a rather insignificant part of the total scattering.

As already mentioned, the base model uses typical values for the CDOM and detritus parameters  $\alpha$ ,  $\gamma$ , and  $n$ . Likewise, a typical chlorophyll fluorescence quantum efficiency of  $\Phi^{\text{chl}} = 0.02$  is used, and the “moderate” CDOM fluorescence quantum efficiency function  $\eta^{\text{CDOM}}$  of Fig. 1b is used. All simulations include the effects of Raman scatter by the water, and of fluorescence by CDOM and chlorophyll.

The effects of wind speed, sun zenith angle, sky condition, and viewing direction on  $R_{\text{rs}}$  have been studied by Mobley (1999). For the present simulations, we therefore consider only one set of environmental conditions, namely

- wind speed  $U = 5 \text{ m s}^{-1}$
- sun zenith angle  $\theta_s = 30^\circ$
- sky radiance distribution characteristic of a clear day
- viewing direction  $\theta_v = 0^\circ$  (a nadir-viewing instrument; perfect removal of reflected sky

radiance and sun glitter is assumed)

- infinitely deep, homogeneous water

These environmental conditions complete the specification of the base model.

Hydrolight was run between 350 and 700 nm with 10 nm bandwidths. Thus the  $R_{rs}$  values to be seen below represent averages of  $R_{rs}(\lambda)$  over bands from 350 to 360 nm, from 360 to 370 nm, etc. The band averages are plotted at the midpoints of the bands, e.g. at 355 nm for the 350-360 nm band.

It is known that the water-leaving radiance at a given wavelength comes almost entirely from the upper two diffuse attenuation depths, i.e. from depths less than  $2/K_d$ , where  $K_d$  is the diffuse attenuation function for downwelling plane irradiance at that wavelength. For the IOPs used in the following simulations,  $2/K_d$  was never more than 20 m. Hydrolight therefore solved the radiative transfer equation to a depth of 20 m, which assured that the predicted  $R_{rs}$  values contain the full effects of the water body, including inelastic scattering effects. The bottom boundary condition imposed at 20 m was that of an infinitely deep, but elastically scattering, water body.

#### 4. Variability Due to Nanoplankton Species Composition

We commented above that it is possible to combine some individual species and use, for example, a generic *Synechococcus* in simulations of the remote-sensing reflectance, but that this cannot be done with the nanoplankton. We must then consider the extent to which the remote-sensing reflectance depends on the particular species composition assumed for the small nanoplankton, of which there are 11 species in the database. Indeed, the “base” concentrations shown in Table 1 are only one possible set of concentrations that could satisfy the -4 power law constraint and keep the total concentration of small nanoplankton fixed. To investigate the variability associated with the small nanoplankton species composition, 22 sets of small nanoplankton concentrations were defined subject to the constraint that the total concentration of small nanoplankton was  $10^9 \text{ m}^{-3}$  and that the size distribution obeyed the -4 power law between 4 and 8  $\mu\text{m}$ . Figure 10 shows three of these 22 sets of concentrations for the 11 small nanoplankton species; the base set of Table 1 is the solid line. The concentrations of the other microbial species were kept at the base values, as were the models for CDOM and detritus.

Figure 11 shows  $R_{rs}$  as predicted for these three sets of small nanoplankton concentrations. The solid line is for the base concentrations, and the dotted and dashed lines are the extremes of  $R_{rs}$  computed for the 22 sets of concentrations – that is to say, the 22  $R_{rs}$  curves all fall between the dotted and dashed lines in Fig. 11. These simulations (and others of a related nature using different contributions by CDOM, detritus, etc., not shown here) show that, *all else being equal, the detailed species composition of the small nanoplankton is not crucial to the prediction of  $R_{rs}$ .*

We are therefore justified in picking any one of the 22 sets of small nanoplankton concentrations for use as a base set in further simulations; this is what was done in picking the set of concentrations shown in Table 1.

We are now at last in position to study the effects of the various IOP model parameters on the remote-sensing reflectance.

## 5. Variability Due to the CDOM Absorption Model

We next consider the variability in predicted  $R_{rs}$  values associated with the  $\alpha$  parameter in the model for CDOM absorption. Three runs were made with the base concentrations, except that  $\alpha$  values of 0.011, 0.014, and 0.019 were used in Eq. (3);  $a_{CDOM}(400)$  was kept at  $0.02 \text{ m}^{-1}$ . Three additional runs were made with a high concentration of CDOM relative to the contributions of the other components, namely  $a_{CDOM}(400) = 0.2 \text{ m}^{-1}$ , with all other concentrations being held at their base levels. This high CDOM concentration relative to the other components is reasonable for Case 2 waters dominated by CDOM. Figure 12 shows the resulting absorption coefficient for  $\alpha = 0.014$ ; very similar measured absorption curves can be seen in Prieur and Sathyendranath (1981; see also Mobley, 1994, Fig. 3.9).

Figure 13 shows the predicted  $R_{rs}$  curves for these three  $\alpha$  values and two CDOM concentrations. Two points can be made from these results. First, there is a sizeable range of predicted  $R_{rs}$  values. For the low CDOM concentration,  $a_{CDOM}(400) = 0.02 \text{ m}^{-1}$ , the spread of  $R_{rs}$  values is about 10% at some wavelengths. For the high CDOM concentration, the spread can be almost 50%. The shaded bands in Fig. 13 show the nominal SeaWiFS sensor bands. Note, for example, that if a ratio of the 412 nm and 490 nm bands were being used to retrieve information about the water body, the ratio  $R_{rs}(412)/R_{rs}(490)$  would vary by a similar amount. Such variability would then be reflected in the retrieved information as an error of unknown magnitude.

Second, it should be noted that the wavelength dependence of the variability in  $R_{rs}$  depends on the model being assumed for CDOM absorption. In Eq. (3), we took the reference wavelength to be 400 nm. Consequently, each of the three  $\alpha$  curves gives the same value at 400 nm. The spread in  $R_{rs}$  is then greatest near 350 nm and at blue-green wavelengths. Had we chosen, say, 440 nm as the reference wavelength in Eq. (3), then the curves would have been the same at 440, and the spread in  $R_{rs}$  values would have been the greatest at 350 nm. If nature were kind, we always would guess the correct value for  $\alpha$  and for  $a_{CDOM}$  at the reference wavelength, and the prediction would then be correct at all wavelengths. But in reality, we must keep in mind that the assumed model for CDOM absorption can affect not just the magnitude of the errors in predicted  $R_{rs}$ , but also the wavelengths where those errors occur. For some applications a

judicious choice of the reference wavelength might minimize the errors induced by variability in  $\alpha$  in the wavelength region of greatest interest, at the expense of greater possible errors at wavelengths of lesser interest.

## 6. Variability Due to the CDOM Fluorescence Model

Figure 1 showed three different fluorescence quantum efficiency functions  $\eta^{\text{CDOM}}(\lambda' \rightarrow \lambda)$ , which would give “weak” to “strong” CDOM fluorescence for a given CDOM concentration. Figure 14 shows  $R_{\text{rs}}$  for the low and high CDOM concentrations [expressed in terms of  $a_{\text{CDOM}}(400)$ ] and for the weak, moderate, and strong  $\eta^{\text{CDOM}}$  functions of Fig 1. Other parameters were taken to be their base values; in particular,  $\alpha = 0.014$  was used in the CDOM absorption model.

Figure 14 shows that there is almost no difference in the three  $\eta^{\text{CDOM}}$  functions for low CDOM concentrations, and at high concentrations the spread in  $R_{\text{rs}}$  values is about 15%. It is not surprising that the extreme values of  $\eta^{\text{CDOM}}$  have less of an effect on  $R_{\text{rs}}$  than do the extreme values for  $\alpha$ , because  $\alpha$  effects the absorption itself whereas  $\eta^{\text{CDOM}}$  effects only the fluoresced light. It is certainly reasonable to use the moderate  $\eta^{\text{CDOM}}$  function of Fig. 1b in simulations. The errors in the predicted  $R_{\text{rs}}$  values will then be at most a few percent, except in waters with very high CDOM concentrations.

## 7. Variability Due to the Detritus Models

Absorption by detritus is modeled by an equation of the same form as Eq. (3), but using  $a_{\text{det}}(400)$  in place of  $a_{\text{CDOM}}(400)$  and using a different exponent parameter  $\gamma$  in place of  $\alpha$ . Scattering by detritus is modeled by Eq. (4). Figure 15 shows the effects of the scattering exponent parameter  $n$  on predicted  $R_{\text{rs}}$  values for low [ $a_{\text{det}}(400) = b_{\text{det}}(400) = 0.02 \text{ m}^{-1}$ ] and high [ $a_{\text{det}}(400) = b_{\text{det}}(400) = 0.2 \text{ m}^{-1}$ ] detritus concentrations. In all cases the absorption parameter  $\gamma$  was set to its base value of 0.011; thus only the wavelength dependence of the scattering varied. For the case of low detritus concentration, the wavelength dependence of the scattering makes little difference in the predicted  $R_{\text{rs}}$ . However, there is a significant difference in the  $R_{\text{rs}}$  curves for the high detritus concentration. For the case of  $n = 0$  in Eq. (4) there is no wavelength dependence of  $b_{\text{det}}$ , and the high scattering at blue to red wavelengths makes  $R_{\text{rs}}$  higher at those wavelengths than it is for the case of  $n = 1$ , in which case the scattering decreases with wavelength. The percentage difference in the  $n = 0$  and 1 cases is about 7% at green wavelengths for the low concentration and 30% for the high concentration. For the high concentration, the difference is over 40% at red wavelengths. These results highlight the need for further studies

of scattering by detritus, because the assumed scattering model of Eq. (4) is one of the most speculative of the IOP models that underlie predictions of  $R_{rs}$ .

Figure 16 shows the range of  $R_{rs}$  values for the published range of  $\gamma = 0.006$  to  $0.014$ . For these runs,  $n = 1$  was used in the scattering model. The maximum spread of  $R_{rs}$  at low detritus concentrations is about 14% in the blue-green. At high concentrations  $R_{rs}$  varies by as much as 65% for the smallest to largest  $\gamma$  values. The dependence of  $R_{rs}$  on  $\gamma$  is stronger than on  $\alpha$  in the CDOM absorption model (for the same absorption by detritus and CDOM at 400 nm) both because of the wider spread of  $\gamma$  values and because the changes in absorption by detritus are compounded by scattering, whereas CDOM is non-scattering.

Just as with CDOM, both the magnitude of the variability in  $R_{rs}$  and the wavelengths where the variability is greatest depends on the reference wavelength used in the detritus absorption and scattering models. In our simulations we have used 400 nm as the wavelength where the detritus absorption and scattering coefficients are assumed known; consequently the curves in Figs. 15 and 16 all cross at that wavelength.

## 8. Variability Due to the Chlorophyll Fluorescence Efficiency

The chlorophyll fluorescence quantum efficiency  $\Phi^{chl}$  affects only the amount of light fluoresced by chlorophyll into the wavelength band from around 650 to 700 nm. All else being equal, a given change in  $\Phi^{chl}$  gives a corresponding change in the height of the chlorophyll fluorescence “bump” centered near 685 nm. This is illustrated in Fig. 17 for values of  $\Phi^{chl} = 0.01, 0.02$ , and  $0.05$ , which cover the typical range of  $\Phi^{chl}$  encountered in nature. For these runs, the wavelength bands were taken to be 5 nm wide between 650 and 700 nm in order to get smoother curves in the region of interest. All parameters other than  $\Phi^{chl}$  were taken at their base values. The figure also shows the case of  $\Phi^{chl} = 0.0$ , for which there is no fluorescence by chlorophyll; this run did include Raman scattering by the water and fluorescence by CDOM. It is clear that any algorithm that uses only the height of the chlorophyll fluorescence bump at 685 nm above some baseline (such as the  $\Phi^{chl} = 0.0$  curve) to recover the chlorophyll concentration will give an estimate that is strongly dependent on the assumed value of  $\Phi^{chl}$ .

## 9. Variability Due to Microbe Concentration

In Section 4 above we showed that the detailed species composition of the small-nanoplankton community does not greatly affect  $R_{rs}$  so long as the total nanoplankton particle concentration remains the same (recall Fig. 11). In Section 4 we kept the total concentration of the small nanoplankton fixed at  $10^9$  particles  $m^{-3}$  while the species composition was varied.

However, if the total concentration of any of the microbe subgroups (e.g., prochlorophytes, *Synechococcus*, or small nanoplankton) is varied, then  $R_{rs}$  will vary. This is illustrated in Fig. 18, which shows  $R_{rs}$  for the base model and for small nanoplankton (species PING through CURV) concentrations twice and five times their base concentrations. Microbial components VIRU through SYMA, and ELON and MICA, were all kept at their base values, as were CDOM and detritus. The chlorophyll concentrations of these three runs were 0.718, 1.046, and 2.03 mg Chl  $m^{-3}$ .

Comparison of Fig. 18 with Figs. 13 and 16 shows that, at some wavelengths, the change in  $R_{rs}$  associated with variability in the CDOM and detritus absorption parameters  $\alpha$  and  $\gamma$  is as great as the change in  $R_{rs}$  associated with a factor-of-two change in the total concentration of small nanoplankton (which, in the present case, corresponds to a ~50% change in the total chlorophyll concentration). Note also that the change in the chlorophyll fluorescence bump near 685 nm in Fig. 18, which is associated with a change in the chlorophyll concentration, is indistinguishable with the changes seen in Fig. 17, which were associated with changes in the quantum efficiency of chlorophyll fluorescence. Although the overall character of these  $R_{rs}$  curves is somewhat different from those seen above, it is not hard to see how inherent variability in the unknown parameters of IOP models can lead to large errors (factors of two) in values of the chlorophyll concentration or other quantities as retrieved from remote-sensing reflectances.

It is of interest to see how other changes in microbe concentrations affect  $R_{rs}$ . A series of runs was therefore made in which the concentration of each microbe from heterotrophic bacteria to the largest dinoflagellate (MICA in Table 1) was increased one at a time to ten times its base concentration. [Previous studies (Mobley and Stramski, 1997) have shown that increasing the concentration of marine viruses has almost no effect on the optical properties of a water body.] The corresponding total chlorophyll concentrations ranged from 0.718 to 2.153 mg Chl  $m^{-3}$ . From an oversimplified viewpoint, each of these runs could be thought of as representing a particular microbe during bloom conditions. Thus, for example, the run with component SYNE at ten times its base could be regarded as a *Synechococcus* bloom, with all other microbes being at non-bloom concentrations.

Figure 19 shows for reference the chlorophyll-specific absorption coefficients  $a^*$  for these runs and for the base concentration, as computed from the total absorption coefficients divided by the associated chlorophyll concentrations. These curves are similar to those seen in Fig. 2, although there is a difference: the  $a^*$  curves of Fig. 2 are for individual species, whereas the  $a^*$  curves of Fig. 19 are for entire microbe communities in which one microbe has a larger-than-usual concentration. Figure 20 shows for reference the corresponding chlorophyll-specific scattering coefficients  $b^*$ . The variability of these  $a^*$  and  $b^*$  curves about the ones for the base concentrations also can be thought of as simulating the variability in  $R_{rs}$  that would arise from



using various chlorophyll-specific absorption and scattering functions in simple bio-optical models, which parameterize the microbial absorption and scattering coefficients in terms of the chlorophyll concentration alone.

It would be of great value to be able to classify blooms in more detail than just their total chlorophyll concentration. For example, we can ask if it is possible to determine from  $R_{rs}$  whether a bloom is made up of “small” or “large” particles. It is also of interest to ask if particular microbial species have sufficiently distinct  $R_{rs}$  signatures to allow their identification during bloom conditions. Therefore in Fig. 21, which shows the  $R_{rs}$  values for this series of runs, the line pattern is used to identify the “small” and “large” particles. The small particles (dotted lines) are taken to be those less than 4  $\mu\text{m}$  in size, namely components HBAC, PROC, SYNE, and SYMA in Table 1. The large particles (dashed lines) are those larger than 4  $\mu\text{m}$  in size, namely components PING to MICA in Table 1. Only HBAC and PROC show clearly distinct  $R_{rs}$  signatures; these two curves and the one for the base concentration are also labeled. The shading shows the nominal SeaWiFS sensor bands.

For these simulations, the small-particle blooms generally give  $R_{rs}$  curves that lie below the large-particle blooms, with the exception of the heterotrophic bacteria bloom (component HBAC at ten times its base concentration). Increasing the concentration of HBAC gives an  $R_{rs}$  curve that lies significantly above the base  $R_{rs}$  curve. As has already been explained (Mobley and Stramski, 1997), the anomalous behavior of HBAC occurs because heterotrophic bacteria are weakly absorbing but strongly scattering. Increasing their concentration therefore increases  $b_b$  relatively more than  $a$ , so that  $b_b/a$  and hence  $R_{rs}$  can increase with increasing concentration. For all other species in the database, the increase in absorption dominates the increase in scattering, and  $R_{rs}$  is less than its base value.

Figure 22 shows four sets of scatter plots of  $R_{rs}(\lambda_1)/R_{rs}(\lambda_2)$  vs. chlorophyll concentration for  $\lambda_1$  and  $\lambda_2$  corresponding closely to various SeaWiFS sensor bands. Such ratios have a venerable history in the retrieval of information such as the chlorophyll concentration or  $K_d(490\text{ nm})$  from remotely sensed “ocean color” signals. Here we wish to see if such plots might be used to deduce information about particle size or type from  $R_{rs}$ . In all figure panels the symbols identify the particle types:  $\times$  is the base concentration,  $*$  is HBAC,  $\Delta$  is PROC,  $\diamond$  is other small particles (SYNE and SYMA), and  $\square$  is the large particles.

Examination of Fig. 21 shows that the ratio  $R_{rs}(415)/R_{rs}(485)$  might best distinguish the HBAC bloom as an outlier from the blooms of all other species; Fig. 22a shows the corresponding scatter plot. As anticipated, the point for the HBAC bloom is well separated from the cluster of all other points. Likewise,  $R_{rs}(485)/R_{rs}(515)$  appears to distinguish the PROC bloom from all others; Fig. 22b shows the scatter plot. The ratios  $R_{rs}(445)/R_{rs}(485)$  or  $R_{rs}(445)/R_{rs}(505)$  appear to show the best chance of distinguishing small particles from large



particles; the results are shown in Figs. 22c and 22d. The clusters of points for small and large particles do not separate as clearly as might be hoped, but the results are encouraging. These particular plots do suggest some ways of extracting certain types of particle information from SeaWiFS or hyperspectral imagery. However, whether such simple ratios would prove useful in practice remains uncertain because of the limited range of simulations made here. Many more simulations would have to be made in order to see how well such algorithms perform under a wide range of complicating environmental and in-water conditions.

## 10. Conclusions and Recommendations

The numerical simulations above show that the errors in predicted values of  $R_{rs}$  that arise from variability in the parameters of the underlying IOP models are often tens of percent in magnitude. In some cases, these errors can be as great as the changes induced in  $R_{rs}$  by a factor-of-two change in the chlorophyll concentration. Clearly, such errors in  $R_{rs}$  place limits on the accuracy of information that can be extracted from remotely sensed ocean color data, regardless of the inversion algorithms employed.

The error induced in  $R_{rs}$ , for example, by unknowingly using a wrong value for the CDOM absorption exponent coefficient  $\alpha$  could be reduced if *a priori* information about a particular water body could be used to improve the guess for the likely value of  $\alpha$ . Carder et al. (1989) have shown that the  $\alpha$  values characteristic of fulvic acids are twice as large as the  $\alpha$  values for humic acids. Thus if some knowledge about the ratio of fulvic to humic acids in the CDOM of a particular water body is available, it may be possible to determine whether an  $\alpha$  value near the high, middle, or low end of the possible range of  $\alpha$  values is likely to apply to the water body in question. Using an improved guess for  $\alpha$  would then lead to less error in the prediction of  $R_{rs}$ , even if the magnitude of the error remains unknown. Similar comments about other IOP model parameters can be made.

Detritus is one of the least-studied components of natural waters, even though its absorption and scattering properties can have a considerable effect on  $R_{rs}$ . The model for scattering by detritus, Eq. (4), is particularly speculative, and further research on the scattering properties of detritus is needed.

The scatter plots of  $R_{rs}(\lambda_1)/R_{rs}(\lambda_2)$  vs. chlorophyll concentration show that it may be possible to extract at least some information about particle type or size from  $R_{rs}$ . However, the results presented here are very tentative and, in any case, more sophisticated algorithms should be evaluated for such analyses. The combination of the Hydrolight numerical model and the ever-growing database of particle optical properties is an ideal tool for the development and evaluation of such algorithms for processing hyperspectral imagery.

## **ACKNOWLEDGMENTS**

The development of the Hydrolight radiative transfer model was partially supported by the Office of Naval Research (ONR) Environmental Optics Program and the Naval Research Laboratory under various contracts to author C.D.M. Development of the database was supported by the ONR Environmental Optics Program by grants N00014-88-J-1216, N00014-93-1-0134 and N00014-95-1-0491, and by NASA grant NAGW-2574, to author D.S. and his colleagues. Further development of the database and modeling methodology was supported by the ONR Environmental Optics Program under contract N00014-97-C-0024 to C.D.M.

## REFERENCES

- Bricaud, A., A. Morel, and L. Prieur, 1981. Absorption by dissolved organic matter of the sea (yellow substance) in the UV and visible domains, *Limnol. Oceanogr.*, **28**(5), 816-832.
- Carder, K. L., R. G. Steward, G. R. Harvey, and P. B. Ortner, 1989. Marine humic and fulvic acids: Their effects on remote sensing of ocean chlorophyll, *Limnol. Oceanogr.*, **34**(1), 68-81.
- Hawes, S. K., 1992. Quantum fluorescence efficiencies of marine fulvic and humic acids, Master's Thesis, Dept. of Marine Science, Univ. of South Florida, St. Petersburg, FL, 92 pages.
- Højerslev, N. K., 1998. spectral light absorption by gelbstoff in coastal waters displaying highly different concentrations, paper presented at *Ocean Optics XIV*, Kona, HI.
- Kiefer, D. A. and R. A. Reynolds, 1992. Advances in understanding phytoplankton fluorescence and photosynthesis. In *Primary Productivity and Biogeochemical Cycles in the Sea*, edited by P. G. Falkowsky and A. D. Woodhead, Plenum Press, New York, 155-174.
- Kiefer, D. A., W. S. Chamberlin, and C. R. Booth, 1989. Natural fluorescence of chlorophyll  $\alpha$ : relationship to photosynthesis and chlorophyll concentration in the western South Pacific gyre, *Limnol. Oceanogr.*, **34**(5), 868-881.
- Lee, Z. P., K. L. Carder, S. K. Hawes, R. G. Steward, T. G. Peacock, and C. O. Davis, 1994. Model for the interpretation of hyperspectral remote-sensing reflectance. *Appl. Optics*, **33**(24), 5721-5732.
- Lee, Z. P., K. L. Carder, T. G. Peacock, C. O. Davis, and J. L. Mueller, 1996. Method to derive ocean absorption coefficients from remote-sensing reflectance. *Appl. Optics*, **35**(3), 453-462.
- Mobley, C. D., 1994. *Light and Water: Radiative Transfer in Natural Waters*, Academic Press, San Diego, 592 pages.
- Mobley, C. D., 1995. Hydrolight 3.0 Users' Guide. Final Report, SRI Project 5632, SRI International, Menlo Park, CA., 65 pages.

Mobley, C. D., 1999. Estimation of the remote-sensing reflectance from above-water measurements. *Appl. Optics*, submitted. (A copy of this paper is attached as Appendix B.)

Mobley, C. D. and D. Stramski, 1997. Effects of microbial particles on oceanic optics: Methodology for radiative transfer modeling and example simulations. *Limnol. Oceanogr.*, **42**(3), 550-560.

Mobley, C. D., B. Gentili, H. R. Gordon, Z. Jin, G. W. Kattawar, A. Morel, P. Reinersman, K. Stamnes, and R. H. Stavn, 1993. Comparison of numerical models for computing underwater light fields, *Appl. Optics*, **32**, 7484-7504.

Prieur, L. and S. Sathyendranath, 1981. An optical classification of coastal and oceanic waters based on the specific spectral absorption curves of phytoplankton pigments, dissolved organic matter, and other particulate materials, *Limnol. Oceanogr.*, **26**(4), 671-689.

Roesler, C. S., M. J. Perry, and K. L. Carder, 1989. Modeling in situ phytoplankton absorption from total absorption spectra in productive inland marine waters, *Limnol. Oceanogr.*, **34**(8), 1510-1523.

Sathyendranath, S., L. Lazzara, and L. Prieur, 1987. Variations in the spectral values of specific absorption of phytoplankton, *Limnol. Oceanogr.*, **32**(2), 403-415.

Smith, R. C. and K. S. Baker, 1981. Optical properties of the clearest natural waters, *Applied Optics* **20**(2), 177-184.

Stramski, D. and C. D. Mobley, 1997. Effects of microbial particles on oceanic optics: A database of single-particle optical properties, *Limnol. Oceanogr.*, **42**(3), 538-549.

Stramski, D., A. Bricaud, and A. Morel, 1998. A database of single-particle optical properties. Paper presented at *Ocean Optics XIV*, Nov 10-13, Kona, HI.

Table 1. Microbes in the database. The notation 1.0e13 means  $1.0 \times 10^{13}$ , etc.

<i>i</i>	Label	Microbe	Mean Diameter ( $\mu\text{m}$ )	Base Concentration (particles/ $\text{m}^3$ )
1	VIRU	Marine viruses	0.07	1.0e13
2	HBAC	Heterotrophic bacteria	0.55	4.0e11
3	PROC	generic prochlorophyte: the average of PMED, <i>Prochlorococcus</i> strain MED	0.59	7.0e10
4	SYNE	PNAS, average of <i>Prochlorococcus</i> strains NATL & SARG generic <i>Synechococcus</i> : the average of SM41, <i>Synechococcus</i> strain MAX41 (Cyanophyceae) SM01, <i>Synechococcus</i> strain MAX01 (Cyanophyceae) SROS, <i>Synechococcus</i> strain ROS04 (Cyanophyceae) SDC2, <i>Synechococcus</i> strain DC2 (Cyanophyceae) S103, <i>Synechococcus</i> strain WH8103 (Cyanophyceae) the average of	0.92 0.94 1.08 1.14 1.14	2.0e10
5	SYMA	SCYS, <i>Synechocystis</i> (Cyanophyceae) MARI, <i>Anacystis marina</i> (Cyanophyceae)	1.39 1.43	8.0e9
6	PING	<i>Pavlova pinguis</i> (Haptophyceae)	3.97	4.5056e8
7	PSEU	<i>Thalassiosira pseudonana</i> (Bacillariophyceae)	3.99	0.9808e8
8	LUTH	<i>Pavlova lutheri</i> (Haptophyceae)	4.26	0.9924e8
9	GALB	<i>Isochrysis galbana</i> (Haptophyceae)	4.45	0.4839e8
10	HUXL	<i>Emiliania huxleyi</i> (Haptophyceae)	4.93	0.4339e8
11	CRUE	<i>Porphyridium cruentum</i> (Rhodophyceae)	5.22	0.4496e8
12	FRAG	<i>Chroomonas fragarioides</i> (Cryptophyceae)	5.57	0.4768e8
13	PARV	<i>Prymnesium parvum</i> (Haptophyceae)	6.41	0.6247e8
14	BIOC	<i>Dunaliella bioculata</i> (Chlorophyceae)	6.71	0.3966e8
15	TERT	<i>Dunaliella tertiolecta</i> (Chlorophyceae)	7.59	0.3570e8
16	CURV	<i>Chaetoceros curvisetum</i> (Bacillariophyceae)	7.73	0.2987e8
17	ELON	<i>Hymenomonas elongata</i> (Haptophyceae)	11.77	1.7e7
18	MICA	<i>Prorocentrum micans</i> (Dinophyceae)	27.64	2.0e6

## Figure Captions

- Fig. 1a. Example of a “weak” CDOM fluorescence quantum efficiency function  $\eta^{\text{CDOM}}$ . This function was measured by Hawes (1992) on a water sample taken in the Peru upwelling.
- Fig. 1b. Example of a “moderate” CDOM fluorescence quantum efficiency function  $\eta^{\text{CDOM}}$ . This function was measured by Hawes (1992) on a water sample taken in the North Atlantic at 60°N, 20°W.
- Fig. 1c. Example of a “strong” CDOM fluorescence quantum efficiency function  $\eta^{\text{CDOM}}$ . This function was measured by Hawes (1992) on a water sample taken in the Gulf of Mexico on the mid-West Florida shelf.
- Fig. 2. Chlorophyll-specific spectral absorption coefficients  $a^*$  for eight species of phytoplankton (from Sathyendranath et al., 1987).
- Fig. 3. Absorption cross sections  $[\sigma_a(\lambda)]_i$  of the 18 microbial components in the database; each component is normalized to its value at 400 nm.
- Fig. 4. Scattering cross sections  $[\sigma_b(\lambda)]_i$  of the 18 microbial components in the database; each component is normalized to its value at 400 nm.
- Fig. 5. The scattering phase function  $\tilde{\beta}_i(\psi, \lambda)$  for *Thalassiosira pseudonana* (species  $i = 7$ , PSEU, in Table 1).
- Fig. 6. Particle number size distributions  $n(x)$  for the 18 microbial species at the base concentrations (light solid lines). The sum of these distributions at each size is shown as the heavy solid line; the dashed line shows the -4 power law.
- Fig. 7. The total absorption coefficient  $a(\lambda)$  for the base concentrations and models (heavy solid line). The line patterns identify the contributions by selected components to the total: the dotted line is the contribution by water; light solid is all microbes; dashed is detritus, dash-dot is CDOM.

- Fig. 8. Same as Fig. 7, but with an expanded ordinate scale. The line patterns identify the contributions by selected components to the total: the dotted line is the contribution by water; light solid is all microbes; dashed is detritus, dash-dot is CDOM.
- Fig. 9. The total scattering coefficient  $b(\lambda)$  for the base concentrations and models (heavy solid line). The line patterns identify the contributions by selected components to the total: the dotted line is the contribution by water; light solid is all microbes; dashed is detritus.
- Fig. 10. Three sets of possible concentrations for the 11 small nanoplankton species; the base set of Table 1 is the solid line.
- Fig. 11.  $R_{rs}$  as predicted using the three sets of small nanoplankton concentrations seen in Fig. 10. The line patterns correspond to those of Fig. 10.
- Fig. 12. The component and total absorption coefficients for  $a_{CDOM}(400) = 0.2 \text{ m}^{-1}$ . The line patterns are as in Fig. 24.
- Fig. 13.  $R_{rs}$  as predicted for low and high CDOM concentrations (as labeled) and for three values of the CDOM exponent parameter  $\alpha$ : solid line,  $\alpha = 0.014$ ; dashed line,  $\alpha = 0.019$ ; dotted line,  $\alpha = 0.011$ . The shaded bars are the SeaWiFS bands.
- Fig. 14.  $R_{rs}$  as predicted for low and high CDOM concentrations (as labeled) and for the strong (dashed lines), moderate (solid lines), and weak (dotted lines)  $\eta^{CDOM}$  functions of Fig. 1.
- Fig. 15.  $R_{rs}$  as predicted for low and high detritus concentrations (as labeled) and for scattering by detritus that is inversely proportional to the wavelength (solid lines;  $n = 1$  in Eq. 4), and independent of wavelength (dotted lines,  $n = 0$  in Eq. 4).
- Fig. 16.  $R_{rs}$  as predicted for low and high detritus concentrations (as labeled) and for three values of the detritus absorption exponent parameter  $\gamma$ : solid line,  $\gamma = 0.011$ ; dashed line,  $\gamma = 0.014$ ; dotted line,  $\gamma = 0.006$ ;  $n = 1$  was used in the detritus scattering model.
- Fig. 17.  $R_{rs}$  as predicted for various chlorophyll fluorescence quantum efficiencies  $\Phi^{chl}$  (as labeled); the curve for  $\Phi^{chl} = 0$  corresponds to no fluorescence by chlorophyll.



- Fig. 18  $R_{rs}$  as predicted for three different total concentrations of the small nanoplankton; other components had their base values. The solid line is for the base concentrations, the dotted line is for double the base concentrations of the small nanoplankton, and the dashed line is for five times their base concentrations.
- Fig. 19. Chlorophyll-specific absorption coefficients  $a^*$  for the base concentration (heavy line) and for the various single-particle bloom conditions (light lines).
- Fig. 20. Chlorophyll-specific scattering coefficients  $b^*$  for the base concentration (heavy line) and for the various single-particle bloom conditions (light lines).
- Fig. 21.  $R_{rs}$  for the base concentrations (solid line) and for the various single-particle blooms. The dotted lines are blooms of small particles ( $< 4\mu\text{m}$  diameter), and the dashed lines are blooms of large particles ( $> 4\mu\text{m}$ ).
- Fig. 22a.  $R_{rs}(415)/R_{rs}(485)$  as a function of the chlorophyll concentration for the base concentration and for various single-particle blooms. The symbols identify the particle types:  $\times$  is the base concentration,  $*$  is the HBAC bloom,  $\Delta$  is PROC,  $\diamond$  is other small particles, and  $\square$  is the large particles.
- Fig. 22b.  $R_{rs}(485)/R_{rs}(515)$  as a function of the chlorophyll concentration for the base concentration and for various single-particle blooms. The symbols are as in Fig. 22a:  $\times$  base,  $*$  HBAC,  $\Delta$  PROC;  $\diamond$  other small particles; and  $\square$  large particles.
- Fig. 22c.  $R_{rs}(445)/R_{rs}(485)$  as a function of the chlorophyll concentration for the base concentration and for various single-particle blooms. The symbols are as in Fig. 22a:  $\times$  base,  $*$  HBAC,  $\Delta$  PROC,  $\diamond$  other small particles, and  $\square$  large particles.
- Fig. 22d.  $R_{rs}(445)/R_{rs}(505)$  as a function of the chlorophyll concentration for the base concentration and for various single-particle blooms. The symbols are as in Fig. 22a:  $\times$  base,  $*$  HBAC,  $\Delta$  PROC,  $\diamond$  other small particles, and  $\square$  large particles.

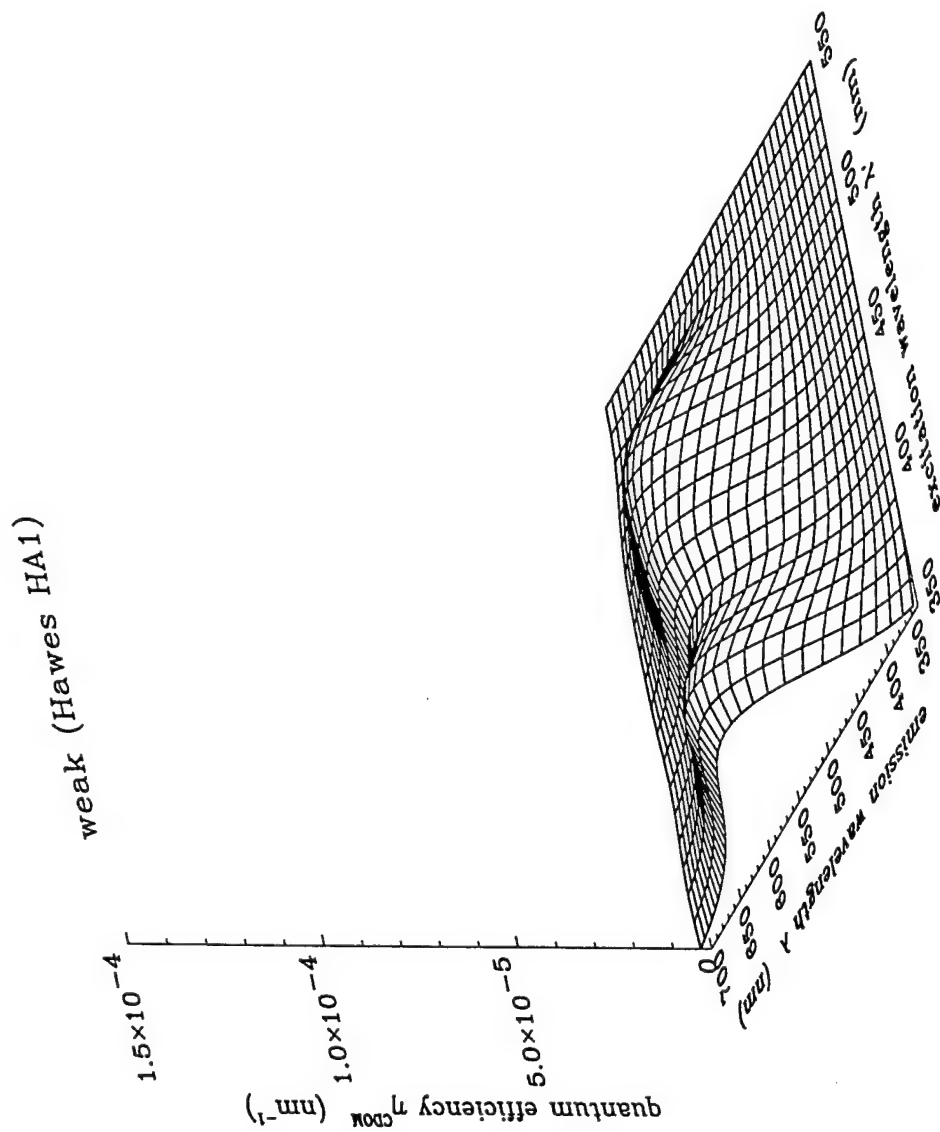


Fig. 1a. Example of a "weak" CDOM fluorescence quantum efficiency function  $\eta^{\text{CDOM}}$ .  
 This function was measured by Hawes (1992) on a water sample taken in the  
 Peru upwelling.

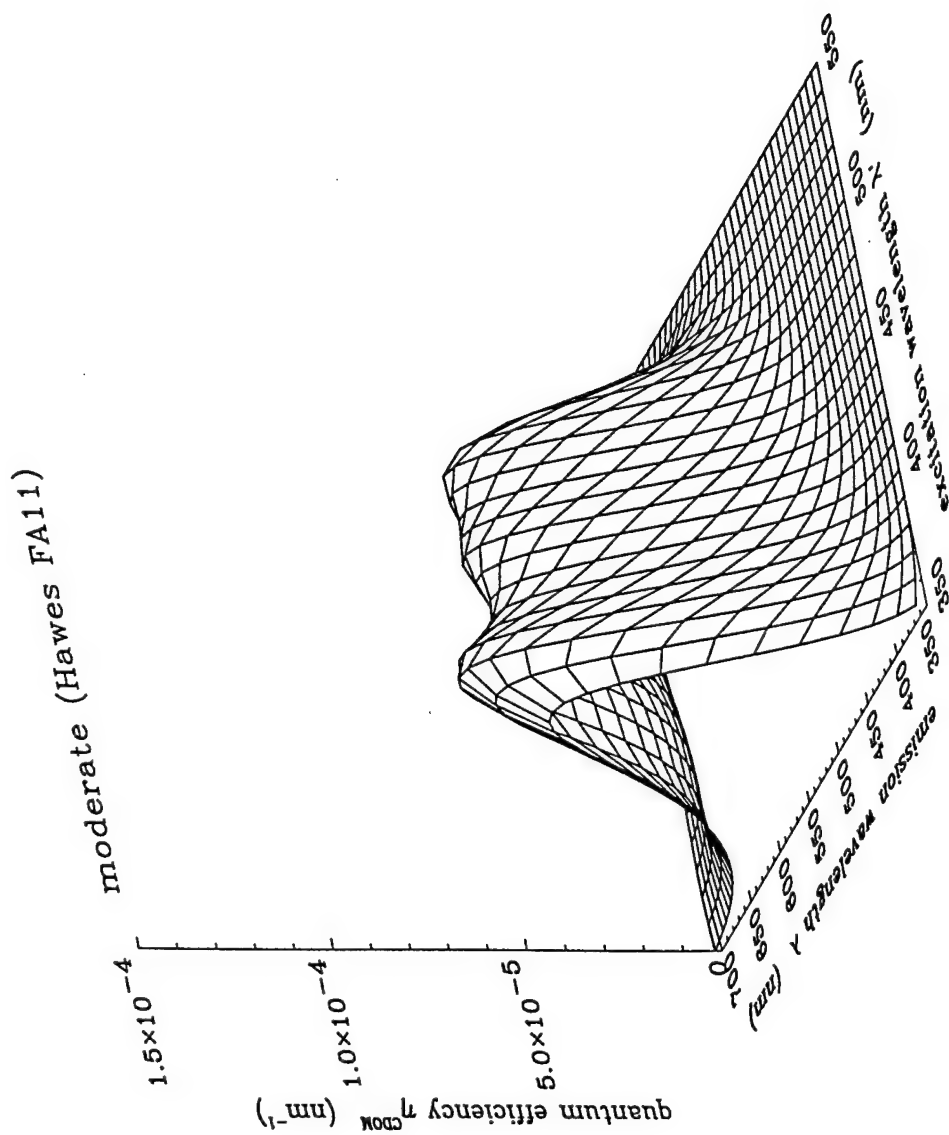


Fig. 1b. Example of a "moderate" CDOM fluorescence quantum efficiency function  $\eta^{\text{CDOM}}$ . This function was measured by Hawes (1992) on a water sample taken in the North Atlantic at 60°N, 20°W.

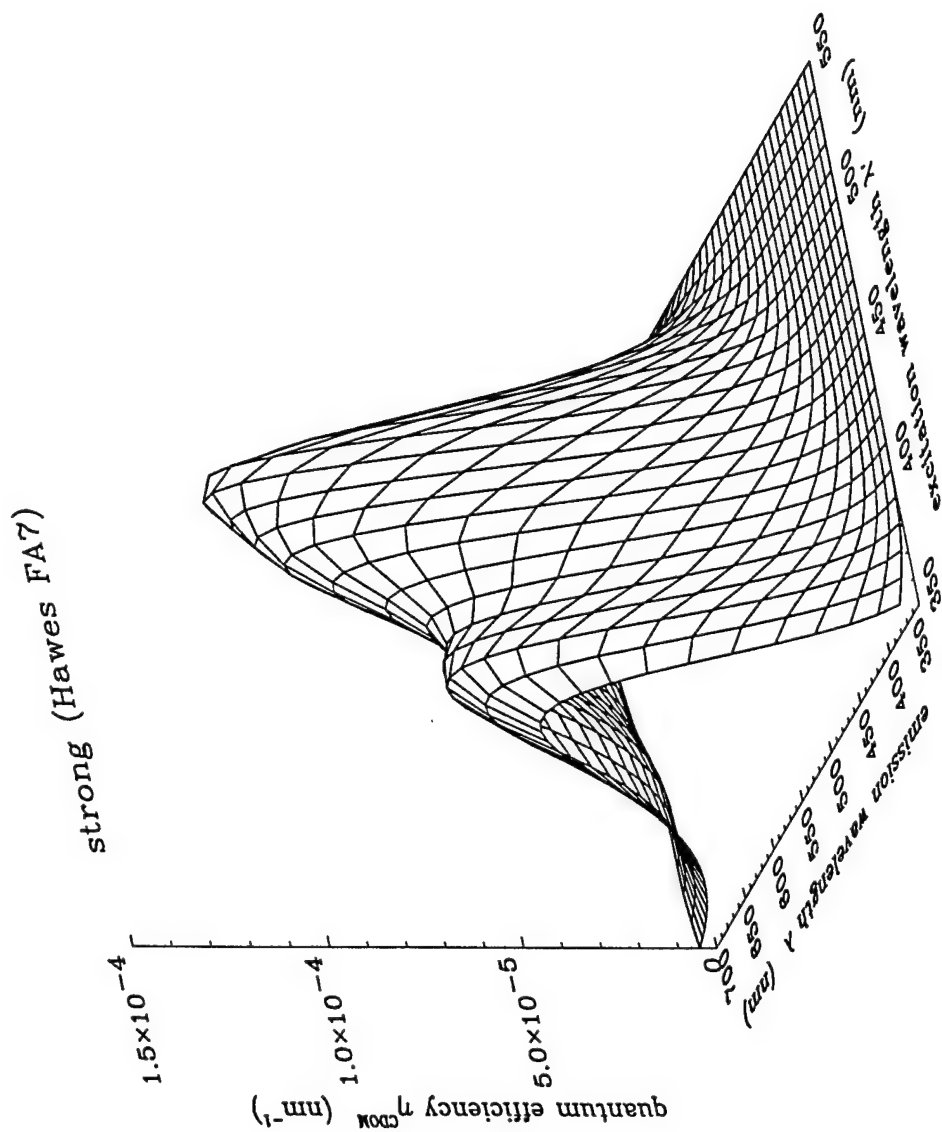


Fig. 1c. Example of a “strong” CDOM fluorescence quantum efficiency function  $\eta^{\text{CDOM}}$ . This function was measured by Hawes (1992) on a water sample taken in the Gulf of Mexico on the mid-West Florida shelf.

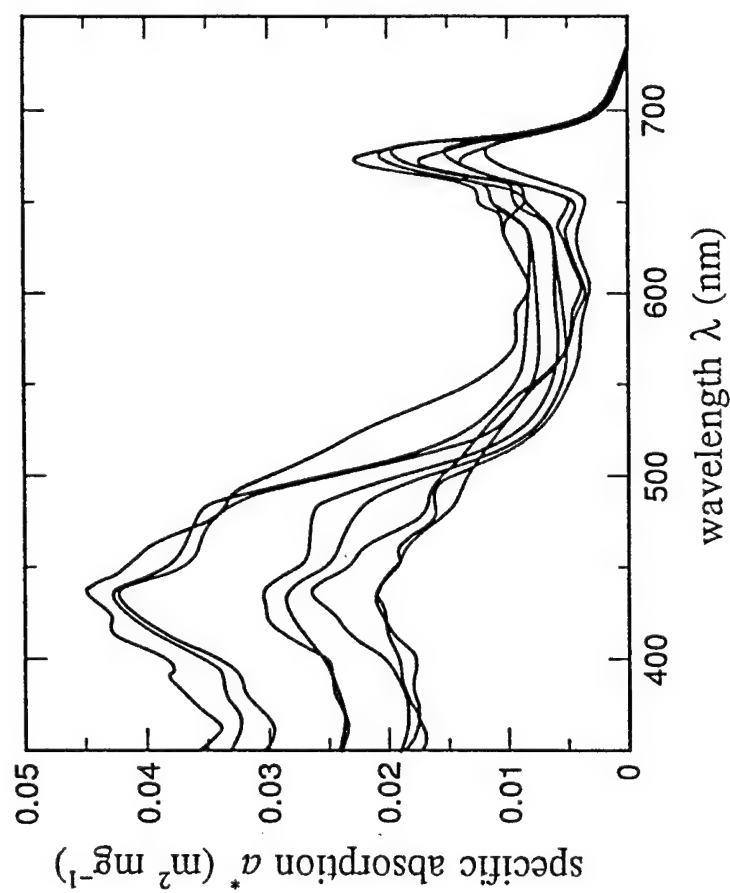


Fig. 2. Chlorophyll-specific spectral absorption coefficients  $a^*$  for eight species of phytoplankton (from Sathyendranath et al., 1987).

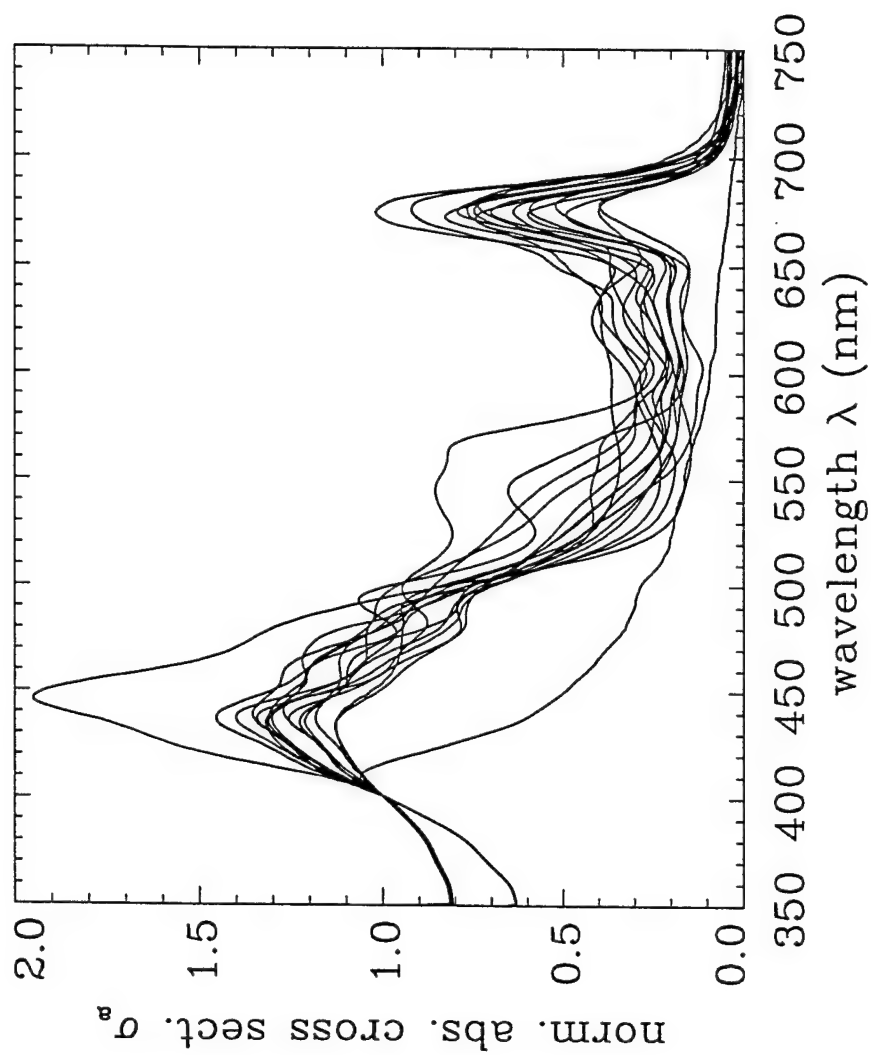


Fig. 3. Absorption cross sections  $[\sigma_a(\lambda)]_i$  of the 18 microbial components in the database; each component is normalized to its value at 400 nm.

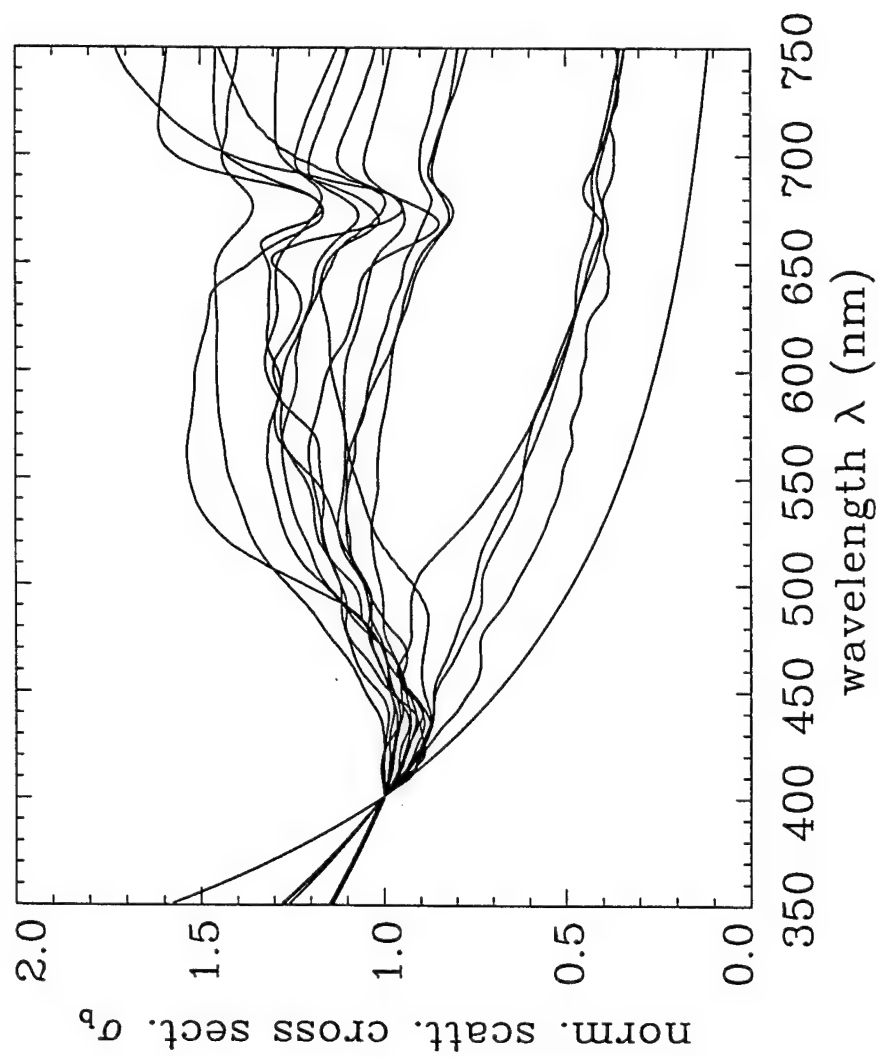


Fig. 4. Scattering cross sections  $[\sigma_b(\lambda)]_i$  of the 18 microbial components in the database; each component is normalized to its value at 400 nm.



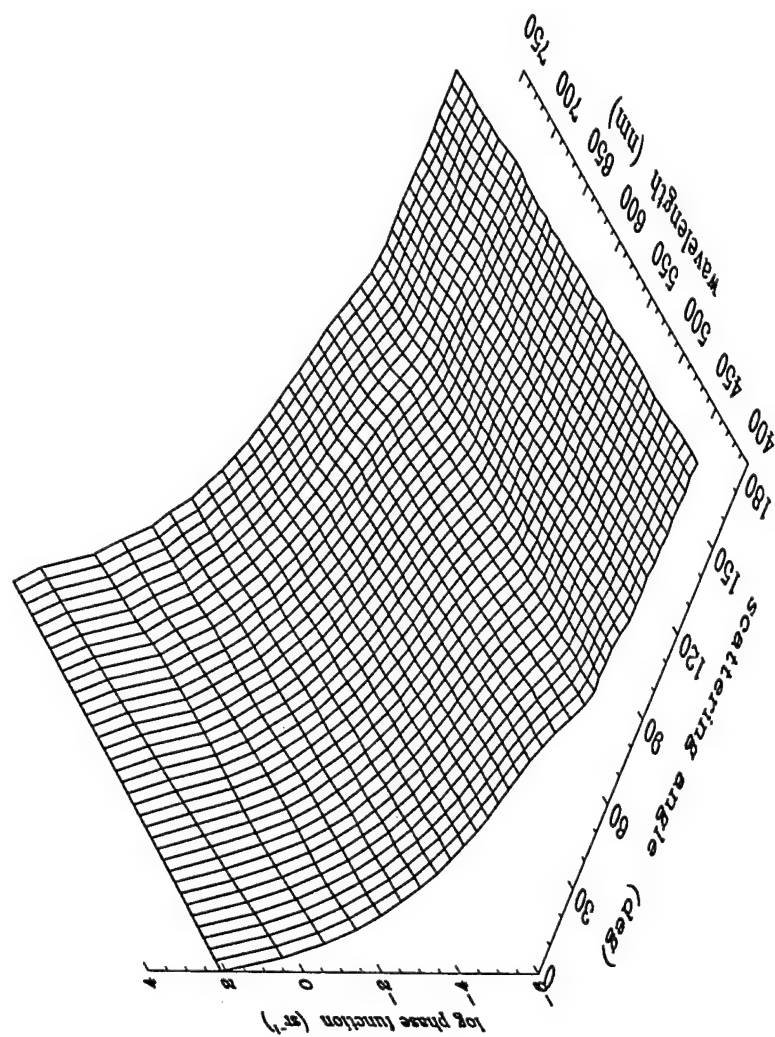


Fig. 5. The scattering phase function  $\tilde{\beta}_i(\psi, \lambda)$  for *Thalassiosira pseudonana* (species  $i = 7$ , PSEU, in Table 1).

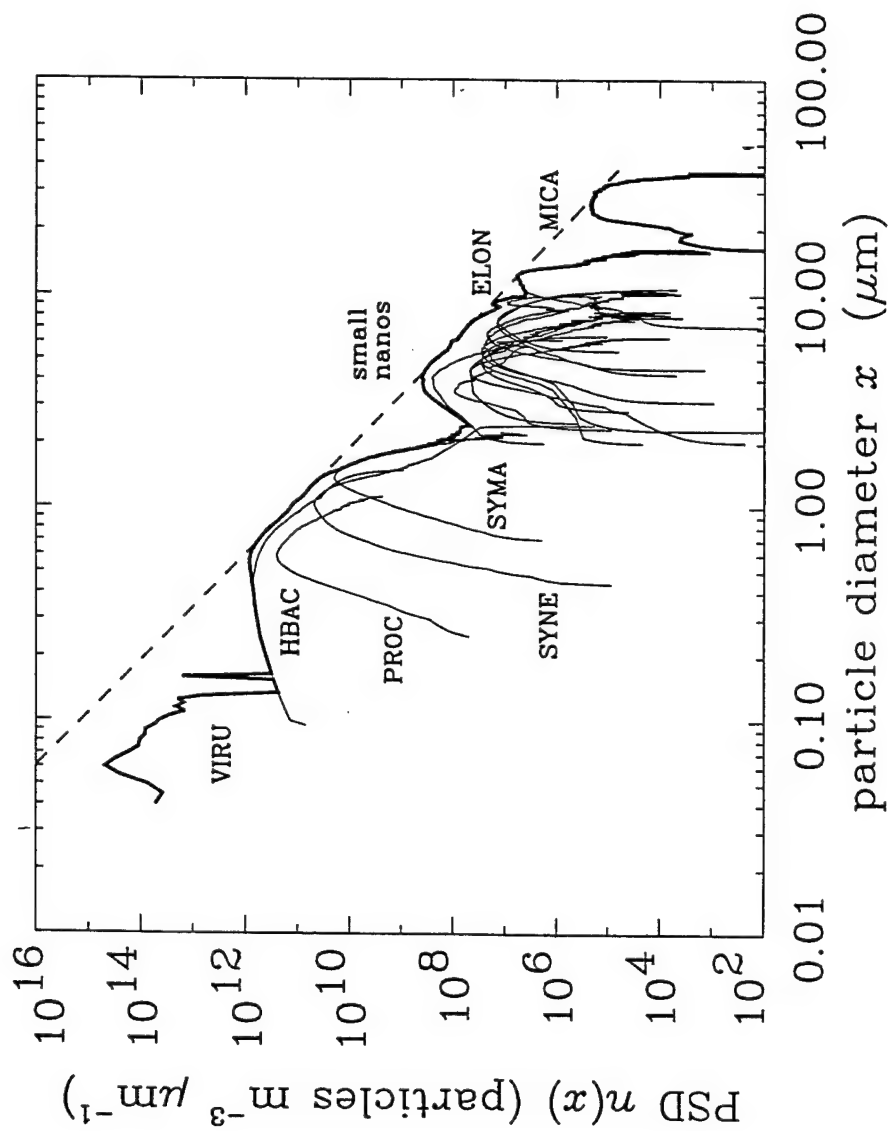


Fig. 6. Particle number size distributions  $n(x)$  for the 18 microbial species at the base concentrations (light solid lines). The sum of these distributions at each size is shown as the heavy solid line; the dashed line shows the -4 power law.

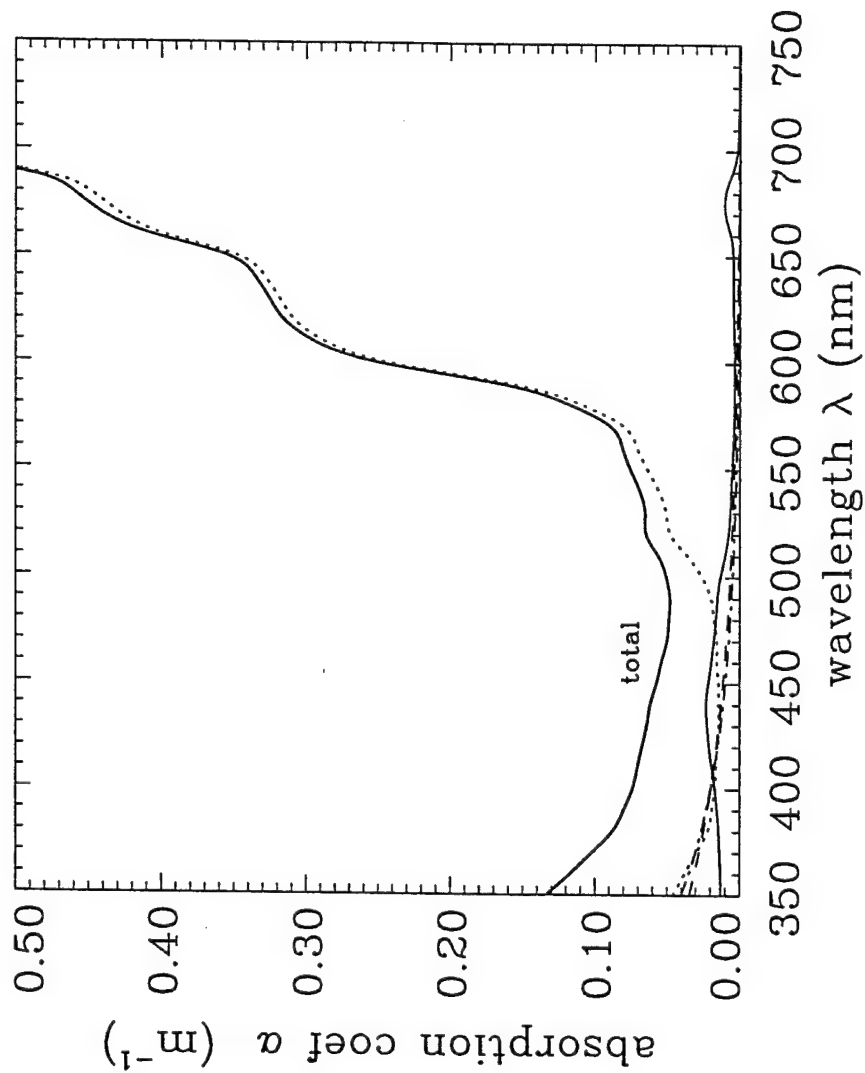


Fig. 7. The total absorption coefficient  $a(\lambda)$  for the base concentrations and models (heavy solid line). The line patterns identify the contributions by selected components to the total: the dotted line is the contribution by water; light solid is all microbes; dashed is detritus, dash-dot is CDOM.

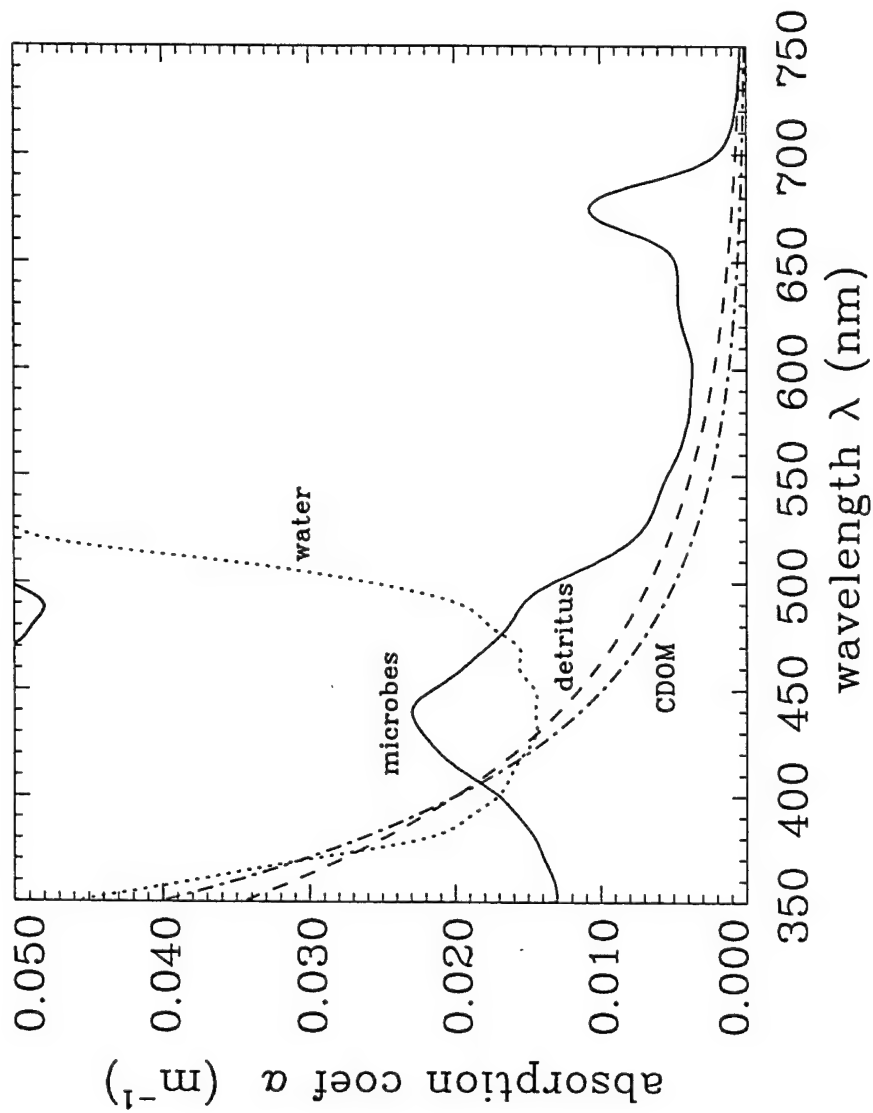


Fig. 8. Same as Fig. 7, but with an expanded ordinate scale. The line patterns identify the contributions by selected components to the total: the dotted line is the contribution by water; light solid is all microbes; dashed is detritus, dash-dot is CDOM.

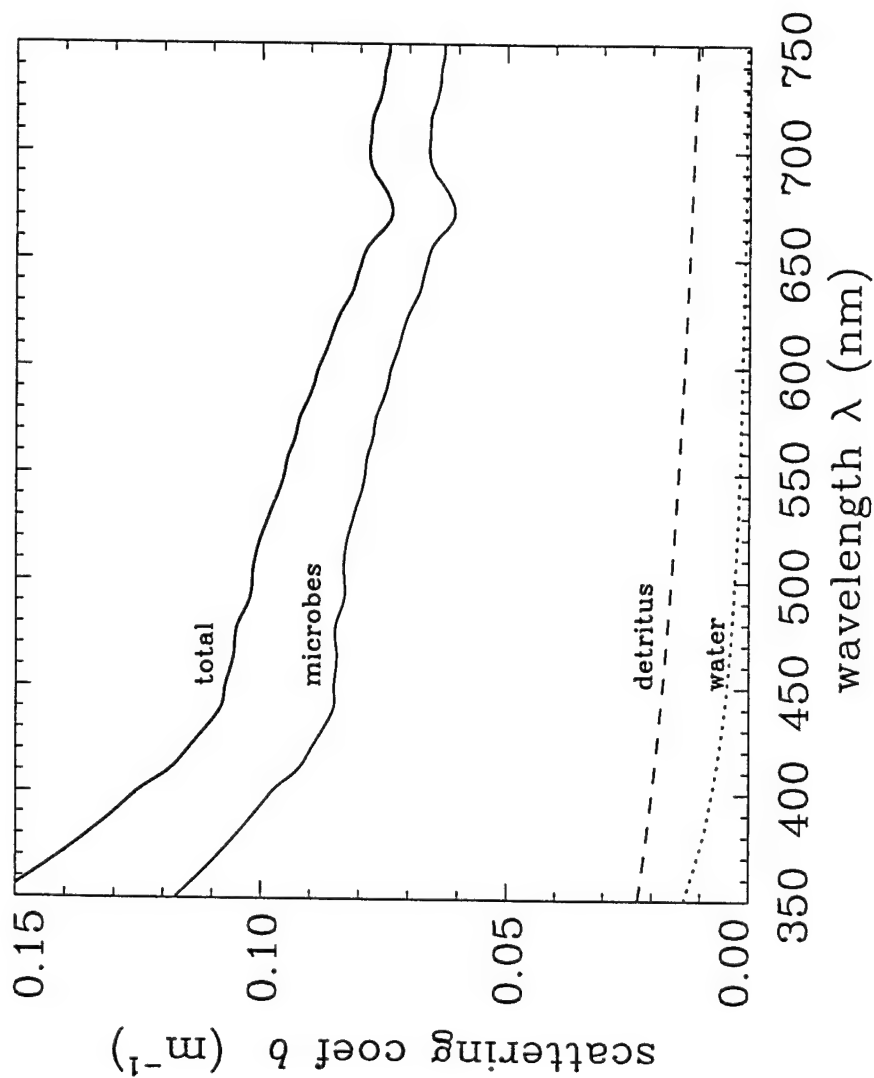


Fig. 9. The total scattering coefficient  $b(\lambda)$  for the base concentrations and models (heavy solid line). The line patterns identify the contributions by selected components to the total: the dotted line is the contribution by water; light solid is all microbes; dashed is detritus.

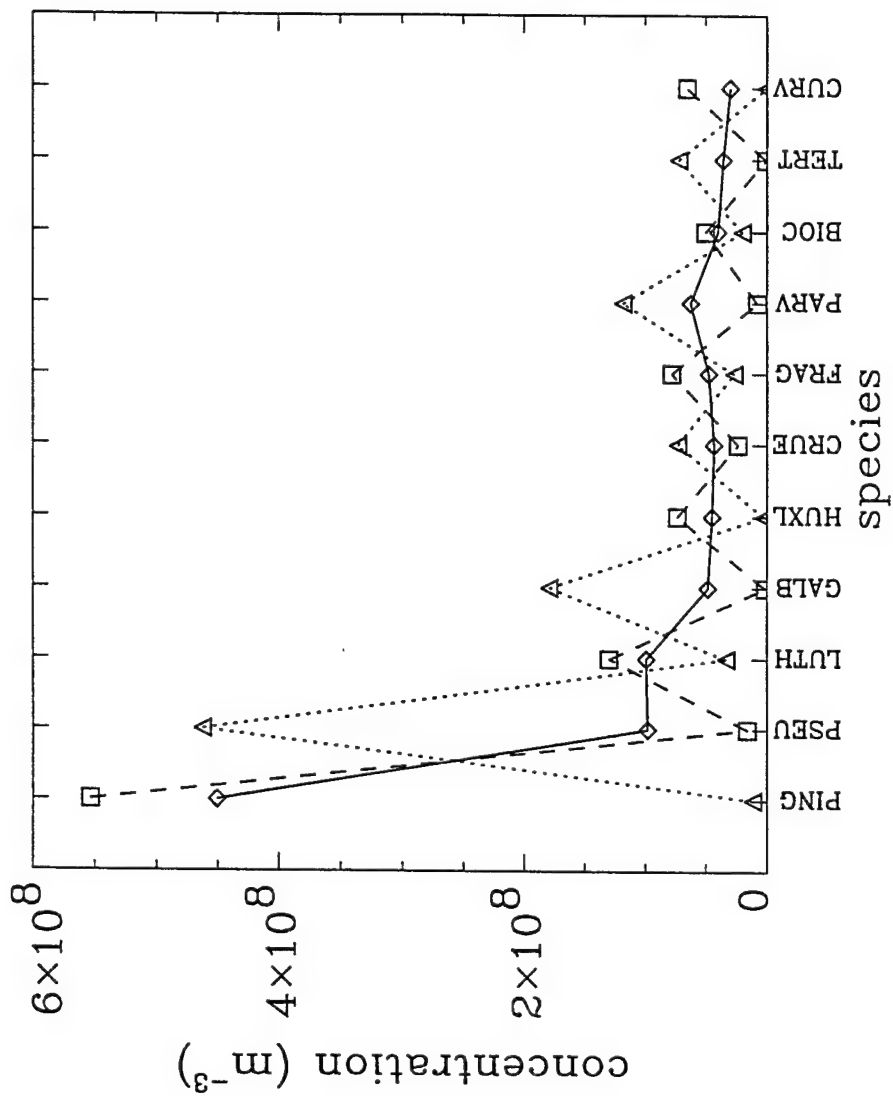


Fig. 10. Three sets of possible concentrations for the 11 small nanoplankton species; the base set of Table 1 is the solid line.

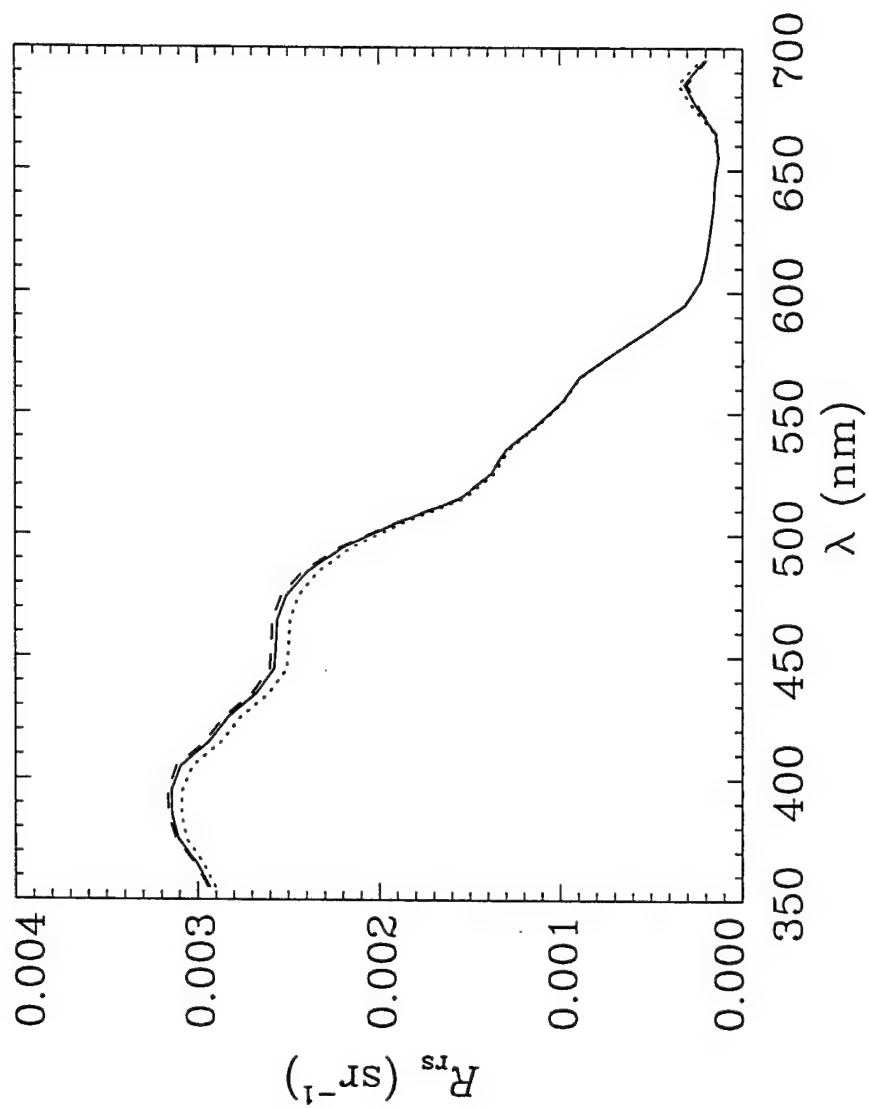


Fig. 11  $R_{rs}$  as predicted using the three sets of small nanoplankton concentrations seen in Fig. 10. The line patterns correspond to those of Fig. 10.



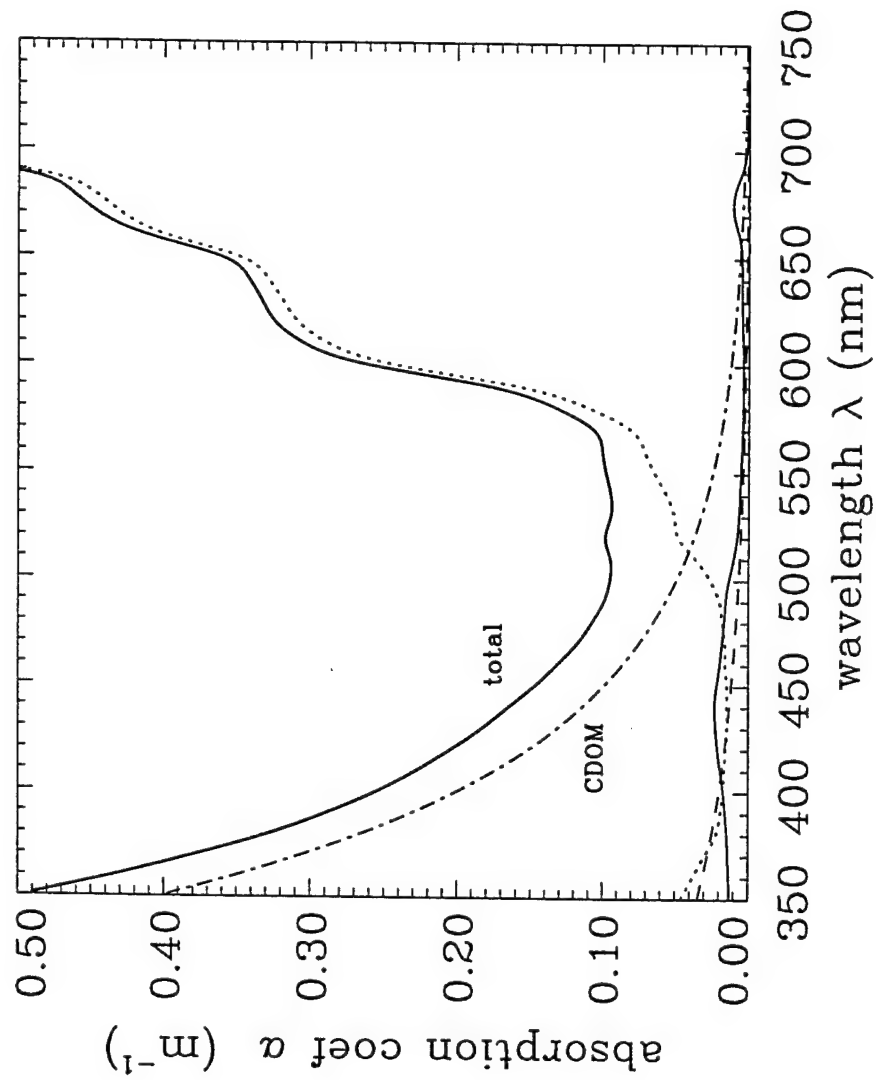


Fig. 12. The component and total absorption coefficients for  $a_{\text{CDOM}}(400) = 0.2 \text{ m}^{-1}$ .  
The line patterns are as in Fig. 7.

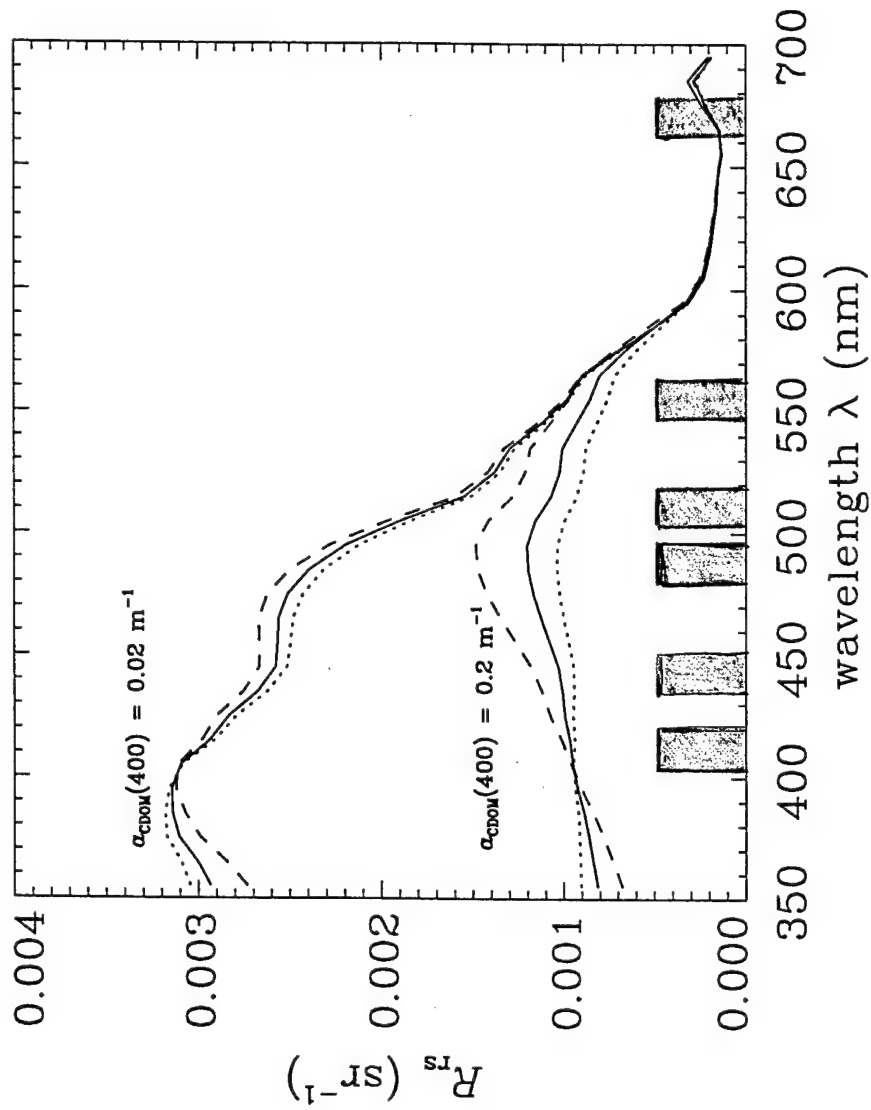


Fig. 13.  $R_{rs}$  as predicted for low and high CDOM concentrations (as labeled) and for three values of the CDOM exponent parameter  $\alpha$ : solid line,  $\alpha = 0.014$ ; dashed line,  $\alpha = 0.019$ ; dotted line,  $\alpha = 0.011$ . The shaded bars are the SeaWiFS bands.

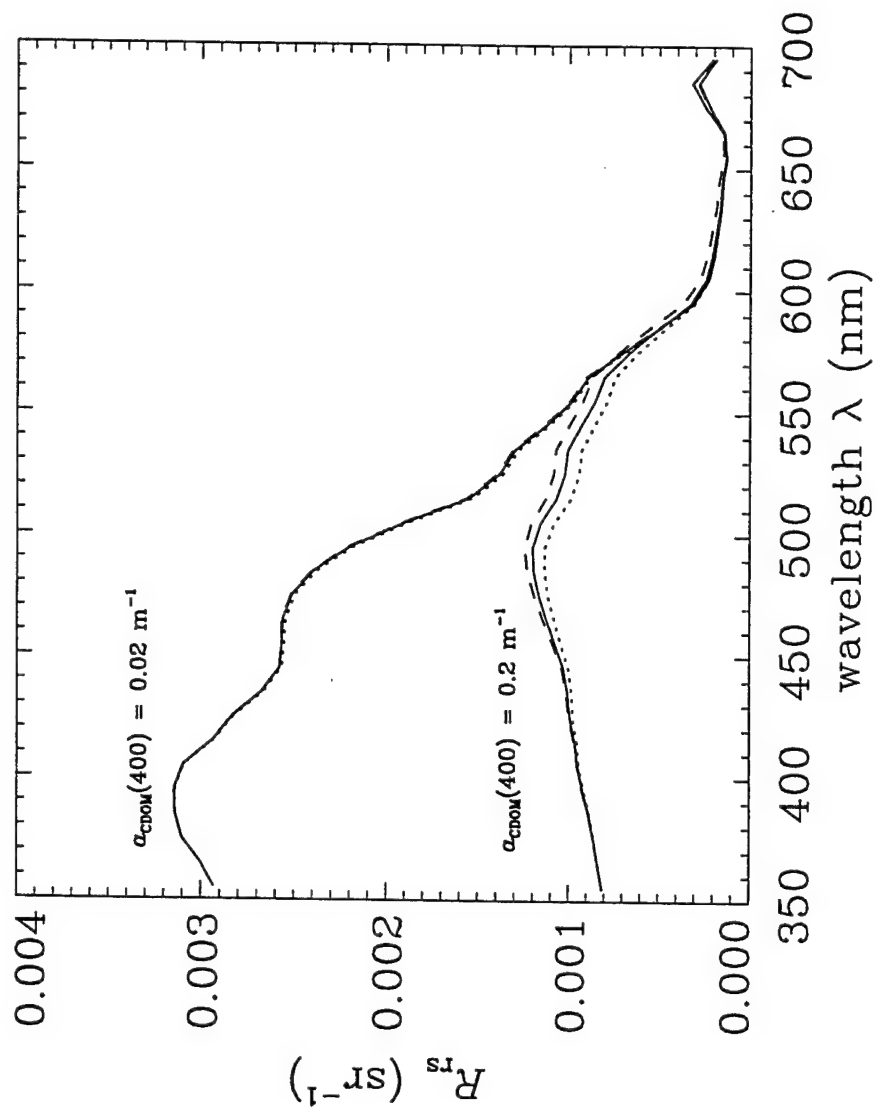


Fig. 14.  $R_{rs}$  as predicted for low and high CDOM concentrations (as labeled) and for the strong (dashed lines), moderate (solid lines), and weak (dotted lines)  $\eta^{\text{CDOM}}$  functions of Fig. 1.

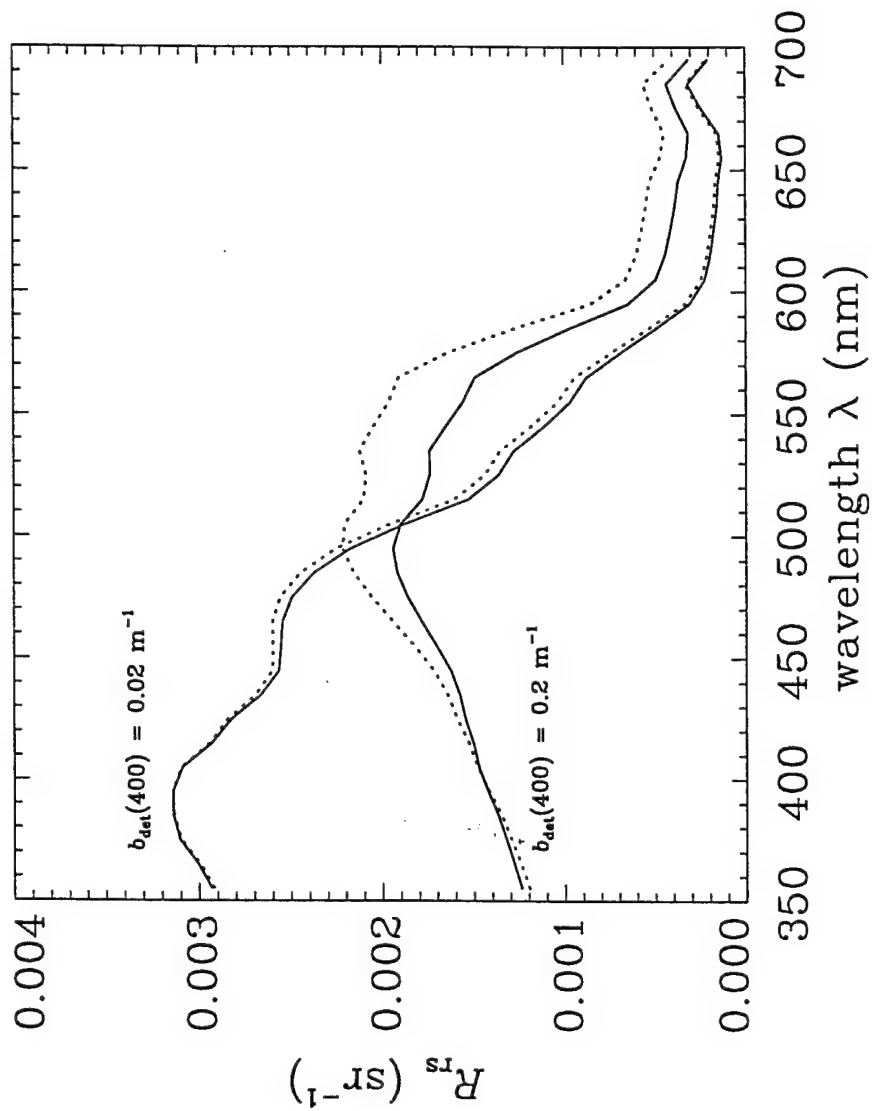


Fig. 15.  $R_{rs}$  as predicted for low and high detritus concentrations (as labeled) and for scattering by detritus that is inversely proportional to the wavelength (solid lines;  $n = 1$  in Eq. 4), and independent of wavelength (dotted lines,  $n = 0$  in Eq. 4).

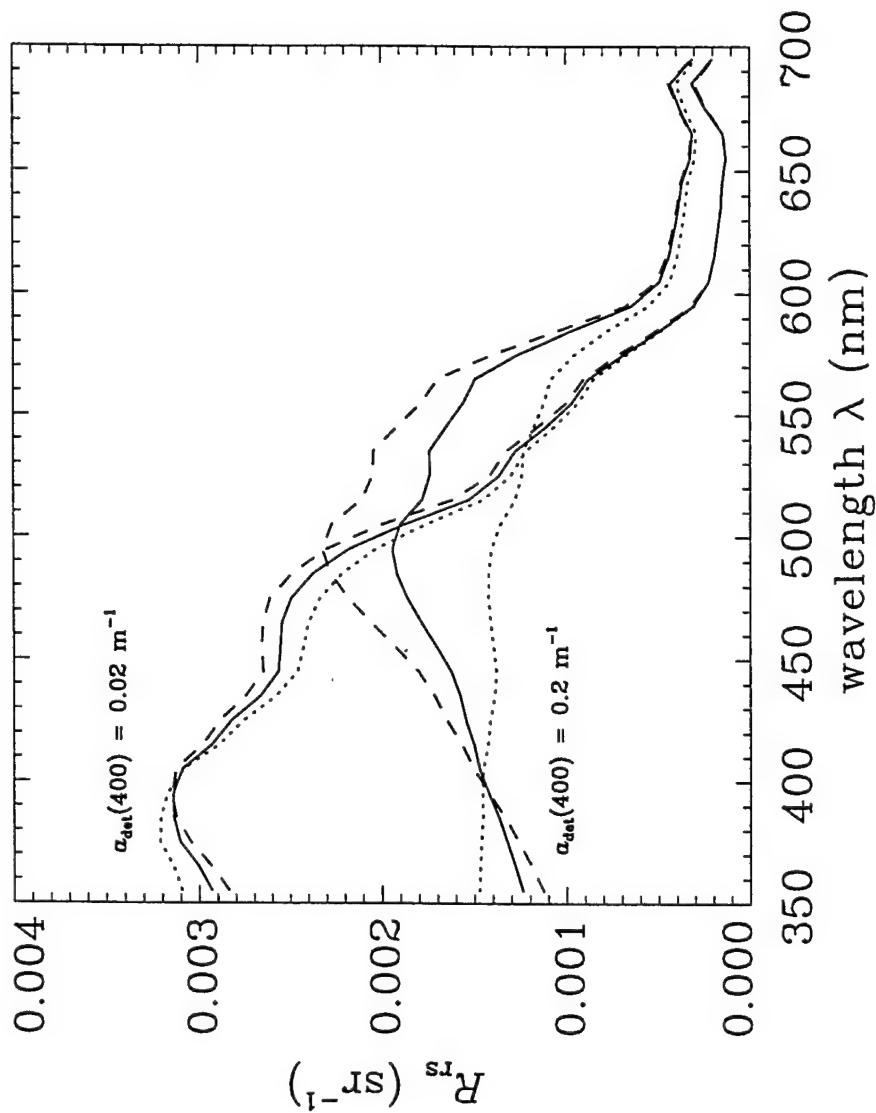


Fig. 16.  $R_{rs}$  as predicted for low and high detritus concentrations (as labeled) and for three values of the detritus absorption exponent parameter  $\gamma$ : solid line,  $\gamma = 0.011$ ; dashed line,  $\gamma = 0.014$ ; dotted line,  $\gamma = 0.006$ ;  $n = 1$  was used in the detritus scattering model.

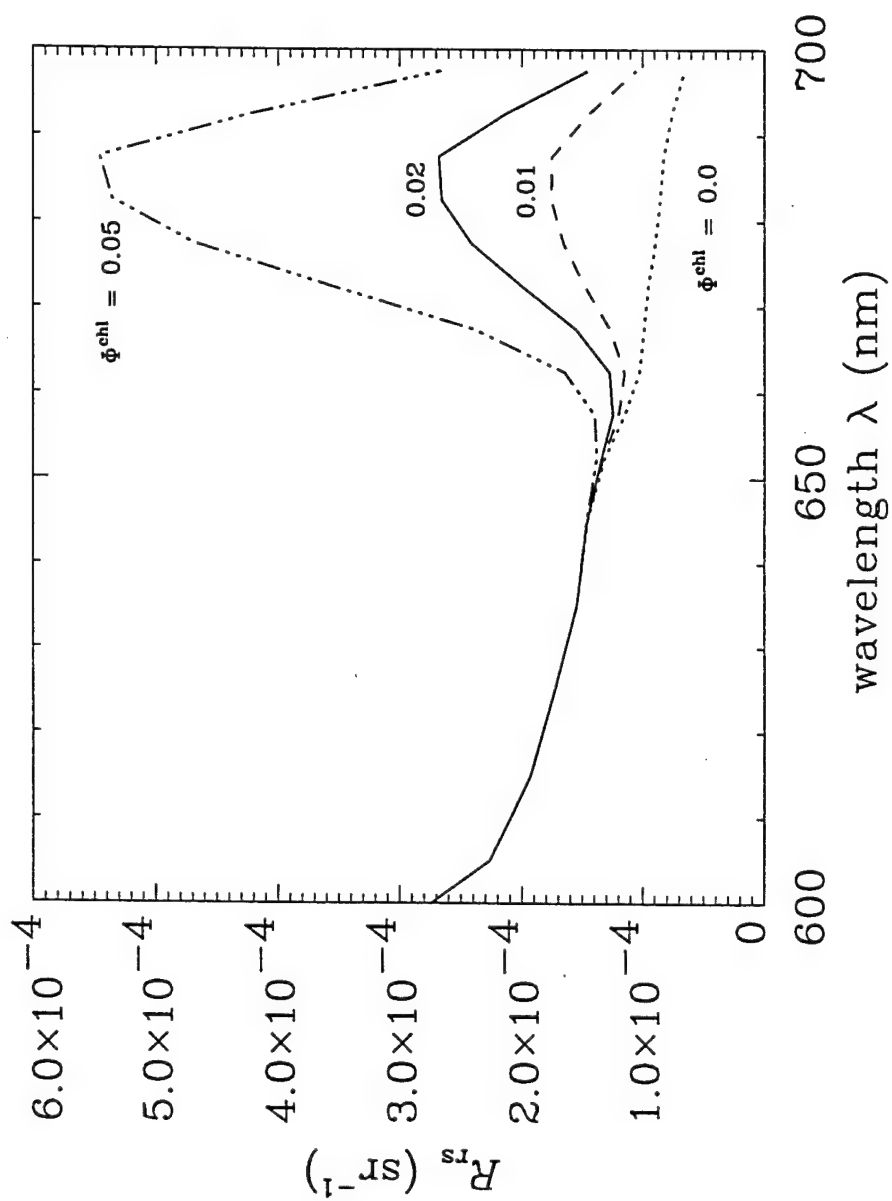


Fig. 17.  $R_{rs}$  as predicted for various chlorophyll fluorescence quantum efficiencies  $\Phi^{\text{chl}}$  (as labeled); the curve for  $\Phi^{\text{chl}} = 0$  corresponds to no fluorescence by chlorophyll.

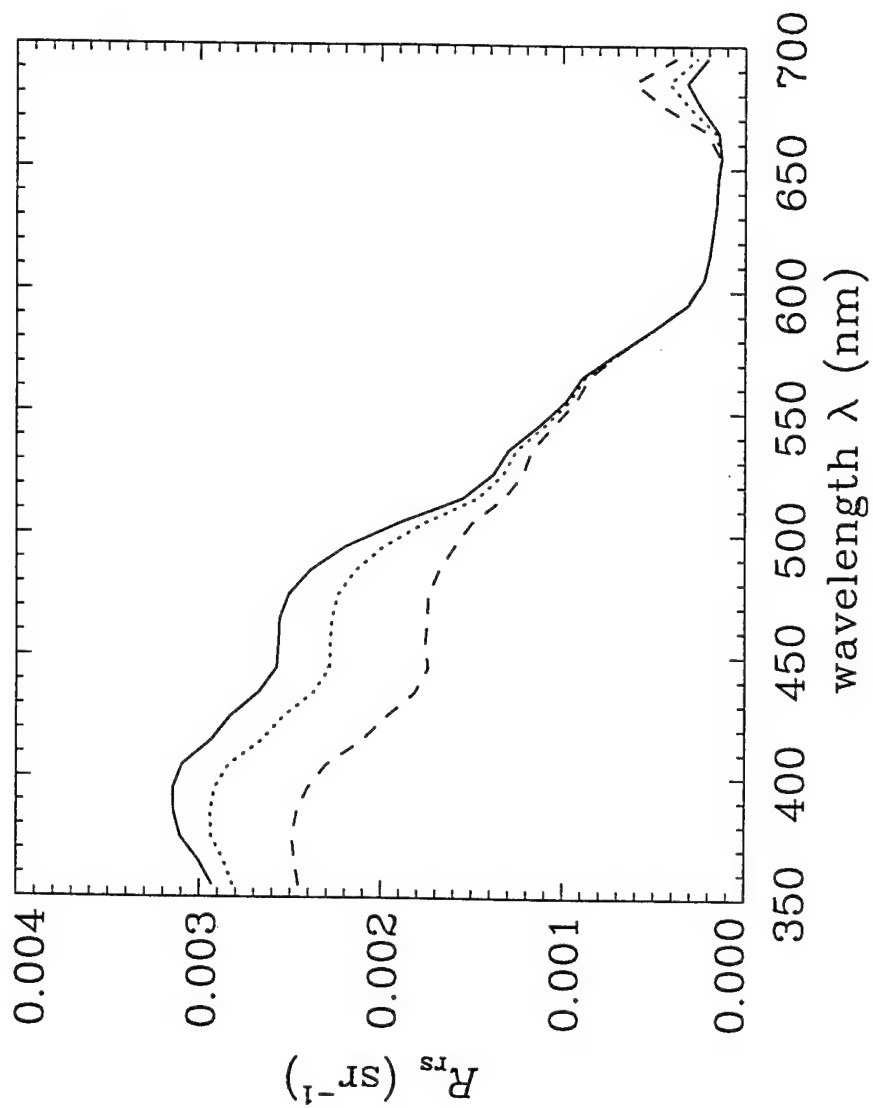


Fig. 18.  $R_{rs}$  as predicted for three different total concentrations of the small nanoplankton; other components had their base values. The solid line is for the base concentrations, the dotted line is for double the base concentrations of the small nanoplankton, and the dashed line is for five times their base concentrations.



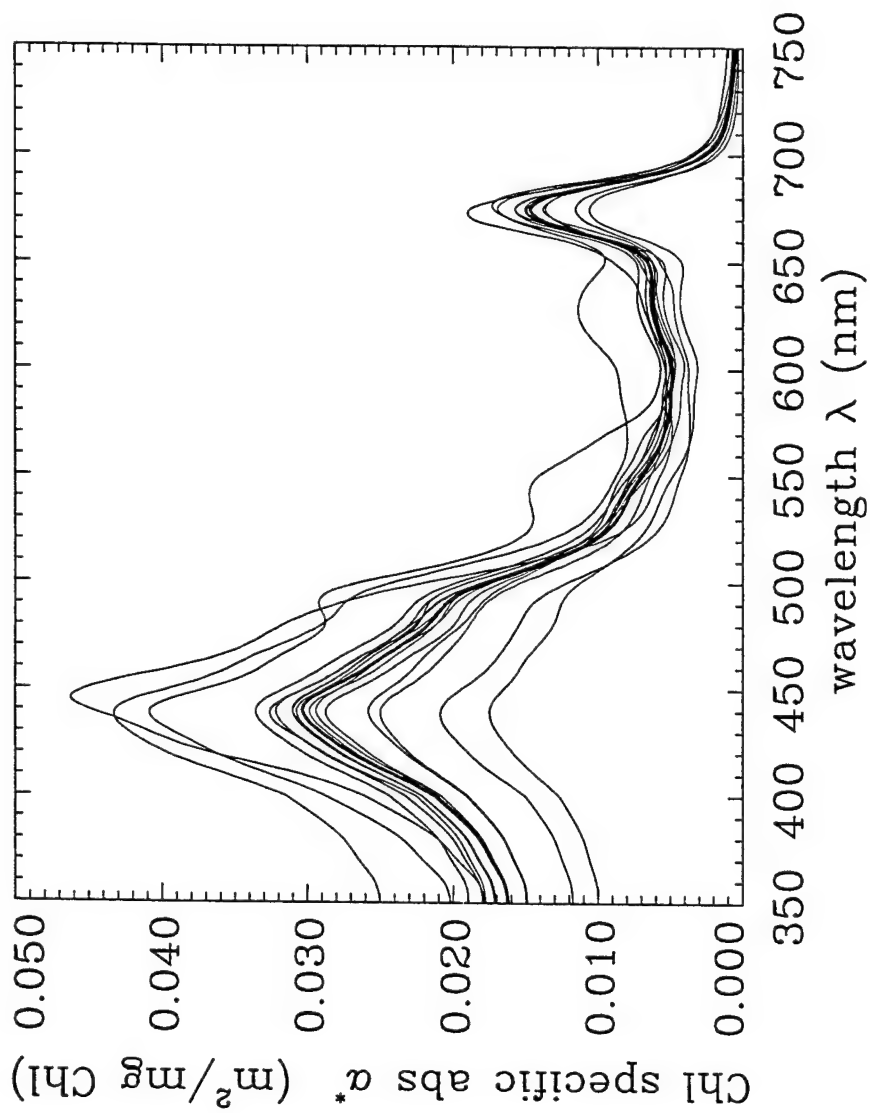


Fig. 19. Chlorophyll-specific absorption coefficients  $a^*$  for the base concentration (heavy line) and for the various single-particle bloom conditions (light lines).

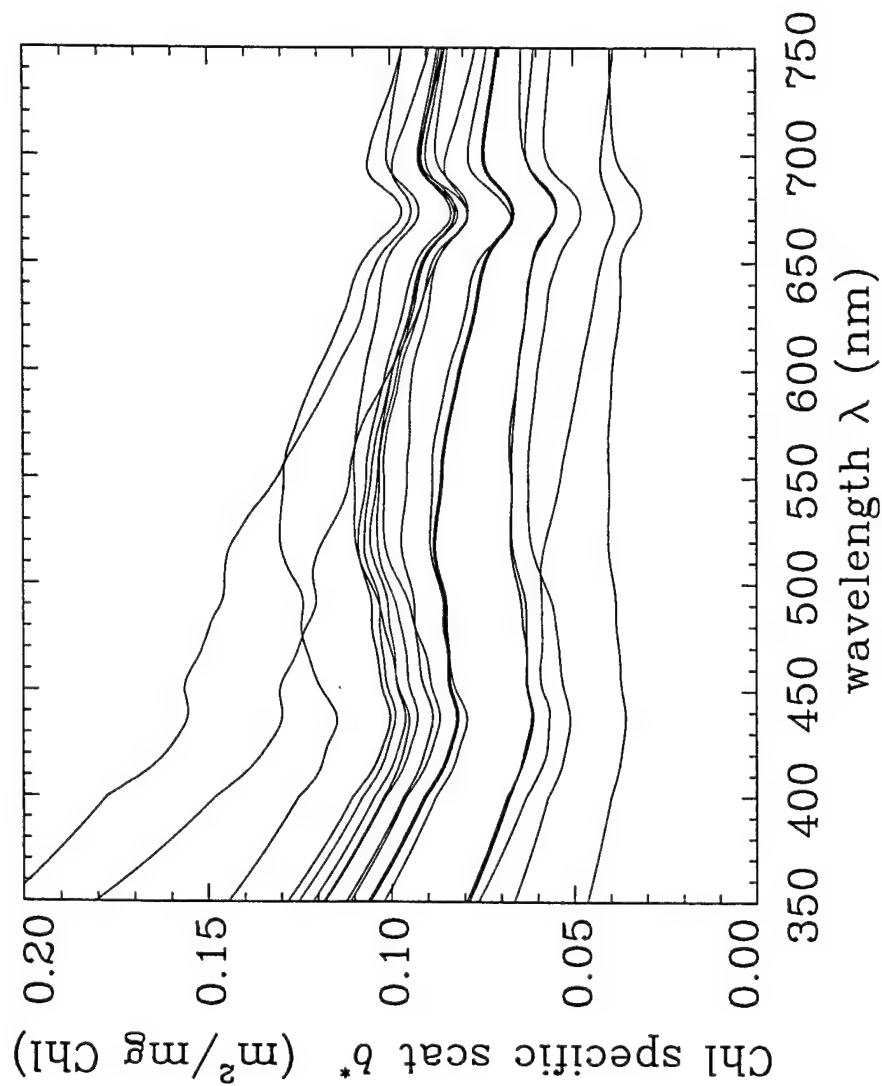


Fig. 20. Chlorophyll-specific scattering coefficients  $b^*$  for the base concentration (heavy line) and for the various single-particle bloom conditions (light lines).

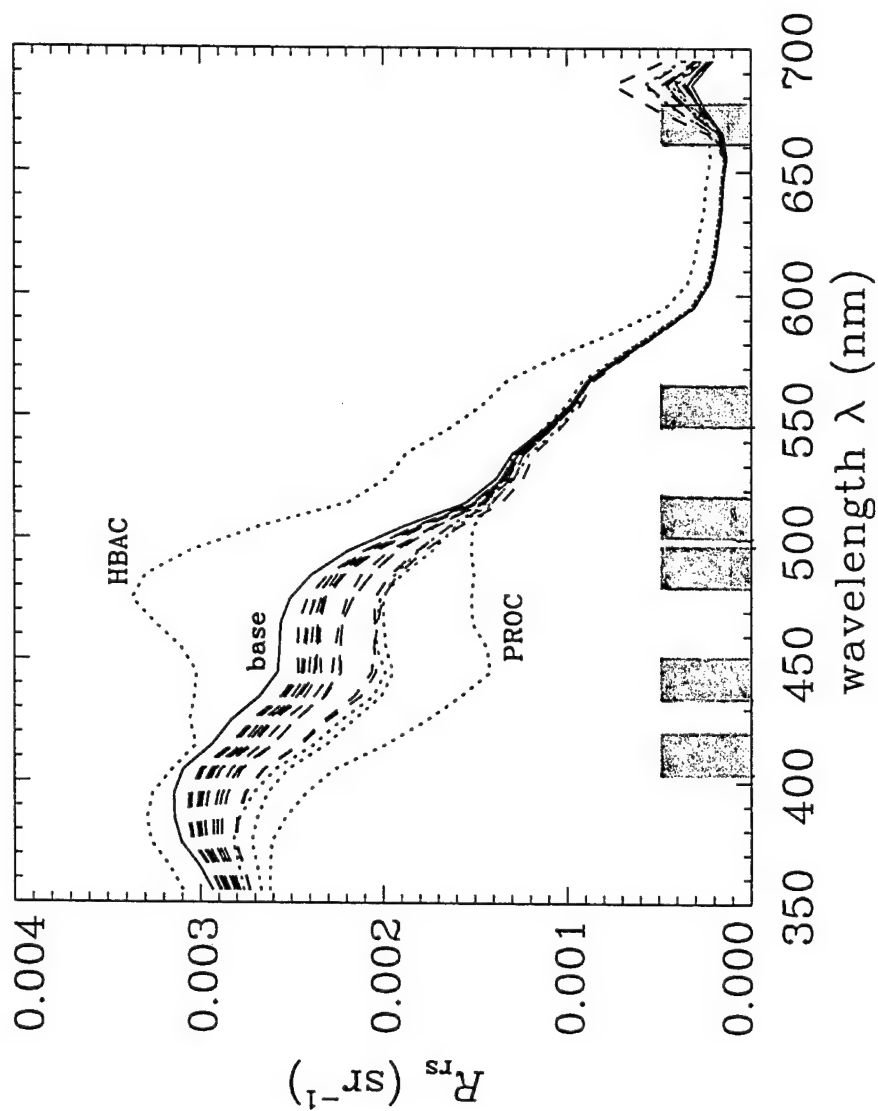


Fig. 21.  $R_{ts}$  for the base concentrations (solid line) and for the various single-particle blooms. The dotted lines are blooms of small particles ( $< 4\mu\text{m}$  diameter), and the dashed lines are blooms of large particles ( $> 4\mu\text{m}$ ).

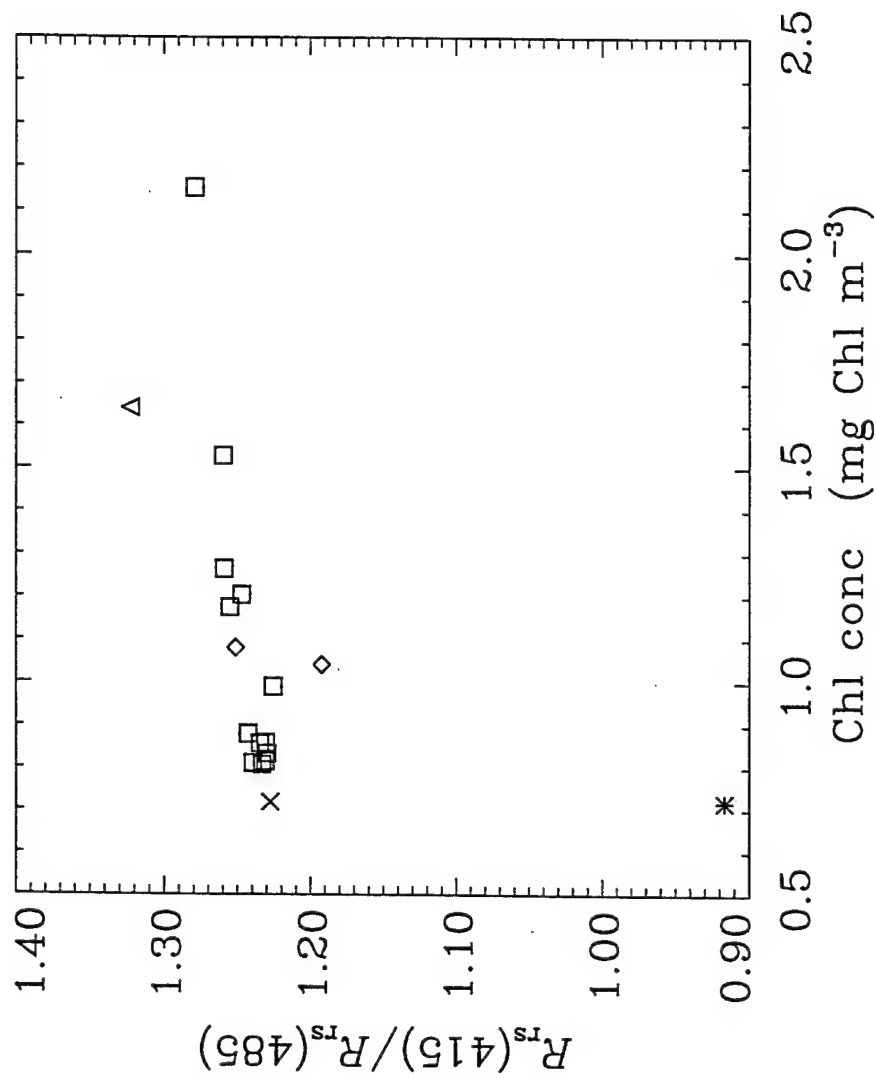


Fig. 22a.  $R_{rs}(415)/R_{rs}(485)$  as a function of the chlorophyll concentration for the base concentration and for various single-particle blooms. The symbols identify the particle types:  $\times$  is the base concentration,  $*$  is the HBAC bloom,  $\Delta$  is PROC,  $\diamond$  is other small particles, and  $\square$  is the large particles.

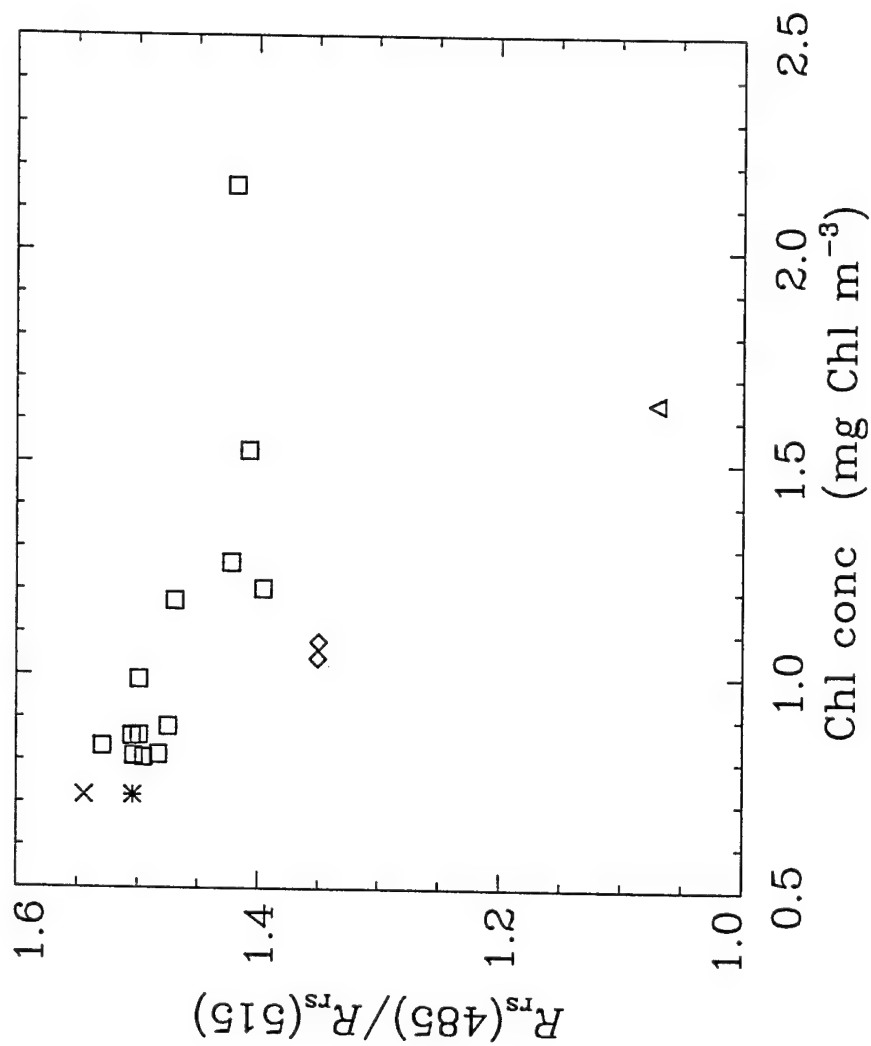


Fig. 22b.  $R_{rs}(485)/R_{rs}(515)$  as a function of the chlorophyll concentration for the base

concentration and for various single-particle blooms. The symbols are as in

Fig. 22a: x base, \* HBAC,  $\Delta$  PROC;  $\diamond$  other small particles; and  $\square$  large particles.

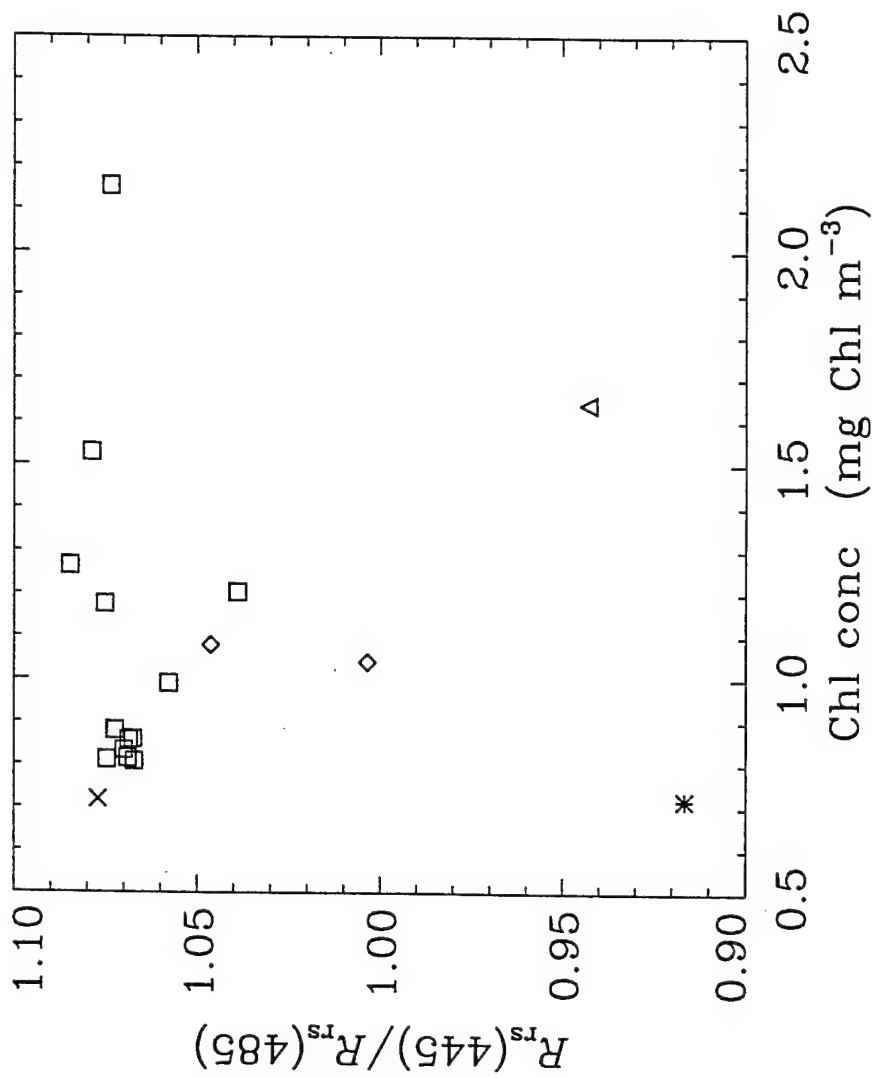


Fig. 22c.  $R_{rs}(445)/R_{rs}(485)$  as a function of the chlorophyll concentration for the base concentration and for various single-particle blooms. The symbols are as in Fig. 22a:  $\times$  base,  $*$  HBAC,  $\Delta$  PROC,  $\diamond$  other small particles, and  $\square$  large particles.

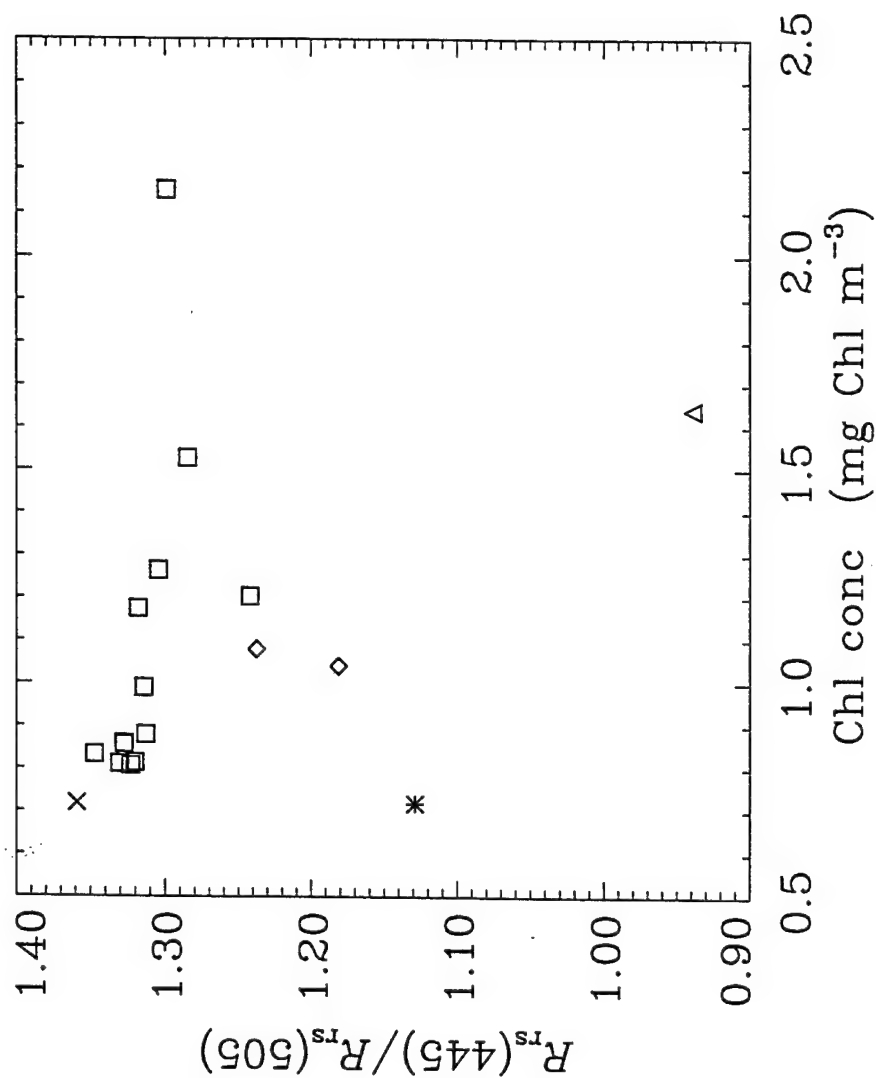


Fig. 22d.  $R_{rs}(445)/R_{rs}(505)$  as a function of the chlorophyll concentration for the base concentration and for various single-particle blooms. The symbols are as in

Fig. 22a: x base, \* HBAC, Δ PROC, ◇ other small particles, and □ large particles.

## APPENDIX E

Reprint of

*Estimation of the remote-sensing reflectance  
from above-surface measurements*

by

Curtis D. Mobley

Submitted to

*Applied Optics*



**Estimation of the Remote-Sensing Reflectance  
from Above-Surface Measurements**

Curtis D. Mobley  
Sequoia Scientific, Inc.  
9725 S.E. 36<sup>th</sup> Street, Suite 308  
Mercer Island, WA 98040

Submitted to *Applied Optics*  
*Lasers, Photonics, and Environmental Optics*

## ABSTRACT

The remote-sensing reflectance  $R_{rs}$  is not directly measurable, and various methodologies have been employed in its estimation. This paper considers the radiative-transfer foundations of the commonly used methods for estimating  $R_{rs}$ , and errors associated with estimating  $R_{rs}$  by removal of surface-reflected sky radiance are evaluated using the Hydrolight radiative transfer numerical model. The dependence of the sea surface reflectance factor  $\rho$ , which is not an inherent optical property of the surface, on sky conditions, wind speed, solar zenith angle, and viewing geometry is examined. If  $\rho$  is not accurately estimated, significant errors can occur in the estimated  $R_{rs}$  for near-zenith sun positions and for high wind speeds, both of which can give considerable sun-glitter effects. The numerical simulations suggest that a viewing direction of 40 degrees from the nadir and 135 degrees from the sun is a reasonable compromise among conflicting requirements. For this viewing direction, a value of  $\rho \approx 0.028$  is acceptable only for wind speeds less than  $5 \text{ m s}^{-1}$ . For higher wind speeds, curves are presented for the determination of  $\rho$  as a function of solar zenith angle and wind speed. If the sky is overcast, use a value of  $\rho \approx 0.028$  at all wind speeds. Problems associated with the use of a polarizing filter on the radiometer are qualitatively examined, with the preliminary conclusion that a polarizer should not be used when estimating  $R_{rs}$ .

**Keywords:** Hydrolight, optical oceanography, remote sensing, ocean color, reflectance, radiative transfer

## 1. Introduction

The remote-sensing reflectance  $R_{rs}$  is widely used in the interpretation of ocean-color data, and well-known formulas [e.g., Eqs. (6), (7), (9) and (10), below] are available to estimate  $R_{rs}$  from measurable quantities. The usefulness of these formulas has been established through their successful application in a variety of problems. Nevertheless, some users have only a vague understanding of the formulas' origins in radiative transfer theory and of the assumptions implicit in their use. Consequently, the formulas are sometimes applied with little understanding of their limitations or of the possible errors in  $R_{rs}$  resulting from their use. The same can be said for the use of polarizers when making above-water measurements. This paper lays out for pedagogical purposes the theoretical foundations for the estimation of the remote-sensing reflectance, and it quantifies some of the errors that can occur in its estimation when using above-water measurements.

The remote-sensing reflectance  $R_{rs}$  is defined as

$$R_{rs}(\theta, \phi, \lambda) = \frac{L_w(\theta, \phi, \lambda)}{E_d(\lambda)} \quad (1)$$

Here  $\theta$  and  $\phi$  specify the polar and azimuthal directions, respectively, in some convenient coordinate system, and  $\lambda$  is the wavelength.  $L_w(\theta, \phi, \lambda)$  is the water-leaving spectral radiance in direction  $(\theta, \phi)$ , that is, the radiance heading upward just above the sea surface that originated from underwater light, which was transmitted upward through the sea surface into direction  $(\theta, \phi)$ .  $E_d(\lambda)$  is the downwelling spectral plane irradiance incident onto the sea surface. The measurements implicit in Eq. (1) are generally made within a few meters of the sea surface and at wavelengths from the near ultraviolet to the near infrared, e.g. for  $\lambda$  from 350 to 800 nm. The  $\lambda$  argument henceforth will be dropped for brevity except when necessary for clarity.

Although  $E_d$  can be directly measured with commonly available instruments, such a measurement is not possible for  $L_w$ . This is because a radiometer pointing toward the sea surface in direction  $(\pi - \theta, \pi + \phi)$  measures the sum of the water-leaving radiance  $L_w(\theta, \phi)$  plus any incident sky radiance that has been reflected by the sea surface into direction  $(\theta, \phi)$ . Let  $L_s$  denote incident sky radiance (which, when weighted by  $\cos\theta$  and integrated over all downward directions, gives  $E_d$ ), and let  $L_r$  denote that part of  $L_s$  that is reflected by the sea surface into the direction of the sensor. The total radiance reaching the detector is then

$$L_t(\theta, \phi) = L_r(\theta, \phi) + L_w(\theta, \phi) \quad (2)$$

Because only  $L_t$  is directly measurable, it is not possible to compute  $R_{rs}$  from direct measurements of the quantities on the right-hand side of Eq. (1). However, the needed  $L_w$  can be *estimated* from

$L_w = L_t - L_r$ , if an accurate estimate of  $L_r$  can be obtained. Any such estimate of  $L_w$  then yields an estimate of  $R_{rs}$ .

The situation becomes complicated when the sea surface is not level and when the finite field of view (FOV) of the radiometer is taken into consideration. This situation is illustrated in Fig. 1. Sky radiance in any downward direction  $(\theta', \phi')$  can in principle be reflected by the wavy surface into the detector. Likewise, upwelling underwater radiance in any upward direction just below the surface, denoted by  $L_u(\theta', \phi')$ , can be transmitted through the surface and into the detector.

A qualitative feeling for the extent to which sky radiance from various directions can be reflected into a detector can be obtained from Fig. 2. This figure shows the sky hemisphere divided into a  $(\theta, \phi)$  grid with a 10 degree spacing in  $\theta$  and a 15 degree spacing in  $\phi$ . These quadrilateral  $(\theta, \phi)$  regions are called quads. The two highlighted quads are centered at  $\theta = 40$  degrees from the zenith direction, which is at the center of the polar cap. The solid angle subtended by these quads is  $\Omega = \Delta(\cos\theta)\Delta\phi = (\cos 35^\circ - \cos 45^\circ)(15^\circ \pi/180^\circ) = 0.029$  sr. This corresponds closely to the solid angle seen by a detector with a circular FOV and a  $5^\circ$  half angle:  $\Omega_{FOV} = 2\pi(1 - \cos 5^\circ) = 0.024$  sr.

Using Monte Carlo techniques as described in Mobley<sup>1</sup> (his Sect. 4.7) and implemented in the Hydrolight 4.0 radiative transfer numerical model,<sup>1-3</sup> rays were generated at random points located in the highlighted quad seen near the top of each panel in Fig. 2. The rays were directed towards a point on the sea surface located directly below the polar cap. The sea surface was modeled as a random surface covered by capillary waves corresponding to a given wind speed  $U$ ; a different sea surface realization was generated for each initial ray traced. In the case of a level sea surface,  $U = 0$ , each ray is specularly reflected. Thus all of the rays starting in one quad reflect into the conjugate quad, which is speckled by the points showing where 100 reflected rays intersected the grid. For non-zero wind speeds, the capillary wave facets reflect the incident rays into various directions, as illustrated by the  $U = 2, 5$ , and  $10 \text{ m s}^{-1}$  cases (which show the results of 5,000 ray tracings, and which include multiple scattering by the surface waves). The spread of reflected rays still centers on the specular reflection direction, but a significant number of rays can reflect into directions that are many tens of degrees away from the specular direction, especially at the higher wind speeds.

By reciprocity, any ray starting at one of the plotted points would be reflected into the original quad, i.e. into the sensor. Thus, a sensor with a typical FOV, when pointed at a wind-blown sea surface as in Fig. 1, is detecting reflected light from a fairly large part of the sky. If the sky radiance distribution is uniform, then the relative contribution of a given portion of the sky is proportional to the density of plotted points seen in Fig. 2. A non-uniform sky is the equivalent of a patchy distribution of points in the figure: more points would indicate, for example, a cumulus cloud which has a greater radiance than the background sky. The situation is complicated even more by the fact that each reflected ray plotted in Fig. 2 has a different Fresnel reflectance, since the ray-surface geometry is different for each ray.

## 2. Theory

The complicated general situation just discussed is described analytically as follows. The total upwelling radiance  $L_t$  entering the detector is related to the sky radiance  $L_s$  incident onto the sea surface from above and to the upwelling underwater radiance  $L_u$  incident onto the sea surface from below by the exact equation [Mobley<sup>1</sup> Eq. (4.3) averaged over the detector FOV]

$$\begin{aligned}
 L_t(\theta, \phi \in \Omega_{\text{FOV}}) &= \frac{1}{\Omega_{\text{FOV}}} \int_{\Omega_{\text{FOV}}} \left[ \int_{2\pi_d} L_s(\theta', \phi') r(\theta', \phi' \rightarrow \theta, \phi) d\Omega(\theta', \phi') \right] d\Omega(\theta, \phi) \\
 &+ \frac{1}{\Omega_{\text{FOV}}} \int_{\Omega_{\text{FOV}}} \left[ \int_{2\pi_u} L_u(\theta', \phi') t(\theta', \phi' \rightarrow \theta, \phi) d\Omega(\theta', \phi') \right] d\Omega(\theta, \phi) \quad (3) \\
 &\equiv L_r(\theta, \phi \in \Omega_{\text{FOV}}) + L_w(\theta, \phi \in \Omega_{\text{FOV}}).
 \end{aligned}$$

Here  $\Omega_{\text{FOV}}$  is the solid angle of the detector field of view, as illustrated in Fig. 1. The notation  $(\theta, \phi \in \Omega_{\text{FOV}})$  denotes the set of  $(\theta, \phi)$  directions seen when the detector is pointed toward the sea surface so as to detect radiance in the nominal  $(\theta, \phi)$  direction. To be precise,  $L_t(\theta, \phi \in \Omega_{\text{FOV}})$  denotes the average radiance over the detector FOV when the detector is pointed in the nominal  $(\theta, \phi)$  direction; the total irradiance entering the detector is then  $L_t(\theta, \phi \in \Omega_{\text{FOV}}) \times \Omega_{\text{FOV}}$ . The hemisphere of all downward directions is denoted by  $2\pi_d$ ; that of all upward directions by  $2\pi_u$ . The quantity  $r(\theta', \phi' \rightarrow \theta, \phi)$  is the time-averaged radiance reflectance of the sea surface, which tells how much of the incident sky radiance traveling downward in any direction  $(\theta', \phi')$  is reflected into any upward direction  $(\theta, \phi)$ , when observations are made over a time interval long enough to include many periods of the surface waves. The quantity  $t(\theta', \phi' \rightarrow \theta, \phi)$  is the time-averaged radiance transmittance of the sea surface, which tells how much of the upwelling radiance traveling in any upward direction  $(\theta', \phi')$  is transmitted through the surface into any upward direction  $(\theta, \phi)$ . Because the sea surface itself is assumed to be nonabsorbing, Eq. (3) fully accounts for all radiative transfer processes at the sea surface, as regards the total upwelling radiance leaving the surface. Equation (3) generalizes Eq. (2) and is the radiative-transfer basis for estimation of the remote-sensing reflectance.

The radiance reflectance  $r(\theta', \phi' \rightarrow \theta, \phi)$  and transmittance  $t(\theta', \phi' \rightarrow \theta, \phi)$  are inherent optical properties (IOPs) of the sea surface, i.e. their values for a given pair of  $(\theta', \phi')$  and  $(\theta, \phi)$  directions depend only on the wave state of the sea surface and on the index of refraction of the water, and not on the incident radiance distributions. The radiance reflectance and transmittance have units of  $\text{sr}^{-1}$ : they tell what fraction of the incident radiance is reflected or transmitted per unit solid angle. The radiance reflectance and transmittance can be numerically estimated to any desired accuracy for a

wind-blown sea surface using the Monte Carlo techniques implemented in the Hydrolight 4.0 radiative transfer numerical model.<sup>1-3</sup> The information required for such calculations consists of the wave-slope statistics of the sea surface, which allow mathematical realizations of the sea surface to be generated numerically and used as the basis for Monte Carlo ray tracing, as was done in generating Fig. 2.

Evaluation of the first term on the right-hand side of Eq. (3) requires that the entire sky radiance distribution  $L_s(\theta', \phi')$  be measured in conjunction with the sea surface wave state. Evaluation of the second term requires that the upwelling underwater radiance distribution  $L_u(\theta', \phi')$  be measured in conjunction with the surface wave state. It is in principle possible to make all of these measurements and therefore to evaluate both terms on the right hand side of Eq. (3). This observation provides two paths to the needed water-leaving radiance  $L_w$ . If the sky radiance and wave state are measured, then  $L_r$  can be computed and  $L_w$  can be obtained from  $L_t - L_r$ . If the underwater upwelling radiance and wave state are measured, then  $L_w$  can be computed directly.

Although it is possible to make the needed measurements of  $L_s$ ,  $L_u$ , and wave state, doing so on a routine basis would be cumbersome and expensive. In practice, as may be inferred from Fig. 2,  $r$  will be nearly zero for directions far away from the specular reflectance directions of a level sea surface. Thus  $L_s$  is needed only for the ranges of  $(\theta', \phi')$  for which  $L_s r$  is large enough to give a significant contribution to the first integral on the right-hand side of Eq. (3). However, it is difficult to determine *a priori* the relevant region of the sky, especially when the additional effects of gravity waves on the sea surface or of clouds (neither of which were modeled when generating Fig. 2) are considered. Similar statements hold for the directions for which  $L_u$  needs to be measured in order to accurately compute the second integral on the rhs of Eq. (3).

### 3. Ad hoc Formulas

Because of the practical difficulties in evaluating Eq. (3), the two terms on its rhs are commonly replaced by simple *ad hoc* formulas. The first term on the rhs of Eq. (3) can be replaced by

$$L_r(\theta, \phi \in \Omega_{\text{FOV}}) \doteq \rho L_s(\theta', \phi' \in \Omega'_{\text{FOV}}) . \quad (4)$$

Here,  $\rho$  is the proportionality factor that relates the radiance measured when the detector views the sky to the reflected sky radiance measured when the detector views the sea surface. The notation  $(\theta', \phi' \in \Omega'_{\text{FOV}})$  denotes the directions seen by the radiometer when it is pointed skyward so as to sample the sky radiance that would be specularly reflected by a level sea surface into directions  $(\theta, \phi \in \Omega_{\text{FOV}})$ , as illustrated in Fig. 1. It is emphasized that, unlike  $r$  in Eq. (3), the reflectance factor  $\rho$  is

*not an inherent optical property of the sea surface.* In particular,  $\rho$  depends not only on direction, wavelength, and wind speed, but also on the detector FOV and on the sky radiance distribution. Although  $\rho$  is often called the Fresnel reflectance, this is incorrect terminology:  $\rho$  depends on, but in general does not equal, the Fresnel reflectance of the surface at viewing angle  $(\theta, \phi)$ . *Only* in the case of a level sea surface and a uniform sky radiance distribution does the integral in Eq. (3) simplify to yield  $\rho$  as the average of the Fresnel reflectance over the detector FOV. Equation (4) should be viewed simply as the definition of the nondimensional quantity  $\rho$ , whose functional dependence can be expressed as

$$\rho = \rho(\theta', \phi', \theta, \phi, \lambda, \Omega_{\text{FOV}}, \text{wind speed, sky radiance distribution}).$$

Sections 4 and 5 discuss the dependence of  $\rho$  on its various parameters.

Although  $E_d$  can be measured directly, it is often estimated by making a radiance reflectance measurement from a "gray" surface (usually a plaque made of Spectralon®), which has a known irradiance reflectance  $R_g$  and which is a Lambertian reflector to a good approximation. When an irradiance  $E_d$  falls onto a Lambertian surface, the uniform radiance  $L_g$  leaving the surface is given by

$$L_g = \frac{R_g}{\pi} E_d. \quad (5)$$

$L_g$  can be directly measured by keeping the downward-looking radiometer pointed in the same  $(\theta, \phi)$  direction as was used in viewing the sea surface, while the level gray plaque is inserted into the radiometer FOV.

Using Eqs. (4) and (5) in (1) gives the equation often used<sup>4</sup> to estimate  $R_{rs}$  from the three separate radiance measurements  $L_t$ ,  $L_s$ , and  $L_g$ :

$$R_{rs} = \frac{L_t - \rho L_s}{\frac{\pi}{R_g} L_g}. \quad (6)$$

The virtue of using Eq. (6) to estimate  $R_{rs}$  is that all measurements are made with the same instrument and, moreover, the instrument does not require an absolute radiometric calibration, because any multiplicative error in the three  $L$ 's will divide out in Eq. (6). Indeed, the radiometer output can be in voltage or digital counts, since the factors converting the detector output to radiance divide out. (Any additive error in the radiometer output will presumably be set to zero in the dark-current calibration of the instrument.)  $R_g$  is accurately known for substances such as Spectralon, so the successful use of Eq. (6) rests on having an accurate value of  $\rho$ .

A variant of Eq. (6) has been adopted as a SeaWiFS protocol<sup>5</sup> for estimating  $R_{rs}$ . This protocol recommends first applying Eq. (6), using the Fresnel reflectance at the viewing angle  $\theta$  for  $\rho$ . Under the assumption that the water-leaving radiance is zero at 750 nm, the value of  $R_{rs}(750 \text{ nm})$  can be attributed to reflected sky radiance. Further assuming that the reflected-sky contribution to  $R_{rs}$  is independent of wavelength, the protocol then recommends that the  $R_{rs}(\lambda)$  values computed by Eq. (6) be adjusted by subtracting  $R_{rs}(750 \text{ nm})$  from  $R_{rs}(\lambda)$  to obtain the final estimate:

$$R_{rs}(\lambda; \text{final}) = R_{rs}(\lambda; \text{by Eq. 6}) - R_{rs}(750 \text{ nm}; \text{by Eq. 6}). \quad (7)$$

Equations (6) and (7) can be compared as follows. If the correct value for  $\rho$  is used at each wavelength, then Eq. (6) gives the correct value for  $R_{rs}(\lambda)$ . Equation (7) recognizes that it is difficult to guess the correct  $\rho$  and attempts to improve the initial estimate by applying a wavelength-independent correction to  $R_{rs}$ . The success of this correction depends on the wavelength dependence of  $\rho$  and on whether the water-leaving radiance is actually zero at 750 nm.

Zaneveld<sup>6</sup> recommends on theoretical grounds using the scalar irradiance  $E_{od}$  in Eq. (1) in place of the plane irradiance  $E_d$ . This substitution should remove some of the angular variability in  $R_{rs}$  that results from the viewing geometry. However, his recommendation seldom has been employed, possibly because his definition requires a direct measurement of  $E_{od}$ . (Note that it is not possible to estimate  $E_{od}$  from gray plaque measurements in a manner similar to that described for  $E_d$  in Eq. (6). This is because the scalar irradiance reflectance  $R_o \doteq E_{ou}/E_{od}$  of a Lambertian surface depends on the incident radiance distribution, unlike the plane irradiance reflectance  $R = E_u/E_d$ , which is independent of the incident lighting for a Lambertian surface.  $R_o$  equals  $R$  only if the Lambertian gray plaque is isotropically illuminated.) The results to follow apply to either definition of  $R_{rs}$ .

The second term on the rhs of Eq. (3) can be replaced by

$$L_w(\alpha; \theta, \phi \in \Omega_{FOV}) \doteq \tau L_u(w; \theta', \phi' \in \Omega_u). \quad (8)$$

Here,  $\tau$  is the nondimensional proportionality factor that relates the upwelling radiance measured by an underwater detector viewing some subset  $\Omega_u$  of  $2\pi_u$  to the water-leaving radiance entering the above-surface detector viewing the sea surface. Depth arguments  $\alpha$  (for air) and  $w$  (for water) have been added to the radiances to remind us that these quantities are being measured on different sides of the sea surface. Like  $\rho$  in Eq. (4),  $\tau$  is not an inherent optical property of the sea surface. In particular,  $\tau$  depends not only on direction and sea state, but also on the detector FOV and on the sky and upwelling radiance distributions.



Consider for the moment a level sea surface and infinitesimal detector FOVs. The directions  $(\theta', \phi')$  and  $(\theta, \phi)$  in Eq. (8) are then related by Snell's law  $\sin\theta = n\sin\theta'$ , where  $n$  is the index of refraction of the water (relative to air), and by  $\phi = \phi'$ . In this case, Eq. (8) just expresses the  $n^2$  law for radiance propagation across the surface. The  $\tau$  factor then can be identified as

$$\tau = \frac{1 - r_F(\theta', \theta)}{n^2},$$

where  $r_F(\theta', \theta)$  is the Fresnel reflectance of the surface as seen from the water side. For  $n \approx 1.34$  and for the range of  $(\theta', \theta)$  values relevant to most remote sensing situations ( $\theta < 50$  degrees),  $r_F$  lies between 0.02 and 0.04, so that  $\tau$  falls between 0.53 and 0.55. The situation is more complicated—and  $\tau$  may be more variable—for wind-blown sea surfaces and finite FOVs, but even then a value of  $\tau \approx 0.54$  often may be reasonable.

Equation (8) can be divided by the sky irradiance incident onto the sea surface to obtain

$$R_{rs}(\theta, \phi) = \tau \frac{L_u(w; \theta', \phi')}{E_d(a)}, \quad (9)$$

where the FOV arguments are dropped for brevity, but an  $a$  argument is added to  $E_d$  to remind us that this irradiance is being measured in air. A virtue of using Eq. (9) to estimate the remote-sensing reflectance is that no correction for surface-reflected sky light is required, as is the case when using Eq. (6). Moreover, commercial instrument packages are available to make the needed measurements.

Equation (9) is often rewritten in terms of in-water quantities by using the exact radiative transfer relationship (Mobley<sup>1</sup> Eq. 4.6)

$$E_d(w) = E_u(w) R_u + E_d(a) (1 - R_s).$$

Here  $R_u$  is the irradiance reflectance of the surface (from the water side) for upwelling irradiance,  $R_s$  is the irradiance reflectance of the surface (from the air side) for the incident sky irradiance, and  $E_d$  and  $E_u$  are plane irradiances in the air or water, as shown. The result is

$$R_{rs}(\theta, \phi) = \left\{ \frac{[1 - r_F(\theta', \theta)] (1 - R_s)}{n^2 (1 - R R_u)} \right\} \frac{L_u(w; \theta', \phi')}{E_d(w)} \doteq T \frac{R}{Q(\theta', \phi')}, \quad (10)$$

where  $T$  is the quantity in braces,  $R = E_u(w)/E_d(w)$ , and  $Q(\theta', \phi') = E_u(w)/L_u(w; \theta', \phi')$ . It should be noted that  $R_s$  and  $R_u$  depend on their respective radiance distributions and are apparent optical properties, even though they describe the reflectance properties of the air-water surface itself. The subsurface irradiance reflectance  $R$  is an apparent optical property of the water body. Note the conceptual difference in  $R_s$ , which describes how the *surface itself* reflects incident sky irradiance, and in the albedo of the sea surface, which is the ratio of total upwelling irradiance (including irradiance transmitted through the surface from the water below) to total downwelling irradiance. A corresponding distinction is made between  $R_u$  and  $R$ . See Mobley<sup>1</sup> for additional discussion of these surface-reflectance quantities.

As already noted,  $r_F$  lies between 0.02 and 0.04 for moderate wind speeds and for  $\theta'$  and  $\theta$  in the angular ranges relevant to most ocean color sensors. For solar zenith angles less than 60 degrees in a clear sky, or for overcast skies,  $R_s < 0.07$ ;  $R_s < 0.03$  for solar angles less than 45 degrees.<sup>7</sup> For typical underwater light fields,  $R_u < 0.7$ .  $R$  values are typically less than 0.05 and are almost always less than 0.1 (at least in Case 1 waters). The bracketed term in Eq. (10), denoted here by  $T$ , then falls in the range of 0.50 to 0.57, with a value of 0.54 being typical. The rough numerical equality between  $\tau$  in Eq. (9) and  $T$  in Eq. (10) is to an extent coincidental;  $\tau$  and  $T$  are conceptually different quantities.

Because the value of  $T$  varies by only a few percent about the value 0.54, most of the variability in  $R_{rs}$  arises from variability in  $R/Q$ . The dependence of  $R/Q$  on the IOPs of the water body—in particular on the absorption and backscatter coefficients—has been studied by Gordon *et al.*<sup>8</sup> The directional dependence of the  $Q$  factor has been numerically studied by Morel and Gentili<sup>9</sup> for various environmental conditions (note that  $R/Q$  depends implicitly on the solar zenith angle, sea state, and water IOPs, all of which affect the underwater radiance distribution). Their results are compared with measurements in Morel *et al.*<sup>10</sup> The results of these thorough studies need not be repeated here.

The virtue of using Eq. (10) to estimate the remote-sensing reflectance is that  $R_{rs}$  is obtained entirely from measurements made within the water. As with Eq. (9), there is no need to correct for surface-reflected sky light. On the other hand, the measurements needed to evaluate Eqs. (9) or (10) come with their own difficulties, such as the effects of wave focusing and self-shading on instruments just beneath the sea surface and the need to extrapolate measured values from the depth of measurement to just below the surface. Both Eqs. (9) and (10) require accurately calibrated instruments. The accuracy of Eq. (10) of course rests on using the correct values for  $T$ ,  $R$ , and  $Q$ . Even though the functional dependence of  $R_{rs}$  is on the ratio  $R/Q$ ,  $R$  and  $Q$  are obtained from separate measurements made by different instruments.  $Q$ , especially, may be inaccurately estimated if  $L_u$  is measured with a nadir-directed radiometer and then used to compute  $R_{rs}$  at off-nadir directions.

The papers just cited<sup>8-10</sup> have adequately studied the quantities seen in Eq. (10). The remainder of the present paper is therefore devoted to studying variability in the  $\rho$  parameter of Eq. (6), which has received less attention.

#### 4. Dependence of $\rho$ on Viewing Geometry and Wind Speed

The Hydrolight radiative transfer numerical model<sup>1-3</sup> is an ideal tool for investigating the variability of  $\rho$  as the sea state and viewing geometry vary. Input to Hydrolight consists of the incident sky radiance distribution, a statistical description of the wind-blown sea surface (usually given as sea-surface slope statistics parameterized in terms of the wind speed), the absorption and scattering properties of the water itself, and the nature of the water bottom boundary (which may be of finite or infinite depth). The model solves the radiative transfer equation to obtain the full radiance distribution within and leaving the water. The model computes separately the water-leaving radiance  $L_w$  and the reflected sky radiance  $L_r$ . This makes it possible to evaluate the individual contributions of  $L_r$  and  $L_w$  to the measurable total upwelling radiance  $L_t$ . In particular, Hydrolight can easily compute  $\rho = L_r/L_t$  for any given set of environmental conditions or viewing geometry.

The figures in this section show the dependence of  $\rho$  on sun zenith angle, viewing direction relative to the solar position, wind speed, and sky conditions. The Hydrolight model does not include polarization, and therefore these results presume that the detector does not pass the light through a polarizing filter before recording the signal. The effects of a polarizing filter on the detected signal are discussed in Sect. 7. It should be noted that  $\rho$  as discussed here *does* include the effects of sun glitter, which may be present in actual measurements.

Most sensors used for field estimation of  $R_{rs}$  have a FOV of about 10 degrees. Therefore, Hydrolight was run with a partition of the set of all directions into 10-degree  $\theta$  and 15-degree  $\phi$  bands, plus two polar caps with a 10-degree full angle. This partitioning of  $\theta$  and  $\phi$  was shown in Fig. 2. As already noted, the solid angles of the  $\theta, \phi$  quads correspond roughly to that of the FOV of a typical instrument. The quads are centered at  $\theta$  values of 0 (the polar cap), 10, 20, 30 degrees, and so on. Hydrolight computes the radiance directionally averaged over each of the quads, just as an instrument measures the average radiance within the instrument FOV. When the sun is placed in a particular quad, say one centered at  $\theta = 30$  degrees, the sun is "spread out" over the  $\theta$  range from 25 to 35 degrees, and over a 15-degree  $\phi$  range, but the average radiance over the quad is the same as would be measured by an instrument with a 10 by 15-degree rectangular FOV when pointed at the sun.

When making field measurements, it is common to orient the radiometer at right angles to the sun's direction. This is done to minimize the effects of sun glitter and of ship shadow. In the simulations below, the sun is at  $\phi = 0$ . The standard sensor orientation then corresponds to  $\phi = 90$

or 270 degrees. The viewing geometry is then completely specified by giving the solar zenith angle  $\theta_s$  and the viewing angle  $\theta_v$ , as shown in Fig. 3.

To study the variability of  $\rho$ , a series of Hydrolight simulations was made for the following conditions:

Wind speeds of  $U = 0, 2, 5, 10$ , and  $15 \text{ m s}^{-1}$  were used to define the random sea surface. The surface was modeled using azimuthally averaged Cox-Munk wave slope statistics appropriate for a sea surface covered by capillary waves. Although an actual capillary wave surface does display some azimuthal asymmetry in the alongwind and crosswind slopes, the effect of this asymmetry on the surface reflectance is small for solar angles and viewing directions that are not near the horizon.<sup>7</sup> By using azimuthally averaged slope statistics, only the azimuthal angle between the sun and viewing directions needs to be specified; the azimuthal direction of the wind is irrelevant.

The semi-empirical sky radiance model of Harrison and Coombes<sup>11</sup> was used to define the angular pattern of the sky radiance distributions incident onto the sea surface. The sun is placed at the desired zenith angle  $\theta_s$ , and the remainder of the sky has a non-uniform radiance distribution that is close to that of a real sky on a clear day. The Harrison and Coombes model is based on many observations of sky radiances and includes both Rayleigh and aerosol scattering effects. Solar zenith angles of  $\theta_s = 0, 10, 20, \dots, 80$  degrees were used.

The results of Sects. 4 and 5 depend only on the sea-surface and sky conditions; they are independent of the water IOPs. Specific water IOP models as needed for the simulations of Sect. 6 will be described there. In all cases, the water was taken to be homogeneous and infinitely deep, because remote-sensing signals are determined by the near-surface water properties.

Austin<sup>12</sup> presents tables of  $\rho$  computed for various wind speeds, solar angles, and viewing angles, using the Cox-Munk capillary wave slope statistics. Austin does not describe the manner in which he made his calculations, but presumably he averaged the Fresnel reflectance for a distribution of angles as determined by the Cox-Munk wave slope statistics. Austin's calculations were made for a uniform sky radiance distribution, and they do not include any specular reflection effects from the sun's direct beam. Figure 4 shows one set of Austin's tabulated values compared with the corresponding  $\rho$  values computed by Hydrolight (using a uniform sky radiance distribution). The wind speed is  $U = 10 \text{ m s}^{-1}$  and the sun zenith angle is  $\theta_s = 60$  degrees. The plotted curves are spline fits to values computed at  $\theta_v$  intervals of 10 degrees. The agreement is clearly excellent for viewing angles  $\theta_v$  less than 80 degrees. For viewing angles near the horizon, the difference between the

Hydrolight and Austin curves is probably due to multiple scattering by the wave facets, which is included in Hydrolight but presumably not in Austin's calculations.

Austin's report<sup>12</sup> is sometimes cited as the justification for using a  $\rho$  value of roughly 0.02 or 0.03 in Eq. (6). Note that  $\rho \approx 0.020$  for viewing angles less than 30 degrees, and  $\rho \approx 0.028$  for  $\theta_v = 40$  degrees. However, *Austin cautions the reader that his results apply only to a uniform sky radiance distribution and only if the viewing geometry is such that there is no specular reflection of the sun's direct beam into the sensor FOV.*

Actual clear-sky radiance distributions are of course not uniform, and sun glitter unavoidably may be present when viewing the sea surface. Figure 5 shows a plot like those of Fig. 2, but with the clear-sky relative radiance pattern as computed by the Harrison and Coombes<sup>11</sup> formulas superimposed on the reflected-ray pattern (radiance is normalized to one near the sun's direction). The wind speed was  $15 \text{ m s}^{-1}$  and the sun was placed at  $\theta_s = 30$  degrees at a right angle to the viewing direction; 10,000 rays are plotted. It is clear from the ray pattern and radiance distribution over the sky hemisphere that the sensor is sampling a large part of the sky, for which the background sky radiance varies by over a factor of ten in magnitude, and that some of the rays come from very near the sun and thus will have very large radiances.

Figure 6 shows how sun glitter and a realistic sky radiance distribution can greatly alter the nominal  $\rho$  values seen in Fig. 4. Figure 6 shows  $\rho$  as obtained from Hydrolight's input  $L_s$  and computed  $L_r$  values in Eq. (4), for various sun zenith angles from 20 to 60 degrees. Because the sea surface generation and ray tracing are performed using Monte Carlo techniques, there is statistical noise in the curves of Fig. 6. The dotted lines for  $\theta_s = 30$  degrees show the results of six independent Monte Carlo simulations, each using 20,000 randomly generated sea surfaces. The Monte Carlo noise is greatest at  $\theta_v = 10$  degrees because the quads centered at 10 degrees have the smallest solid angles and therefore receive fewer reflected rays than do the other quads (recall Fig. 2). The heavy line for  $\theta_s = 30$  degrees is the average of the six simulations. The curves for the other  $\theta_s$  values are from only one Monte Carlo simulation. (All curves are plotted from spline fits to the values computed at intervals of  $\theta_v = 10$  degrees.)

The  $\rho$  curve for  $\theta_s = 60$  degrees in Fig. 6 is noticeably greater than the Austin curve. This is a consequence of the non-uniform sky radiance distribution; recall that Fig. 4 was for a uniform sky radiance. Note that for viewing angles of  $\theta_v < 40$  degrees,  $\rho$  increases as the sun climbs higher in the sky. This is because sun glitter cannot be avoided when both  $\theta_s$  and  $\theta_v$  are small. If, for example,  $\theta_v$  is 30 degrees—a typical value used in the field—and the sun is at  $\theta_s = 20$  degrees, then the correct value of  $\rho$  is about 0.1, which is over three times the often-used value of 0.028. In practice, an observer likely would notice the glitter in the sensor FOV and would then use a greater viewing angle to avoid the obvious glitter. But even if the observer uses a viewing angle of 40 to 50 degrees, which would minimize the glitter effect, the correct value of  $\rho$  is still almost twice the

nominal value of 0.028. At viewing angles beyond 50 degrees,  $\rho$  again rises because of the increase in the Fresnel reflectance of the surface at angles greater than 50 degrees. Thus for a  $10 \text{ m s}^{-1}$  wind and a 20 degree sun angle, there is no viewing angle for which  $\rho \approx 0.028$  would be a good value.

Figure 7 shows contour plots of  $\rho$  for  $\theta_s = 30$  degrees and for  $U = 5$  and  $10 \text{ m s}^{-1}$ . The dotted circles represent lines of constant polar viewing direction:  $\theta_v$  is 0 at the center and 60 degrees at the outer rim of the plots. The azimuthal angle in the plots represents  $\phi_v$  as labeled. The  $\rho$  values are contoured at intervals of 0.03, 0.04, ..., 0.12. The irregular pattern of some of the contour lines near the centers of the plots and at the outer edges is a consequence of the irregular  $(\theta_v, \phi_v)$  grid used for contouring and of Monte Carlo noise in  $\rho$  for small  $\theta_v$  values, as mentioned above. Qualitative inspection of these plots suggests that an azimuthal viewing direction of  $\phi_v = 90$  degrees is not optimum for the purpose of estimating  $\rho$ . When moving from the center of the plots to their top, i.e. when increasing  $\theta_v$  from 0 to 60 degrees while holding  $\phi_v$  constant at 90 degrees,  $\rho$  tends to remain large until a fairly narrow minimum is reached near  $\theta_v = 40$  degrees, as was seen in Fig. 6. Note also that a small change in  $\phi_v$  when near  $\phi_v = 90$  degrees (e.g., making observations at  $\phi_v = 80$ ) can cause a large change in  $\rho$ . However, at larger  $\phi_v$  values,  $\rho$  decreases more quickly with  $\theta_v$  and has a broader minimum with lower values than at  $\phi_v = 90$  degrees. Using a  $\phi_v$  value of 180 degrees might be optimum for estimating  $\rho$  but could lead to other problems such as shadowing of the reflectance plaque or "glory" effects from water backscatter.<sup>5</sup> Therefore, a  $\phi_v$  value of  $\sim 135$  degrees from the sun appears to be a good compromise that would minimize shadowing problems while also giving a better estimate for  $\rho$  than can be obtained for  $\phi_v = 90$  degrees. (Figure 7 also makes clear that  $\rho$  is not equal to the Fresnel reflectance, whose contours would be concentric circles.)

Figure 8 shows  $\rho$  as a function of wind speed and  $\theta_v$  for  $\phi_v = 90$  (dotted lines) and 135 (solid lines) degrees, for  $\theta_s = 30$  degrees as in Fig. 7. The  $\rho$  values have a broader minimum and, more importantly, show less dependence on wind speed for  $\phi_v = 135$  than for  $\phi_v = 90$  degrees. If observations are made at  $\theta_v = 30$  to 40 degrees, then for  $\phi_v = 135$  degrees  $\rho$  increases from  $\sim 0.025$  at low wind speeds to  $\sim 0.04$  at  $U = 15 \text{ m s}^{-1}$ , whereas  $\rho$  increases to  $\sim 0.08$  at  $15 \text{ m s}^{-1}$  for  $\phi_v = 90$ . Thus there is a factor of two less variability in  $\rho$  at  $\phi_v = 135$  degrees.

Figure 9 shows  $\rho$  as a function of wind speed and solar zenith angle  $\theta_s$  for a viewing angle of  $\theta_v = 40$  degrees. As in Fig. 8, the solid lines are for  $\phi_v = 135$  degrees and the dotted lines are for  $\phi_v = 90$ . Figure 9 can be used to estimate the value of  $\rho$  that should be used in Eq. (6). For clear skies,  $\rho$  is almost independent of wavelength because both the angular pattern of the sky radiance and the water index of refraction are nearly independent of wavelength. However, there will always be some wavelength dependence in  $\rho$  because the white sun glint has a different spectral dependence than the reflected blue sky radiance.



## 5. Dependence of $\rho$ on Clouds

The simulations above have all been for a clear sky as modeled by the Harrison and Coombes<sup>11</sup> formulas for a cloud parameter of  $C = 0$  ( $C$  ranges from 0 for clear skies to 1 for heavy overcast). However, if clouds are present in the portion of the sky being reflected into the detector viewing the sea surface, then the value  $\rho$  will change because clouds are generally brighter than the background sky and thus give "cloud glitter" effects in analogy to sun glitter.

To investigate the effects of clouds on  $\rho$ , idealized clouds were simulated in Hydrolight by simply increasing the Harrison and Coombes clear-sky radiance by a factor  $C_L$  for selected directions representing the locations of the clouds. Figure 10 shows the normalized clear-sky radiance distribution (contour lines) and the region of sky seen for a  $10 \text{ m s}^{-1}$  wind (points), as in Fig. 5. As in Figs. 2 and 5, the small rectangle shows the region of the sky that would be imaged for a level sea surface and which is used to measure  $L_s$  as in Fig. 1. The shaded areas of figure panels 1, 2, and 3 represent the locations of clouds in the Hydrolight quad partitioning of the sky. Cloud 1 represents a single cumulus cloud in an otherwise clear sky; cloud 2 represents a bank of clouds covering much of the horizon, and cloud 3 represents several cumulus clouds in the relevant part of the sky. Panel 4 shows the sky radiance for a uniformly overcast sky with  $C = 0.5$  in the Harrison and Coombes formulas.

To obtain an idea of what values to use for  $C_L$  in the Hydrolight simulations, MODTRAN<sup>13</sup> Version 4.0 was used first to generate the clear-sky spectral radiance at sea level corresponding to the viewing geometry seen in Fig. 10. Typical values were used for atmospheric parameters, e.g., 1976 U.S. Standard Atmosphere profiles with an open-ocean marine aerosol profile in the boundary layer, and azimuthally dependent multiple scattering was used in the radiance calculations. The computed clear-sky radiance  $L_s$  (at the centers of the small rectangles in Fig. 10) is shown in Fig. 11. The apparent radiance of a bright white cumulus cloud was then simulated as follows. The MODTRAN-computed spectral irradiance at 2 km altitude,  $E_c$ , was taken as being incident onto the vertical side of the cloud. The cloud was assumed to be a Lambertian reflector with an albedo of 80 per cent, so that the radiance leaving the cloud was  $(0.8/\pi)E_c$ . This radiance was then propagated to the sea surface using the MODTRAN-computed spectral transmittance along the slant-path from the cloud to the sea surface. The resulting cloud radiance,  $L_c$ , is also shown in Fig. 11. The factor  $C_L$  is then just the ratio  $L_c/L_s$ . As seen in Fig. 11,  $C_L$  varies from less than two at 350 nm to more than 40 at 800 nm. This suggests that Hydrolight runs made with  $C_L$  values up to 50 would simulate the possible range of cloud radiances that might be encountered in nature. (The dashed curve of Fig. 11 is well described by a quadratic function of  $\lambda$ , except near 730 nm. Such a function was used for  $C_L(\lambda)$  in the simulations for Fig. 14 below.)

Table 1 shows the values of  $C_L$  used for various simulations of clouds in an otherwise clear sky, along with the resulting  $\rho$  values. For this wind speed of  $10 \text{ m s}^{-1}$  and sun and viewing geometry, the clear sky  $\rho$  value is 0.0337. For the single cloud labeled cloud 1 in Fig. 10,  $\rho$  increases to 0.0362 for  $C_L = 5$ , i.e., for the cloud having five times the radiance of the clear sky in the same direction, as is typical at blue wavelengths. The value of  $\rho$  reaches 0.0639 for  $C_L = 50$ , which is possible at infrared wavelengths. Thus, depending on wavelength, the proper value to use for  $\rho$  varies by almost a factor of two. The situation is even worse for cloud 2, which represents a cloud bank near the horizon:  $\rho$  now ranges from 0.0463 for  $C_L = 5$  to 0.1879 for  $C_L = 50$ . This cloud has a greater effect on  $\rho$  both because it is larger and because its location near the horizon means that its radiance is reflected into the sensor more strongly because the Fresnel reflectances are larger for the wave facets that reflect near-horizon radiances into the sensor. The cumulus clouds arranged as in cloud 3 give  $\rho$  values that are similar to those of the cloud 1 case. A uniformly overcast sky, which is represented by the cloud 4 case, gives almost no change in  $\rho$  as the cloud cover increases (i.e., as the cloud parameter  $C$  of the Harrison and Coombes formulas increases). The minimum value of  $\rho = 0.0248$  occurs when there is a heavy overcast: in this case the sky is fairly uniform and there is no sun glint at all.

Additional and more realistic cloud simulations could be made. However, the results of a comprehensive study of randomly arranged clouds of various types likely would have to be presented in statistical form, which would still leave the user uncertain of what  $\rho$  value should be used for the clouds present during a particular observation. The simulations presented are sufficient to reach the conclusion that the  $\rho$  value to be used in correcting for surface-reflected sky radiance is strongly dependent on sky conditions, viewing geometry, sea state, and sometimes wavelength. Bear in mind that there are additional complications not modeled above, such as the effects of gravity waves or whitecaps, which will increase the uncertainty in  $\rho$  even more. Even though the uncertainty in  $\rho$  can be minimized by a judicious choice of viewing directions, it is still difficult for a researcher in the field to guess the correct value of  $\rho$  to use in Eq. (6), especially if clouds have introduced a wavelength dependence in  $\rho$ .

## 6. Effects of Errors in $\rho$ on Estimated $R_{rs}$

Given that even an educated guess for  $\rho$  may be in error by a factor of two or more when using Eq. (6), it is necessary to investigate the consequence of such errors in  $\rho$  on the estimation of  $R_{rs}$ . As is clear from Eq. (6), if  $L_t$  is dominated by  $L_w$ , then imprecise correction for sky radiance may be of little importance. On the other hand, if the reflected sky radiance is much greater than the water-leaving radiance, then any error in removing the sky radiance may be significant. The relative



contributions of  $L_w$  and  $L_r$  to  $L_t$  depend on the water absorption and scattering properties, and thus on wavelength, as well as on viewing geometry.

To illustrate this dependence, a homogeneous water body with a chlorophyll concentration of  $2 \text{ mg m}^{-3}$  was simulated using bio-optical models for the absorption<sup>14</sup> and scattering<sup>15</sup> coefficients of Case 1 waters, as built into Hydrolight. The left panel of Fig. 12 shows the ratio of clear-sky water-leaving radiance to total radiance,  $L_w/L_t$ , as a function of wind speed and wavelength for  $\theta_s = 30$  degrees and for the traditional viewing direction of  $(\theta_v, \phi_v) = (30^\circ, 90^\circ)$ . We see that the contribution of  $L_w$  to the measurable radiance can range from over 80 per cent at low wind speeds and blue to green wavelengths to less than 20 per cent at red wavelengths at high wind speeds. The relative contribution of  $L_w$  to the total decreases as the wind speed increases because wave facets reflect more of the brighter, near-sun sky into the detector. (The Hydrolight simulations did not include Raman scatter by the water or chlorophyll fluorescence, which for these water conditions noticeably affect only the chlorophyll fluorescence band near 685 nm.) The right panel of Fig. 12 shows  $L_w/L_t$  for the same simulation, but for a viewing direction of  $(\theta_v, \phi_v) = (40^\circ, 135^\circ)$  as recommended above in the discussion of  $\rho$ . The ratio of  $L_w$  to  $L_t$  is now somewhat higher at all wavelengths, and the ratio is less dependent on wind speed because there is less sun glitter for the  $(40^\circ, 135^\circ)$  viewing direction. Note that even though this is a simulation of Case 1 water, the water-leaving radiance is never zero at 750 nm, and can be as much as 20 per cent of the total upwelling radiance above the surface at 750 nm for the water conditions of this simulation.

Figure 13 shows the exact and estimated  $R_{rs}$  for the same simulation as used in Fig. 12 for the  $10 \text{ m s}^{-1}$  wind. The solid line shows the exact  $R_{rs}$  computed from  $L_w/E_d$ . The left panel shows estimates of  $R_{rs}$  based on the traditional viewing geometry of  $(\theta_v, \phi_v) = (30^\circ, 90^\circ)$ . The dashed line is the estimate of  $R_{rs}$  obtained by using  $\rho = 0.0222$  (the Fresnel reflectance for  $\theta_v = 30^\circ$ ) in Eq. (6), as recommended by the SeaWiFS protocol.<sup>5</sup> The estimated  $R_{rs}$  is greater than the true  $R_{rs}$  because, as can be seen in Figs. 6 or 8, the correct  $\rho$  value for this geometry is about 0.06; using a value of 0.0222 therefore removes too little of the reflected sky radiance, making the numerator of Eq. (6) too large. The dotted line is the SeaWiFS estimate obtained from subtracting the value at 750 nm from the dashed curve. This gives the final estimate of  $R_{rs}$  by Eq. (7), which is seen to be quite close to the exact  $R_{rs}$ . The dash-dot line in the left panel is the estimate of  $R_{rs}$  obtained by using  $\rho = 0.06$ , as estimated from Fig. 8, in Eq. (6). Using this better guess for  $\rho$  improves the estimate when using Eq. (6), although the agreement is not as good as that of Eq. (7). The exact values of  $\rho$  that should be used in Eq. (6) varied from 0.0425 at 350 nm to 0.0850 at 800 nm. This wavelength dependence of the clear-sky  $\rho$  results from the different wavelength dependencies of the white sun glitter and the blue sky radiance, just as has been discussed for clouds. Using  $\rho = 0.06$  thus removes too much reflected radiance at blue wavelengths and too little at red wavelengths, as is seen in the figure.

These simulations are consistent with the conclusions of Toole *et al.*,<sup>16</sup> who did a detailed comparison of  $R_{rs}$  spectra determined by several methodologies based on Eqs. (6), (7), and (10). They used the traditional viewing direction of  $\phi_v = 90$  degrees in the application of Eq. (6). They concluded that “It seems likely that the reflected sky radiance is severely underestimated following these protocols.” That is to say, using a value of  $\rho \approx 0.03$  in Eq. (6) is incorrect at higher wind speeds.

The right panel of Fig. 13 shows the exact and estimated  $R_{rs}$  for the recommended viewing geometry of  $(\theta_v, \phi_v) = (40^\circ, 135^\circ)$ . The dashed line shows the estimate obtained from Eq. (6) using the Fresnel reflectance of 0.0253 (the value for  $\theta_v = 40^\circ$ ) for  $\rho$ ; this value is quite close to the exact value. Using a value of  $\rho = 0.034$ , as obtained from Fig. 9 for this wind speed and solar angle, gives an estimate of  $R_{rs}$  that is almost indistinguishable from the exact value. Likewise, the final SeaWiFS estimate is excellent. For wind speeds of  $5 \text{ m s}^{-1}$  or less (figures not shown), the agreement between the exact and estimated (using  $\rho = 0.0253$ )  $R_{rs}$  is much better, because  $\rho = 0.0253$  is close to the correct value for both viewing geometries.

Figure 14 shows two simulations for a  $10 \text{ m s}^{-1}$  wind and cloud case 3 as shown in Fig. 10. The viewing direction is  $(\theta_v, \phi_v) = (40^\circ, 135^\circ)$  in both panels. The left panel is the same Case 1 water as was used in Fig. 13; only the sky conditions have been changed to include clouds. The right panel of the figure also is for the cloud 3 sky conditions, but for a simulation of Case 2 water. This water body had a chlorophyll concentration of  $5 \text{ mg m}^{-3}$ , a CDOM concentration that gave absorption at 440 nm than was comparable to that by chlorophyll, and mineral particles consistent with a concentration of  $10 \text{ g m}^{-3}$  of clay particles.<sup>17,18</sup> The mineral particles were modeled with a wavelength-independent absorption coefficient and a scattering coefficient that varied as  $1/\lambda$ . The biological and mineral particles of this simulation made the water-leaving radiance at 750 nm comparable to that of the surface-reflected sky radiance.

As before, the solid line shows the exact  $R_{rs}$ . Because of the clouds, the value of  $\rho$  varies from 0.0332 at 350 nm to 0.0619 at 800 nm. The dashed lines show the estimates of  $R_{rs}$  using  $\rho = 0.0332$  in Eq. (6), and the dash-dot lines show the estimates using  $\rho = 0.0619$ . These two curves highlight the effect of the cloud-induced spectral dependence of  $\rho$ , which is especially noticeable for the Case 2 water. The dotted lines show the SeaWiFS estimate based on Eq. (7) and a  $\rho$  value of 0.0253. The SeaWiFS estimate is quite good for the Case 1 water, but is much too low for the Case 2 water because the assumption of zero water-leaving radiance at 750 nm is not satisfied. Figure 9 gives a  $\rho$  value of about 0.034, which generates an estimate that is indistinguishable from the dashed lines in the figure. Thus, for this particular Case 2 water body, an estimate based on Eq. (6) is much better than the “corrected” estimate based on Eq. (7).

The result just seen, namely that Eq. (6) can give better estimates than Eq. (7) for Case 2 water, holds for other sky conditions and wind speeds. Figure 15 shows simulations for the same Case 2

water body, but for clear skies with wind speeds of  $U = 0$  and  $10 \text{ m s}^{-1}$ . Figure 9 gives  $\rho = 0.026$  for  $U = 0$  and  $0.034$  for  $U = 10 \text{ m s}^{-1}$ . Using these clear-sky values in Eq. (6) gives  $R_{rs}$  estimates that are almost indistinguishable from the exact values, whereas Eq. (7) always gives a bad estimate because the water-leaving radiance is not zero at 750 nm.

Even in the worst cases of Figs. 14 and 15, the spectral shape of  $R_{rs}$  is fairly well preserved; only the magnitude is in error. This situation may be acceptable for some applications. However, significant errors can arise when taking the ratio of  $R_{rs}$  at two different wavelengths, especially if ratioing blue/green to orange/red wavelengths. For example, although the ratio  $R_{rs}(445)/R_{rs}(555)$  is in error by less than one per cent for the SeaWiFS curves of Fig. 15,  $R_{rs}(555)/R_{rs}(670)$  is off by 25 per cent.

Although it is difficult to generalize from the limited simulations made here, Figs. 12-15 do suggest the following: (1) a viewing direction of  $(\theta_v, \phi_v) = (40^\circ, 135^\circ)$  gives less sun glint and thus better estimates of  $R_{rs}$  than does the traditional direction of  $(\theta_v, \phi_v) = (30^\circ, 90^\circ)$  (Figs. 12 and 13); (2) although the SeaWiFS protocol of Eq. (7) can give satisfactory results in Case 1 waters, it can give poor results in waters where the water-leaving radiance at 750 nm is not close to zero (Figs. 14 and 15); (3) an  $R_{rs}$  estimate based on Eq. (6) and the  $\rho$  values of Fig. 9 can give better estimates than Eq. (7) in waters where the water-leaving radiance at 750 nm is not zero (Figs. 14 and 15).

## 7. Use of Polarizers in Estimating $R_{rs}$

As has been seen, the variability in  $\rho$  for different environmental conditions makes it difficult to estimate the water-leaving radiance  $L_w$  from a measurement of the total upwelling radiance  $L_t$ . Several researchers<sup>19,20</sup> have suggested using a polarizing filter to reduce the contribution of  $L_t$  to  $L_b$ , thereby obtaining a better estimate of  $L_w$ . This section reviews the basis for using a polarizing filter to estimate  $L_w$  and notes additional problems that can arise when a polarizing filter is used.

Polarized light is described by a four-component Stokes vector  $S = (S_0, S_1, S_2, S_3)^T$ , where T denotes the transpose. The first component of the Stokes vector,  $S_0$ , gives the radiance of the light beam as measured by a detector that is not sensitive to the state of polarization. The effect of an air-water surface on polarized light that is reflected by or transmitted through the air-water surface is described by a 16-element Mueller matrix,  $M$ . The Stokes vector describing the incident light is multiplied by the appropriate Mueller matrix to give a new Stokes vector describing the state of polarization after reflection or transmission by the surface. The components of the Stokes vector, and hence of Mueller matrices, can be defined in various ways; the particular forms of the Stokes vectors and Mueller matrices used here are those given by Collett,<sup>21</sup> who takes particular care in treating certain subtleties involved in transmission through a boundary separating two dielectric media, e.g., through an air-water surface.

Sky light is generally partially polarized. The polarization arises from Rayleigh scattering of unpolarized sunlight by atmospheric gasses. The Rayleigh-scattered light has the highest degree of polarization at scattering angles of 90 degrees, i.e. for viewing directions at right angles to the sun, which is the geometry traditionally used in making  $R_{rs}$  measurements. Scattering by atmospheric aerosols tends to depolarize the light. Therefore, the degree of polarization depends on the viewing direction relative to the sun and on the concentration and size distribution of atmospheric aerosols.

When incident sky light of arbitrary polarization reflects off of a level water surface at exactly the Brewster angle  $\theta_B = \tan^{-1}n$ , the reflected light is completely linearly polarized, with the light's electric field vector being normal to the plane of incidence and reflection. Such light is said to be horizontally polarized because, in this case, the electric vector oscillates in a plane parallel to the horizontal sea surface.

For water with an index of refraction of  $n = 1.34$ , the Brewster angle for air-incident light is  $\theta_B = 53.27^\circ$ . At this incident angle the Mueller matrix for reflection is simply (Collett<sup>21</sup> page 143)

$$M_{r,B} = 0.0405 \begin{pmatrix} 1 & 1 & 0 & 0 \\ 1 & 1 & 0 & 0 \\ 0 & 0 & 0 & 0 \\ 0 & 0 & 0 & 0 \end{pmatrix}.$$

If  $S_s = (S_{0s}, S_{1s}, S_{2s}, S_{3s})^T$  represents the arbitrarily polarized incident sky radiance (denoted by  $L_s$  above, in the unpolarized case), then the reflected sky radiance (denoted by  $L_r$  above) has the Stokes vector

$$S_r = M_{r,B} S_s = \begin{pmatrix} 0.0405(S_{0s} + S_{1s}) \\ 0.0405(S_{0s} + S_{1s}) \\ 0 \\ 0 \end{pmatrix}.$$

A Stokes vector of this form describes light that is completely horizontally plane polarized.

The water-leaving radiance ( $L_w$  above) will in general be polarized to an extent that depends on the viewing direction and on the water's scattering properties. If we let  $S_w = (S_{0w}, S_{1w}, S_{2w}, S_{3w})^T$  denote the unknown (and not directly measurable) Stokes vector of the water-leaving radiance, then the total upward radiance reaching a detector looking downward at the Brewster angle is

$$S_t = S_w + S_r = \begin{pmatrix} S_{0w} + 0.0405(S_{0s} + S_{1s}) \\ S_{1w} + 0.0405(S_{0s} + S_{1s}) \\ S_{2w} \\ S_{3w} \end{pmatrix}.$$

An ideal vertical polarizer passes only vertically polarized light, i.e. light whose electric vector oscillates only in the plane of incidence and reflection, which is a vertical plane relative to the horizontal air-water surface. If such a polarizer with Mueller matrix  $M_v$  is placed in front of the detector, the light reaching the detector then has a Stokes vector  $S_d$  given by

$$S_d = M_v S_t = \frac{1}{2} \begin{pmatrix} 1 & -1 & 0 & 0 \\ -1 & 1 & 0 & 0 \\ 0 & 0 & 0 & 0 \\ 0 & 0 & 0 & 0 \end{pmatrix} \begin{pmatrix} S_{0w} + 0.0405(S_{0s} + S_{1s}) \\ S_{1w} + 0.0405(S_{0s} + S_{1s}) \\ S_{2w} \\ S_{3w} \end{pmatrix} = \begin{pmatrix} \frac{1}{2}(S_{0w} - S_{1w}) \\ -\frac{1}{2}(S_{0w} - S_{1w}) \\ 0 \\ 0 \end{pmatrix}, \quad (11)$$

which shows the form of  $M_v$ . A Stokes vector of this form describes completely vertically plane polarized light. The important thing to note in Eq. (11) is that none of the reflected sky light reaches the detector. This observation is the incentive for placing a vertical polarizer in front of the detector.

Unfortunately, the simple result seen in Eq. (11) is deceiving. First, for real instruments with finite fields of view and for wind-blown surfaces, the instrument is seeing surface wave facets that are tilted at many different angles, which in general are not equal to the Brewster angle. For such facets, the full Mueller matrix must be used, and the reflected light is not completely horizontally polarized. Thus the light reaching the detector will still contain some reflected sky light. How much reflected light reaches the detector is not easily predicted because of the dependence on viewing geometry, sea state, and polarization of the incident sky light.

Second, even if the sea surface is level and is viewed at the Brewster angle, the underwater light that is transmitted upward through the surface (the water-leaving radiance) toward the detector has an unknown state of polarization. Thus *the effect of passing the water-leaving radiance through the vertical polarizer cannot be predicted in any simple fashion*. This results in a detected quantity that is a function of the water-leaving radiance, but whose functional dependence on  $L_w$  is both unknown and variable.

Finally, note that even a perfect linear polarizer reduces the radiance of an unpolarized beam by a factor of  $\frac{1}{2}$ . Any real polarizer has additional losses arising from absorption by the polarizer material and from reflection by the polarizer surface. Thus the factor of  $\frac{1}{2}$  seen in Eq. (11) should be replaced by some factor  $f$ , where  $f < \frac{1}{2}$ . The factor  $f$  depends on wavelength, and even high quality glass polarizing filters have little transmission below 400 nm. Although  $f(\lambda)$  can be determined for a given polarizer, this loss of signal can be important in situations where the detector signal is already small, such as in very clear waters or at wavelengths greater than 700 nm. Note, of course, that the gray plaque must also be viewed with the polarizer in place, so that a corresponding reduction of the denominator occurs in Eq. (6).

The preceding arguments, although qualitative, indicate that the use of a linear polarizer may introduce as many uncertainties as it removes in the estimation of  $R_{rs}$ . Although some investigators have found little difference in  $R_{rs}$  estimated with and without polarizers,<sup>22</sup> and others have claimed the use of polarizers helpful,<sup>20</sup> still other practitioners<sup>23</sup> have abandoned their use because of difficulties in interpreting data taken with polarizers. In any case, no investigator has quantified the potential errors discussed above. Therefore, pending quantification of these uncertainties via vector-level radiative transfer modeling (as in Kattawar and Adams<sup>24</sup>), which can separate polarization effects *per se* from other sources of error, and a resulting clear demonstration that the advantages of polarizers outweigh their disadvantages, it seems unwise to use polarizing filters in the estimation of the remote-sensing reflectance.

## 8. Recommendations for Estimating $R_{rs}$

The simulations presented above show that it is difficult to determine the correct value of the reflectance  $\rho(\lambda)$  that should be used to remove the surface-reflected sky light from a measured total radiance. Nevertheless, both the simulations of Sect. 6 and the established success of the use of Eqs. (6) and (7) with  $\rho \approx 0.028$  indicate that the errors induced in the estimated  $R_{rs}$  by the use of incorrect  $\rho$  values are often, but not always (e.g., Figs. 14 and 15) small. There is certainly room for improvement over this method of estimating the remote-sensing reflectance.

Lee *et al.*<sup>25</sup> recently proposed a new protocol for the estimation of  $R_{rs}$ . Their method partitions the skylight into Rayleigh and aerosol components. The radiance distribution arising from Rayleigh scattering is assumed to be uniform, so that its contribution to  $L_t$  can be removed by use of a  $\rho$  value,  $\rho_{Ray}$ , corresponding to a completely uniform sky, i.e. a sky without any sun present. The contributions of aerosol scattering, which makes the sky bright in the vicinity of the sun, and of glitter by the sun's direct beam are then removed from  $L_t$  by a sophisticated optimization procedure that makes use of data over the broad spectral range from 400 to 830 nm. Lee *et al.* suggest using a value of  $\rho_{Ray} \approx 0.021$  for the removal of the Rayleigh component of the reflected sky light when

the viewing angle is  $\theta_v = 30^\circ$ . Hydrolight-generated  $\rho$  values for a completely uniform sky (not shown here; see Mobley and Stramski<sup>26</sup>) show that in this case the wind speed has little effect on  $\rho$  and that using a value of 0.021 or 0.022 for  $\rho_{Ray}$  is justified.

The optimization method of Lee *et al.* (or some similar algorithm) may prove to be a significant improvement over the traditional ways of estimating  $R_{rs}$ . Until an improved method becomes available, however, the following suggestions can be made for using the traditional method based on Eq. (6).

A viewing direction of  $\theta_v \approx 40^\circ$ ,  $\phi_v \approx 135^\circ$  will minimize the effects of sun glint and non-uniform sky radiance while also avoiding instrument shading problems. For this viewing direction, a value of  $\rho \approx 0.028$  is acceptable for wind speeds less than  $5 \text{ m s}^{-1}$ . At higher wind speeds, the clear-sky  $\rho$  value should be increased in accordance with Fig. 9. If the sky is heavily overcast, use a value of  $\rho \approx 0.028$  at all wind speeds. There is little justification for attempting to be more precise than this in practice, especially if clouds are present. Although residual sun-glint effects can be further corrected in some cases by subtracting the value of  $R_{rs}(750 \text{ nm})$  as suggested in the SeaWiFS protocol, this procedure will give less accurate estimates in highly scattering waters than those based solely on Eq. (6) and the  $\rho$  values of Fig. 9. Finally, do not use a polarizing filter on the radiometer making the measurements.

## Acknowledgments

This work was supported by the Environmental Optics Program of the U. S. Office of Naval Research and by the Remote Sensing Division of the Naval Research Laboratory. Dave Siegel and Tonya Clayton made helpful suggestions on an early version of the manuscript.



## REFERENCES

1. C. D. Mobley, *Light and Water: Radiative Transfer in Natural Waters* (Academic Press, San Diego, 1994).
2. C. D. Mobley, B. Gentili, H. R. Gordon, Z. Jin, G. W. Kattawar, A. Morel, P. Reinersman, K. Stamnes, and R. H. Stavn, "Comparison of numerical models for computing underwater light fields," *Applied Optics*, **32**, 7484-7504 (1993).
3. C. D. Mobley, "Hydrolight 4.0 Users' Guide (Second Printing)," Sequoia Scientific, Inc., Mercer Island, WA. (1998).
4. K. L. Carder and R. G. Steward, "A remote-sensing reflectance model of a red-tide dinoflagellate off west Florida," *Limnol. Oceanogr.*, **30**(2), 286-298 (1985).
5. J. L. Mueller and R. W. Austin, "Ocean Optics Protocols for SeaWiFS Validation, Revision 1." SeaWiFS Technical Report Series, vol. 25, NASA Tech. Memo. 104566, S. B. Hooker, E. R. Firestone, and J. G. Acker, Editors (1995).
6. J. R. V. Zaneveld, "An asymptotic closure theory of irradiance in the sea and its inversion to obtain the inherent optical properties," *Limnol. Oceanogr.*, **34**(8), 1442-1452 (1989).
7. R. W. Preisendorfer and C. D. Mobley, "Albedos and glitter patterns of a wind-roughened sea surface," *J. Phys. Oceanogr.*, **16**(7), 1293-1316 (1986).
8. H. R. Gordon, O. B. Brown, R. H. Evans, J. W. Brown, R. C. Smith, K. S. Baker, and D. C. Clark, "A semianalytic radiance model of ocean color," *J. Geophys. Res.*, **93**(D9), 10,909-10,924 (1988).
9. A. Morel and B. Gentili, "Diffuse reflectance of oceanic waters. II. Bidirectional aspects," *Applied Optics*, **32**, 6864-6879 (1993).
10. A. Morel, K. J. Voss, and B. Gentili, "Bidirectional reflectance of oceanic waters: A comparison of modeled and measured upward radiance fields," *J. Geophys. Res.*, **100**(C7), 13,143-13,150 (1995).



11. A. W. Harrison and C. A. Coombes, "An opaque cloud cover model of sky short wavelength radiance," *Solar Energy*, **41**(4), 387-392 (1988).
12. R. Austin, Page 2-2 in Duntley, *et al.*, "Ocean Color Analysis," SIO Ref. 74-20, Scripps Inst. Oceanogr., La Jolla, CA (1974).
13. P.K. Acharya, *et al.*, "MODTRAN User's Manual Versions 3.7 and 4.0 (Draft)," Air Force Research Laboratory, Space Vehicles Directorate, Hanscom Air Force Base, MA (1998)
14. A. Morel, "Light and marine photosynthesis: a spectral model with geochemical and climatological implications," *Prog. Oceanogr.*, **26**, 263-306 (1991).
15. H. R. Gordon and A. Morel, "Remote assessment of ocean color for interpretation of satellite visible imagery, a review." *Lecture Notes on Coastal and Estuarine Studies*, vol. 4 (Springer Verlag, New York, 1983).
16. D. A. Toole, D. A. Siegel, D. W. Menzies, J. J. Neumann, and R. C. Smith, "Remote sensing reflectance determinations in coastal environments—impacts of instrumental characteristics and environmental variability," *Applied Optics*, submitted.
17. C. H. Whitlock, L. R. Poole, J. W. Usry, W. M. Houghton, W. G. Witte, W. D. Morris, and E. A. Gurganus, "Comparison of reflectance with backscatter and absorption parameters for turbid waters," *Applied Optics*, **20**(3), 517-522 (1981).
18. R. P. Bukata, J. H. Jerome, K. Ya. Kondratyev, and D. V. Pozdnyakov, *Optical Properties and Remote Sensing of Inland and Coastal Waters* (CRC Press, Inc., New York, 1995).
19. K. L. Carder, P. Reinersman, R. F. Chen, and F. Mueller-Karger, "AVIRIS calibration and application in coastal oceanic environments," *Remote Sens. Environ.* **44**, 205-216 (1993).
20. M. Sydor and R. A. Arnone, "Effect of suspended particulate and dissolved organic matter on remote sensing of coastal and riverine waters," *Applied Optics*, **36**(27), 6905-6912 (1997).
21. E. Collett, *Polarized Light: Fundamentals and Applications* (Marcel Dekker, Inc., New York, 1993).

22. J. L. Mueller, J. R. V. Zaneveld, S. Pegau, E. Valdez, H. Maske, S. Alvarez-Borrego, and R. Lara-Lara, "Remote sensing reflectance: preliminary comparisons between in-water and above-water measurements, and estimates modelled from measured inherent optical properties," in *Ocean Optics XIII*, S. G. Ackleson and R. Frouin, Editors, Proc. SPIE 2963, 502-507 (1997).
23. W. J. Rhea and C. O. Davis, "A comparison of the SeaWiFS chlorophyll and CZCS pigment algorithms using optical data from the 1992 JGOFS Equatorial Pacific Time Series," *Deep-Sea Res. II* **44**, 1907-1925 (1997).
24. G. W. Kattawar and C. N. Adams, "Stokes vector calculations of the submarine light field in an atmosphere-ocean with scattering according to a Rayleigh phase matrix: Effect of interface refractive index on radiance and polarization," *Limnol. Oceanogr.*, **34**(8), 1453-1472 (1989).
25. Z. P. Lee, K. L. Carder, R. G. Steward, T. G. Peacock, C. O. Davis, and J. L. Mueller, "Remote-sensing reflectance and inherent optical properties of oceanic waters derived from above-water measurements," in *Ocean Optics XIII*, S. G. Ackleson and R. Frouin, Editors, Proc. SPIE **2963**, 160-166 (1997).
26. C. D. Mobley and D. Stramski, "Origins of variability in remote-sensing reflectances (Final Report)," Sequoia Scientific, Inc., Mercer Island, WA. (1997).

Table 1. Simulations of cloud effects on  $\rho$ . The locations of the clouds are shown in Fig. 10. Cloud parameters  $C_L$  and  $C$  are described in the text.

cloud case	$C_L$	$C$	$\rho$	comment
	1.0	0.0	0.0337	clear sky
cloud 1	5.0	0.0	0.0362	single cumulus cloud; 400 nm
	10.0	0.0	0.0392	single cumulus cloud; 500 nm
	20.0	0.0	0.0454	single cumulus cloud; 600 nm
	50.0	0.0	0.0639	single cumulus cloud; 700-800 nm
cloud 2	5.0	0.0	0.0463	cloud bank on horizon; 400 nm
	10.0	0.0	0.0620	cloud bank on horizon; 500 nm
	20.0	0.0	0.0935	cloud bank on horizon; 600 nm
	50.0	0.0	0.1879	cloud bank on horizon; 700-800 nm
cloud 3	5.0	0.0	0.0365	scattered cumulus clouds; 400 nm
	10.0	0.0	0.0400	scattered cumulus clouds; 500 nm
	20.0	0.0	0.0470	scattered cumulus clouds; 600 nm
	50.0	0.0	0.0679	scattered cumulus clouds: 700-800 nm
cloud 4	—	0.25	0.0286	thin uniform overcast
	—	0.50	0.0264	increasing overcast
	—	0.75	0.0254	increasing overcast
	—	1.0	0.0248	thick overcast; no sun visible

## Figure Captions

- Fig. 1 Illustration of concepts for a wind-blown sea surface.  $L_r$  is the surface-reflected part of the incident sky radiance  $L_s$ .  $L_w$  is the transmitted part of the upwelling underwater radiance  $L_u$ . The downward-looking radiometer has a field of view with solid angle  $\Omega_{\text{FOV}}$ .
- Fig. 2. Illustration of the sky regions “seen” by a detector looking at the sea surface.  $U$  is the wind speed. The detector and specular point are centered at  $\theta = 40^\circ$  from the zenith. One hundred points are plotted for  $U = 0$ , and 5,000 points are plotted for the other cases.
- Fig. 3. Sun and sensor geometry as often used in field measurements.
- Fig. 4. Comparison of  $\rho$  as computed by Hydrolight (solid line) and by Austin<sup>12</sup> (dashed line). The wind speed is  $10 \text{ m s}^{-1}$  and the sun is at  $\theta_s = 60^\circ$  in a uniform background sky.
- Fig. 5. Illustration of the sky region seen by a detector for  $U = 15 \text{ m s}^{-1}$ , as in Fig. 2; 10,000 points are plotted. The solid lines are contours of the relative sky radiance computed by the formulas of Harrison and Coombes<sup>11</sup> for  $\theta_s = 30^\circ$  in a clear sky.
- Fig. 6. Effects of sun glitter and non-uniform sky radiance on  $\rho$ . The wind speed is  $U = 10 \text{ m s}^{-1}$  and the sky has a radiance distribution characteristic of a clear sky (as in Fig. 5);  $\theta_s$  is the solar zenith angle. The dotted lines are different Monte Carlo simulations for the  $\theta_s = 30^\circ$  case. The dashed line is Austin’s curve from Fig. 4.
- Fig. 7. Contour plots of  $\rho$  as a function of viewing direction  $(\theta_v, \phi_v)$  for  $\theta_s = 30$  degrees and two wind speeds. Contour values are 0.03 to 0.12 by 0.01. The \* symbols shows the specular direction of the sun, and the  $\theta_v$  contours are labeled along the  $\phi_v = 135$  degree direction.
- Fig. 8. Effect of wind speed and viewing direction on  $\rho$  for a sun zenith angle of  $\theta_s = 30$  degrees and a clear-sky radiance distribution. The solid lines are for an azimuthal viewing direction of  $\phi_v = 135$  degrees, and the dotted lines are for  $\phi_v = 90$  degrees.
- Fig. 9. Effect of wind speed and sun zenith angle on  $\rho$  for a viewing direction of  $\theta_v = 40$  degrees and a clear-sky radiance distribution. The solid lines are for an azimuthal viewing direction of  $\phi_v = 135$  degrees, and the dotted lines are for  $\phi_v = 90$  degrees.

Fig. 10. Representations of clouds. The shaded areas in panels 1, 2, and 3 show the locations of clouds in an otherwise clear sky (sky radiance contours as in Fig. 5); panel 4 shows the sky radiance distribution for a cloud parameter value of  $C = 0.5$  in the Harrison and Coombes<sup>11</sup> formulas. The sun is at  $\theta_s = 30$  degrees and the viewing direction is  $(\theta_v, \phi_v) = (40^\circ, 135^\circ)$ . As in Figs. 2 and 5, the small rectangle shows the region of the sky that would be seen by a detector for zero wind speed, and the dots illustrate the region of the sky seen for a  $10 \text{ m s}^{-1}$  wind (2,000 points plotted).

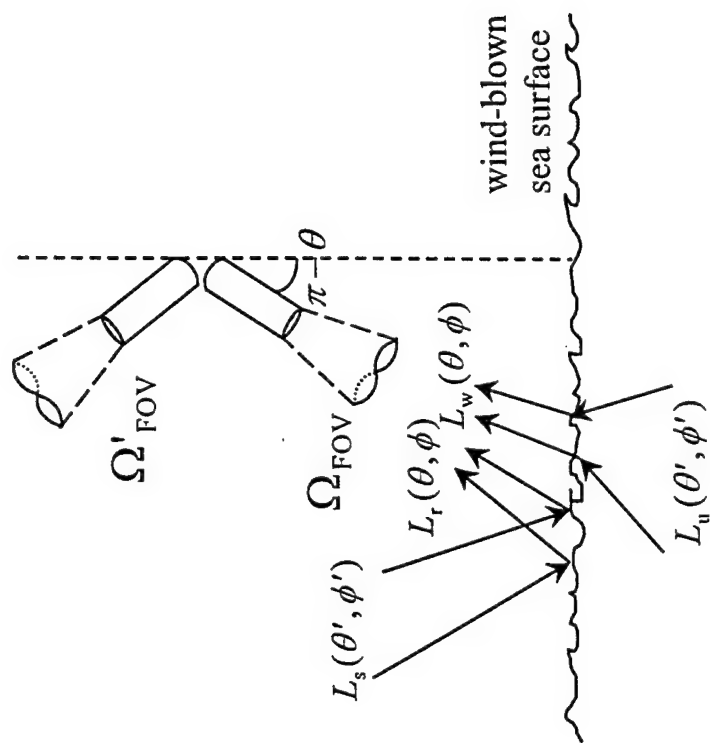
Fig. 11. MODTRAN-simulated blue-sky ( $L_s$ ) and cumulus cloud ( $L_c$ ) radiances for the viewing geometry of Fig. 10. The dashed line shows the ratio  $C_L = L_c/L_s$ .

Fig. 12. Relative contribution of the water-leaving radiance  $L_w$  to the total upward radiance  $L_t$  as a function of wind speed  $U$  and wavelength, for a Case 1 water body with  $2 \text{ mg m}^{-3}$  of chlorophyll and for  $\theta_s = 30$  degrees. The left panel is for a viewing direction of  $(\theta_v, \phi_v) = (30^\circ, 90^\circ)$ , and the right panel is for  $(\theta_v, \phi_v) = (40^\circ, 135^\circ)$ .

Fig. 13. Exact and estimated  $R_{rs}$  for a wind speed of  $U = 10 \text{ m s}^{-1}$ , and for  $\theta_s = 30$  degrees in a clear sky. The left panel is for a viewing direction of  $(\theta_v, \phi_v) = (30^\circ, 90^\circ)$ , and the right panel is for  $(\theta_v, \phi_v) = (40^\circ, 135^\circ)$ . The water body is the same as for Fig. 12. The line patterns denote the exact  $R_{rs}$ , solid lines;  $R_{rs}$  estimated using  $\rho = 0.0222$ , dashed lines;  $\rho = 0.06$  in Eq. (6), left panel, dash-dots or  $\rho = 0.034$  in Eq. (6), right panel, dash-dots; and the SeaWiFS estimate based on Eq. (7), dotted lines.

Fig. 14. Exact and estimated  $R_{rs}$  for a wind speed of  $U = 10 \text{ m s}^{-1}$ , and for  $\theta_s = 30$  degrees in a sky with clouds arranged as in the cloud 3 case of Fig. 10. Both panels have  $(\theta_v, \phi_v) = (40^\circ, 135^\circ)$ . The left panel is for Case 1 water and the right panel is for Case 2 water, as described in the text. In both panels the lines denote the exact  $R_{rs}$ , solid lines; estimates made with  $\rho = 0.0332$ , dashed lines, and  $\rho = 0.0619$ , dash-dots; and the SeaWiFS estimate, dotted lines.

Fig. 15. Exact and estimated  $R_{rs}$  for a wind speeds of  $U = 0$  and  $10 \text{ m s}^{-1}$ , for  $\theta_s = 30$  degrees in a clear sky. The water body is the Case 2 water described in the text. The line patterns denote the exact  $R_{rs}$ , solid lines; the estimate made with Eq. (6) and the appropriate  $\rho$  value from Fig. 9, as labeled, dashed lines; and the SeaWiFS estimate, dotted lines. The bars at the bottom of the left panel show the nominal SeaWiFS bands.



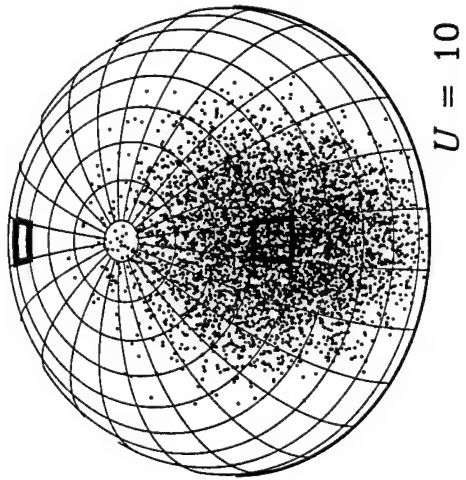
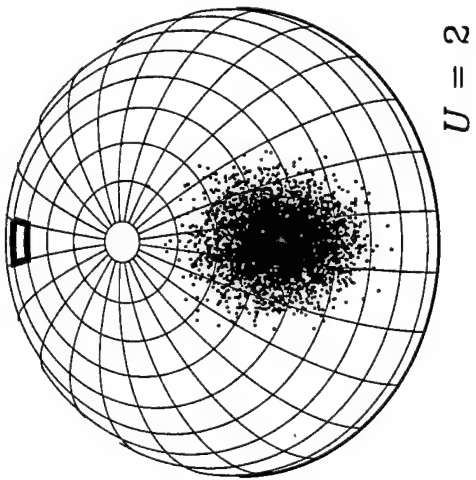
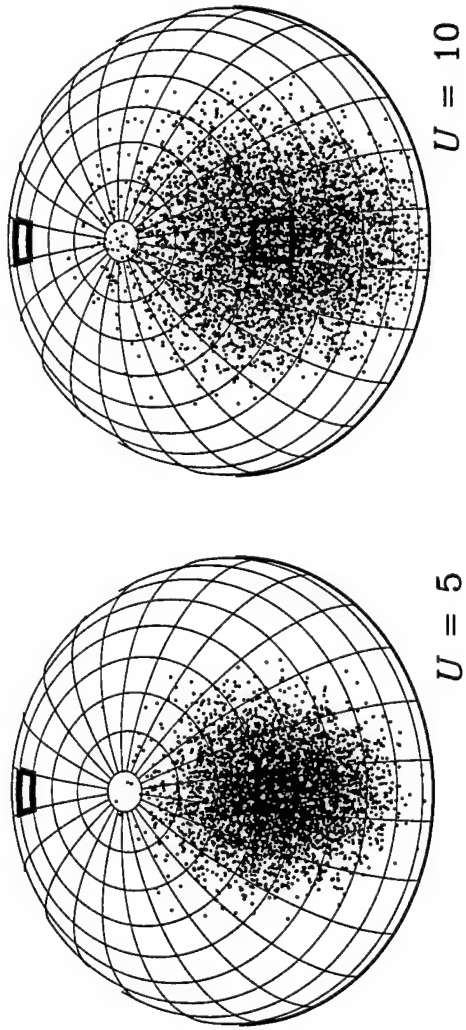
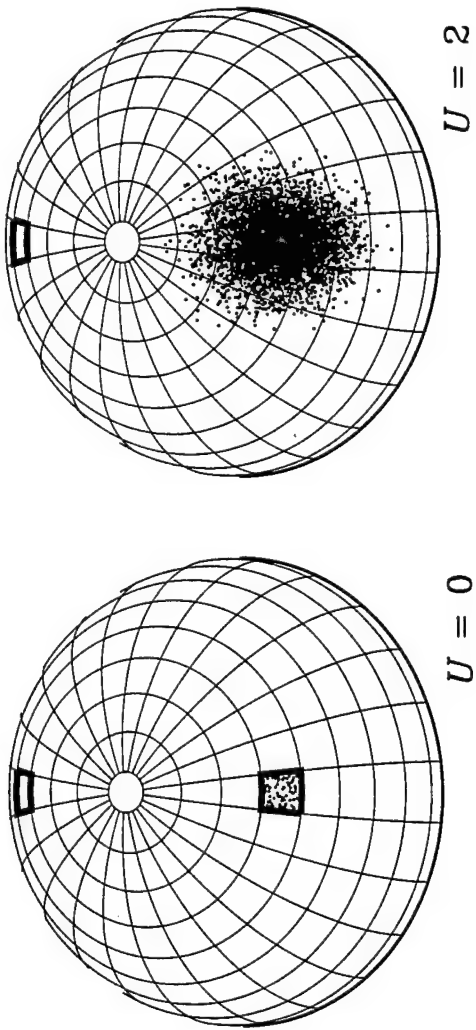
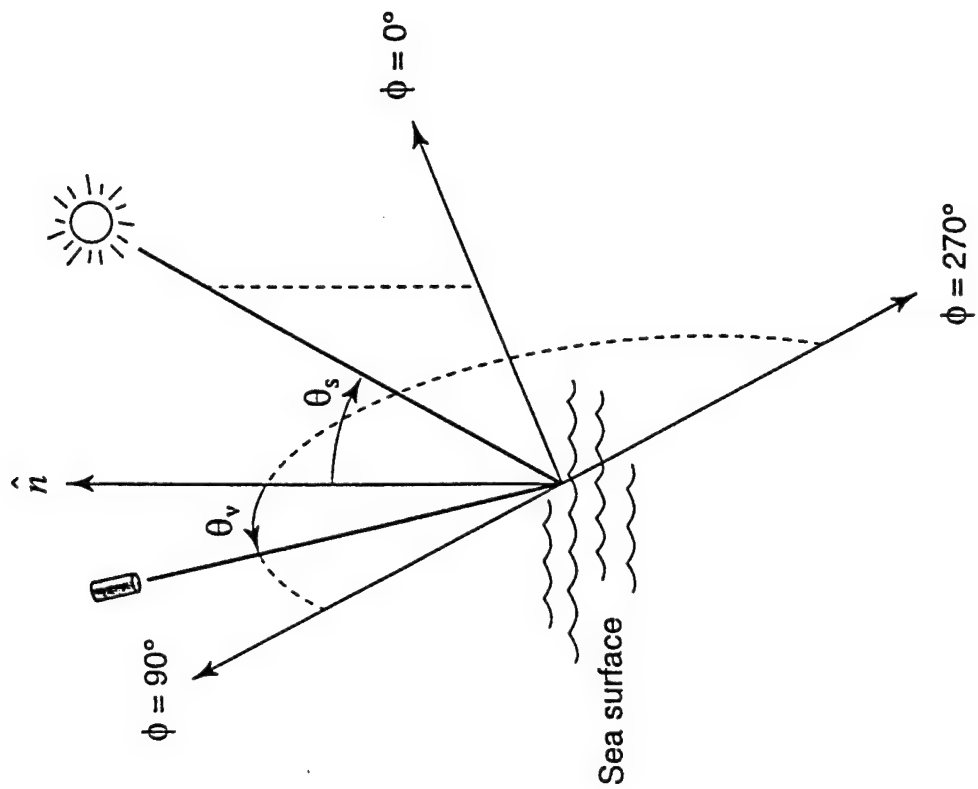
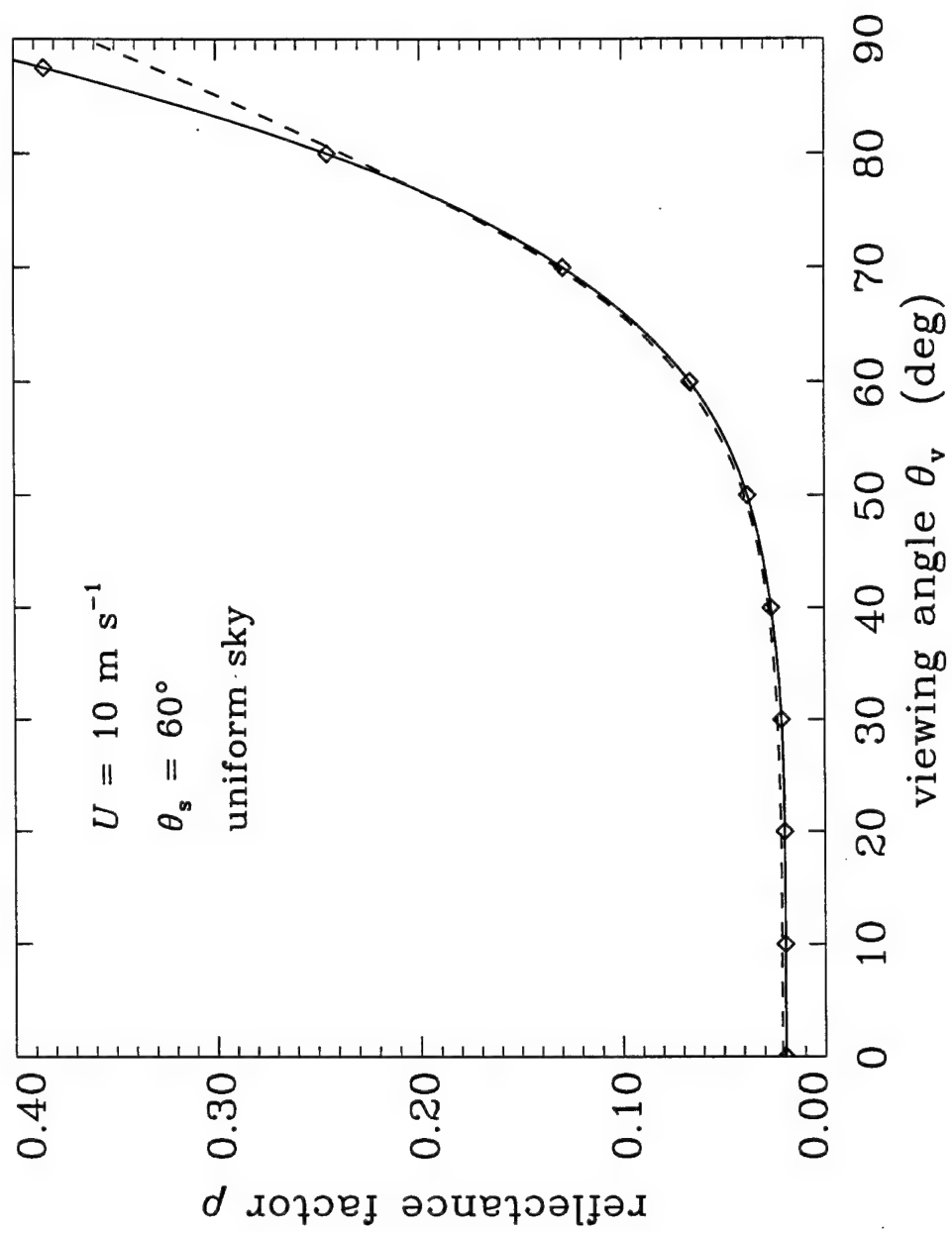


Fig. 2







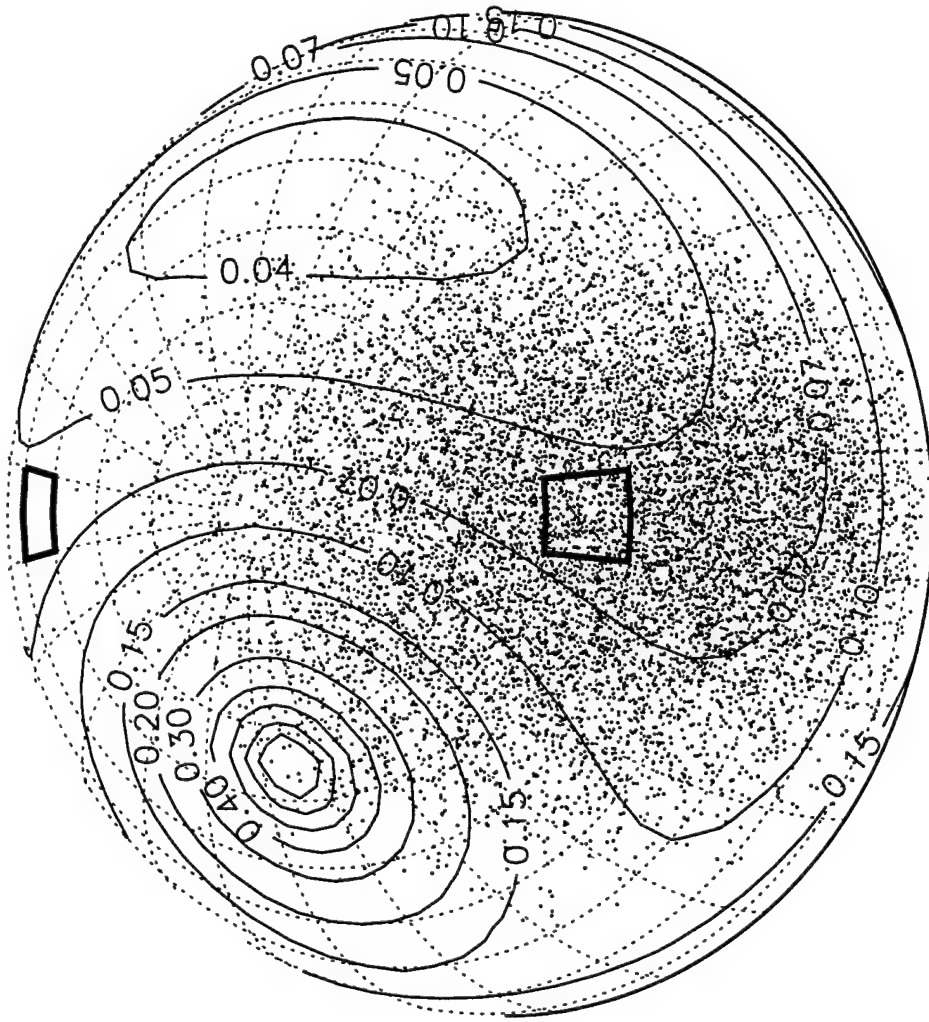


Fig. 5

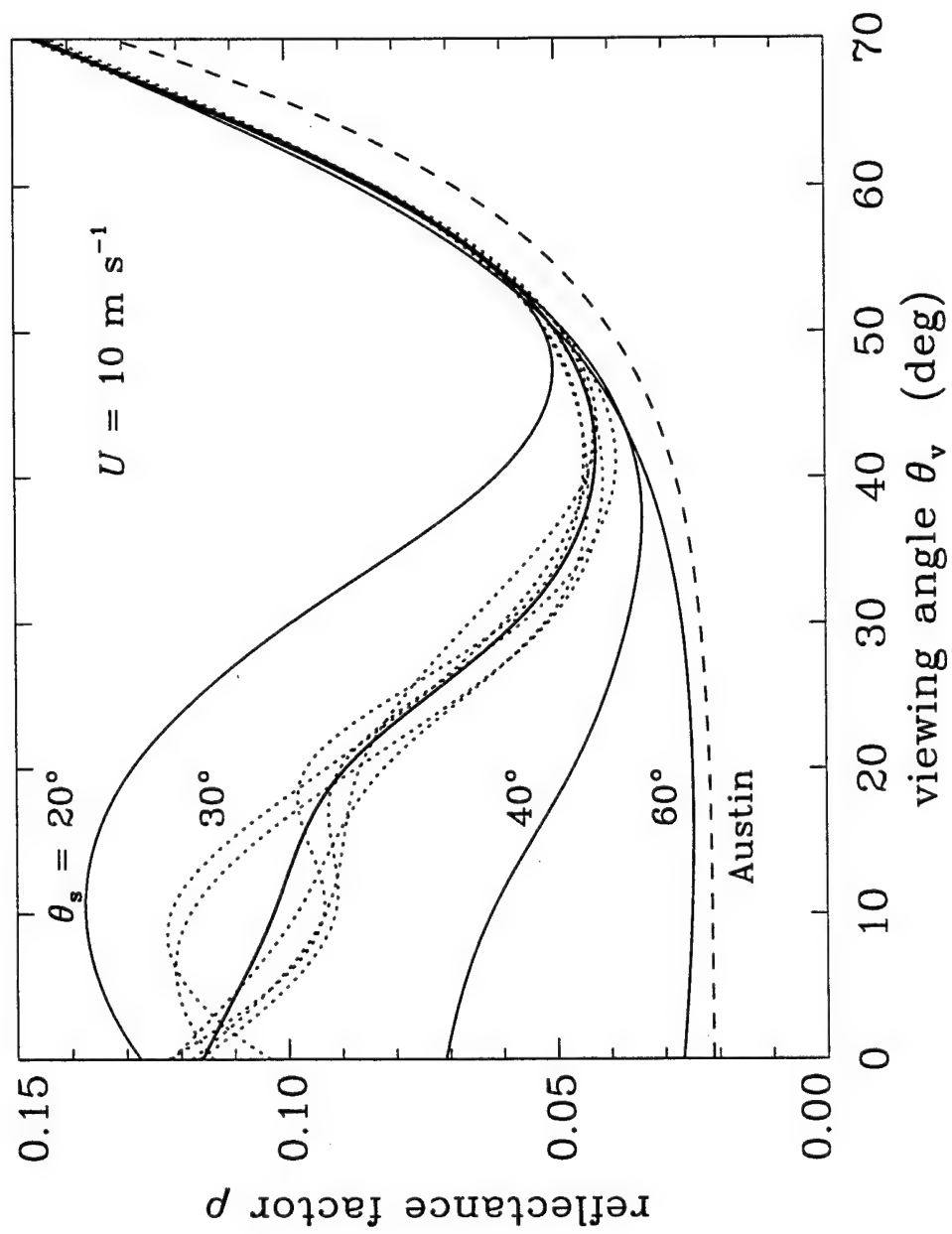


Fig. 6

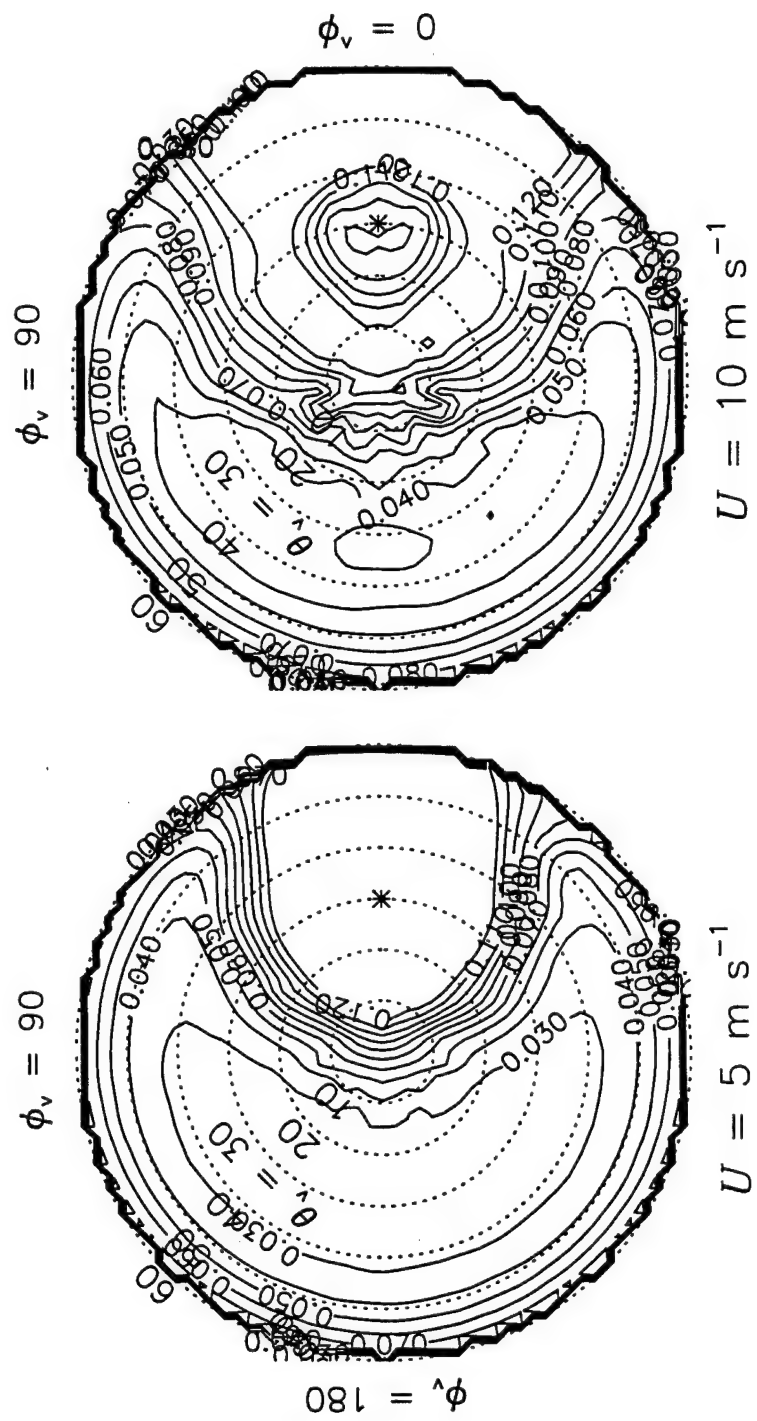


Fig. 7

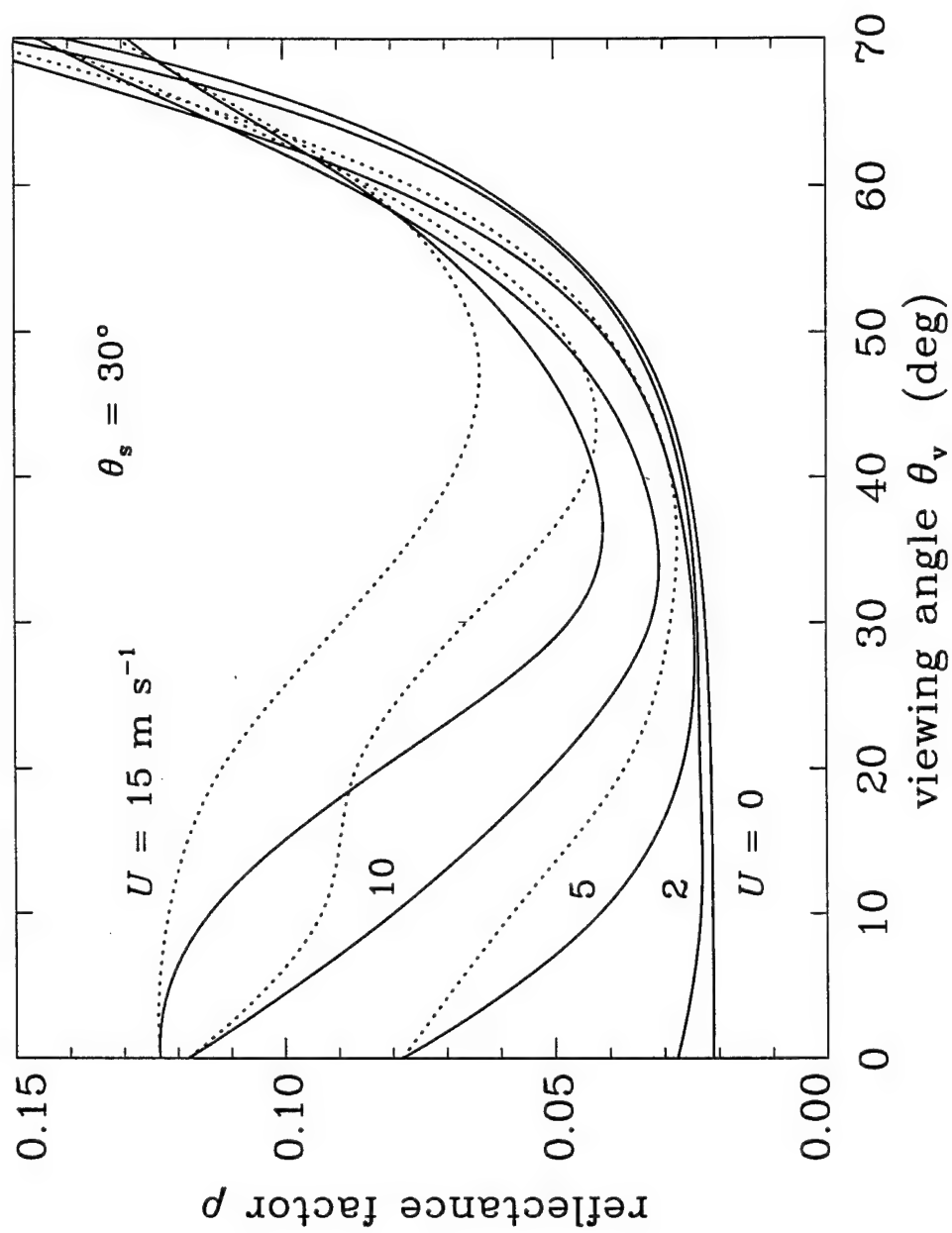
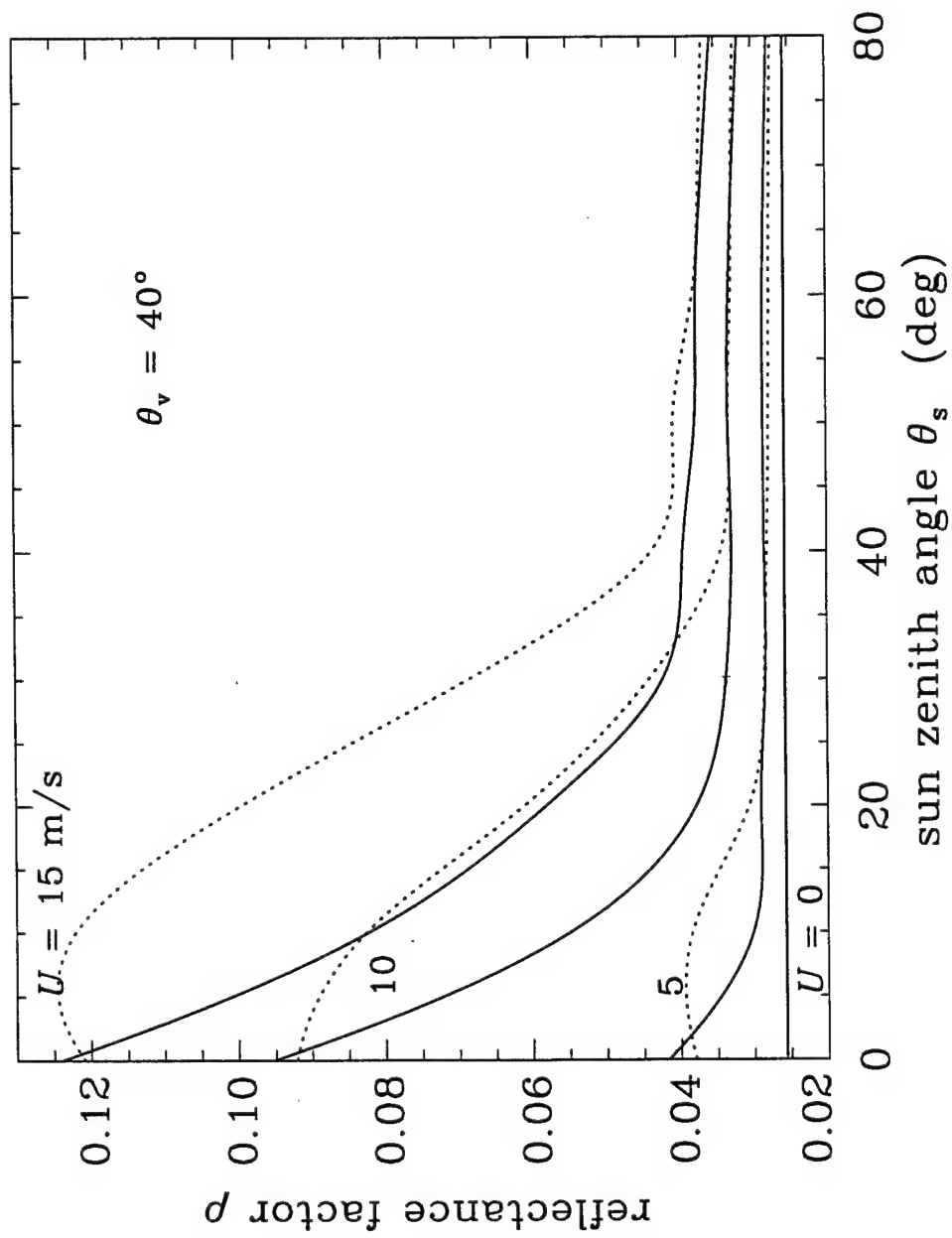


Fig. 8



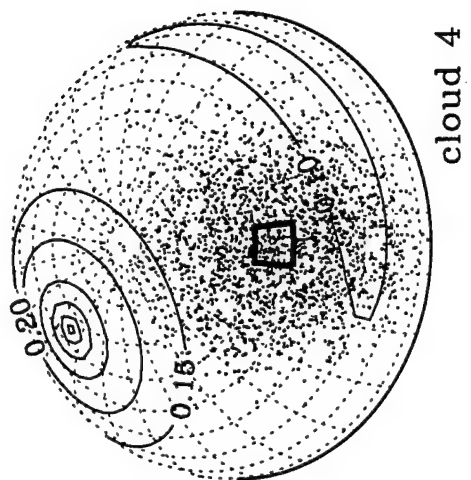
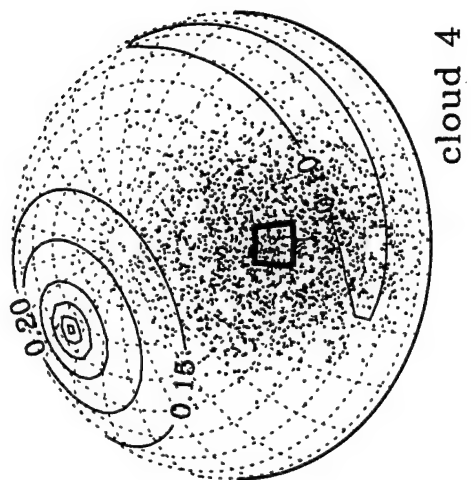
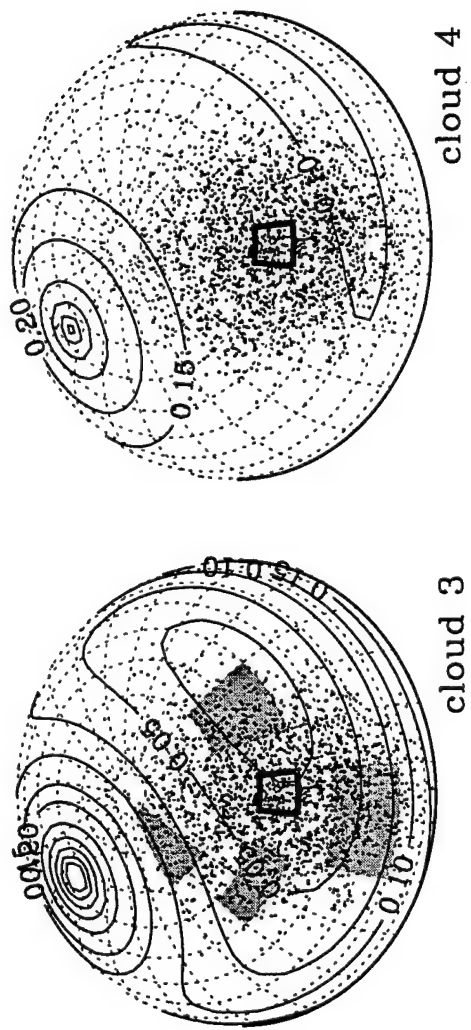
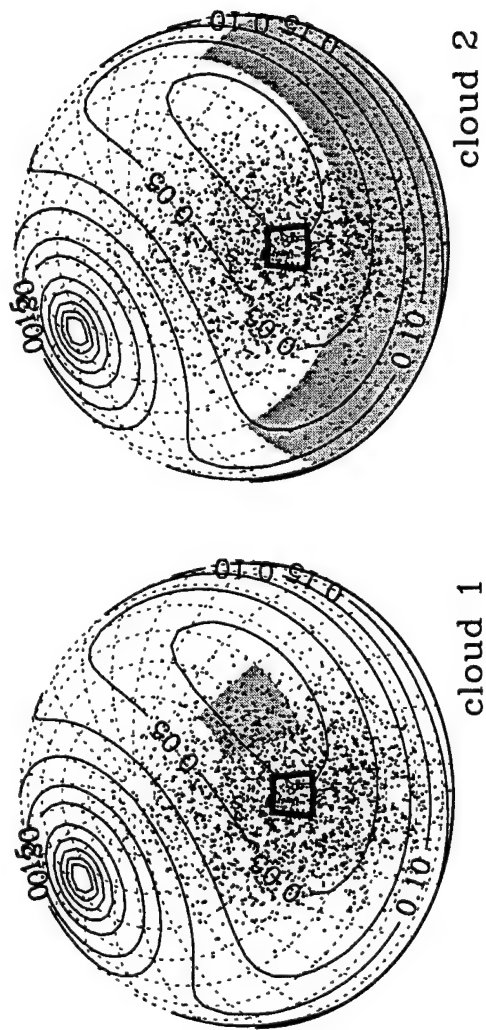


Fig. 10

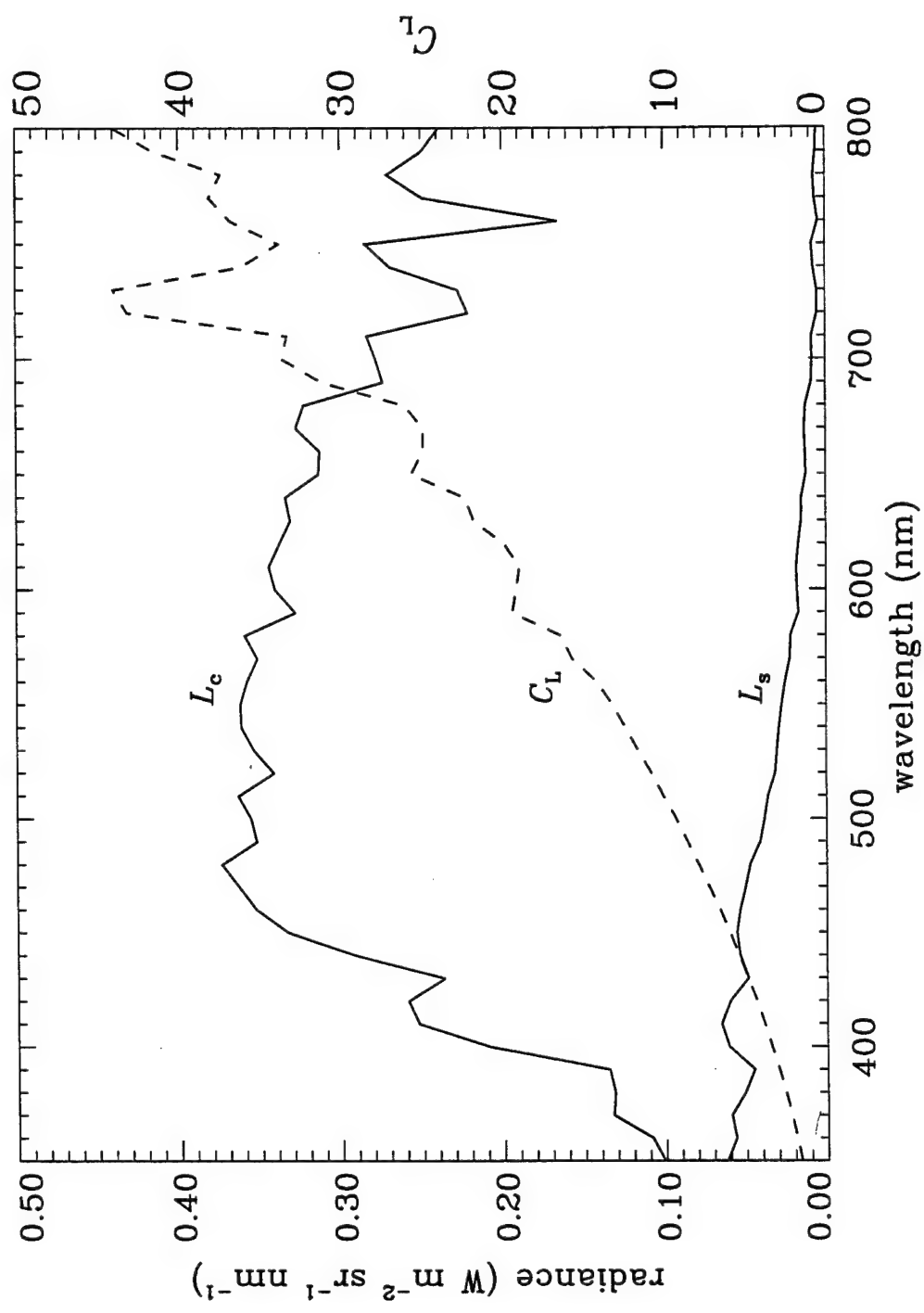
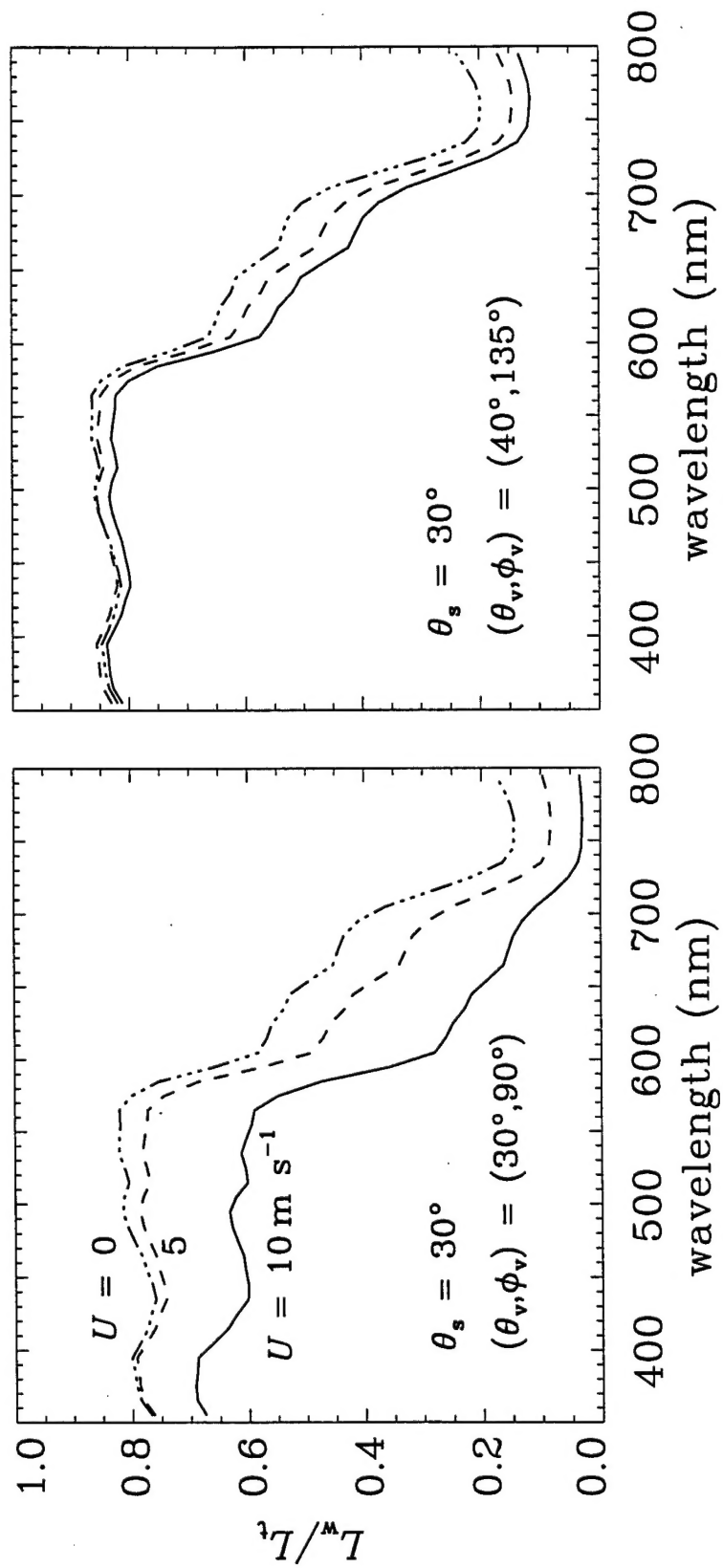


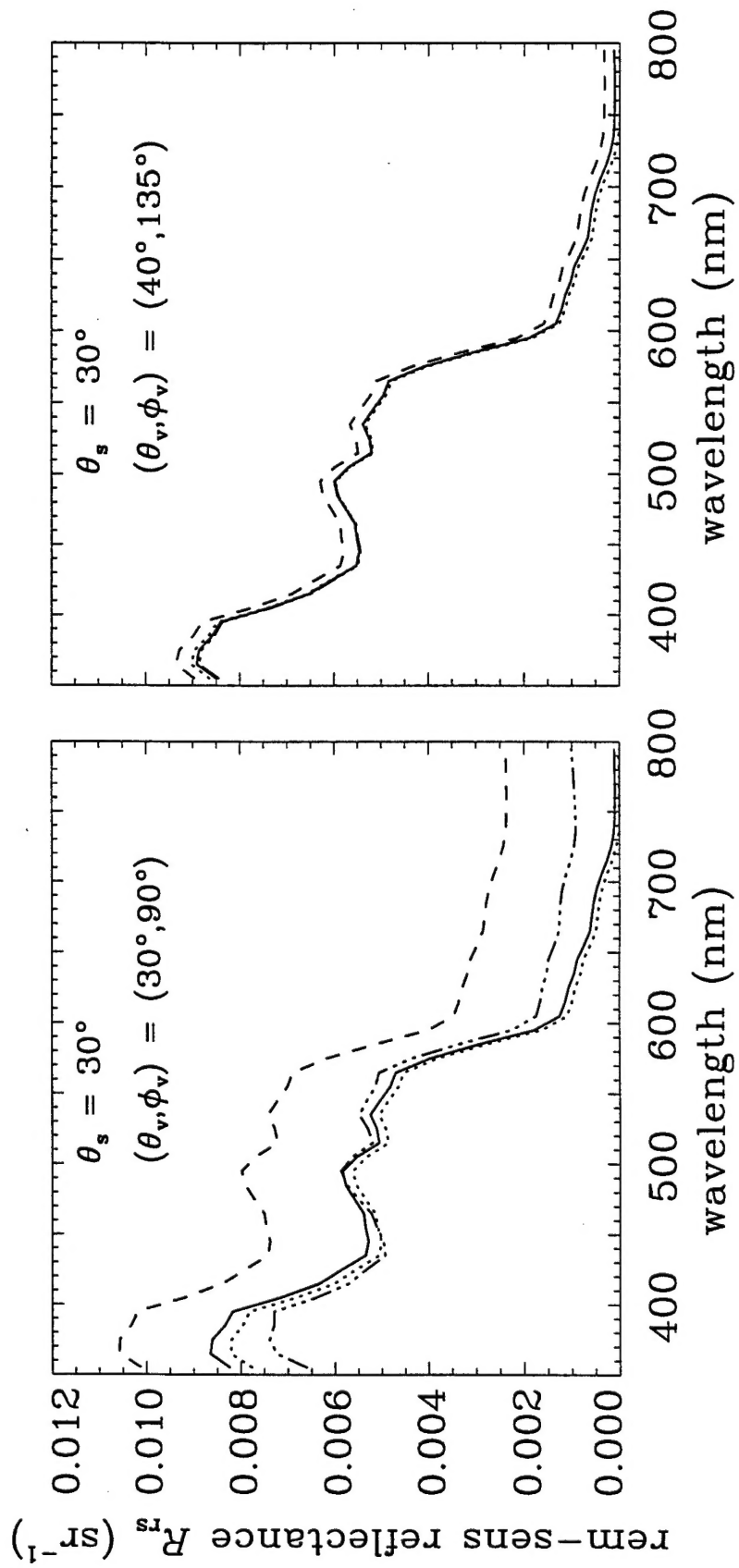
Fig. 11

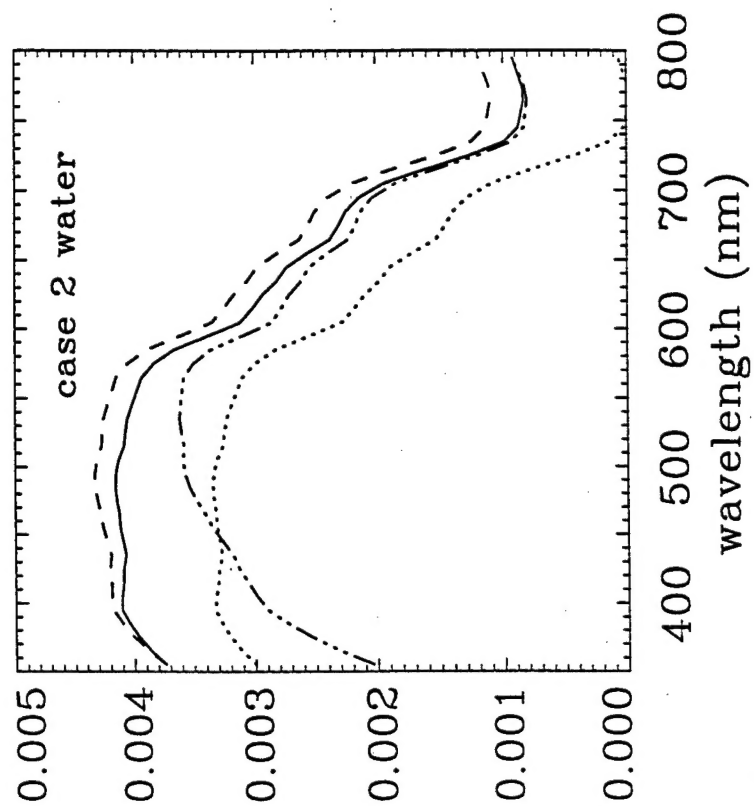
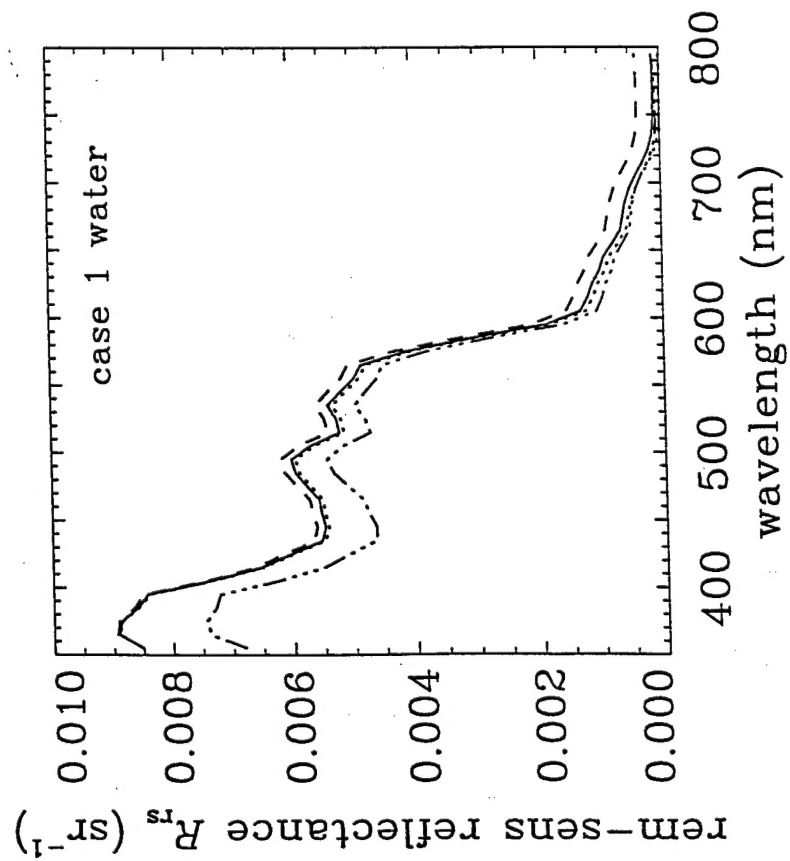




E42

Fig. 12





E44

Fig. 14

